Západočeská univerzita v Plzni
Fakulta aplikovaných věd

URČENÍ LOKÁLNÍHO MODELU GEOIDU Z LETECKÝCH TÍHOVÝCH DAT

Ing. Mgr. Jitka Hájková

disertační práce
k získání akademického titulu doktor
v oboru Geomatika

Školitel: Prof. Ing. Pavel Novák, Ph.D.

Katedra: Katedra matematiky

Plzeň 2014

University of West Bohemia
Faculty of Applied Sciences

LOCAL GEOID DETERMINATION BASED ON AERIAL GRAVITY DATA

Ing. Mgr. Jitka Hájková

Dissertation thesis in partial fulfillment of requirements for the degree of Doctor of Philosophy in specialization Geomatics

Supervisor: Prof. Ing. Pavel Novák, Ph.D.

Department: Department of Mathematics

Pilsen 2014

Declaration

I hereby declare that this Ph.D. thesis is completely my own work and that I used only the cited sources.

.....

Jitka Hájková

Acknowledgments

I would like to express my gratitude to Prof. Pavel Novák for his supervision and guidance during my PhD study. His expert advices as well as his support and encouragement were essential for the completion of this thesis. I am also grateful for providing FORTRAN codes for an evaluation of the one-step integration and a harmonic synthesis.

I would like to thank Prof. Cheinway Hwang for kindly providing the preprocessed airborne gravity data, the Digital Terrain Model of 3 arcsec resolution and the GPS/levelling test points.

Prof. Wolfgang Keller is appreciated for providing me the opportunity to cooperate with him on the development of 4D wavelet transform.

I thank my colleagues for their friendship and support.

Finally, I would like to appreciate my husband Aleš for his understanding, patience and support, and our children Jan and Lucie for being brave sweethearts while missing their mom for many weeks. I thank my parents for their support and encouragement during my studies.

Abstrakt

Popis tíhového pole Země a jeho ekvipotenciální plochy zvané geoid je jedním ze základních úkolů geodézie. Předkládaná disertační práce se zabývá určením lokálního modelu geoidu z leteckých tíhových dat z oblasti Taiwanu.

V teoretické části disertační práce je popsána teorie tíhového pole Země včetně určení geoidu z měřených tíhových dat a popisu již existujících lokálních modelů geoidu v oblasti Taiwanu. Dále je popsána stručná historie letecké gravimetrie, významné letecké gravitační kampaně z posledních let a základní principy leteckých gravitačních měření.

Pro určení lokálního modelu geoidu byla použita data ze třech leteckých gravitačních kampaní realizovaných v oblasti Taiwanu. Kvůli frekvenčnímu rozsahu dostupných leteckých gravitačních dat a jejich lokálnímu charakteru byla při zpracování těchto dat použita metoda zvaná "remove-compute-restore". Okrajová úloha pro určení frekvenčně limitovaného poruchového tíhového potenciálu z frekvenčně limitovaných leteckých tíhových poruch byla formulována ve sférické aproximaci. Pro výpočet frekvenčně limitovaného poruchového tíhového potenciálu byly použity dva přístupy, při jejichž numerické realizaci jsme využili různé numerické metody. Jedná se o "jednokrokový postup" s numerickou integrací realizovanou pomocí Newton-Cotesových vzorců a s vlnkovou transformací a o dvoukrokový postup. Tyto metody byly vybrány ze dvou důvodů. Prvním cílem bylo porovnání dvou vybraných známých postupů, které se využívají v letecké gravimetrii, a určení vhodnějšího postupu pro zpracování lokalních leteckých dat v oblasti Taiwanu. Druhým cílem bylo testování *nové numerické metody, 4D vlnkové transformace*, na jejímž vývoji se autorka disertační práce podílela. Kvůli požadavku na harmoničnost frekvenčně limitovaného tíhového potenciálu byl při zpracování leteckých gravitačních dat uvažován také vliv topografie na měřená data.

V numerické části disertační práce byla nejdříve určena přesnost použitých numerických metod (Newton-Cotesovy vzorce pro numerickou integraci, 4D vlnková transformace a Taylorova řada) pomocí syntetických tíhových dat. Poté byly pomocí "jednokrokového postupu" a dvoukrokového postupu vypočteny z dostupných leteckých gravitačních dat lokální modely geoidu v oblasti Taiwanu. Přesnost vypočtených modelů geoidu byla odhadnuta pomocí GNSS/nivelačních bodů a následně porovnána s přesností modelu geoidu určeného pouze z globálního gravitačního modelu.

Pro výpočet lokálního modelu geoidu byly v disertační práci použity tři metody. Výsledky zpracování všech dostupných leteckých tíhových dat ukazují, že *nejpřesnější model geoidu byl určen "jednokrokovým postupem" s numerickou integrací realizovanou pomocí Newton-Cotesových vzorců*. Zlepšení modelu geoidu spočteného pouze z EGM08 bylo na úrovni milimetrů. Vysoká přesnost EGM08 se nicméně vztahuje spíše k nížinným oblastem, jelikož GNSS/nivelační body se nachází především podél cest v pobřežních nížinách. V oblasti vysokých pohoří, kde je nedostatek pozemních dat, předpokládáme při použití leteckých tíhových dat výraznější zlepšení modelu určeného pouze z EGM08. Přesnost našeho řešení je také nižší než přesnosti lokálního modelů geoidu v jiných geografických oblastech. Porovnávané modely se však liší např. metodami zpracování nebo použitými tíhovými daty (letecká, pozemní, ...). Lze předpokládat, že použití dalších lokálních tíhových dat nebo vytvoření hybridního modelu geoidu by zvýšilo přesnost našeho modelu geoidu na srovnatelnou úroveň.

Abstract

Description of the Earth's gravity field and one of its equipotential surfaces called geoid is one of the basic tasks of geodesy. In this thesis, the determination of the local geoid model from aerial gravity data in the area of Taiwan is discussed.

In the theoretical part of the thesis the theory of the Earth gravity field is presented, including a determination of the geoid from measured gravity data. The available local geoid models of Taiwan are also introduced. Then, a historical overview including the recent major aerial gravitational surveys is described as well as the basic principles of aerial gravitational measurements.

Aerial gravitational data from three aerial gravitational surveys performed in the area of Taiwan were processed in order to determine the local geoid model. The limited frequency range of available aerial gravitational data and their geographic restriction lead to using the "remove-compute-restore" concept. The boundary-value problem for determination of the band-limited disturbing gravity potential from the band-limited aerial gravity disturbances is formulated in the spherical approximation. The two approaches with different numerical methods are used for the evaluation of the band-limited disturbing gravity potential: "one-step approach" with both Newton-Cotes formulas for numerical integration and wavelet transform, and two-step approach. These methods were chosen for two reasons: to compare the two selected known approaches used in aerial gravimetry and to determine the more convenient approach for processing the aerial gravity data in the area of Taiwan; to test *the new numerical method, 4D wavelet transform*. The author of the thesis took part in development of this numerical method. Since the band-limited disturbing gravity potential is assumed to be harmonic outside the geoid, the gravitational effect of topography on measured aerial gravitational data (the second Helmert method of

gravity reduction) is taken into account.

In the numerical part of the thesis different numerical methods, the Newton-Cotes formulas for numerical integration, 4D wavelet transform and the Taylor series, are tested first using synthetic gravity data. Then, "one-step approach" and two-step approach are applied on available aerial gravitational data in order to determine the local geoid model of Taiwan. The accuracies of evaluated local geoid models are determined by comparing them with the GNSS/levelling points and subsequently compared with the accuracy of the EGM08-only geoid model.

The three methods for computation of the local geoid model in the area of Taiwan were compared in the thesis. Results based on the available aerial gravitational data show that *the "one-step approach" computed using Newton-Cotes formulas for numerical integration with the topographical effects evaluated by the integration is the optimal method* providing the most accurate local geoid model of Taiwan. The improvement of EGM08-only geoid is just at the level of millimetres. Nevertheless, the very high accuracy of EGM08 relates rather to the lowlands than to the entire island, because the GNSS/levelling points are located mostly along routes within coastal lowlands. The improvement of EGM08 could be more significant in the mountainous areas of Taiwan because the lack of available terrestrial gravity data in these areas. The accuracy of our solution is lower than the accuracy of the local geoid models from the other areas. However, these models differ, e.g., in processing methods or the used gravity data (aerial, terrestrial, ...). It can be assumed that using the other local gravity data in the area of Taiwan or creating a hybrid geoid model could lead to the local geoid model with the comparable accuracy.

Contents

Abstrakt **v**

Abstract **vii**

List of figures **xii**

List of tables **xvii**

Nomenclature **xviii**

Introduction **1**

0.1 Aerial gravimetry 3

0.2 Outline of the thesis 5

1 Earth's gravity field **6**

1.1 Introduction to the potential theory 8

1.2 Normal gravity field 10

1.3 Disturbing gravity field 12

1.3.1 Gravity disturbance and gravity anomaly 13

1.3.2 Other definitions of telluroid 17

1.4 Geoid 19

1.4.1 Low-frequency component of the geoid 20

1.4.2 Global gravitational model 22

1.4.3 High-frequency component of the geoid 23

1.4.4 Local geoid models of Taiwan 26

2 Aerial gravimetry **27**
2.1 Historical overview 27
2.2 The principle of aerial gravimetry 29

3 Aerial data of Taiwan **31**
3.1 Taiwan Island Survey 2004-2005 32
3.2 Kuroshio Current Survey 2006-2008 32
3.3 Taiwan Strait Survey 2008-2009 33

4 Processing of aerial gravity data **35**
4.1 Formulation of BVPs for aerial gravity 35
4.1.1 Methods of transformation of $\delta g(R+D)$ to $T(R)$ 41
4.2 Numerical integration 42
4.3 Wavelet transform 43
4.3.1 Introduction to wavelet transform in geodesy 44
4.3.2 Wavelet decomposition and reconstruction in 1D 46
4.3.3 N-dimensional wavelet analysis 51
4.3.4 Computation of the local geoid model using 4D wavelet transform 54
4.4 Taylor series 55
4.5 Topographical effects on observed gravity 56
4.5.1 Direct topographical effect on gravity 58
4.5.2 Indirect topographical effect on potential 60

5 Testing numerical methods using synthetic gravity data **62**

6 Application to aerial data of Taiwan – numerical results **68**
6.1 Remove step 70
6.2 Computation step 73
6.3 Restore step 76
6.4 Comparison with GNSS/levelling points 76
6.5 Accuracy of numerical results 78

7 Conclusions and recommendations **83**
7.1 Conclusions 83
7.1.1 Summary of results 85
7.2 Recommendations 89

Bibliography **91**

List of Publications **109**

A Geocentric coordinate system **110**

B Coordinates **111**
B.1 Cartesian coordinates 111
B.2 Spherical coordinates 111
B.3 Gauss ellipsoidal coordinates (geodetic coordinates) 112
B.4 Astronomical (natural) coordinates 114

C Mathematical operators **115**
C.1 Gradient 115
C.2 Curl 116
C.3 Divergence 116
C.4 Laplacian 116

D Numerical results – synthetic gravity data **117**

E Numerical results – aerial gravity data **122**
E.1 Remove step – test area 123
E.2 Remove step – all available gravity data 128
E.3 Restore step – test area 142
E.4 Restore step – all available gravity data 160
E.5 Comparison with GNSS/levelling points – test area 172
E.6 Comparison with GNSS/levelling points – all available gravity data . . . 178
E.7 Comparison with GNSS/levelling points – GGMs only 183

List of figures

1.1 Gravity vector g 7
1.2 Definition of heights 15
1.3 Telluroid Σ as an approximation to the Earth's surface S 17

3.1 Aerial gravity data – Taiwan Island Survey 33
3.2 Aerial gravity data – Taiwan Strait and Kuroshio Current Surveys 34

4.1 Band-limited integration kernel $\mathcal{I}_b$ – dependence on degree n 39
4.2 Band-limited integration kernel $\mathcal{I}_b$ – dependence on spherical distance ψ . 40
4.3 Multi-resolution analysis (MRA) of $L^2(\mathbb{R})$ 46
4.4 Scheme of the Mallat algorithm 50
4.5 Scheme of the inverse Mallat algorithm 51
4.6 Schemes of the n-dimensional Mallat (left) and inverse Mallat (right) algorithm 54
4.7 Daubechies wavelet ψ (D4) 55

5.1 Scheme of testing using synthetic gravity 64
5.2 Random noise ϵ 64

6.1 Diagram of the evaluation of geoidal heights from gravity disturbances . . 69
6.2 Aerial gravity data – test area 70
6.3 Distribution of GNSS/levelling points in Taiwan 77

B.1 Cartesian coordinates x, y and z 112
B.2 Spherical coordinates r, θ and λ 113

D.1 Histograms of the geoid noise ϵ^N for NC, $\epsilon = 0$ mGal 118
D.2 Histograms of the geoid noise ϵ^N for NC, $\epsilon = 3$ mGal 119
D.3 Histograms of the geoid noise ϵ^N for WT, $\epsilon = 0$ mGal 120
D.4 Histograms of the geoid noise ϵ^N for WT, $\epsilon = 3$ mGal 121

E.1 Test area ($H_1 = 5156$ m), remove step – GOCO03s to degree and order $n = m = 200$ 123
E.2 Test area ($H_1 = 5156$ m), remove step – EGM08 to degree and order $n = m = 200$ 124
E.3 Test area ($H_1 = 5156$ m), remove step – EGM08 to degree and order $n = m = 360$ 125
E.4 Test area ($H_1 = 5156$ m), remove step – EGM08 to degree and order $n = m = 1080$ 126
E.5 Test area ($H_1 = 5156$ m), remove step – EGM08 to degree and order $n = m = 2160$ 127
E.6 Central area ($H_1 = 5156$ m), remove step – GOCO03s to degree and order $n = m = 200$ 129
E.7 Central area ($H_1 = 5156$ m), remove step – EGM08 to degree and order $n = m = 200$ 130
E.8 Central area ($H_1 = 5156$ m), remove step – EGM08 to degree and order $n = m = 360$ 131
E.9 Central area ($H_1 = 5156$ m), remove step – EGM08 to degree and order $n = m = 1080$ 132
E.10 Central area ($H_1 = 5156$ m), remove step – EGM08 to degree and order $n = m = 2160$ 133
E.11 Western and eastern area ($H_2 = 1620$ m), remove step – GOCO03s to degree and order $n = m = 200$ 135
E.12 Western and eastern area ($H_2 = 1620$ m), remove step – EGM08 to degree and order $n = m = 200$ 136
E.13 Western and eastern area ($H_2 = 1620$ m), remove step – EGM08 to degree and order $n = m = 360$ 137

E.14 Western and eastern area ($H_2 = 1620$ m), remove step – EGM08 to degree and order $n = m = 1080$ . . . 138
E.15 Western and eastern area ($H_2 = 1620$ m), remove step – EGM08 to degree and order $n = m = 2160$ . . . 139
E.16 Test area, restore step (N-NC, I) – GOCO03s to degree and order $n = m = 200$ . . . 142
E.17 Test area, restore step (N-NC, FS) – GOCO03s to degree and order $n = m = 200$ . . . 143
E.18 Test area, restore step (N-NC, I) – EGM08 to degree and order $n = m = 200$ . . . 144
E.19 Test area, restore step (N-NC, FS) – EGM08 to degree and order $n = m = 200$ . . . 145
E.20 Test area, restore step (N-NC, I) – EGM08 to degree and order $n = m = 360$ . . . 146
E.21 Test area, restore step (N-NC, FS) – EGM08 to degree and order $n = m = 360$ . . . 147
E.22 Test area, restore step (N-NC, I) – EGM08 to degree and order $n = m = 1080$ . . . 148
E.23 Test area, restore step (N-NC, FS) – EGM08 to degree and order $n = m = 1080$ . . . 149
E.24 Test area, restore step (N-NC, I) – EGM08 to degree and order $n = m = 2160$ . . . 150
E.25 Test area, restore step (N-WT, AC+H) – GOCO03s to degree and order $n = m = 200$ . . . 153
E.26 Test area, restore step (N-WT, AC+H) – EGM08 to degree and order $n = m = 200$ . . . 154
E.27 Test area, restore step (N-WT, AC+H) – EGM08 to degree and order $n = m = 360$ . . . 155
E.28 Test area, restore step (N-WT, AC+H) – EGM08 to degree and order $n = m = 1080$ . . . 156

E.29 Test area, restore step (N-WT, AC+H) – EGM08 to degree and order $n = m = 2160$ . . . 157
E.30 All available data, restore step (N-NC) – GOCO03s to degree and order $n = m = 200$ . . . 160
E.31 All available data, restore step (N-WT, AC+H) – GOCO03s to degree and order $n = m = 200$ . . . 161
E.32 All available data, restore step (N-NC) – EGM08 to degree and order $n = m = 200$ . . . 162
E.33 All available data, restore step (N-WT, AC+H) – EGM08 to degree and order $n = m = 200$ . . . 163
E.34 All available data, restore step (N-NC) – EGM08 to degree and order $n = m = 360$ . . . 164
E.35 All available data, restore step (N-WT, AC+H) – EGM08 to degree and order $n = m = 360$ . . . 165
E.36 All available data, restore step (N-NC) – EGM08 to degree and order $n = m = 1080$ . . . 166
E.37 All available data, restore step (N-WT, AC+H) – EGM08 to degree and order $n = m = 1080$ . . . 167
E.38 All available data, restore step (N-NC) – EGM08 to degree and order $n = m = 2160$ . . . 168
E.39 All available data, restore step (N-WT, AC+H) – EGM08 to degree and order $n = m = 2160$ . . . 169
E.40 Histograms of the differences – test area (GOCO03s to $n = m = 200$) . . 173
E.41 Histograms of the differences – test area (EGM08 to $n = m = 200$) . . . 174
E.42 Histograms of the differences – test area (EGM08 to $n = m = 360$) . . . 175
E.43 Histograms of the differences – test area (EGM08 to $n = m = 1080$) . . . 176
E.44 Histograms of the differences – test area (EGM08 to $n = m = 2160$) . . . 177
E.45 Histograms of the differences – all available gravity data (GOCO03s to $n = m = 200$) . . . 178
E.46 Histograms of the differences – all available gravity data (EGM08 to $n = m = 200$) . . . 179

E.47 Histograms of the differences – all available gravity data (EGM08 to $n = m = 360$) 180
E.48 Histograms of the differences – all available gravity data (EGM08 to $n = m = 1080$) 181
E.49 Histograms of the differences – all available gravity data (EGM08 to $n = m = 2160$) 182
E.50 Histograms of the differences – GGMs only 183

List of tables

1.1 Selected parameters of the actual, normal and disturbing gravity fields . . 14

5.1 Synthetic geoidal heights N from EGM08 65
5.2 Geoid noise ϵ^N for NC 66
5.3 Geoid noise ϵ^N for WT 67

6.1 Statistics of aerial gravity data in the "remove" step – test area 73
6.2 Statistics of aerial gravity data in the "remove" step – all available gravity data 74
6.3 Differences between the GNSS/levelling and the computed geoidal heights – test area 80
6.4 Differences between the GNSS/levelling and the computed geoidal heights – all available gravity data 81
6.5 Differences between the GNSS/levelling and the computed geoidal heights – GGMs only 82

E.1 Statistics of aerial gravity data in the "remove" step – central area 134
E.2 Statistics of aerial gravity data in the "remove" step – western area 140
E.3 Statistics of aerial gravity data in the "remove" step – eastern area 141
E.4 Statistics of the parameters in the "restore" step (N-NC) – test area 152
E.5 Statistics of the parameters in the "restore" step (N-WT, AC+H) – test area 159
E.6 Statistics of the parameters in the "restore" step (N-NC, N-WT, AC+H) – all available gravity data 171

Nomenclature

Acronyms

AC+H – two-step approach (Analytic Continuation + Hotine's formula)

BVP – Boundary-Value Problem

CHAMP – CHAllenging Minisatellite Payload

DGNSS – Differential Global Navigation Satellite Systems

DLR – Deutsche Forschungsanstalt für Luft und Raumfahrt

DTE – Direct Topographical Effect

EGM96 – Earth Gravitational Model 1996

EGM08 – Earth Gravitational Model 2008

ESA – European Space Agency

FFT – Fast Fourier Transform

FS – Finite Series

GFZ – GeoForschungsZentrum

GGM – Global Gravitational Model

GMT – Generic Mapping Tools

GNSS – Global Navigation Satellite Systems

GOCE – Gravity field and steady-state Ocean Circulation Explorer

GOCO03s – GGM from the project GOCO (Combination of GOCE data with complementary gravity field information; Gravity Observation Combination)

GPS NAVSTAR – Global Positioning System - NAVigation System with Timing And Ranging

GRACE – Gravity Recovery And Climate Experiment

GRAV-D – Gravity for the Redefinition of the American Vertical Datum

GRS 80 – Geodetic Reference System 1980

I – numerical Integration

ICGEM – International Centre for Global Earth Models

ITE – Indirect Topographical Effect

LTS – Linear part of the Taylor Series

MRA – Multi-Resolution Analysis

NASA – National Aeronautics and Space Administration

NC – Newton-Cotes formulas for numerical integration

N-NC – "one-step approach" (solution of Neumann's BVP) using the Newton-Cotes formulas for numerical integration

N-WT – "one-step approach" (solution of Neumann's BVP) using the Wavelet Transform

OSU91a – GGM produced by the Ohio State University in 1991

QTS – Quadratic part of the Taylor Series

TRF – Terrestrial Reference Frame

TRS – Terrestrial Reference System

WT – Wavelet Transform

Symbols

Scalars and functions

a – major semi-axis of the ellipsoid of revolution; equatorial radius of the Earth

b – minor semi-axis of the ellipsoid of revolution

$c_{m,k},\ d_{m,k}$ – coefficients of the linear combination of the scaling functions and wavelets, respectively (used in the Mallat algorithm)

e – first eccentricity

$f(x)$ – continuous space dependent signal

g – actual gravity

g_k – coefficients of the mother wavelet

h – Gauss's ellipsoidal (geodetic) height

h_n – scaling coefficients

l – minimum degree in terms of the spherical harmonic expansion

m – order of the spherical harmonic expansion

n – degree of the spherical harmonic expansion

x, y, z – Cartesian coordinates

A – direct topographical effect on gravity

A_b – band-limited direct topographical effect on gravity

$A_{n,m},\ B_{n,m}$ – Stokes's coefficients

$\overline{A}_{n,m},\ \overline{B}_{n,m}$ – fully-normalized Stokes's coefficients

D – flight height above the geocentric sphere

G – Newton's gravitational constant

GM – geocentric gravitational constant

$H(\psi)$ – Hotine's spherical kernel function

H_N – normal (Molodensky's) height

H_O – orthometric height

$H_n^2,\ H_n^3$ – Laplace harmonics of the squared and cubed topographical height functions

J_2 – dynamical form factor of the Earth (Stokes's zonal coefficient)

$\mathcal{J}_1(r, R, \psi),\ \mathcal{J}_2(r, R, \psi)$ – integration kernels in the evaluation of DTE

$\mathcal{I}_b(r, R, \psi)$ – band-limited integration kernel in the "one-step approach"

$K(r, R, \psi)$ – Green's integral kernel

L – maximum degree in terms of the spherical harmonic expansion

M – mass of the Earth

$\mathcal{M}_1(\psi),\ \mathcal{M}_2(\psi)$ – integration kernels in the evaluation of ITE

N – geoidal height; transverse radius of curvature of the reference ellipsoid

N_{GGM} – low-frequency part of the geoid

$N_{GNSS/lev}$ – GNSS/levelling points

N_L – filtered geoidal heights

N_b^H – Helmert's residual co-geoid

N^H – co-geoid (Helmert's geoid)

P – indirect topographical effect on the geoid (also point on the geoid)

P_b – band-limited indirect topographical effect on the geoid

$P_n(t)$ – Legendre's polynomials

$P_{n,m}(t)$ – associated Legendre's functions of the first kind

$\overline{P}_{n,m}(t)$ – fully-normalized associated Legendre's functions of the first kind

R – radius of a geocentric sphere

$R_{n,k}(t)$ – Paul's coefficients

$S(\psi)$ – Stokes's spherical kernel function

T – disturbing gravity potential

T_b – band-limited disturbing gravity potential

T_{GGM} – low-frequency part of the disturbing gravity potential

T_L – filtered disturbing gravity potential

T_b^H – Helmert's residual disturbing gravity potential

T^H – Helmert's disturbing gravity potential

T^ϵ – disturbing gravity potential with propagated noise ϵ^T

$T_n(\Omega)$ – surface spherical harmonics

U – gravity potential of the ellipsoid of revolution (normal gravity potential)

U_c – centrifugal part of the normal gravity potential

U_g – gravitational part of the normal gravity potential

U_0 – normal gravity potential on the reference ellipsoid

$V_n(D, \psi_0)$ – truncation coefficients

V^{ct} – gravitational potential of condensed topography

V^t – gravitational potential of topography

W – gravity potential of the Earth's gravity field (actual gravity potential)

W_c – centrifugal part of the actual gravity potential

W_g – gravitational part of the actual gravity potential

W_0 – actual gravity potential on the geoid

$\alpha_n,\ \alpha_{n,m}$ – normalization factor

γ – normal gravity

γ_e – normal gravity on the equator

γ_p – normal gravity on the poles

$\delta_{j,k}$ – Kronecker delta

ϵ – random noise for testing numerical methods

ϵ^N – noise propagated to the geoidal heights

ϵ^T – noise propagated to the disturbing gravity potential

ϵ_t – truncation error

θ – spherical co-latitude

κ – wavelength of a function

λ – Gauss ellipsoidal (geodetic) longitude; spherical longitude

ρ – mass density

φ – Gauss ellipsoidal (geodetic) latitude; scaling function

ψ – spherical distance between two points; mother wavelet

ω – angular velocity of the Earth's rotation

Θ – deflection of the vertical

Λ – astronomical longitude

Φ – astronomical latitude

Ω – geocentric direction ($\Omega = (\theta, \lambda)$)

Ω_0 – solid angle corresponding to the limited geographical area (spherical cap)

Ω_S – solid angle of the whole sphere

δg – gravity disturbance

δg_b – band-limited gravity disturbance

δg_{GGM} – low-frequency part of the gravity disturbance

δg_L – filtered gravity disturbance

δg_b^H – Helmert's residual gravity disturbances

δg^ϵ – gravity disturbance with random noise

δV – indirect topographical effect on the disturbing gravity potential (Helmert's residual potential)

δV_b – band-limited indirect topographical effect on the disturbing gravity potential

Δg – gravity anomaly

Vectors, matrices and sequences

$\mathbf{a_c}$ – centrifugal acceleration vector

$\mathbf{a_g}$ – gravitational acceleration vector

$\mathbf{f}$ – vector of the non-gravitational acceleration (specific force vector)

$\mathbf{g}$ – gravity vector

$\mathbf{i}, \mathbf{j}, \mathbf{k}$ – unit vectors of the coordinate system

$\mathbf{n}$ – tangent to the plumbline of the normal gravity field (the ellipsoidal normal)

$\mathbf{o}$ – zero vector

$\mathbf{r}$ – position vector of the point of interest

$\mathbf{r_e}$ – position vector of the point on the reference ellipsoid

$\mathbf{r_g}$ – position vector of the point on the geoid

$\mathbf{t}$ – tangent to the plumbline of the actual gravity field

$\boldsymbol{\gamma}$ – normal gravity vector

$\delta\mathbf{g}$ – gravity disturbance vector

$\Delta\mathbf{g}$ – gravity anomaly vector

$\mathbf{A}$ – matrix of the coefficients in the Galerkin method

$\mathbf{I}$ – identity matrix

$\mathbf{M}$ – matrix of the second derivatives of the normal gravity potential U

$\mathbf{R}$ – rotation matrix

$\boldsymbol{\Omega}^l_{ie},\ \boldsymbol{\Omega}^l_{el}$ – skew-symmetric matrices

$\mathbf{d}$ – multi-index in the n-dimensional wavelet transform

Localization of points

P – point on the geoid (also indirect topographical effect on the geoid)

P' – point on the topography

Q – point on the reference ellipsoid

Q' – point on the telluroid

S – the Earth's surface

Σ – telluroid

Sets

$\mathbb{Z}$ – integers

$\mathbb{R}$ – real numbers

Spaces and projectors

$L^2(\mathbb{R})$ – space of square integrable functions on $\mathbb{R}$

$l_2(\mathbb{Z})$ – space of square summable sequences on $\mathbb{Z}$

$V_i \subset L^2(\mathbb{R}),\ W_j \subset L^2(\mathbb{R})$ – subspaces of $L^2(\mathbb{R})$

$U \oplus V$ – direct sum of the spaces U and V

$P_i,\ Q_i$ – projectors into subspace V_i and the corresponding orthogonal complement W_i

Operators and mathematical notations

$H,\ G$ – decomposition operators of the Mallat algorithm

$H^*,\ G^*$ – adjoint operators of the decomposition operators H, G

$\mathbf{f} \cdot \mathbf{g}$ – scalar product of the vectors $\mathbf{f}$ and $\mathbf{g}$

$\mathbf{f} \times \mathbf{g}$ – cross product of the vectors $\mathbf{f}$ and $\mathbf{g}$

$\mathrm{curl}\mathbf{F}$ – curl of the vector field $\mathbf{F}$

$\mathrm{div}\mathbf{F}$ – divergence of the vector field $\mathbf{F}$

$\nabla \mathbf{f}$ – gradient of the vector $\mathbf{f}$

$\Delta \mathbf{f}$ – the Laplace operator of the vector $\mathbf{f}$ (Laplacian)

$\langle f, g \rangle_{L^2}$ – discrete scalar product of two complex functions f and g in $L^2(\mathbb{R})$

Introduction

Description of the Earth's gravity field is one of the basic tasks of geodesy. Determination of a certain equipotential surface of this gravity field called geoid (vertical datum for orthometric heights, i.e., heights above the mean-sea level) is very important for conversion of ellipsoidal heights obtained by GNSS (Global Navigation Satellite Systems) to orthometric heights obtained by levelling. The geoid can be replaced by the quasigeoid in order to convert the ellipsoidal heights to the normal (Molodensky) heights. The height system based on the normal heights is used for example in the Czech Republic. The precise description of the gravity field of the Earth is also very useful in geophysics and geodynamics for studying anomalous mass structures within the Earth, tectonic forces (e.g., earthquake prediction), oceanic lithosphere, Earth rotation, as well as ocean tides, currents and sea surface topography.

The gravity field of the Earth can be described by a scalar function of position and time called the gravity potential. The gravity potential cannot be directly measured. Nevertheless, his directional derivatives are measurable. Gravimetry[1] deals with measurements of the first directional derivatives - gradient of the gravity potential. Gradiometry[2] deals with a measurement of the second directional derivatives of the gravity potential – Marussi[3] tensor. The gravity potential can be computed from his directional derivatives. Measurements are performed on the ground (terrestrial gravity and gradiometry), on board of an

[1]The beginnings of gravimetry are connected with Galileo Galilei (1564-1642), an Italian physicist, mathematician, engineer, astronomer and philosopher. The gal, an unit of acceleration used extensively in gravimetry, is named after him (1 Gal $= 10^{-2}$ ms^{-2}).

[2]The unit used in gradiometry is Eotvos (1 E $= 10^{-9}$ s^{-2}), named after Hungarian physicist Loránd Eötvös (Vásárosnaményi Báró Eötvös Loránd, 1848-1919).

[3]Marussi, Antonio (1908-1984) - Italian geodesist and geophysicist.

aircraft (aerial gravity and gradiometry), of a ship (marine gravity and gradiometry) and of a satellite (satellite gravity and gradiometry).

Gravity-dedicated satellite missions CHAMP[4], GRACE[5] and GOCE[6] provide gravity data that cover almost a whole surface of the Earth, except of polar regions. Since orbital altitudes of these satellites are at a level of hundreds of kilometres, only a global (low-frequency/long-wavelength) part of the gravity potential can be determined from their data. Local gravity data are obtained from terrestrial, aerial and marine gravity surveys or satellite altimetry. Measurements are performed on the ground or at locations very close to the Earth surface, thus, a local (high-frequency/short-wavelength) part of the gravity potential is determined. The main disadvantage of local gravity data is their space limitation. These gravity data are usually available just within limited areas. In the case of terrestrial data, moreover, measurements cannot be performed within inaccessible areas (mountains, jungles, ...).

Methods often used in the geoid determination include a least-squares collocation (Krarup 1969; Moritz 1980; Forsberg and Kenyon 1994; Marchenko et al. 2001; Forsberg 2002), radial base functions (Schmidt et al. 2007; Klees et al. 2008; Antoni, Keller and Weigelt 2009), variational methods (Holota 1995, 1997; Holota and Nesvadba 2008) and integral formulas for the solution of geodetic boundary-value problems as the Stokes integral (Stokes 1849), the Hotine integral (Hotine 1969) and the Molodensky integral series (Molodensky, Eremeev and Yurkina 1960). The numerical approaches include the fast Fourier transform (FFT) techniques (Sideris and Schwarz 1986; Schwarz, Sideris and Forsberg 1990), wavelet transform (WT) techniques (Freeden and Windheuser 1997;

[4]CHAMP (CHAllenging Minisatellite Payload) – German small satellite mission for geoscientific and atmospheric research and applications, managed by GFZ (GeoForschungsZentrum – German research center for geoscience) in Potsdam, launched in July 2000, ended in September 2010. Source: http://www.gfz-potsdam.de/champ/.

[5]GRACE (Gravity Recovery And Climate Experiment) – joint partnership between the National Aeronautics and Space Administration (NASA) in the United States and Deutsche Forschungsanstalt für Luft und Raumfahrt (DLR) in Germany, launched in March 2002, currently operating in an extended mission phase, which is expected to continue through at least 2015. Source: http://www.nasa.gov/mission_pages/Grace/.

[6]GOCE (Gravity Field and Steady-State Ocean Circulation Explorer) - first of ESA's Living Planet Programme satellites intended to map the Earth's gravity field, launched in March 2009, ended in November 2013. Source: http://www.esa.int/.

Freeden and Schneider 1998; Keller 2004; Kuroishi and Keller 2005; Roland and Denker 2005) and the spherical harmonic expansion (Heiskanen and Moritz 1967).

Spherical harmonic expansion of the gravity potential provides an effective way for modelling of the long-wavelength gravity field in order to get a reference field for a local approximation. The geopotential models are therefore used in all methods of precise geoid determination. There are many geopotential models that differ in maximum degree and order of the harmonic expansion or in types of input data sets (see, e.g., http://icgem.gfz-potsdam.de/ICGEM/). The Earth Gravitational Model 2008 (EGM08, Pavlis et al. 2012) has the maximum degree and order of the harmonic expansion from all available official geopotential models. It was developed up to the degree and order 2160 and corresponds to a set of global mean gravity data with the equiangular resolution (half-wavelength) of $5'$ (approximately 10 km at the Earth's surface).

The medium-wavelength and short-wavelength part of the gravity potential can be obtained from local gravity data using the collocation, FFT, WT or integral formulas (the Stokes integral, the Hotine integral and the Molodensky series).

0.1 Aerial gravimetry

Aerial gravimetry is a fast and efficient method of gravitational data collection. Whereas ground gravity data are measured mostly along roads or in flat terrain, aerial gravimetry can cover areas with more complicated relief as well as inaccessible regions (mountains, rainforests, seas, glaciers, off-coast regions, ...). It is an ideal technique to complement satellite-only gravity models. It is also an efficient tool to provide a transition between terrestrial and marine gravity data.

The beginning of aerial gravimetry is dated to the fifties of the 20th century. In the late 1950's, the first test of aerial gravity meter systems based on gravimetry was performed and others followed (Lundberg 1957; Thompson and LaCoste 1960). Although first results were promising, their accuracy was affected by a lack of accurate navigation data (Nettleton, LaCoste and Harrison 1960). The major breakthrough came with a development of Global Navigation Satellite Systems (GNSS) during the mid 1980's (Hammer 1983; Brozena and Peters 1988). Since then many wide-area aerial gravitational surveys

have been performed with increasing spatial resolution and accuracy.

In aerial gravimetry, gravitational data are obtained along a flight trajectory. An aerial gravitational system measures a non-gravitational acceleration[7], that is subsequently separated into two parts – the dynamic acceleration of an aircraft and gravitation acceleration (Li 2000). The non-gravitational acceleration is measured either by strapdown inertial navigation systems, that determine the orientation of the sensors (three accelerometers) mathematically (Schwarz and Wei 1993; Wei and Schwarz 1998), or by platform inertial navigation systems, that stabilize a gravimeter in a vertical direction physically (Knickmeyer 1990; Salychev et al. 1994). Aircraft dynamic acceleration is obtained by differentiating in time the accurate position and velocity provided by DGNSS measurements (Wei, Ferguson and Schwarz 1992; Czompo 1994).

Since the beginning of the nineties, the aerial gravimetry has been used for a large-scale surveys. Campaigns were performed for example over Greenland (Brozena 1992; Brozena and Peters 1994; Brozena, Peters and Salman 1997; Forsberg and Kenyon 1994; Forsberg and Rubek 1998; Forsberg, Olesen and Keller 1999; Olesen et al. 2000), Switzerland (Klingelé et al. 1995; Verdun et al. 2003), Antarctica (Bell et al. 1992; Bell et al. 1999), Skagerrak and Azores (Forsberg et al. 1997; Hehl et al. 1997), Nordic Baltic region (Forsberg and Solheim 2000) and Arctic ocean (Childers et al. 2001; Forsberg et al. 2003). Recent major projects represent the national geoid and regional surveys of Malaysia, Mongolia and Ethiopia (Olesen and Forsberg 2007), Taiwan (Hwang et al. 2007, 2012, 2014), Alabama (Huang et al. 2013; Wang et al. 2013) and the United States (GRAV-D, http://www.ngs.noaa.gov). The reported accuracies of these campaigns were at the mGal level (about $1.5 - 3$ mGal for the spatial resolution of $5 - 6$ km).

In geodesy, one of the main applications of aerial gravitational data is local geoid determination. By combining them with the accurate low-frequency satellite gravitational models, the geoid can be determined from aerial gravimetry data with the decimetre-level accuracy or better. However, for the conversion of ellipsoidal heights to orthometric heights, the geoid with the centimetre-level accuracy is required. The better spatial resolution and accuracy of aerial gravimetry can be achieved either by improving of the sensors or by developing improved methodologies for processing of aerial gravitational data. In

[7]The measured non-gravitational acceleration is also called specific force (Torge 1980, p. 186).

this thesis, the focus is on processing of aerial gravitational data, in particulary on the transformation of measured aerial gravitational data to the geoid.

0.2 Outline of the thesis

The determination of the local geoid model from aerial gravitational data in Taiwan is discussed in the thesis. The first section is an introduction to the potential theory. The Earth's gravity field, the normal gravity field of an ellipsoid of revolution and the disturbing gravity field are introduced. The determination of the disturbing gravity potential from gravimetric measurements are also described in this section. Since there is a difference in determination of the global and local parts of the disturbing gravity potential, each case is discussed separately. A spherical harmonic synthesis is used for the evaluation of the global component. The local part is obtained as the solution of boundary-value problems.

The second section deals with the aerial gravimetry. After a short historical overview, the principle of the aerial gravimetry are described.

In the third section, the available aerial gravitational data in the area of Taiwan are presented.

The fourth section introduces the conversion of aerial gravitational data to the disturbing gravity potential. First, the boundary-value problem is formulated in the spherical approximation. Then, the mathematical background of each step of the conversion is described. As a new method of transformation of aerial gravity disturbances to the disturbing gravity potential, the 4D wavelet transformation in presented.

Results of testing the different numerical methods using synthetic gravity data are presented in the fifth section.

The numerical results for the aerial gravitational data from Taiwan are introduced in the sixth section. The comparison of the evaluated models of the local geoid in the area of Taiwan with the "real" geoid at GNSS/levelling points is also presented. The accuracy of the geoid obtained just using EGM08 and the improvement of this model using EGM08 and the aerial gravitational data is discussed.

In the last section, the conclusions and recommendations are given.

Chapter 1

Earth's gravity field

The Earth as every rotating massive body generates a gravity field. This vector field can be characterized, e.g., by the gravity vector $\mathbf{g}$. The total force on a unit mass – gravity $\mathbf{g}$ – is the resultant of the gravitational acceleration $\mathbf{a_g}$ and the centrifugal acceleration $\mathbf{a_c}$

$$\mathbf{g} = \mathbf{a_g} + \mathbf{a_c}\,. \tag{1.1}$$

The gravitational acceleration directs approximately to the centre of mass of the Earth while the centrifugal acceleration vector is orthogonal to the axis of rotation of the Earth and points out, outward this axis (see Fig. 1.1).

Although the magnitude of the gravity vector is measurable (at least in the direction of a plumbline), it is not practical to describe the gravity field this way because in a three-dimensional space the gravity vector has three components. Therefore, its description by some scalar function of position and time is much more convenient.

A vector field described by the vector $\mathbf{g}'$ is called conservative if for each simple piecewise smooth oriented closed curve C holds

$$\oint_C \mathbf{g}'(\mathbf{r}) \cdot \mathrm{d}\mathbf{r} = 0\,, \tag{1.2}$$

where "$\cdot$" stands for a scalar product and $\mathbf{r}$ stands for the position vector (see Appendix B.1) of the point of interest. Assume that the vector field is defined on an open set[1]. Then there

[1] Definition of an open set can be found in (Lebedev and Vorovich 2003), p. 18.

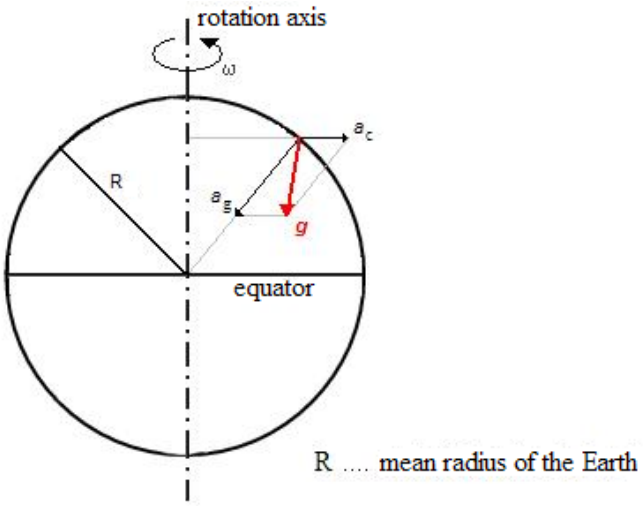

Figure 1.1: Gravity vector g

exists a scalar function W' for which holds

$$\mathbf{g}'(\mathbf{r}) = \nabla W'(\mathbf{r})\,, \tag{1.3}$$

where "∇" is the gradient (see Appendix C.1). Using the operator $\operatorname{curl}\mathbf{g}' = \nabla \times \mathbf{g}'$, see Appendix C.2, on Eq. (1.3) yields

$$\nabla \times \mathbf{g}'(\mathbf{r}) = \nabla \times \nabla W'(\mathbf{r})\,, \tag{1.4}$$

where "$\times$" stands for a cross product. We get from the definition of the gradient and the curl

$$\nabla \times \nabla W'(\mathbf{r}) = \mathbf{o}\,, \tag{1.5}$$

where $\mathbf{o}$ is the zero vector ($|\mathbf{o}| = 0$). Substituting Eq. (1.5) to Eq. (1.4) gives

$$\nabla \times \mathbf{g}'(\mathbf{r}) = \mathbf{o}\,, \tag{1.6}$$

i.e., the vector field is irrotational. Therefore, the conservative vector field is always irrotational.

Since the static gravity field is a conservative and irrotational vector field, the gravity vector g in any point relates, according Eq. (1.3), to the scalar function W (Heiskanen and Moritz 1967, p. 47)

$$\mathbf{g}(\mathbf{r}) = \nabla W(\mathbf{r})\,, \tag{1.7}$$

which is called the gravity potential. The surfaces, on which the gravity potential W is constant, i.e., $W(\mathbf{r}) = \text{const.}$, are called equipotential surfaces.

The most important equipotential surface of the Earth's gravity field is called the geoid (Gauss 1828; Listing 1873), see Sec. 1.4. The geoid is a (mean) surface of the ideal oceans with the gravity potential $W(\mathbf{r_g}) = W_0 = \text{const.}$, $\mathbf{r_g}$ is the position vector of the point on the surface of the geoid. The determination of the constant W_0 is one of the tasks of geodesy which is not discussed in the thesis. In the following text, the constant W_0 is assumed to be known.

The geoid is a vertical datum for orthometric heights that are usually obtained by spirit levelling. In Molodensky's theory of normal heights, the geoid is replaced by the quasigeoid (Molodensky 1945). The quasigeoid is no longer an equipotential surface of the Earth's gravity field. It differs from the geoid inside topographic masses but the differences are small, within the range of ± 1.5 m (higher the mountains, larger the differences). The normal heights are used in many countries, including the Czech Republic.

1.1 Introduction to the potential theory

Since the gravity vector $\mathbf{g}$ consists of the gravitational acceleration $\mathbf{a_g}$ and the centrifugal acceleration $\mathbf{a_c}$, see Eq. (1.1), the gravity potential W also has two parts corresponding to these vectors – gravitational potential W_g and centrifugal potential W_c. The gravitational potential can be evaluated by Newton's integral (Newton 1686; Pick, Pícha and Vyskočil 1973, p. 21)

$$W_g(\mathbf{r}) = G \iiint_B \frac{\rho(\mathbf{r}')}{|\mathbf{r}' - \mathbf{r}|} \, \mathrm{d}B(\mathbf{r}') \,, \tag{1.8}$$

where G stands for Newton's gravitational constant, B is the volume of the Earth, $|\mathbf{r}' - \mathbf{r}|$ is the Euclidean distance between the volume element $\mathrm{d}B$ (with the position vector $\mathbf{r}'$) of the mass density ρ and the point of interest $\mathbf{r}$. The centrifugal potential is determined by (Huygens 1703; Heiskanen and Moritz 1967, p. 47)

$$W_c(\mathbf{r}) = \frac{1}{2} p^2 \omega^2 \,, \tag{1.9}$$

where all inputs are known (ω is the angular velocity of the Earth's rotation, p is the distance of the point determined by the geocentric vector $\mathbf{r}$ from the rotation axis of the

Earth, $p = |\mathbf{r}| \sin\theta$ in the spherical coordinates, see Appendix B.2). Unfortunately, since the distribution of mass density inside the Earth, see Eq. (1.8), is not known with the sufficient accuracy, Newton's integral cannot be used directly. Therefore, one has to determine the gravitational potential in a different way, from available data measured on and outside the Earth's surface, see Sec. 1.4. Since the centrifugal potential W_c can accurately be evaluated for the known position $\mathbf{r}$ through Eq. (1.9), it is required to determine only the gravitational potential W_g from available gravity data.

In the case of measuring data at points connected with the Earth, both gravitational and centrifugal accelerations are present. Only the gravitational acceleration is present if measurement relates to points outside the Earth.

The gravitational potential W_g may be shown to satisfy Poisson's differential equation (Heiskanen and Moritz 1967, p. 5)

$$\Delta W_g(\mathbf{r}) = -4\pi G\rho(\mathbf{r})\,, \tag{1.10}$$

where "Δ" is the Laplace operator (Laplacian), see Appendix C.4, which in Cartesian coordinates (x, y, z), see Appendix B.1, has the form

$$\Delta = \frac{\partial^2}{\partial x^2} + \frac{\partial^2}{\partial y^2} + \frac{\partial^2}{\partial z^2}\,, \tag{1.11}$$

and in the spherical coordinates (r, θ, λ), see Appendix B.2,

$$\Delta = \frac{\partial^2}{\partial r^2} + \frac{2}{r}\frac{\partial}{\partial r} + \frac{1}{r^2}\frac{\partial^2}{\partial \theta^2} + \frac{\cos\theta}{r^2\sin\theta}\frac{\partial}{\partial\theta} + \frac{1}{r^2\sin^2\theta}\frac{\partial^2}{\partial\lambda^2}\,. \tag{1.12}$$

Assume the geocentric position of a point of interest is defined by the triplet of Cartesian coordinates $\mathbf{r} = (x, y, z)$. Consider the gravity potential W in the form

$$W(\mathbf{r}) = W_g(\mathbf{r}) + W_c(\mathbf{r}) = G\iiint\limits_B \frac{\rho(\mathbf{r}')}{|\mathbf{r}' - \mathbf{r}|}\,\mathrm{d}B(\mathbf{r}') + \frac{1}{2}p^2\omega^2\,, \tag{1.13}$$

where W_c could be expressed in the Cartesian coordinates (Heiskanen and Moritz 1967)

$$W_c(x, y) = \frac{1}{2}\omega^2(x^2 + y^2)\,. \tag{1.14}$$

By differentiating Eq. (1.14), we get

$$\Delta W_c(\mathbf{r}) = \frac{\partial^2 W_c(\mathbf{r})}{\partial x^2} + \frac{\partial^2 W_c(\mathbf{r})}{\partial y^2} + \frac{\partial^2 W_c(\mathbf{r})}{\partial z^2} = 2\omega^2\,. \tag{1.15}$$

Applying the Laplacian on Eq. (1.13) and taking Eq. (1.10) into account finally yields (Heiskanen and Moritz 1967, p. 47)

$$\Delta W(\mathbf{r}) = \Delta W_g(\mathbf{r}) + \Delta W_c(\mathbf{r}) = -4\pi G\rho(\mathbf{r}) + 2\omega^2\,, \tag{1.16}$$

which is the Poisson equation for the actual gravity potential W. Consider the point of interest $\mathbf{r}$ above the Earth, i.e., outside the masses that generate the gravity potential W, then $\omega = 0$ because the point is not connected with the Earth. If we neglect the density of all masses outside the Earth (e.g., an atmosphere), then also $\rho(\mathbf{r}) = 0$. Thus, Eq. (1.16) becomes (Heiskanen and Moritz 1967, p. 5)

$$\Delta W(\mathbf{r}) = 0\,, \tag{1.17}$$

which is the Laplace equation for the actual gravity potential W. A function, that satisfies the Laplace equation (1.17) at every point of a region v, is called harmonic in v. If the region v is the exterior of a certain closed surface S, e.g., the exterior of the solid Earth, then the function must in addition vanishes like $1/l$ for $l \to \infty$ (Heiskanen and Moritz 1967, p. 15)

1.2 Normal gravity field

Since the Earth resembles closely an ellipsoid of revolution, its actual gravity field can successfully be approximated by the "normal" gravity field of the homogeneous rotating geocentric ellipsoid. The ellipsoid of revolution (reference ellipsoid) can be made an equipotential surface of the normal potential U:

$$U(\mathbf{r_e}) = U_0 = \text{const.}\,, \tag{1.18}$$

where $\mathbf{r_e}$ is the position vector of the point on the surface of the ellipsoid. The functional value U is uniquely determined by means of the ellipsoidal surface (semi-axes a, b), the enclosed mass M and the angular velocity ω. Any other system of four independent parameters may be also used as defining constants. The reference ellipsoid of the Geodetic Reference System 1980 (GRS 80), based on the theory of the geocentric equipotential ellipsoid [2], is defined by the following conventional constants (Moritz 1984):

[2] The theory of the equipotential ellipsoid was first given by Italian mathematicians Paolo Pizzetti (1860-1918) (Pizzetti 1911) and Carlo Somigliana (1860-1955) (Somigliana 1929).

- equatorial radius of the Earth
  $a = 6378137$ m,
- geocentric gravitational constant (including the Earth's atmosphere)
  $GM = 3986005 \times 10^8$ m^3 s^{-2},
- dynamical form factor of the Earth (excluding the permanent tidal deformation)
  $J_2 = 108263 \times 10^{-8}$,
- angular velocity of the Earth
  $\omega = 7292115 \times 10^{-11}$ rad s^{-1}.

The constant U_0 is defined by

$$U_0 = W(\mathbf{r_g}) = W_0\,, \tag{1.19}$$

where W_0 is the actual gravity potential W on the geoid ($\mathbf{r_g}$ is the geocentric position vector of the point on the geoid).

Following the case of the actual gravity potential W of the Earth, the normal gravity potential U can be split into two parts – normal gravitational potential U_g and normal centrifugal potential U_c (Hofmann-Wellenhof and Moritz 2005, p. 65)

$$U(\mathbf{r}) = U_g(\mathbf{r}) + U_c(\mathbf{r})\,, \tag{1.20}$$

where

$$U_c(x, y) = \frac{1}{2}\omega^2(x^2 + y^2)\,, \tag{1.21}$$

in the Cartesian coordinates. Outside the reference ellipsoid the normal gravitational potential U_g satisfies the Laplace equation (note that inside the reference ellipsoid the normal gravitational potential U_g is not defined), i.e.,

$$\Delta U_g(\mathbf{r}) = 0\,, \quad |\mathbf{r}| > |\mathbf{r_e}|\,. \tag{1.22}$$

Applying the Laplacian on Eq. (1.20), we get Poisson's equation for the normal gravity potential U at the points outside the ellipsoid

$$\Delta U(\mathbf{r}) = \Delta U_g(\mathbf{r}) + \Delta U_c(\mathbf{r}) = 0\,. \tag{1.23}$$

The normal gravity field is also conservative and irrotational as well as the actual gravity field, therefore also (Hofmann-Wellenhof and Moritz 2005, p. 69)

$$\boldsymbol{\gamma}(\mathbf{r}) = \nabla U(\mathbf{r})\,, \tag{1.24}$$

where $\boldsymbol{\gamma}$ stands for the normal gravity vector. Since the normal gravity field can be described mathematically (Pizzetti 1911; Somigliana 1929), a rigorous formula exists for the magnitude of the normal gravity vector on the reference ellipsoid (Moritz 1984)

$$|\boldsymbol{\gamma}| = \gamma(\varphi) = \frac{a\gamma_e \cos^2\varphi + b\gamma_p \sin^2\varphi}{\sqrt{a^2\cos^2\varphi + b^2\sin^2\varphi}}\,, \tag{1.25}$$

where the constant γ_e stands for the magnitude of the normal gravity vector on the equator, γ_p for the magnitude of the normal gravity vector on the poles and φ for the geodetic latitude, see Appendix B.3.

1.3 Disturbing gravity field

The difference of the actual gravity field from the normal gravity field is called the disturbing gravity field. The difference between the actual gravity potential W and the normal gravity potential U is called the disturbing gravity potential T (Hofmann-Wellenhof and Moritz 2005, pp. 90-91)

$$T(\mathbf{r}) = W(\mathbf{r}) - U(\mathbf{r})\,, \quad |\mathbf{r}| > |\mathbf{r_e}|\,, \tag{1.26}$$

where $\mathbf{r_e}$ is the position vector of the point on the surface of the ellipsoid. The rotation of the ellipsoid of revolution is chosen to have the same angular velocity as the Earth's rotation, thus, $U_c(\mathbf{r}) = W_c(\mathbf{r})$. Because of this equality, we get

$$T(\mathbf{r}) = W_g(\mathbf{r}) - U_g(\mathbf{r})\,. \tag{1.27}$$

Therefore in the case of the disturbing gravity potential T the adjectives "gravitational" and "gravity" can be interchanged. Applying the Laplacian Δ on Eq. (1.27) and considering only points outside both the Earth and the reference ellipsoid yields Laplace's equation for the disturbing gravity potential T

$$\Delta T(\mathbf{r}) = \Delta[W_g(\mathbf{r}) - U_g(\mathbf{r})] = \Delta W_g(\mathbf{r}) - \Delta U_g(\mathbf{r}) = 0\,. \tag{1.28}$$

Equation (1.28) is valid, i.e., the disturbing gravity potential T is harmonic, in every point outside the Earth and the ellipsoid (mass-free space).

We can represent the disturbing gravity field by the vector $\delta\mathbf{g}$ (Heiskanen and Moritz 1967, p. 84)

$$\delta\mathbf{g}(\mathbf{r}) = \mathbf{g}(\mathbf{r}) - \boldsymbol{\gamma}(\mathbf{r})\,, \tag{1.29}$$

which is called the gravity disturbance vector. Since

$$\begin{aligned} \mathbf{g}(\mathbf{r}) &= \nabla W(\mathbf{r})\,, \\ \boldsymbol{\gamma}(\mathbf{r}) &= \nabla U(\mathbf{r})\,, \end{aligned} \tag{1.30}$$

the gravity disturbance vector becomes (Heiskanen and Moritz 1967, p. 85)

$$\delta\mathbf{g}(\mathbf{r}) = \nabla(W - U)(\mathbf{r}) = \nabla T(\mathbf{r})\,. \tag{1.31}$$

The magnitude of $\delta\mathbf{g}(\mathbf{r})$ is the gravity disturbance

$$\delta g(\mathbf{r}) = |\delta\mathbf{g}(\mathbf{r})| = |\mathbf{g}(\mathbf{r})| - |\boldsymbol{\gamma}(\mathbf{r})| = g(\mathbf{r}) - \gamma(\mathbf{r})\,. \tag{1.32}$$

The difference in the direction of the actual gravity vector and normal gravity vector is called the deflection of the vertical

$$\Theta(\mathbf{r}) = \angle[\boldsymbol{\gamma}(\mathbf{r}), \mathbf{g}(\mathbf{r})] = \angle[\mathbf{n}(\mathbf{r}), \mathbf{t}(\mathbf{r})]\,, \tag{1.33}$$

where $\mathbf{n}$ is the tangent to the plumbline of the normal gravity field, which is approximately the ellipsoidal normal, and $\mathbf{t}$ is the tangent to the plumbline of the actual gravity field. Parameters describing the actual, normal and disturbing gravity fields are listed in Tab. 1.1.

1.3.1 Gravity disturbance and gravity anomaly

To obtain the gravity disturbance δg, see Eq. (1.29), we need to know the actual gravity g and the normal gravity γ at the same point. Let us assume now the point with the geocentric radius vector $\mathbf{r}$ lies on the topography. We denote it P'. The actual gravity g can be measured at the point P' whereas the normal gravity γ at the point P' has to be evaluated. Since the rigorous formula for the magnitude of the normal gravity vector

	ACTUAL gravity field	NORMAL gravity field	DISTURBING gravity field
Gravity potential	W	U	T
Gravity vector	$\nabla W(\mathbf{r}) = \mathbf{g}(\mathbf{r})$	$\nabla U(\mathbf{r}) = \gamma(\mathbf{r})$	$\nabla T(\mathbf{r}) = \delta\mathbf{g}(\mathbf{r})$
"Direction" of gravity vector	plumbline $\mathbf{t}$	normal $\mathbf{n}$	$\Theta(\mathbf{r}) = \angle[\mathbf{n}(\mathbf{r}), \mathbf{t}(\mathbf{r})]$

Table 1.1: Selected parameters of the actual, normal and disturbing gravity fields

$\gamma = |\boldsymbol{\gamma}|$ on the reference ellipsoid is known, see Eq. (1.25), one can use the Taylor series to get the value γ in the particular point P' above the reference ellipsoid (Abramowitz and Stegun 1972, p. 880)

$$\gamma(P') = \gamma(Q) + \sum_{j=1}^{\infty} \frac{1}{j!} \frac{\partial^j \gamma}{\partial n^j}|_Q h^j \,, \tag{1.34}$$

where Q is the orthogonal projection of the point P' onto the reference ellipsoid and h is the geodetic (Gauss ellipsoidal) height of the point P', i.e., the distance between points P' and Q reckoned along the ellipsoidal normal, see Fig. 1.2.

However, the geodetic height h is available only due to use of GNSS positioning. In the times "before" GNSS, only levelled heights (orthometric heights H_O, normal heights H_N, ...) were available. Therefore, the other parameter called the gravity anomaly Δg had to be introduced instead of the gravity disturbance δg. The gravity anomaly Δg is also defined as a difference between the actual gravity g and the normal gravity γ. Unlike the gravity disturbance, which corresponds just to one point P', the gravity anomaly corresponds to two points – P' and Q'. The point Q' satisfies two conditions

- points P' and Q' lie on the same ellipsoidal normal ,
- actual gravity potential W at P' is equal to the normal gravity potential U at Q', i.e., $W(P') = U(Q')$.

Considering the point P' on the topography, the point Q' lies on the surface called the telluroid (Hirvonen 1960; Grafarend 1978; Heck 1986). The gravity anomaly is then defined

$$\Delta g(P', Q') = g(P') - \gamma(Q') \,, \tag{1.35}$$

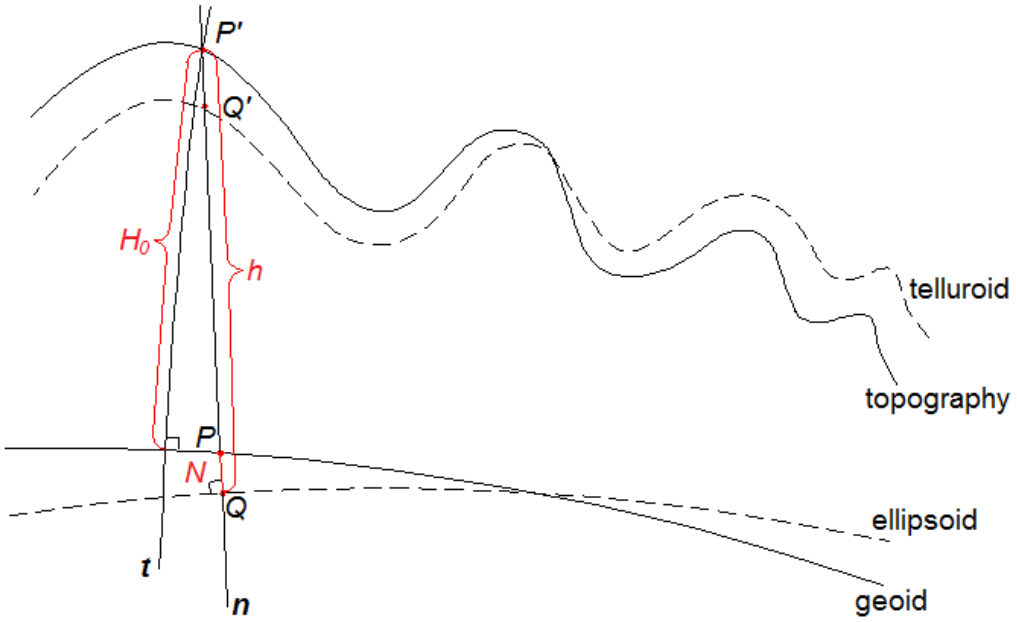

Figure 1.2: Definition of heights – geodetic height h, orthometric height H_0 and geoidal height N

where, using the Taylor series again,

$$\gamma(Q') = \gamma(Q) + \sum_{j=1}^{\infty} \frac{1}{j!} \frac{\partial^j \gamma}{\partial n^j}|_Q H^j \,. \tag{1.36}$$

Let us denote P the point on the geoid. Since the largest component of the gradient in Eq. (1.7) is the component in the direction of the tangent of a plumbline, we can write (Heiskanen and Moritz 1967, p. 50)

$$g(P) \approx -\frac{\partial W}{\partial t}|_P \,. \tag{1.37}$$

Using the deflection of the vertical, the direction t can be replaced by the direction of the ellipsoidal normal n. Since the elevation h is reckoned along the ellipsoidal normal n, we get:

$$g(P) \approx -\frac{\partial W}{\partial h}|_P \,. \tag{1.38}$$

Accordingly we have for the normal gravity vector

$$\gamma(P) \approx -\frac{\partial U}{\partial n}|_P = -\frac{\partial U}{\partial h}|_P \,. \tag{1.39}$$

Therefore, the gravity disturbance δg becomes

$$\delta g(P) = g(P) - \gamma(P) \approx -\frac{\partial W}{\partial h}|_P - \left(-\frac{\partial U}{\partial h}|_P\right) = -\frac{\partial (W-U)}{\partial h}|_P \,. \tag{1.40}$$

Finally, we get the following approximate formula for the gravity disturbance δg (Heiskanen and Moritz 1967, p. 85)

$$\delta g(P) \approx -\frac{\partial T}{\partial h}|_P \,, \tag{1.41}$$

or in an equivalent form

$$\delta g(P) + \frac{\partial T}{\partial h}|_P \approx 0 \,. \tag{1.42}$$

In the approximate formulas above the ellipsoidal corrections must by applied for high precise applications (Molodensky, Eremeev and Yurkina 1960; Moritz 1980; Martinec and Grafarend 1997; Fei and Sideris 2000).

For the gravity anomaly Δg the situation is more complicated than for the gravity disturbance. Consider the gravity anomaly corresponding to the points P on the geoid and Q on the reference ellipsoid. Then

$$\Delta g(P,Q) = g(P) - \gamma(Q) \,. \tag{1.43}$$

Since

$$\gamma(P) \approx \gamma(Q) + \frac{\partial \gamma}{\partial h}|_Q N \,, \tag{1.44}$$

where N is the geoidal height, see Fig. 1.2, the gravity anomaly becomes

$$\Delta g(P,Q) \approx g(P) - \gamma(P) + \frac{\partial \gamma}{\partial h}|_Q N = -\frac{\partial T}{\partial h}|_P + \frac{\partial \gamma}{\partial h}|_Q N \,. \tag{1.45}$$

Using the well known Bruns formula (Bruns 1878; Heiskanen and Moritz 1967, p. 85)

$$N(P,Q) \approx \frac{T(P)}{\gamma(Q)} \,, \tag{1.46}$$

we get

$$\Delta g(P,Q) \approx -\frac{\partial T}{\partial h}|_P + \frac{1}{\gamma(Q)}\frac{\partial \gamma}{\partial h}|_Q T(P) \,. \tag{1.47}$$

The equivalent form (Heiskanen and Moritz 1967, p. 86)

$$\frac{\partial T}{\partial h}|_P - \frac{1}{\gamma(Q)}\frac{\partial \gamma}{\partial h}|_Q T(P) + \Delta g(P,Q) \approx 0 \,, \tag{1.48}$$

is called the fundamental equation of physical geodesy. Equations (1.41) and (1.47) are valid everywhere outside the reference ellipsoid and the geoid.

1.3.2 Other definitions of telluroid

A generalization of the concept of the telluroid was given by Krarup (1973). The telluroid Σ is in this more general formulation an arbitrary given surface close to the Earth surface S. The points Q' of the telluroid are in one-to-one correspondence with the points P' of S, see Fig. 1.3 (Moritz 1977, p. 11). Assume Σ and the normal gravity potential U

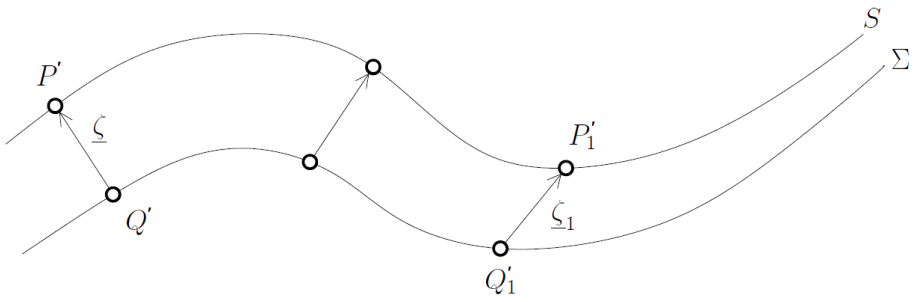

Figure 1.3: The telluroid Σ as an approximation to the Earth's surface S

are given, thus, we can compute U and γ at Q', see Eq. (1.24). Also the actual gravity potential W and gravity vector $\mathbf{g}$ are supposed to be given on S, i.e., at every point P'. The differences (Moritz 1977, pp. 11-12)

$$\begin{aligned} \Delta W &= W(P') - U(Q')\,, \\ \Delta \mathbf{g} &= \mathbf{g}(P') - \gamma(Q')\,, \end{aligned} \tag{1.49}$$

are called potential anomaly and gravity anomaly vector, respectively.

If the telluroid is defined by an appropriate way, it is possible to make one of the two anomalies equal zero. The usual definition described in Sec. 1.3.1 is

$$\Delta W = 0\,, \tag{1.50}$$

i.e., $U(Q') = W(P')$. The points P' and Q' are supposed to lie on the same ellipsoidal normal. Since the normal through P' is not known, the point Q' is defined by three conditions (Moritz 1977, p. 12)

$$U(Q') = W(P'), \quad \varphi(Q') = \Phi(P'), \quad \lambda(Q') = \Lambda(P')\,. \tag{1.51}$$

The geodetic latitude φ and longitude λ, see Appendix B.3, determine the direction of the normal gravity vector γ

$$\gamma = \begin{bmatrix} \gamma \cos\varphi \cos\lambda \\ \gamma \cos\varphi \sin\lambda \\ \gamma \sin\varphi \end{bmatrix} , \tag{1.52}$$

in the same way as the astronomical latitude Φ and longitude Λ, see Appendix B.4, define the direction of the gravity vector $\mathbf{g}$

$$\mathbf{g} = \begin{bmatrix} g \cos\Phi \cos\Lambda \\ g \cos\Phi \sin\Lambda \\ g \sin\Phi \end{bmatrix} . \tag{1.53}$$

Since the telluroid is determined by three "Marussi coordinates" (Marussi 1985) potential, latitude, longitude, see Eq. (1.51), Krarup (1973) called it the "Marussi telluroid".

Another definition of the telluroid is to put

$$\Delta\mathbf{g} = 0 . \tag{1.54}$$

Then $\gamma(Q') = \mathbf{g}(P')$, expressed in terms of magnitude and direction of the vectors (Moritz 1977, p. 13)

$$\begin{aligned} \gamma(Q') &= g(P') , \\ \varphi(Q') &= \Phi(P') , \\ \lambda(Q') &= \Lambda(P') . \end{aligned} \tag{1.55}$$

The conditions in Eq. (1.55) completely determine the point Q'. Since g, Φ, Λ may be called "gravimetric coordinates", the corresponding surface of the points Q' is called by Krarup (1973) the "gravimetric telluroid".

In the most general case, both differences in Eq. (1.49) are nonzero, i.e., $\Delta W \neq 0$, $\Delta\mathbf{g} \neq 0$, and conditions for the definition of the telluroid is not so simple as in the two cases described above. In Moritz (1977), the equation which holds on the telluroid Σ is presented

$$T + \mathbf{m}^T \,\mathrm{grad}T = \Delta W + \mathbf{m}^T \Delta\mathbf{g} , \tag{1.56}$$

with

$$\mathbf{m} = -\mathbf{M}^{-1}\gamma\,, \tag{1.57}$$

where $\mathbf{M}$ is a matrix of the second derivatives of the normal gravity potential U (see Moritz 1977, pp. 13-17). Equation (1.56) is a generalization of the fundamental equation of physical geodesy, i.e., Eq. (1.48).

1.4 Geoid

The geoid as the vertical datum for orthometric heights is the most important equipotential surface of the Earth's gravity field. The original idea comes from C.F. Gauss[3] and its name from J.B. Listing[4]. The geoid is a continuous, smooth and convex closed surface, one of the equipotential surfaces of the Earth's gravity potential, of which (mean) surface of the ideal oceans forms a part. The geoid is orthogonal in every point to the direction of a plumbline.

If we were able to determine the disturbing gravity potential T as a continuous function at the geoid, we could determine the geoidal heights N through the Bruns formula in Eq. (1.46). Therefore, our aim is to determine the disturbing gravity potential T at the geoid from available observations of gravity field parameters.

Since we cannot measure values of the disturbing gravity potential T, it is necessary to use other ways to determine T. There are several possibilities how to determine the disturbing gravity potential T from gravimetric (or gradiometric) measurements. In general, we can divide this problem into two parts according to input data: determination

[3]Carl Friedrich Gauss (1777-1855) – German mathematician and scientist; the Gauss "definition" of the geoid (Gauss C.F. 1828, p. 49): What we call in the geometric sense the surface of the Earth is nothing else but that surface which intersects the direction of gravity at right angles and from which the surface of the world ocean is a part (Vaníček and Christou 1994).

[4]Johann Benedict Listing (1808-1882) – German mathematician; Listing's "definition" of the geoid (Listing J.B. 1873, pp. 33, 45): According to our opinion we have to determine numerically in the future the derivations of the plumbline as long as they have visible origin, namely by a topographic surface of the continental relief, by a geological determination of the mass density of its constituents and by a systematic survey of the oceans according to well-established methods ... We shall call the previously defined mathematical surface of the Earth, of which the ocean surface is a part, geoidal surface of the Earth or the geoid (Vaníček and Christou 1994).

of the global (low-frequency) part of T and determination of the local (high-frequency) part of T. By current standards, the global part means the part of the series in Eq. (1.58) approximately to degree $n = 200$, the rest of this series represents the local part.

1.4.1 Low-frequency component of the geoid

The basic idea of global modelling comes from the potential theory which was first published at the end of the 18th century by P.S. Laplace[5]. Since the disturbing gravity potential T is a harmonic function outside all masses, i.e., T satisfies Laplace's equation (1.28), it can be expressed in the form of an infinite harmonic series. In the spherical coordinates, we can write (Heiskanen and Moritz 1967, p. 88)

$$T(r,\theta,\lambda) = \frac{GM}{R}\sum_{n=0}^{\infty}\left(\frac{R}{r}\right)^{n+1} T_n(\theta,\lambda)\,, \tag{1.58}$$

where G stands for Newton's gravitational constant, M for the mass of the Earth, R is a radius of the geocentric sphere which approximates geoid in some sense (e.g., the Brillouin sphere[6]) and T_n are (Laplace's) surface spherical harmonics (Heiskanen and Moritz 1967, p. 21)

$$T_n(\theta,\lambda) = \sum_{m=0}^{n}\left(A_{n,m}\cos m\lambda + B_{n,m}\sin m\lambda\right) P_{n,m}(\cos\theta)\,. \tag{1.59}$$

Functions $P_{n,m}$ are called associated Legendre's functions of degree n and order m (Abramowitz and Stegun 1972, Sec. 8), $A_{n,m}$ and $B_{n,m}$ are numerical coefficients. Because of a numerical stability of a computation of the harmonic series in Eq. (1.59), the fully-normalized coefficients $\overline{A}_{n,m}$, $\overline{B}_{n,m}$ and fully-normalized associated Legendre's functions $\overline{P}_{n,m}$ are used. Using the normalization factor (Heiskanen and Moritz 1967, pp. 31-32)

$$\begin{aligned} \alpha_{n,m} &= \sqrt{\frac{2(2n+1)(n-m)}{(n+m)!}}\,, \quad \text{for } m \neq 0\,, \\ \alpha_n &= \sqrt{2n+1}\,, \quad \text{for } m = 0\,, \end{aligned} \tag{1.60}$$

[5]Pierre-Simon Laplace (1749-1827) – French mathematician and astronomer; memoirs: Théorie du Mouvement et de la figure elliptique des planètes, Part II (1784); Méchanique céleste (1802).

[6]Brillouin sphere – concentric sphere that includes all masses of the Earth; named after the French scientist who proposed gravity reduction to a level surface completely outside the Earth (Moritz 1977, p. 50).

yields

$$\begin{aligned} \overline{P}_{n,m} &= \alpha_{n,m} P_{n,m}\,, \\ \overline{A}_{n,m} &= \alpha_{n,m}^{-1} A_{n,m}\,, \\ \overline{B}_{n,m} &= \alpha_{n,m}^{-1} B_{n,m}\,. \end{aligned} \tag{1.61}$$

With respect to the definition of the reference ellipsoid (the mass of the ellipsoid is the same as the mass of the Earth, the centre of gravity of the Earth and of the ellipsoid coincide with the origin of the coordinate system), we can assume surface spherical harmonics of degree $n = 0, n = 1$ as equal to zero. The harmonic series in Eq. (1.58) then starts from degree $n = 2$ (Heiskanen and Moritz 1967, pp. 98-99),

$$T(r,\theta,\lambda) = \frac{GM}{R} \sum_{n=2}^{\infty} \left(\frac{R}{r}\right)^{n+1} T_n(\theta,\lambda)\,. \tag{1.62}$$

Applying the operator [7] $-\frac{\partial}{\partial r}$ on Eq. (1.62) yields (Heiskanen and Moritz 1967, p. 88)

$$\delta g(r,\theta,\lambda) = \frac{GM}{R^2} \sum_{n=2}^{\infty} (n+1) \left(\frac{R}{r}\right)^{n+2} T_n(\theta,\lambda)\,, \tag{1.63}$$

which is the harmonic expansion for the gravity disturbance δg in the spherical approximation. Applying the operator $-\frac{\partial}{\partial r} - \frac{2}{r}$ on Eq. (1.62), we get the formula for the gravity anomaly (Heiskanen and Moritz 1967, p. 89)

$$\Delta g(r,\theta,\lambda) = \frac{GM}{R^2} \sum_{n=2}^{\infty} (n-1) \left(\frac{R}{r}\right)^{n+2} T_n(\theta,\lambda)\,. \tag{1.64}$$

Using different operators one can get harmonic expansions of the other parameters of the disturbing gravity field (deflection of the vertical, ...). Since the quantities on the left-hand side of the expansions are available almost over whole Earth due to the satellite gravity and gravimetric measurements, the coefficients $A_{n,m}, B_{n,m}$ in Eq. (1.59) and $\overline{A}_{n,m}, \overline{B}_{n,m}$ in Eq. (1.61), respectively, can be evaluated up to a certain degree and order numerically. Nevertheless, satellite gravity data can be used just for determination of the low-frequency part of the disturbing gravity potential T (degree n and order m up to approximately 200). The high-frequency part is not measurable because of the altitude of

[7] General definition of an operator can be found in (Lebedev and Vorovich 2003), p. 51.

the gravity-dedicated satellites which ranges from 250 km to 500 km. In such a distance from the Earth an observation noise overlaps the attenuated high-frequency part of the measured signal.

1.4.2 Global gravitational model

The Global Gravitational Model (GGM) is represented by a set of the coefficients $A_{n,m}$, $B_{n,m}$, see Eq. (1.59), of the harmonic expansion of the Earth's (including solid, liquid and gas component) gravitational potential. GGM is defined also by the corresponding parameters, e.g., the Earth's gravitational constant or the radius of the reference sphere on which values of the coefficients $A_{n,m}, B_{n,m}$ were derived using a spherical harmonic analysis.

The first GGM was released in 1966 (Lundquist and Veis 1966) with the maximum degree and order $n = m = 15$. It was computed only from satellite tracking data. Many other models have been released over the next decades. A detailed overview of the development of GGMs can be found on the web pages of the International Centre for Global Earth Models (ICGEM, http://icgem.gfz-potsdam.de/ICGEM/). In late 70's, the combined GGMs to the degree and order $n = m = 180$ were developed. In the late eighties and early nineties, combined GGMs that contained the coefficients to the degree and order $n = m = 360$ were published at the Ohio State University, Columbus, USA. The most widely used was the last one, GGM Ohio State University 1991 (OSU91a; Rapp, Wang and Pavlis 1991). A precision of the coefficients of higher degrees and orders was low because of a lack of available terrestrial gravity data. The combined GGM with the same maximum degree and order and higher precision was the Earth Gravitational Model 1996 (EGM96; Lemoine et al. 1998) released in 1996. In 2008, the combined GGM with the highest resolution Earth Gravitational Model 2008 (EGM08; Pavlis et al. 2008) was published. It containes the coefficients $A_{n,m}, B_{n,m}$ up to the degree and order $n = m = 2160$. Since 2008, mostly satellite-only GGMs based on data of gravity-dedicated satellite missions were developed in order to improve the long-wavelength part of the gravitational field.

In the thesis, EGM08 and GOCO03s[8] (Mayer-Gürr et al. 2012) are used for the determination of global components of the gravity disturbances δg_{GGM} and the disturbing gravity potential T_{GGM}. EGM08 was chosen as GGM with the highest maximum degree and order (up to $n = m = 2160$), GOCO03s was chosen as a representant of the latest satellite-only GGMs. The aim is to find out if using the satellite-only GGM that includes gravity signal from the GOCE satellite mission (ESA 1999) is able to influence (improve) significantly the accuracy of the computed local geoid model of Taiwan.

1.4.3 High-frequency component of the geoid

The high-frequency part of the disturbing gravity potential T can be determined by the harmonic synthesis, i.e., by the evaluation of the harmonic series in Eq. (1.58) to the high degree and order, using the combined GGM with the high resolution (e.g., EGM08). When a satellite-only GGM with a low resolution is used, the high-frequency part of T cannot be determined from satellite gravity data and other gravity data (terrestrial, marine, aerial, ...) have to be used. Unfortunately, these gravity data are usually available just within limited geographical areas. Thus, the solution of Laplace's equation (1.28) in the form of a harmonic series cannot be applied. In order to obtain the high-frequency (local) part of the disturbing gravity potential T, boundary-value problems (BVPs) of the potential theory have to be solved. There are three basic BVPs used in geodesy – Dirichlet's BVP, Neumann's BVP and Newton's (Robin's) BVP. Considering the value of T or some functional of T as known over some simple boundary, we can solve T outside this boundary. In the spherical approximation we formulate the BVPs as follows (as the known boundary we consider the geocentric sphere of radius R):

- *Dirichlet's BVP* (Kellogg 1929, Sec. 9.4; Martinec 1998, p. 103):

$$\begin{aligned} \Delta T(\mathbf{r}) &= 0, \quad \text{for } |\mathbf{r}| > R\,, \\ T(\mathbf{r}) &= T(R), \text{ for } |\mathbf{r}| = R\,, \\ \lim_{|\mathbf{r}|\to\infty} T(\mathbf{r}) &= 0\,. \end{aligned} \tag{1.65}$$

[8] GOCO stands for "Combination of GOCE data with complementary gravity field information" (Pail et al. 2010).

- *Neumann's BVP* (Hofmann-Wellenhof and Moritz 2005, pp. 29, 95):

$$\begin{aligned} \Delta T(\mathbf{r}) &= 0, \quad \text{for } |\mathbf{r}| > R\,, \\ -\frac{\partial T}{\partial r}|_{\mathbf{r}} &= \delta g(\mathbf{r}), \ \text{for } |\mathbf{r}| = R\,, \\ \lim_{|\mathbf{r}|\to\infty} T(\mathbf{r}) &= 0\,. \end{aligned} \tag{1.66}$$

- *Newton's BVP* (Heiskanen and Moritz 1967, p. 92; Hofmann-Wellenhof and Moritz 2005, pp. 30, 95):

$$\begin{aligned} \Delta T(\mathbf{r}) &= 0, \quad \text{for } |\mathbf{r}| > R\,, \\ -\frac{\partial T}{\partial r}|_{\mathbf{r}} - \frac{2T(\mathbf{r})}{|\mathbf{r}|} &= \Delta g(\mathbf{r}), \ \text{for } |\mathbf{r}| = R\,, \\ \lim_{|\mathbf{r}|\to\infty} T(\mathbf{r}) &= 0\,. \end{aligned} \tag{1.67}$$

Considering the values on the boundary as known, we solve the disturbing gravity potential T outside the boundary. If the boundary surface is a sphere, the BVPs listed above are well-posed[9]. Thus, there exists a unique solution in a form of the Green integral (Green 1828). In spherical coordinates (r, θ, λ) we get the following solutions:

- *Solution of Dirichlet's BVP – Abel-Poisson's integral* (Kellogg 1929, Sec. 9.4, p. 241; Bjerhammar 1963; Martinec 1998, p. 104):

$$T(r,\theta,\lambda) = \frac{1}{4\pi}\int_0^{2\pi}\int_0^{\pi} T(R,\theta',\lambda')K(r,R,\psi)\sin\theta'\,\mathrm{d}\lambda'\,\mathrm{d}\theta'\,. \tag{1.68}$$

  The Green integral kernel K can be expressed in the form of an infinite series (Kellogg 1929, Sec. 9.4)

$$K(r,R,\psi) = \sum_{n=0}^{\infty}(2n+1)\left(\frac{R}{r}\right)^{n+1} P_n(\cos\psi)\,, \tag{1.69}$$

  or as the closed formula (Kellogg 1929, Sec. 9.4)

$$K(r,R,\psi) = \frac{r(r^2-R^2)}{(r^2+R^2-2rR\cos\psi)^{\frac{3}{2}}}\,. \tag{1.70}$$

[9] Solution is "well posed in the sense of Hadamard", if: 1) the solution exists, 2) the solution is unique for given data, 3) the solution depends continuously on the data (Hadamard 1902).

The term P_n stands for Legendre's polynomials and ψ is the spherical distance between the computing point represented by (r, θ, λ) and the integrating point represented by (R, θ', λ'), so that

$$\cos\psi = \cos\theta\cos\theta' + \sin\theta\sin\theta'\cos(\lambda - \lambda')\,. \tag{1.71}$$

- *Solution of Neumann's BVP – Hotine's integral* (Hotine 1969; Hofmann-Wellenhof and Moritz 2005, p. 115):

$$T(R,\theta,\lambda) = \frac{R}{4\pi}\int_0^{2\pi}\int_0^{\pi}\delta g(R,\theta',\lambda')H(\psi)\sin\theta'\,\mathrm{d}\lambda'\,\mathrm{d}\theta'\,, \tag{1.72}$$

where the integral kernel (Pick, Vyskočil and Pícha 1973, p. 474)

$$H(\psi) = \sum_{n=2}^{\infty}\frac{2n+1}{n+1}P_n(\cos\psi)\,, \tag{1.73}$$

is called Hotine's function. The closed expression of Hotine's function is given by (Hotine 1969; Pick, Vyskočil and Pícha 1973, p. 472)

$$H(\psi) = \left(\sin\frac{\psi}{2}\right)^{-1} - \ln\left[1 + \left(\sin\frac{\psi}{2}\right)^{-1}\right]\,. \tag{1.74}$$

- *Solution of Newton's BVP – Stokes's integral* (Stokes 1849; Heiskanen and Moritz 1967, p. 93):

$$T(R,\theta,\lambda) = \frac{R}{4\pi}\int_0^{2\pi}\int_0^{\pi}\Delta g(R,\theta',\lambda')S(\psi)\sin\theta'\,\mathrm{d}\lambda'\,\mathrm{d}\theta'\,, \tag{1.75}$$

where the integral kernel called Stokes's function is expressed as an infinite series (Heiskanen and Moritz 1967, p. 97)

$$S(\psi) = \sum_{n=2}^{\infty}\frac{2n+1}{n-1}P_n(\cos\psi)\,, \tag{1.76}$$

or in the closed form (Stokes 1849; Heiskanen and Moritz 1967, p. 94)

$$S(\psi) = \left(\sin\frac{\psi}{2}\right)^{-1} - 6\sin\frac{\psi}{2} + 1 - 5\cos\psi - 3\cos\psi\ln\left(\sin\frac{\psi}{2} + \sin^2\frac{\psi}{2}\right)\,. \tag{1.77}$$

1.4.4 Local geoid models of Taiwan

Geoid models for Taiwan have been developed by numerous researchers (e.g., Chang, Chang and Lee 1990; Tsuei et al. 1995; Hwang 1996). An improved geoid model for Taiwan based on surface gravity data was computed by Hwang (1997a). Although this model yielded 2 cm standard deviation when comparing the modelled geoidal heights and the observed geoidal heights along a testing levelling profile at the west coast of Taiwan, it contained errors at long wavelengths ($100 - 300$ km), partly due to the OSU91a model (Rapp, Wang and Pavlis 1991) and partly due to the used gravity data (Hwang 1997b). In 2000, a geoid model for Taiwan was developed using terrestrial and sea gravity anomalies and altimetry-derived geoid gradients by least-squares collocation (Hwang and Hwang 2002) with the estimated model accuracy ranging from 2 cm in flat areas to 10 cm in mountainous areas. The geoid model based on aerial gravity data (a survey performed from 2004 to 2005), surface gravity data and the KMS02 altimetry-derived gravity data (Andersen et al. 1999) was developed by Hwang et al. (2007). The accuracy of the geoid model was determined by comparing with GNSS/levelling points (differences between the GNSS-derived ellipsoidal heights at the centimetre-level accuracy and the precision levelling-derived orthometric heights at the millimetre-level accuracy). The standard deviations ranged from centimetre in coastal plains to decimetre in high mountains (Hwang et al. 2007).

Chapter 2

Aerial gravimetry

Aerial gravimetry is a fast and efficient method of gravitational data collection. It is an observation technique capable of providing accurate gravitational data at the spatial resolution of 2 km or larger. Whereas ground gravity[1] data are measured mostly along roads or in a flat terrain, aerial gravimetry can cover areas with more complicated relief and inaccessible regions (mountainous areas, rainforests, sea, polar regions, off-coast regions, ...). The main disadvantage of this method is the lower spectral resolution of the measured data because of the high-frequency observation noise caused by flight dynamics. Nevertheless, aerial gravimetry is an ideal technique to complement satellite-only gravitational models. It is also an efficient tool to provide a transition between terrestrial and marine gravity data.

2.1 Historical overview

The concept of aerial gravity was proposed in a beginning of the fifties of the 20th century (Hammer 1950). The first reported test of aerial gravity measurements is described in Lundberg (1957), but a used system was based on the principle of gradiometry. The first test of aerial gravity meter system based on gravimetry was performed in 1958 by the U.S.

[1] In the case of measuring data at points connected with the Earth, both gravitational and centrifugal accelerations (i.e., the *gravity* acceleration) are present. Only the *gravitational* acceleration is present if measurement relates to points outside the Earth.

Air Force (Thompson and LaCoste 1960). Other tests followed in 1960. Results of the tests suffered mainly by the inaccurate determination of the aircraft position and velocity (Nettleton, LaCoste and Harrison 1960). The first successful measurement of gravity from a helicopter was performed in 1965 by the U.S. Naval Oceanographic Office (Gumert and Cobb 1970; Gumert 1998). The major breakthrough in the aerial gravimetry was a development of the Global Positioning System - NAVigation System with Timing And Ranging (GPS NAVSTAR) during the mid 1980's.[2] It was an impulse for new activities in designing and operating aerial gravity systems (Schwarz 1980; Hammer 1983; Brozena and Peters 1988; Forsberg 1993). Especially the use of carrier phase measurements and Differential GNSS (DGNSS) opened new ways to resolve navigational problems (see, e.g., Brozena, Mader and Peters 1989; Schwarz, Cannon and Wong 1989; Kleusberg, Peyton and Wells 1990).

Since the beginning of the nineties, the aerial gravimetry has been used for large-scale surveys. Campaigns were performed over Greenland (Brozena 1992; Brozena and Peters 1994; Brozena, Peters and Salman 1997; Forsberg and Kenyon 1994; Forsberg and Rubek 1998; Forsberg, Olesen and Keller 1999; Olesen et al. 2000), Switzerland (Klingelé et al. 1995; Verdun et al. 2003), Antarctica (Bell et al. 1992; Bell et al. 1999), Skagerrak and Azores (Forsberg et al. 1997; Hehl et al. 1997), Nordic Baltic region (Forsberg and Solheim 2000), Arctic ocean (Childers et al. 2001; Forsberg et al. 2003). Recent major projects were the national geoid and regional surveys of Malaysia, Mongolia and Ethiopia (Olesen and Forsberg 2007), Taiwan (Hwang et al. 2007, 2012, 2014), Alabama (Huang et al. 2013; Wang et al. 2013) and the United States (GRAV-D[3]). The reported accuracies of these campaigns were at the mGal level (about $1.5 - 3$ mGal for the spatial resolution of $5 - 6$ km).

[2]Since GPS NAVSTAR another Global Navigation Satellite Systems (GNSS) or Regional Navigation Satellite System (RNSS) have been developed, e.g., GLONASS (Russian GNSS), GALILEO (European GNSS), BeiDou/COMPASS (Chinese GNSS) or IRNSS (Indian RNSS).

[3]The Gravity for the Redefinition of the American Vertical Datum (GRAV-D) is a project of the National Geodetic Survey to re-define the vertical datum of the United States by 2022. The expected accuracy of the gravity-based vertical datum resulting from this project is at the level of 2 cm. Source: http://www.ngs.noaa.gov.

2.2 The principle of aerial gravimetry

In the aerial gravimetry, the gravitational data are measured along the flight trajectory. The following classification is generally used for aerial gravitational measurements (e.g., Schwarz and Li 1997; Wei 1999; Alberts 2009):

- scalar gravimetry,
- vector gravimetry.

The principle of aerial gravimetry is based on Newton's second law od motion (Newton 1686). Since a gravimeter (i.e., a highly sensitive accelerometer) is in motion, it cannot distinguish between dynamic and gravitational accelerations. An aerial gravity system measures a non-gravitational acceleration $\mathbf{f}$ (so-called specific force) that is subsequently separated into two parts – the dynamic acceleration of an aircraft and gravitational acceleration (Li 2000). The Newton second law of motion in the inertial reference frame i (Feynman 1963, Sec. 9.1) is expressed by (Li 2000; Alberts 2009)

$$\ddot{\mathbf{r}}^i = \mathbf{f}^i + \mathbf{a_g}^i \,, \tag{2.1}$$

where $\ddot{\mathbf{r}} = d^2\mathbf{r}/dt^2$ is the second derivative in time of the position vector $\mathbf{r}$, i.e., the aircraft acceleration, $\mathbf{f}$ is the vector of measured non-gravitational acceleration and $\mathbf{a_g}$ is the gravitational acceleration vector. In the local astronomic system (also called local level system; Torge 1980, Sec. 2.6.2) the gravitational acceleration vector $\mathbf{a_g}$ is expressed by (Torge 1980, p. 186; Alberts 2009)

$$\mathbf{a_g}^l = \ddot{\mathbf{r}}^l - \mathbf{R}^l_b \mathbf{f}^b + (2\boldsymbol{\Omega}^l_{ie} + \boldsymbol{\Omega}^l_{el})\dot{\mathbf{r}}^l \,, \tag{2.2}$$

where $\boldsymbol{\Omega}^l_{ie}$ and $\boldsymbol{\Omega}^l_{el}$ are skew-symmetric matrices due to the Earth rotation and aircraft rate and $\dot{\mathbf{r}} = d\mathbf{r}/dt$ is the aircraft velocity. Moreover, it is assumed that the accelerometers are fixed to the aircraft, which requires a transformation from the aircraft's body frame b to the local level system l. The corresponding rotation matrix $\mathbf{R}$ contains the orientation angles between the two frames.

In scalar gravimetry the magnitude of the gravitational acceleration vector is determined. The non-gravitational acceleration is measured either by a strapdown inertial

navigation system, that determines the orientation of the sensors (three accelerometers) mathematically (Schwarz and Wei 1993; Wei and Schwarz 1998), or by a platform inertial navigation system, that stabilizes a gravimeter in a vertical direction physically (Knickmeyer 1990; Salychev et al. 1994). Aircraft dynamic acceleration is obtained by differentiating in time the accurate position and velocity provided by DGNSS measurements (Wei, Ferguson and Schwarz 1992; Czompo 1994).

In vector gravimetry, all three components of the gravitational vector are determined (Jekeli and Kwon 1999). The accuracy of the components differs, the vertical component is much more accurate than the horizontal components due to attitude errors caused by gyro drifts (Bruton 2000).

Chapter 3

Aerial data of Taiwan

Taiwan is a very interesting area for testing methods for local gravity field modelling. There are lowlands as well as high mountains with the highest peak of about 4000 metres above the sea level on this island. There is also a deep ocean trench on the east created by the subduction of the Philippine Sea Plate into the Eurasian Plate. On this quite small island (around 36 thousands squared kilometres) there is a very miscellaneous relief which creates large anomalies in the gravity field.

In Taiwan, three aerial gravity surveys were performed from 2004 to 2009 (Hwang et al. 2007, 2012). By courtesy of prof. Cheinway Hwang of the National Chiao Tung University aerial gravity data in the form of low-pass filtered gravity disturbances at constant altitudes (Taiwan Island Survey, Kuroshio Current Survey and Taiwan Strait Survey) were kindly provided to the geodetic group of the University of West Bohemia in order to determine a local geoid model of Taiwan. The aerial gravity surveys were carried out over the altitude of 5156 m (Taiwan Island Survey) and over the altitude of 1620 m (Kuroshio Current Survey and Taiwan Strait Survey). A coherence analysis showed that the resolving wavelengths of the three aerial gravity datasets range from 4 to 6 km (Hwang et al. 2007, 2014). For the kinematic positioning of the aircraft, GNSS data at seven permanent GNSS ground tracking stations around Taiwan and one tracking station on the west coast of Taiwan near Taichung airport were collected. Using overlapping trajectory analysis, the overall GNSS positioning accuracy at the dm level was determined (Hwang et al. 2014) with the velocity error at the mm/s level. The aerial gravity data were collected

by the LaCoste and Romberg (LCR) System II air-sea gravimeter (serial number: S-133) with the nominal resolution of 0.01 mGal and accuracy of better than ±1 mGal (Hwang et al. 2007; L&R Air-sea Gravity System II 2003). From the analysis of crossover differences and repeated aerial measurements the assessment of the overall accuracy of the aerial gravity disturbances is about ±2-3 mGal at the spatial resolution (half wavelength) of 4-6 km (Hwang et al. 2007, 2012).

3.1 Taiwan Island Survey 2004-2005

Over the period of May 2004 to May 2005 an aerial gravity survey had been performed which covered the entire Taiwan Island (Hwang et al. 2007), see Fig. 3.1. In the thesis, the Taiwan Island area is called the "central area". The flight speed was 306 km/hour relative to the ground surface. Most of the flight lines are in the north-south direction because of the shape of Taiwan. The cross-line spacing is 4.5 km for all survey lines, except the east-west lines, which are spaced at 20 km. Gravity readings were sampled at 1 Hz, corresponding to an 85 m sampling interval on the ground.

The aerial gravity data have been pre-processed by a low-pass filter because of the high-frequency observation noise in the measured gravity signal. The filter width of 150 s for the Gaussian filter corresponding to the 6 km spatial resolution (half wavelength) was used. The aerial gravity data are at the constant flight altitude of 5156 m above the mean sea level.

3.2 Kuroshio Current Survey 2006-2008

Over the period of March 2006 to August 2008, an aerial gravity survey had been made over the Kuroshio Current east of Taiwan (Hwang et al. 2012), see Fig. 3.2. In the thesis, the Kuroshio Current east of Taiwan area is called the "eastern area". The aircraft used were Beechcraft King Air 200 and 350, with the Trimble 5700 GNSS receiver onboard the aircraft.

The Kuroshio Current Survey contains 36 lines in the north-south direction and 7 lines in the east-west direction. The cross-line spacing is 5 km for all north-south lines and

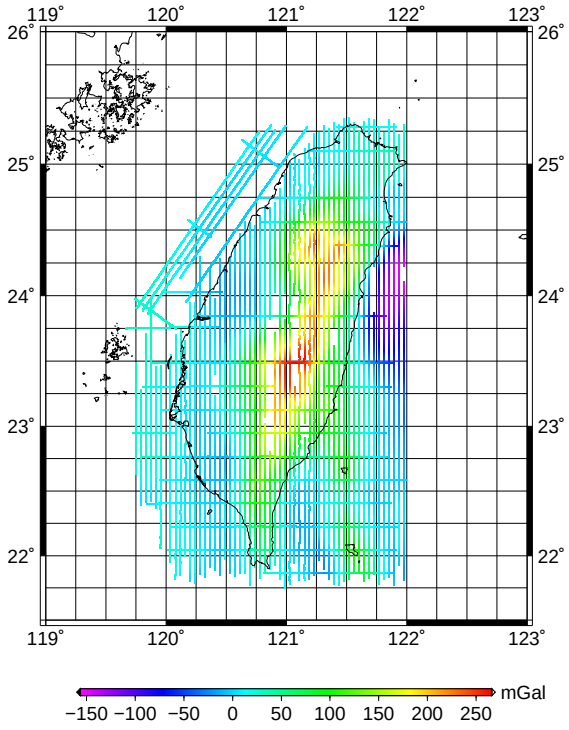

Figure 3.1: Aerial gravity data (mGal) – Taiwan Island Survey, $H_1 = 5156$ m (192,336 points)

60 km for east-west lines. The flight altitude over the Kuroshio Current was set to 1620 m above the mean sea level to increase the spatial resolution of aerial gravity data. The flight speed was 280 km/hour with 1 Hz sampling rate, corresponding to the 77 m interval on the ground.

3.3 Taiwan Strait Survey 2008-2009

The gravity values at altitude 1620 m above the mean sea level over the Taiwan Strait were collected over 2008–2009 (Hwang et al. 2012), see Fig. 3.2. In the thesis, the Taiwan Strait area is called the "western area". The ground spacings along the 54 north-south and 15 east-west lines are 5 and 25 km, respectively. The flight speed and the

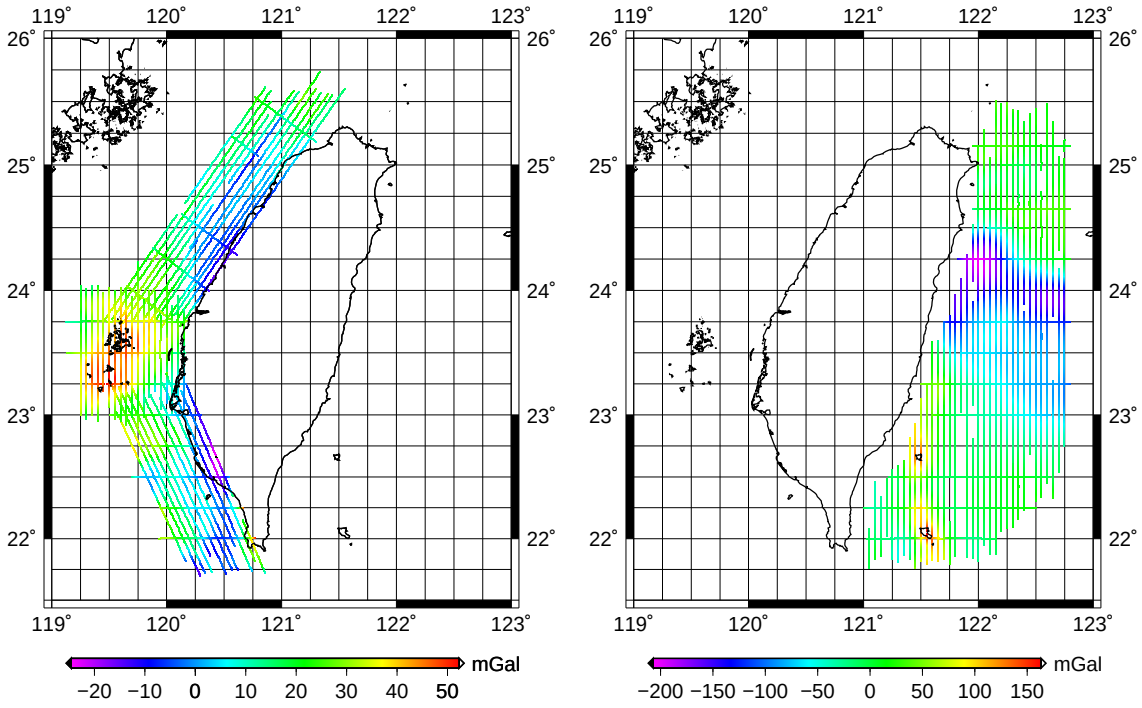

Figure 3.2: Aerial gravity data (mGal) – Taiwan Strait Survey, $H_2 = 1620$ m (left; 8,624 points); Kuroshio Current Survey, $H_2 = 1620$ m (right; 16,826 points)

corresponding gravity sampling interval are the same as for the Kuroshio Current Survey, i.e., 280 km/hour and 77 m.

Chapter 4

Processing of aerial gravity data

Measured aerial gravity data are processed in order to determine the geoid. There are two parts of the processing procedure: pre-processing and a transformation of the aerial gravity disturbances to the disturbing gravity potential. An important part of the pre-processing is the determination and elimination of data noise and errors. It mostly includes low-pass filtering of data to suppress their high-frequency noise and a cross-over adjustment to eliminate bias and drift terms. A summary of the pre-processing techniques can be found, e.g., in Alberts (2009, Sec. 3.1). In the following sections, the transformation of the aerial gravity disturbances to the disturbing gravity potential is discussed.

4.1 Formulation of BVPs for aerial gravity

In an aerial gravimetry, gravity observations correspond due to GNSS positioning to points represented by the geodetic coordinates (h, φ, λ), see Appendix B.3. The transformation of the geodetic coordinates (Gauss's ellipsoidal coordinates) into the geocentric spherical coordinates (r, θ, λ) can easily be done for the selected geocentric sphere (Heiskanen and Moritz 1967, pp. 18, 182). The triplet of the spherical coordinates then defines the geocentric position of a point of interest, i.e., $(r, \theta, \lambda) = (r, \Omega)$. In the following, the spherical approximation of the geoid by the geocentric sphere of radius R is used for the definition of BVPs. It is assumed that flight trajectories can be approximated by the geocentric sphere of radius $R + D$, i.e., the flight height D above the sphere of

radius R is constant.

Since we deal with aerial gravity data, their frequency limitation has to be taken into account. Processing the aerial data by a low-pass filter yields the filtered gravity disturbances δg_L, where L is the maximum degree in terms of the spherical harmonic expansion which can be resolved. The Gaussian filter used in case of the aerial gravity data of Taiwan, see Sec. 3, corresponds to the $4 - 6$ km spatial resolution (half wavelength) and degree $L \approx 3340$ (Novák, Kostelecký and Klokočník 2009). Moreover, since the aerial gravity data are available only within a restricted geographic area, we are not able to determine from them low frequencies of the potential T. Thus, the "remove-compute-restore" concept (e.g., Rapp and Rummel 1975; Schwarz, Sideris and Forsberg 1990) is used. The low-frequency part of T is evaluated using GGM up to the degree and order $l - 1$ as well as the low-frequency part of the gravity disturbances δg_{GGM} which is removed before the transformation. Removing the low-frequency part δg_{GGM} from the filtered gravity disturbances δg_L yields

$$\delta g_b = \delta g_L - \delta g_{GGM} \,, \tag{4.1}$$

where δg_b are the band-limited gravity disturbances, i.e., $\delta g_b = \sum_{n=l}^{L} (\delta g_b)_n$. The most important part of the gravitational effects of the masses outside the geoid and the reference ellipsoid (topography, atmosphere, ice and sea water) on gravity is subtracted with the low-frequency part δg_{GGM} from GGM, see Sec. 6.1. Since we assume the residual effect of atmosphere, ice and sea water on gravity is small, we do not consider this effect in the thesis and only the residual gravitational effects of topography (Direct Topographical Effect (DTE) and Indirect Topographical Effect (ITE), see Sec. 4.5), are taken into account. Thus, the "remove-compute-restore" process consists of the following steps, see the scheme 6.1:

- remove the low-frequency part δg_{GGM} from the filtered gravity disturbances: $\delta g_L \rightarrow \delta g_b$,
- remove the band-limited DTE A_b: $\delta g_b \rightarrow \delta g_b^H$ (see Sec. 4.5.1),
- transform (compute) the Helmert residual gravity disturbances δg_b^H to the Helmert residual disturbing gravity potential T_b^H,

- restore the band-limited ITE δV_b: $T_b^H \rightarrow T_b$ (see Sec. 4.5.2),
- restore the low-frequency part of the disturbing gravity potential T_{GGM}: $T_b \rightarrow T_L$.

The computation of the low-frequency part of the gravity disturbances δg_{GGM} and the disturbing gravity potential T_{GGM} is done using available GGMs, in particularly, EGM08 and GOCO03s. EGM08 was chosen as GGM with the highest maximum degree and order (up to $n = m = 2160$), GOCO03s was chosen as a representant of the latest satellite-only GGMs based on data of gravity-dedicated satellite missions. The gravitational effect of topography on the gravity disturbances (DTE) and on the disturbing gravity potential (ITE) is discussed in Secs. 4.5.1 and 4.5.2, respectively. The only step remaining is the transformation of δg_b^H to T_b^H. Assuming gravity disturbances δg_b^H available at the constant flight level D above the geocentric sphere of radius R all over the Earth, we can formulate the problem as Neumann's BVP, see Eq. (1.66) (Novák et al. 2003b),

$$\begin{aligned} \Delta T_b^H(r,\Omega) &= 0, \quad \text{for } r > R\,, \\ -\frac{\partial T_b^H}{\partial r}|_{(r,\Omega)} &= \delta g_b^H(r,\Omega), \ \text{for } r = R + D\,, \\ \lim_{r\to\infty} T_b^H(r,\Omega) &= 0\,. \end{aligned} \tag{4.2}$$

Our aim is to recover T_b^H on the boundary R. Formally, this is no longer BVP but rather an initial-value problem, since the gravity disturbances $\delta g_b^H(r,\Omega) = -\frac{\partial T_b^H}{\partial r}|_{(r,\Omega)}$ are given in the solution domain and not on the boundary. There are two main assumptions for the problem of Eqs. (4.2):

- disturbing gravity potential T_b^H is harmonic outside the geoid represented by the geocentric sphere of radius R (i.e., there are no gravitating masses outside the geoid) ,
- input gravity data are band-limited, i.e., $\delta g_b^H = \sum_{n=l}^{L} (\delta g_b^H)_n$.

Due to the "remove-compute-restore" concept described above, both of these assumptions are satisfied. The solution to the problem of Eqs. (4.2) is well-posed for the band-limited gravity data (e.g., Martinec 1998; Novák and Heck 2002). Assuming the band-limited gravity disturbances δg_b^H at the sphere of radius $R+D$, the band-limited disturbing gravity

potential T_b^H restricted at the sphere of radius R is given as follows ("one-step approach" in Novák and Heck (2002))

$$T_b^H(R,\Omega) = \frac{R+D}{4\pi} \iint\limits_{\Omega_S} \delta g_b^H(R+D,\Omega')\, \mathcal{I}_b(R+D,R,\psi)\, \mathrm{d}\Omega' \,, \quad \text{for } D \geq 0 \,, \tag{4.3}$$

where Ω_S stands for the solid angle of the whole sphere, ψ is the spherical distance between the geocentric direction $\Omega = (\theta,\lambda)$ of the point of interest and the geocentric direction $\Omega' = (\theta',\lambda')$ of the integrating point and the band-limited integration kernel $\mathcal{I}_b$ is (Novák and Heck 2002)

$$\mathcal{I}_b(R+D,R,\psi) = \sum_{n=l}^{L} \frac{2n+1}{n+1} \left(\frac{R+D}{R}\right)^{n+1} P_n(\cos\psi) \,. \tag{4.4}$$

In the text above, the knowledge of the gravity disturbances δg_b^H at the flight level D all over the Earth was assumed. Since the surveys described in Sec. 3 provide the gravity disturbances δg_b^H only within the limited geographical area corresponding to the solid angle Ω_0, we split the integral in Eq. (4.3) into two parts

$$\begin{aligned} T_b^H(R,\theta,\lambda) \;=\; & \frac{R+D}{4\pi} \iint\limits_{\Omega_0} \delta g_b^H(R+D,\Omega')\, \mathcal{I}_b(R+D,R,\psi)\, \mathrm{d}\Omega' + \\ & + \frac{R+D}{4\pi} \iint\limits_{\Omega_S-\Omega_0} \delta g_b^H(R+D,\Omega')\, \mathcal{I}_b(R+D,R,\psi)\, \mathrm{d}\Omega' \,, \end{aligned} \tag{4.5}$$

where the integration over Ω_0 gives the contribution of the near zone (i.e., the zone where aerial gravity data are available, so-called spherical cap) and the integration over $\Omega_S - \Omega_0$ is the contribution of the distant zone. Since the kernel function $\mathcal{I}_b$ in Eq. (4.4) depends on the spherical distance ψ of the computing point and the point of interest, it can be considered as a spatial weight function of a contribution of the gravity data. The kernel function $\mathcal{I}_b$ for $l = 201$ and $L = 3000$ is plotted in Figs. 4.1 (flight altitudes are $H_1 = 5156$ m – blue line and $H_2 = 1620$ m – red line) and 4.2. Although the band-limited integration kernel $\mathcal{I}_b$ oscillates with the increasing amplitude for increasing degree n of the series expansion, see Fig. 4.1, it can be evaluated numerically without any modification even for $L = 3000$, i.e., the maximum L used in the thesis. Figure 4.2 shows that $\mathcal{I}_b$ oscillates

with the amplitude decreasing to the zero for increasing spherical distance ψ except for the part where the spherical distance approaches the value $\psi = 180°$. In the case of aerial

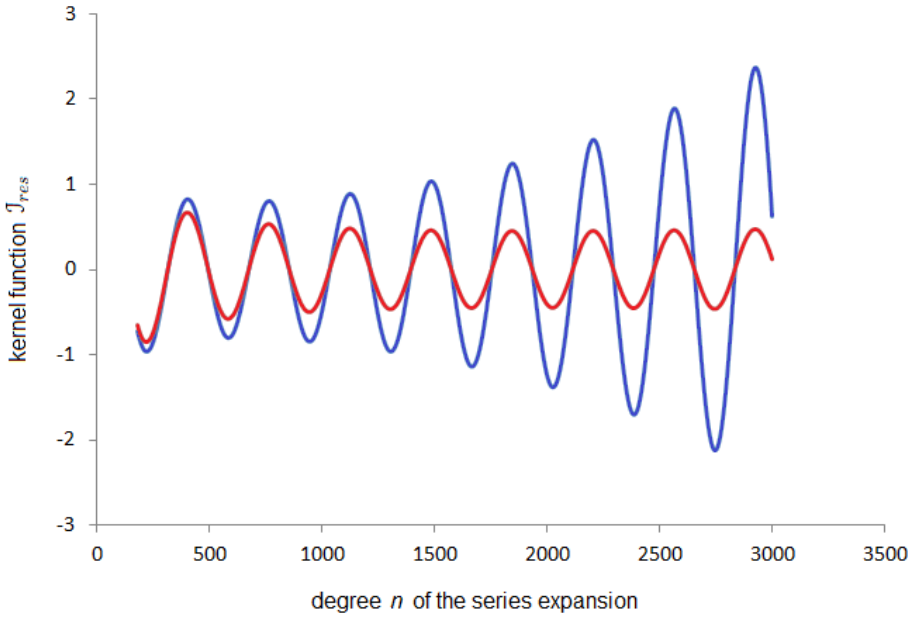

Figure 4.1: Band-limited integration kernel $\mathcal{J}_b$ for $181 \leq n \leq 3000$, $\psi_0 = 1°$ and the flight altitudes $H_1 = 5156$ m (blue line) and $H_2 = 1620$ m (red line)

gravity data of Taiwan the maximum spherical distance used in computations is $\psi_0 = 0.9°$ around each point. It can be seen from the Fig. 4.2 that the contribution of the gravity data within the distant zone (also called truncation error or distant-zone effect), i.e., for $\psi > \psi_0$, should not be neglected. This contribution cannot be computed by integration over geographically limited aerial gravity data, because they are not available within the distant zone. Thus, it is estimated using EGM08 up to the maximum degree and order $n_{max} = m_{max} = 2160$. The truncation error ϵ_t resulting from spherical cap integration in terms of the harmonic expansion is (Novák and Heck 2002)

$$\epsilon_t = \frac{GM}{2(R+D)} \sum_{n=l}^{n_{max}} (n+1) \left(\frac{R}{R+D}\right)^{n+1} V_n(D,\psi_0) T_n(\Omega)\,, \tag{4.6}$$

where the truncation coefficients V_n of the kernel function $\mathcal{J}_b$ are

$$V_n(D,\psi_0) = \sum_{k=l}^{L} \frac{2k+1}{k+1} \left(\frac{R+D}{R}\right)^{k+1} R_{n,k}(\psi_0)\,, \quad l \leq n \leq n_{max}\,. \tag{4.7}$$

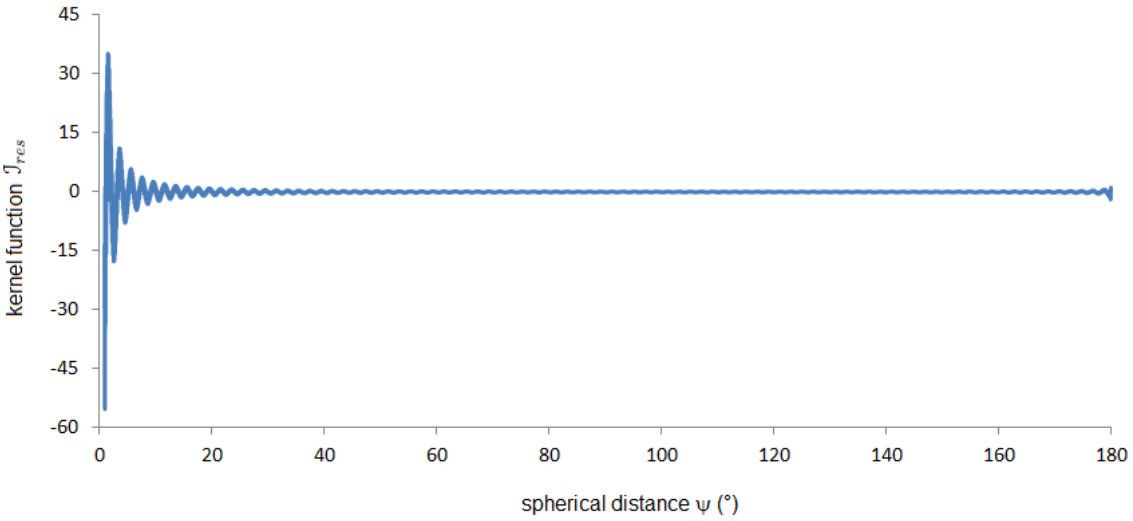

Figure 4.2: Band-limited integration kernel $\mathfrak{I}_b$ for $181 \leq n \leq 3000$ and the flight altitude $D = 1620$ m

Let $\cos\psi_0 \equiv t$, the Paul coefficients $R_{n,k}$ are (Paul 1973, p. 416)

for $n \neq k$:

$$R_{n,k}(t) = \frac{\frac{n(n+1)}{2n+1}P_k(t)[P_{n+1}(t) - P_{n-1}(t)] - \frac{k(k+1)}{2k+1}P_n(t)[P_{k+1}(t) - P_{k-1}(t)]}{(n-k)(n+k+1)}, \tag{4.8}$$

for $n = k$:

$$\begin{aligned} R_{n,n}(t) &= \frac{(n+1)(2n-1)}{n(2n+1)}R_{n+1,n-1}(t) - \frac{n-1}{n}R_{n,n-2}(t) + \\ &\quad + \frac{2n-1}{2n+1}R_{n-1,n-1}(t)\,, \end{aligned} \tag{4.9}$$

with the initial values

$$\begin{aligned} P_0(t) &= 1\,, \\ P_1(t) &= t\,, \\ R_{0,0}(t) &= t+1\,, \\ R_{1,1}(t) &= \frac{t^3+1}{3}\,, \end{aligned} \tag{4.10}$$

and the recurrence relation for the Legendre polynomials

$$P_n(t) = \frac{2n-1}{n}tP_{n-1}(t) - \frac{n-1}{n}P_{n-2}(t)\,. \tag{4.11}$$

Function T_n in Eq. (4.6) is the Laplace surface harmonic of degree n (Heiskanen and Moritz 1967, p. 21) that is evaluated using EGM08.

4.1.1 Methods of transformation of $\delta g(R+D)$ to $T(R)$

In geodesy, the determination of the geoid includes processing of different types of data. There are global gravity data provided by gravity-dedicated satellite missions CHAMP (Reigber, Lühr and Schwintzer 2002), GRACE (Tapley et al. 2004) and GOCE (ESA 1999; Drinkwater et al. 2003) and local gravity data obtained from aerial, marine and terrestrial gravity surveys or satellite altimetry. Methods often used in the geoid determination include a least-squares collocation (Krarup 1969; Moritz 1980; Forsberg and Kenyon 1994; Marchenko et al. 2001; Forsberg 2002), radial base functions (Schmidt et al. 2007; Klees et al. 2008; Antoni, Keller and Weigelt 2009), variational methods (Holota 1995, 1997; Holota and Nesvadba 2008) and integral formulas for the solution of geodetic BVPs as the Stokes integral (Stokes 1849), the Hotine integral (Hotine 1969) and the Molodensky integral series (Molodensky, Eremeev and Yurkina 1960). The numerical approaches include the FFT techniques (Sideris and Schwarz 1986; Schwarz, Sideris and Forsberg 1990), wavelet transform techniques (Freeden and Windheuser 1997; Freeden and Schneider 1998; Keller 2004; Kuroishi and Keller 2005; Roland and Denker 2005) and spherical harmonic expansions (Heiskanen and Moritz 1967).

In the thesis, two numerical methods are used for evaluation of the integral formula in Eq. (4.3) – numerical integration (Newton-Cotes formulas) and the 4D wavelet transform. Using the Newton-Cotes formulas represents a standard method for the numerical integration, 4D wavelet transform (Keller and Hájková 2011) represents a numerical technique related to the solution of the so-called Galerkin equations. Wavelet transform is a powerful tool in evaluating some singular geodetic integrals (e.g., Liu and Sideris 2005). Our aim is to find out if it remains the efficient tool also for evaluation of non-singular surface integrals. Both methods are tested on synthetic gravity data sets first, see Sec. 5. Then, the measured aerial gravity disturbances at the flight level within the area of Taiwan are transformed to the disturbing gravity potential at the sea level using these two methods.

For a comparison with the "one-step approach" described above, see Eq. (4.3) (Novák and Heck 2002), we used also the standard two-step approach where an analytic contin-

uation of the aerial gravity disturbances from a flight altitude to the geocentric reference sphere R is done by the quadratic part of the Taylor series and the transformation of the gravity disturbances to the disturbing gravity potential at the geocentric reference sphere R is done by the Hotine formula (Hotine 1969; Hofmann-Wellenhof and Moritz 2005, p. 115), see Eq. (1.72). For the evaluation of the Hotine formula, a numerical integration by the Newton-Cotes formulas is used.

4.2 Numerical integration

For transformation of the gravity disturbances δg_b^H at the constant height D above the geocentric sphere of radius R to the disturbing gravity potential δT_b^H, see Eq. (4.3), we used Newton-Cotes formulas (Abramowitz and Stegun 1972, p. 886) for the numerical integration. The minimum degree l in the integration kernel, see Eq. (4.4), and the radius of integration correspond to the same values as in the evaluation of DTE. A wavelength κ of a function (e.g., the gravity disturbance or the disturbing gravity potential) on the geocentric sphere of radius R, computed using a spherical harmonic series up to the maximum degree n, yields (Novák, Kostelecký and Klokočník 2009)

$$\kappa = \frac{2\pi R}{n}\,. \tag{4.12}$$

Due to a connection between a wavelength and a spatial distance ψ (in radians), $\psi = \frac{\kappa}{n}$ (Novák, Kostelecký and Klokočník 2009), the spatial distance ψ can be assigned to the maximum degree and order of the used GGM. Thus, $l = 201$ and $\psi_{max} = 54'$ for EGM08/GOCO03s used to the degree and order $n = m = 200$, $l = 361$ and $\psi_{max} = 30'$ for EGM08 used to the degree and order $n = m = 360$, $l = 1081$ and $\psi_{max} = 10'$ for EGM08 used to the degree and order $n = m = 1080$ and $l = 2161$ and $\psi_{max} = 5'$ for EGM08 used to the degree and order $n = m = 2160$. The maximum degree L depends on the width of the filter which was applied on measured data. For aerial gravity data of Taiwan, the degree $L = 3000$ was chosen, see Sec. 4.1. In the case of numerical integration using Newton-Cotes formulas, the truncation error resulting from spherical cap integration, see Eq. (4.6), were taken into account (Novák and Heck 2002).

The integral in the "one-step method", see Eq. (4.3), corresponds for $D = 0$ to the Hotine integral. Thus, the Newton-Cotes formulas for numerical integration of the

integral in Eq. (4.3) for $D = 0$ are used for evaluation of the Hotine integral in the two-step approach.

4.3 Wavelet transform

Wavelet transform is a numerical technique related to the solution of the so-called Galerkin equations (e.g., Zienkiewicz, Taylor and Zhu 1967). It can be used for the evaluation of integral operators, both convolution and non-convolution ones. Assume the integral transformation in the form (Keller and Hájková 2011)

$$S(\mathbf{x}) = \int_{\mathbb{R}^n} K(\mathbf{x}, \mathbf{y})\, s(\mathbf{y})\, \mathrm{d}\mathbf{y}\,, \tag{4.13}$$

where S stands for the given data and s for the unknown solution (e.g., Abel-Poisson's integral, Kellogg 1927, p. 241) or vice versa (e.g., the Stokes formula, Heiskanen and Moritz 1967, p. 93). In the following text we assume the first case, i.e., S stands for the given data and s for the unknown solution. The basic idea of the wavelet transform is to approximate both the functions S and s by linear combinations of given orthonormal base functions φ_j and ψ_k

$$s(\mathbf{y}) = \sum_{j=1}^{n} \alpha_j\, \varphi_j(\mathbf{y}), \quad S(\mathbf{x}) = \sum_{k=1}^{n} \beta_k\, \psi_k(\mathbf{x})\,, \tag{4.14}$$

where α_j and β_k are corresponding coefficients of the linear combinations. Inserting these expansions into Eq. (4.13) yields

$$\sum_{k=1}^{n} \beta_k\, \psi_k(\mathbf{x}) = \sum_{j=1}^{n} \alpha_j \int_{\mathbb{R}^n} K(\mathbf{x}, \mathbf{y})\, \varphi_j(\mathbf{y})\, \mathrm{d}\mathbf{y}\,. \tag{4.15}$$

Multiplication with ψ_i and integration leads (because of the orthonormality of the functions ψ_j) to the system of linear equations (Keller and Hájková 2011)

$$\beta_i = \sum_{j=1}^{n} \left(\int_{\mathbb{R}^n} \int_{\mathbb{R}^n} K(\mathbf{x}, \mathbf{y})\, \varphi_j(\mathbf{y})\, \psi_i(\mathbf{x})\, \mathrm{d}\mathbf{y}\, \mathrm{d}\mathbf{x} \right) \alpha_j\,, i = 1, ..., n\,. \tag{4.16}$$

The numerical properties (density/sparsity) of the matrix

$$\mathbf{A} = \left(\int_{\mathbb{R}^n} \int_{\mathbb{R}^n} K(\mathbf{x}, \mathbf{y})\, \varphi_j(\mathbf{y})\, \psi_i(\mathbf{x})\, \mathrm{d}\mathbf{y}\, \mathrm{d}\mathbf{x} \right)_{i,j}, \tag{4.17}$$

strongly influence the numerical efficiency of the Galerkin method.

In Sec. 4.3.1, an overview of different methods depending on the numerical properties of the matrix $\mathbf{A}$ and on the dimension of integral formula (planar, spherical, ...) can be found. Basic ideas of the wavelet decomposition and reconstruction in 1D are described in Sec. 4.3.2. In Sec. 4.3.3, the N-dimensional wavelet transform developed in Keller and Hájková (2011) is presented. In the thesis, the 4D wavelet transform described in Keller and Hájková (2011) was used for the transformation of the aerial gravity disturbances δg_b^H at the constant flight level D above the geocentric sphere of radius R to the disturbing gravity potential δT_b^H at the sea level, see Eq. (4.3). Parameters of this transformation are described in Sec. 4.3.4.

4.3.1 Introduction to wavelet transform in geodesy

In the case of a diagonal matrix, the sparsest possible matrix, the spectrum of the solution is obtained by dividing (S known, s unknown function) or multiplying (S unknown, s known function) the spectrum of the data by the spectrum of the kernel, which is the core of the FFT technique (Sideris and Schwarz 1986; Schwarz, Sideris and Forsberg 1990). Since the 2D FFT techniques are restricted to planar approximation, they cannot be directly used on the sphere, where the corresponding integral kernels are no longer convolution kernels. Different methods have been developed to solve this problem. Evaluation of spherical integral formulas on a sequence of strips, each of them bounded by two parallels, was presented in Strang van Hees (1990) and Haagmans, de Min and van Gelderen (1993). In each strip the kernel is approximately a convolution kernel and can be evaluated by FFT techniques. A similar technique restricted to so-called invariant spherical pseudo-differential operators[1] (ISPDO) was described in Windheuser (1995). It

[1] Pseudo-differential operators – operators whose kernels can be represented as convergent series of Legendre polynomials (Windheuser 1995).

uses for the evaluation of spherical integral formulas spherical wavelets. In general, cubature formulas are applied for the spherical wavelet transform and for the inverse spherical wavelet transform. An overview of the theory of spherical wavelets and of some of their applications can be found in Freeden (1999).

Block-wise constant base functions, that are frequently used in the case of a non-convolution kernel, lead to a fully occupied matrix $\mathbf{A}$ with a small number of large and a large number of small entries. The idea of operator compression, i.e., neglecting the small entries with only the small accuracy loss, was already discussed in numerical analysis (e.g., Beylkin, Coifman and Rohlin 1991, 1992; Koornwinder 1993). Since block-wise functions are simple wavelets – the tensor-Haar wavelets (see, e.g., Keller 2004, p. 207), in order to maximize the compression rate of the matrix $\mathbf{A}$ without losing much of the accuracy, a higher order orthogonal wavelet should be used as a base function. With the decomposition depth of more than one level, a much higher compression rate and consequently a much more efficient solution technique can be constructed (Keller and Hájková 2011).

The using of wavelets in physical geodesy is a rather new technique, although in the geodynamics is well established (e.g., Gibert, Holschneider and Le Mouël 1998; Schuh, Nagel and Seitz 2001). Significant contributions on using wavelets in physical geodesy can be found for instance in Salomonovicz (2000), Gilbert and Keller (2000), Liu and Sideris (2003) and Elhabiby (2007). The technique for evaluation of non-convolution integrals described in Elhabiby (2007) leads to impressive compression rates that could be achieved without degrading the evaluation accuracy. Nevertheless, this approach does not allow a decomposition depth of more than one level. Moreover, the convolution kernel is treated as a sequence of 2D decompositions, although the kernel is 4D (assume both the computation and the running points have two variable coordinates).

In order to achieve the maximal possible efficiency and compression rate, formulas for the 4D wavelet decomposition and reconstruction and for the multiplication of the 4D spectrum of the kernel with the 2D spectrum of the data was developed in Keller and Hájková (2011). The main ideas are described in the text below. In the thesis, this method was used for the transformation of the aerial gravity disturbances δg_b^H at the constant flight level D above the geocentric sphere of radius R to the disturbing gravity potential

δT_b^H at the sea level, see Eq. (4.3).

4.3.2 Wavelet decomposition and reconstruction in 1D

The main idea of the wavelet transform is to decompose a signal into disjunct frequency bands, a high-frequency and a low-frequency part. Let $f \in L^2(\mathbb{R})$ be a signal from a certain subspace $V_{-1} \subset L^2(\mathbb{R})$. The low-frequency (smooth) part is obtained by an orthogonal projection $P_0 f$ into a smaller subspace $V_0 \subset V_{-1}$, which contains only the smooth functions of V_{-1}. The projection denoted as $Q_0 f$ of the signal f into the orthogonal complement W_0 of V_0 in V_{-1} gives the high-frequency (rough) part. The signal f can be decomposed in the following way (Keller 2004, p. 43):

$$\begin{aligned} f &= P_0 f + Q_0 f \,, \\ V_{-1} &= V_0 \oplus W_0 \,, \end{aligned} \tag{4.18}$$

where "$\oplus$" is a direct sum (see, e.g., Rektorys et al. 1963, p. 828). Repeating this decomposition for the low-frequency part $P_0 f$ gives

$$P_0 f = P_1 P_0 f + Q_1 P_0 f \,, \tag{4.19}$$

where P_1 and Q_1 are the projectors into subspace $V_1 \subset V_0$ and the corresponding orthogonal complement W_1. The decomposition of the signal f, schematically displayed in Fig. 4.3 (Keller 2004, p. 45), into different frequency bands is the core of the multi-resolution analysis.

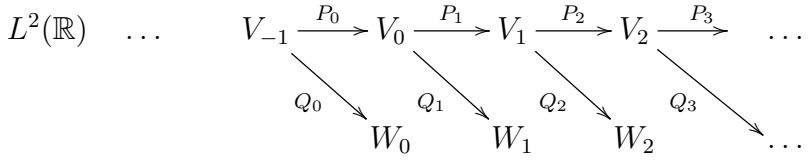

Figure 4.3: Multi-resolution analysis (MRA) of $L^2(\mathbb{R})$

The Multi-Resolution Analysis (MRA) of $L^2(\mathbb{R})$ is defined as a sequence of closed linear subspaces $V_j \subset L^2(\mathbb{R})$, schematically (Keller 2004, p. 44)

$$\{0\} \subset \ldots \subset V_2 \subset V_1 \subset V_0 \subset V_{-1} \subset V_{-2} \subset \ldots \subset L^2(\mathbb{R}) \,, \tag{4.20}$$

if the following statements holds (Daubechies 1992, p. 14; Koornwinder 1995)

a) $V_{j+1} \subset V_j\,,$ (4.21)

b) $\overline{\bigcup_{j\in\mathbb{Z}} V_j} = L^2(\mathbb{R})\,,$ (4.22)

c) $\bigcap_{j\in\mathbb{Z}} V_j = \{0\}\,,$ (4.23)

d) $f(x) \in V_j \Leftrightarrow f(2^j x) \in V_0, \quad \text{or} \quad f(x) \in V_j \Leftrightarrow f(2x) \in V_{j-1}\,,$ (4.24)

e) $f(x) \in V_0 \Rightarrow f(x-n) \in V_0,\, \forall n \in \mathbb{Z}\,,$ (4.25)

f) there exists a function (scaling function) $\varphi \in V_0$, that the set

$$\{\varphi_{0,n}; n \in \mathbb{Z}\} = \{\varphi(x-n); n \in \mathbb{Z}\}, \tag{4.26}$$

is the Riesz[2] base of V_0.

According Eq. (4.24) all spaces of MRA are scaled versions of the base space V_0. We define the scaled versions of φ in the following way (Daubechies 1992, p. 130):

$$\varphi_{j,n}(x) := 2^{-\frac{j}{2}}\varphi(2^{-j}x - n)\,. \tag{4.27}$$

Since the space V_0 is spanned by the shifted versions of the scaling function φ, see Eq. (4.26), the spaces V_j are spanned by the shifted versions of $\varphi_{j,n}$ that constitute the Riesz base of V_j.

According Eq. (4.21), for the scale function $\varphi \in V_0$ it also holds $\varphi \in V_{-1}$. Thus, there exists a uniquely determined sequence of real numbers $\{h_n\}_{n\in\mathbb{Z}}$ called scaling coefficients, such that (Daubechies 1992; Keller 2004, p. 47)

$$\varphi(x) = \sum_{n\in\mathbb{Z}} h_n \varphi_{-1,n}(x) = \sqrt{2}\sum_{n\in\mathbb{Z}} h_n \varphi(2x-n)\,, \tag{4.28}$$

[2]Definition of the Riesz base can be found in Koornwinder (1995), p. 21.

where

$$h_n = \int_{-\infty}^{\infty} \varphi(x)\overline{\sqrt{2}\varphi(2x-n)}\,\mathrm{d}x \;=\; \sqrt{2}\int_{-\infty}^{\infty} \varphi(x)\overline{\varphi(2x-n)}\,\mathrm{d}x\,,$$

$$\sum_{n\in\mathbb{Z}} |h_n|^2 \;=\; 1\,. \tag{4.29}$$

Equation (4.28) is called the scaling equation of MRA. In order to get the orthogonal wavelets, the orthogonal Riesz base of V_0 is required, i.e., for the scaling functions it must hold

$$\langle \varphi(x-k), \varphi(x-l)\rangle_{L^2} = \delta_{k,l},\ k,l \in \mathbb{Z}\,, \tag{4.30}$$

where $\delta_{k,l}$ stands for the Kronecker delta[3] and $\langle\cdot,\cdot\rangle_{L^2}$ stands for the discrete scalar product of two complex functions in $L^2(\mathbb{R})$ (e.g., Rektorys et al. 1963, p. 827). Equation (4.30) yields for the scaling parameters (Keller 2004, p. 48)

$$\sum_{n\in\mathbb{Z}} h_n h_{n+2m} = \delta_{0,m}. \tag{4.31}$$

If the nested sequence of the spaces V_j satisfies the properties in Eqs. (4.21) to (4.26), then there exists ψ such that (Daubechies 1992, p. 14)

$$P_{j-1}f = P_j f \;+\; \sum_{k\in\mathbb{Z}} \langle f, \psi_{j,k}\rangle_{L^2}\psi_{j,k}\,, \tag{4.32}$$

where P_j is the orthogonal projection into space V_j. Base functions $\psi_{j,k}$ are the shifted versions of the mother wavelet ψ,

$$\psi_{j,k}(x) = 2^{-\frac{j}{2}}\psi(2^{-j}x-k)\,, \tag{4.33}$$

which is defined using the scaling function φ from Eq. (4.26) and the scaling coefficients (Keller 2004, p. 51)

$$\psi(x) = \sqrt{2}\sum_{n\in\mathbb{Z}} g_n\varphi(2x-n) = \sqrt{2}\sum_{n\in\mathbb{Z}}(-1)^n h_{1-n}\varphi(2x-n) = \sum_{n\in\mathbb{Z}}(-1)^n h_{1-n}\varphi_{-1,n}\,. \tag{4.34}$$

[3]Kronecker delta is a function of two variables. It is 1 if the variables are equal, otherwise it is 0:

$$\delta_{j,k} = \begin{cases} 1, & j = k\,, \\ 0, & j \neq k\,. \end{cases}$$

For every Riesz base of the space V_0 we can construct the Riesz base of the space W_0, which is the orthogonal complement of V_0 in V_{-1}, using the relationship between the scaling coefficients h_k of φ and the coefficients g_k of ψ (Keller 2004, p. 51)

$$g_k = (-1)^k h_{1-k} \,. \tag{4.35}$$

Assume the signal $f \in V_0 \subset L^2(\mathbb{R})$. Since the scaling functions φ constitute the Riesz base of V_0, the signal f can be determined as a linear combination of these functions, such as (Keller 2004, pp. 55-56)

$$f(x) = \sum_{k\in\mathbb{Z}} c_{0,k}\varphi(x-k) = \sum_{k\in\mathbb{Z}} c_{0,k}\varphi_{0,k}(x)\,, \quad c_{0,k} = \langle f, \varphi_{0,k}\rangle_{L^2} \,. \tag{4.36}$$

According Eq. (4.18), the function $f \in V_0 \subset L^2(\mathbb{R})$ can be decomposed into a low-frequency part from the subset V_1 and a high-frequency part from the subset W_1. The Riesz base of V_1 and W_1 is constituted by the scaling functions φ and wavelets ψ, respectively. Thus, the decomposition of the signal f can be written as follows:

$$f(x) = \sum_{k\in\mathbb{Z}} c_{1,k}\varphi_{1,k}(x) + \sum_{k\in\mathbb{Z}} d_{1,k}\psi_{1,k}(x)\,, \tag{4.37}$$

where $c_{1,k} = \langle f, \varphi_{1,k}\rangle_{L^2}$ and $d_{1,k} = \langle f, \psi_{1,k}\rangle_{L^2}$. In general, every function $f \in V_{m-1}$, $V_{m-1} \subset L^2(\mathbb{R})$ can be decomposed as follows

$$\begin{aligned} f(x) &= \sum_{k\in\mathbb{Z}} c_{m,k}\varphi_{m,k}(x) + \sum_{k\in\mathbb{Z}} d_{m,k}\psi_{m,k}(x)\,, \\ c_{m,k} &= \langle f, \varphi_{m,k}\rangle_{L^2}\,, \\ d_{m,k} &= \langle f, \psi_{m,k}\rangle_{L^2}\,. \end{aligned} \tag{4.38}$$

It is not effective to compute the coefficients $c_{m,k}$ and $d_{m,k}$ by the numerical evaluation of the scalar products. Using the scaling equation (4.28) and the defining equation of the wavelet (4.34), a relation between the coefficients c_{m-1} and c_m, d_m called the Mallat algorithm is derived (Keller 2004, p. 56):

$$c_{m,k} = \sum_{l\in\mathbb{Z}} c_{m-1,l} h_{l-2k}\,, \tag{4.39}$$

$$d_{m,k} = \sum_{l\in\mathbb{Z}} c_{m-1,l} g_{l-2k}\,. \tag{4.40}$$

The Mallat algorithm can be described using decomposition operators H and G, that are defined as follows (Keller 2004, p. 57):

$$\begin{aligned} H : l_2(\mathbb{Z}) &\rightarrow l_2(\mathbb{Z}) \\ c &\mapsto Hc = \{(Hc)_k = \sum_{l\in\mathbb{Z}} h_{l-2k}c_l\}\,, \end{aligned} \tag{4.41}$$

$$\begin{aligned} G : l_2(\mathbb{Z}) &\rightarrow l_2(\mathbb{Z}) \\ c &\mapsto Gc = \{(Gc)_k = \sum_{l\in\mathbb{Z}} g_{l-2k}c_l\}\,. \end{aligned} \tag{4.42}$$

Using the operators H and G, the scheme of the Mallat algorithm is shown in Fig. 4.4.

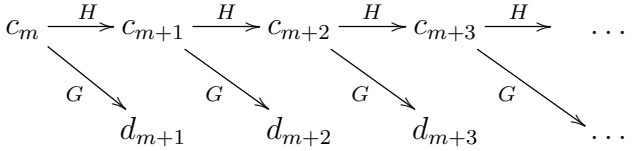

Figure 4.4: Scheme of the Mallat algorithm

A similar relation can be derived for the reconstruction of the function $f \in V_m$, $V_m \subset L^2(\mathbb{R})$, see, e.g., Keller (2004). Assuming the coefficients c_m and d_m are known, the coefficients c_{m-1} are computed as follows

$$c_{m-1,k} = \sum_{l\in\mathbb{Z}} (c_{m,l}h_{k-2l} + d_{m,l}g_{k-2l})\,. \tag{4.43}$$

We define the adjoint operators H^*, G^* of the decomposition operators H, G (Keller 2004, p. 58):

$$\begin{aligned} H^* : l_2(\mathbb{Z}) &\rightarrow l_2(\mathbb{Z}) \\ c &\mapsto H^*c = \{(H^*c)_k = \sum_{l\in\mathbb{Z}} h_{k-2l}c_l\}\,, \end{aligned} \tag{4.44}$$

$$\begin{aligned} G^* : l_2(\mathbb{Z}) &\rightarrow l_2(\mathbb{Z}) \\ c &\mapsto G^*c = \{(G^*c)_k = \sum_{l\in\mathbb{Z}} g_{k-2l}c_l\}\,. \end{aligned} \tag{4.45}$$

The scheme of the inverse Mallat algorithm using the adjoint operators H^* and G^* is shown in Fig. 4.5.

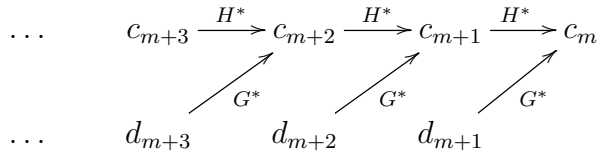

Figure 4.5: Scheme of the inverse Mallat algorithm

4.3.3 N-dimensional wavelet analysis

Similar to the 1D case, MRA of $L^2(\mathbb{R}^n)$ is a nested sequence of subspaces (Keller and Hájková 2011)

$$\{0\} \subset \ldots \subset V_2 \subset V_1 \subset V_0 \subset V_{-1} \subset V_{-2} \subset \ldots \subset L^2(\mathbb{R}^n)\,, \tag{4.46}$$

with the following statements

a) $V_{j+1} \subset V_j\,,$

b) $\overline{\bigcup_{j\in\mathbb{Z}} V_j} = L^2(\mathbb{R}^n)\,,$

c) $\bigcap_{j\in\mathbb{Z}} V_j = \{0\}\,,$

d) $f(\mathbf{x}) \in V_j \Leftrightarrow f(2\mathbf{I}\mathbf{x}) \in V_{j-1}\,,$

e) there exists a function (scaling function) $\varphi \in V_0$, that the set

$$\{\varphi_{0,\mathbf{k}}; \mathbf{k} \in \mathbb{Z}^n\} = \{\varphi(\mathbf{x}-\mathbf{k}); \mathbf{k} \in \mathbb{Z}^n\},$$

is the Riesz base of V_0.

There exist $2^n - 1$ wavelets $\psi^{(1)}, \ldots, \psi^{(2^n-1)}$ which generate the orthogonal complements W_0^j, $j = 1, \ldots, 2^n - 1$ of V_0 in V_{-1} (Louis, Maaß and Rieder 1998)

$$V_{-1} = V_0 \oplus (\oplus_{j=1}^{2^n-1} W_0^{(j)})\,. \tag{4.47}$$

Assuming the scaling function and wavelet of the 1D MRA are known, we define the multi-index $\mathbf{d}$ and his modulus $|\mathbf{d}|$:

$$\mathbf{d} = (d_1, d_2, \ldots, d_n), \quad d_i \in 0, 1, \tag{4.48}$$

$$|\mathbf{d}| = \sum_{k=1}^{n} d_k 2^{k-1}. \tag{4.49}$$

The scaling function φ and wavelet $\psi^{(j)}$ of the n-dimensional MRA can be constructed in the following way (Keller and Hájková 2011):

$$\varphi(\mathbf{x}) = \varphi(x_1) \cdot \varphi(x_2) \ldots \varphi(x_n), \tag{4.50}$$

$$\begin{aligned} \psi^{(|\mathbf{d}|)}(\mathbf{x}) &= (\varphi(x_1)\delta_{0,d_1} + \psi(x_1)\delta_{1,d_1}) \cdot (\varphi(x_2)\delta_{0,d_2} + \psi(x_2)\delta_{1,d_2}) \cdot \ldots \cdot \\ &\quad (\varphi(x_n)\delta_{0,d_n} + \psi(x_n)\delta_{1,d_n}), \end{aligned} \tag{4.51}$$

$$\mathbf{x} = (x_1, x_2, \ldots, x_n) \in \mathbb{R}^n.$$

The corresponding scaled and shifted versions are defined by

$$\varphi_{l,\mathbf{m}}(\mathbf{x}) = 2^{-nl/2}\varphi(2^{-l}\mathbf{x} - \mathbf{m}), \tag{4.52}$$

$$\psi^{(|\mathbf{d}|)}_{l,\mathbf{m}}(\mathbf{x}) = 2^{-nl/2}\psi^{(|\mathbf{d}|)}(2^{-l}\mathbf{x} - \mathbf{m}). \tag{4.53}$$

There are 2^n scaling equations in $L^2(\mathbb{R}^n)$ (Keller and Hájková 2011):

$$\varphi(\mathbf{x}) = 2^{n/2} \sum_{\mathbf{k}\in\mathbb{Z}^n} h_{\mathbf{k}} \varphi(2\mathbf{x} - \mathbf{k}), \tag{4.54}$$

$$\psi^{(|\mathbf{d}|)}(\mathbf{x}) = 2^{n/2} \sum_{\mathbf{k}\in\mathbb{Z}^n} g^{(|\mathbf{d}|)}_{\mathbf{k}} \psi(2\mathbf{x} - \mathbf{k}), \quad |\mathbf{d}| > 0, \tag{4.55}$$

where the sequences $\{h_{\mathbf{k}}\}$, $\{g^{(|\mathbf{d}|)}_{\mathbf{k}}\}$ are defined as follows:

$$h_{\mathbf{k}} = h_{k_1} \cdot h_{k_2} \ldots h_{k_n}, \tag{4.56}$$

$$g^{(|\mathbf{d}|)}_{\mathbf{k}} = (h_{k_1}\delta_{0,d_1} + g_{k_1}\delta_{1,d_1}) \cdot (h_{k_2}\delta_{0,d_2} + g_{k_2}\delta_{1,d_2}) \cdot \ldots \cdot (h_{k_n}\delta_{0,d_n} + g_{k_n}\delta_{1,d_n}). \tag{4.57}$$

In order to derive the n-dimensional Mallat algorithm, the function $f \in V_{-1}$ is represented with respect to the base of V_{-1} and, because of Eq. (4.47), with respect to the bases of V_0

and $W_0^{(j)}$, respectively (Keller and Hájková 2011)

$$f(\mathbf{x}) = \sum_{\mathbf{k}\in\mathbb{Z}^n} c_{\mathbf{k}}^{(-1)} \varphi_{-1,\mathbf{k}}(\mathbf{x}) \,, \tag{4.58}$$

$$f(\mathbf{x}) = \sum_{\mathbf{k}\in\mathbb{Z}^n} \left(c_{\mathbf{k}}^{(0)} \varphi_{0,\mathbf{k}}(\mathbf{x}) \sum_{|\mathbf{d}|=1}^{2^n-1} d_{\mathbf{k}}^{(0,(|\mathbf{d}|))} \psi_{0,\mathbf{k}}^{(|\mathbf{d}|)}(\mathbf{x}) \right) . \tag{4.59}$$

Similar as in 1D case, the coefficients c_{-1} and c_0, $d_0^{(|\mathbf{d}|)}$ are related as follows

$$c_{0,\mathbf{k}} = \sum_{\mathbf{l}\in\mathbb{Z}^n} c_{-1,\mathbf{l}}\, h_{\mathbf{l}-2\mathbf{k}} \,, \tag{4.60}$$

$$d_{0,\mathbf{k}}^{(|\mathbf{d}|)} = \sum_{\mathbf{l}\in\mathbb{Z}^n} c_{-1,\mathbf{l}}\, g_{\mathbf{l}-2\mathbf{k}} \,. \tag{4.61}$$

The n-dimensional Mallat algorithm is based on the relations (4.60) and (4.61). The decomposition filters H and $G^{(|\mathbf{d}|)}$ are (Keller and Hájková 2011)

$$\begin{aligned} H : l_2(\mathbb{Z}^n) &\to l_2(\mathbb{Z}^n) \\ \mathbf{c} &\mapsto H\mathbf{c} = \{(H\mathbf{c})_{\mathbf{k}} = \sum_{\mathbf{l}\in\mathbb{Z}^n} h_{\mathbf{l}-2\mathbf{k}}\, c_{\mathbf{l}}\} \,, \end{aligned} \tag{4.62}$$

$$\begin{aligned} G^{(|\mathbf{d}|)} : l_2(\mathbb{Z}^n) &\to l_2(\mathbb{Z}^n) \\ \mathbf{c} &\mapsto G^{(|\mathbf{d}|)}\mathbf{c} = \{(G^{(|\mathbf{d}|)}\mathbf{c})_{\mathbf{k}} = \sum_{\mathbf{l}\in\mathbb{Z}^n} g_{\mathbf{l}-2\mathbf{k}}^{(|\mathbf{d}|)}\, c_{\mathbf{l}}\} \,. \end{aligned} \tag{4.63}$$

The n-dimensional adjoint filters are defined as follows:

$$\begin{aligned} H^* : l_2(\mathbb{Z}^n) &\to l_2(\mathbb{Z}^n) \\ \mathbf{c} &\mapsto H^*\mathbf{c} = \{(H^*\mathbf{c})_{\mathbf{k}} = \sum_{\mathbf{l}\in\mathbb{Z}^n} h_{\mathbf{k}-2\mathbf{l}}\, c_{\mathbf{l}}\} \,, \end{aligned} \tag{4.64}$$

$$\begin{aligned} (G^{(|\mathbf{d}|)})^* : l_2(\mathbb{Z}^n) &\to l_2(\mathbb{Z}^n) \\ \mathbf{c} &\mapsto (G^{(|\mathbf{d}|)})^*\mathbf{c} = \{((G^{(|\mathbf{d}|)})^*\mathbf{c})_{\mathbf{k}} = \sum_{\mathbf{l}\in\mathbb{Z}^n} g_{\mathbf{k}-2\mathbf{l}}^{(|\mathbf{d}|)}\, c_{\mathbf{l}}\} \,. \end{aligned} \tag{4.65}$$

In Fig. 4.6 the schemes of the n-dimensional Mallat algorithm (left) and the corresponding inverse Mallat algorithm (right) are shown.

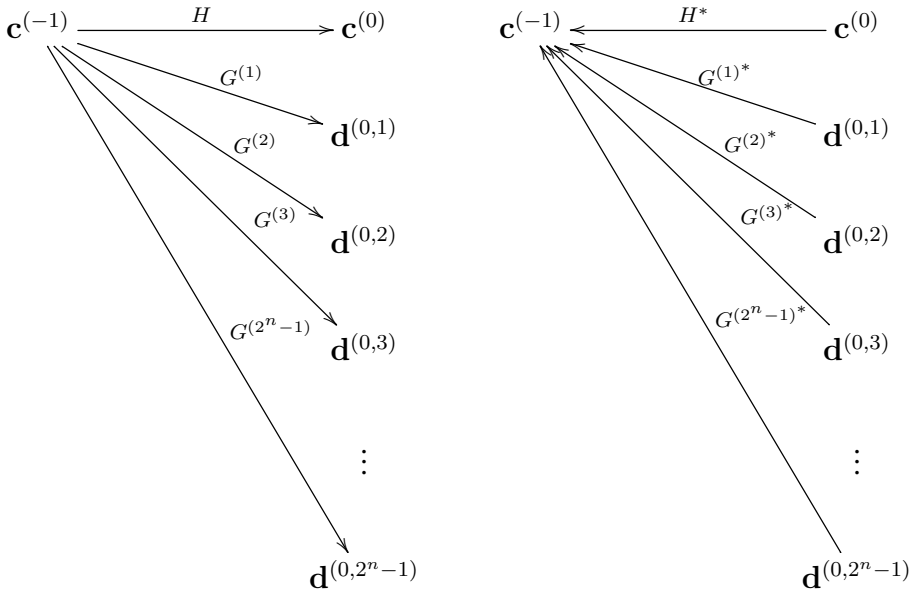

Figure 4.6: Schemes of the n-dimensional Mallat (left) and inverse Mallat (right) algorithm

4.3.4 Computation of the local geoid model using 4D wavelet transform

The wavelet approach described in Keller and Hájková (2011) for solving Eq. (4.3) consists of the following four steps:

- transformation of the band-limited integration kernel $\mathfrak{I}_b$ into the wavelet domain,
- transformation of the residual aerial gravity disturbances $\delta g_b^H(R + D)$ into the wavelet domain,
- computation of the wavelet spectrum of the disturbing gravity potential $\delta T_b^H(R)$,
- backward transformation of the disturbing gravity potential spectrum in estimated disturbing gravity potential.

As base functions the compactly supported orthogonal wavelets were used, particularly the Daubechies wavelet ψ (D4) with the scaling coefficients (Daubechies 1992; Keller

2004, p. 93)

$$\{h_0, h_1, h_2, h_3\} = \left\{ \frac{1+\sqrt{3}}{4\sqrt{2}}, \frac{3+\sqrt{3}}{4\sqrt{2}}, \frac{3-\sqrt{3}}{4\sqrt{2}}, \frac{1-\sqrt{3}}{4\sqrt{2}} \right\}, \tag{4.66}$$

and

$$\{g_0, g_1, g_2, g_3\} = \left\{ \frac{1+\sqrt{3}}{4\sqrt{2}}, -\frac{3-\sqrt{3}}{4\sqrt{2}}, \frac{3+\sqrt{3}}{4\sqrt{2}}, -\frac{1+\sqrt{3}}{4\sqrt{2}} \right\}. \tag{4.67}$$

The Daubechies wavelet ψ (D4) and the corresponding scale function φ are plotted in Fig. 4.7.

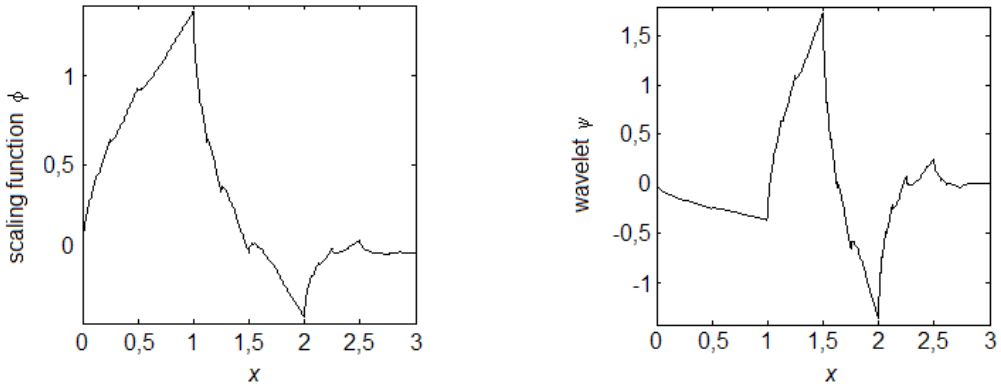

Figure 4.7: Daubechies wavelet ψ (D4) and the corresponding scale function φ

As in the case of numerical integration, the minimum degree l in the integration kernel, see Eq. (4.4), corresponds to degree and order of a low-frequency part of GGMs and the maximum degree $L = 3000$ depends on the width of the filter which was applied on measured aerial gravity data.

4.4 Taylor series

Depending on a distance, on which an analytic continuation is performed, linear or quadratic terms of the Taylor series (Abramowitz and Stegun 1972, p. 880) are used in the thesis. The continuation over height differences, that reach 150 m in maximum, is done only using the linear part of the Taylor series

$$\delta g(R+D, \Omega) \approx \delta g(r, \Omega) + \frac{\partial \delta g}{\partial r}\Big|_{(r,\Omega)} (R+D-r). \tag{4.68}$$

When the analytic continuation over the longer distances at the level of kilometres is needed, the height difference is divided into segments of the length of 500 m (+ one segment about 500 m) and the quadratic part of the Taylor series is used for every segment separately

$$\begin{aligned}\delta g(R+D_d,\Omega) &\approx \delta g(R+D_u,\Omega)+\frac{\partial \delta g}{\partial r}\Big|_{(R+D_u,\Omega)}(D_d-D_u)+\\ &+\frac{1}{2}\frac{\partial^2 \delta g}{\partial r^2}\Big|_{(R+D_u,\Omega)}(D_d-D_u)^2\,,\quad D_u>D_d\,,\end{aligned}\tag{4.69}$$

where D_u stands for the altitude of the first point and D_d for the altitude of the last point of each segment.

4.5 Topographical effects on observed gravity

One of the main assumptions of the boundary-value problem of Eqs. (4.2) is that the disturbing gravity potential T is harmonic everywhere outside the geoid (in the spherical approximation of the geoid outside the geocentric sphere) and the reference ellipsoid. Actually this assumption is not satisfied because of the masses outside the geoid and ellipsoid (topography, sea water, ice and atmosphere). The most important part of the gravitational effect of topography, atmosphere, ice and sea water on gravity is subtracted with the reference part from the GGM, see Sec. 6.1. Since we assume the residual effect of atmosphere, ice and sea water on gravity is small, we do not consider this effect in the thesis. For the residual gravitational effect of topography the second Helmert method of gravity reduction is used in the thesis because of the small effect on the disturbing gravity potential on the geoid.

The main aim of the topographical reduction is to remove the topographic masses outside the geoid. The masses can completely be removed as in the Bouguer reduction (Heiskanen and Moritz 1967, p. 137) or an isostatic reduction can be used, where the topography is removed together with its compensation. Examples of this method are Pratt-Hayford reduction, Airy-Heiskanen reduction and Helmert reduction (Heiskanen and Moritz 1967, pp. 138, 145).

In the case of the second Helmert method of gravity reduction (Heiskanen and Moritz 1967, p. 145; Martinec 1998, p. 42; Heck 2003; Novák et al. 2003a), the topography

is condensed to the form of a single layer on the reference sphere of the radius R that approximates the geoid. In the following text, the effect on gravity and the geoid due to the Helmert reduction of the Earth's gravity field is derived for the full-signal gravity data first and then for the band-limited gravity disturbances and the band-limited geoid.

The Helmert disturbing gravity potential T^H at the constant flight level $R + D$ is related to the disturbing gravity potential T as follows (Martinec 1993)

$$T^H(R + D, \Omega) = T(R + D, \Omega) - \delta V(R + D, \Omega)\,, \tag{4.70}$$

where δV is the Helmert residual potential, which is defined as the difference between the gravitational potential of topography V^t and the gravitational potential of condensed topography V^{ct} (Vaníček et al. 1995)

$$\delta V(R + D, \Omega) = V^t(R + D, \Omega) - V^{ct}(R + D, \Omega)\,. \tag{4.71}$$

Applying the operator $-\frac{\partial}{\partial r}$ to Eq. (4.70) yields

$$\begin{aligned} \delta g^H(R + D, \Omega) &= -\frac{\partial T^H}{\partial r}|_{R+D} = -\frac{\partial T}{\partial r}|_{R+D} + \frac{\partial \delta V}{\partial r}|_{R+D} = \\ &= \delta g(R + D, \Omega) + A(R + D, \Omega)\,. \end{aligned} \tag{4.72}$$

The term $A(R + D, \Omega) = \frac{\partial \delta V}{\partial r}|_{R+D}$ is called the direct topographical effect on gravity and represents the change in gravity due to the Helmert reduction of the Earth's gravity field. The change in the disturbing gravity potential (and the geoid) is called the indirect topographical effect. Equation (4.70) for the geocentric radius R becomes

$$T^H(R, \Omega) = T(R, \Omega) - \delta V(R, \Omega)\,. \tag{4.73}$$

Using the spherical Bruns theorem (Bruns 1878; Heiskanen and Moritz 1967, p. 85) yields

$$N(\Omega) = \frac{T(R, \Omega)}{\gamma(\theta)} = \frac{T^H(R, \Omega)}{\gamma(\theta)} + \frac{\delta V(R, \Omega)}{\gamma(\theta)} = N^H(\Omega) + P(\Omega)\,, \tag{4.74}$$

where γ is normal gravity at the reference ellipsoid, N^H is the co-geoid (Helmert's geoid), δV and P is the indirect topographical effect corresponding to the disturbing gravity potential and to the geoid, respectively.

4.5.1 Direct topographical effect on gravity

The direct topographical effect (DTE) on gravity $A(R+D,\Omega)$ represents the change in gravity due to the Helmert reduction of the Earth's gravity field. It can be obtained by applying the partial radial derivative to the Helmert residual potential δV, see Eq. (4.72). According Eq. (4.71), the potential δV is the difference between the gravitational potential of the topography V^t and the condensed topography V^{ct}. In the development by Vaníček et al. (1995), only the first three terms of the infinite series occurring in evaluation of V^t are considered. Thus, the sign "$\approx$" is used in the following formulas for the DTE instead of the equality sign.

Assuming the topographical mass density as a constant value, i.e., $\rho(r',\Omega') = \rho = \text{const.}$, the following formula can be derived for DTE (Vaníček et al. 1995; Novák et al. 2003a)

$$A(R+D,\Omega) \approx GR\rho \iint_{\Omega_S} \left[\left(\frac{H(\Omega')}{R}\right)^2 \mathcal{J}_1(R+D,R,\psi) + \left(\frac{H(\Omega')}{R}\right)^3 \mathcal{J}_2(R+D,R,\psi) \right] \mathrm{d}\Omega' \,, \tag{4.75}$$

where G stands for the universal gravitational constant, ρ for the mean topographical mass density, Ω_S for the solid angle of the whole sphere, ψ is the spherical distance between the geocentric direction $\Omega = (\theta,\lambda)$ of the point of interest and the geocentric direction $\Omega' = (\theta',\lambda')$ of the integrating point and $H(\Omega')$ is the orthometric height of the topography reckoned along the geocentric direction Ω'. The integration kernels $\mathcal{J}_1$ and $\mathcal{J}_2$ are defined by series that are convergent for $D > 0$

$$\mathcal{J}_1(R+D,R,\psi) = -\sum_{n=0}^{\infty} \frac{n(n+1)}{2} \left(\frac{R}{R+D}\right)^{n+2} P_n(\cos\psi) \,, \tag{4.76}$$

$$\mathcal{J}_2(R+D,R,\psi) = -\sum_{n=0}^{\infty} \frac{n(n+1)(n+3)}{6} \left(\frac{R}{R+D}\right)^{n+2} P_n(\cos\psi) \,. \tag{4.77}$$

Alternatively, DTE can be written as an infinite series, expanding both the integral kernels

and topographical heights (Novák et al. 2003a):

$$A(R+D,\Omega) \approx -2\pi\frac{G\rho}{R}\sum_{n=0}^{\infty}\frac{n(n+1)}{2n+1}\left(\frac{R}{R+D}\right)^{n+2}H_n^2(\Omega) - \\ -2\pi\frac{G\rho}{R^2}\sum_{n=0}^{\infty}\frac{n(n+1)(n+3)}{2n+1}\left(\frac{R}{R+D}\right)^{n+2}H_n^3(\Omega)\,. \quad (4.78)$$

Laplace harmonics of the squared topographical height function H_n^2 and of the cubed topographical height function H_n^3 are defined as follows (Novák et al. 2003a)

$$H_n^2(\Omega) = \sum_{m=0}^{n}(a_{n,m}\cos m\lambda + b_{n,m}\sin m\lambda)P_{n,m}(\cos\theta)\,, \quad (4.79)$$

$$H_n^3(\Omega) = \sum_{m=0}^{n}(c_{n,m}\cos m\lambda + d_{n,m}\sin m\lambda)P_{n,m}(\cos\theta)\,. \quad (4.80)$$

The coefficients $a_{n,m}, b_{n,m}, c_{n,m}$ and $d_{n,m}$ are obtained by the spherical harmonic analysis of the squared and cubed heights of topography computed from DTM2006.0 global topography model related to EGM08 (Pavlis, Factor and Holmes 2007; Pavlis et al. 2012).

Since we have the band-limited aerial gravity disturbances as input data, DTE should correspond to the same frequency band. When using Eq. (4.75), band limitation is approximately achieved by integrating only over the limited spherical cap Ω_0:

$$A_b(R+D,\Omega) \approx GR\rho\iint_{\Omega_0}\left[\left(\frac{H(\Omega')}{R}\right)^2\mathcal{J}_1(R+D,R,\psi) + \right. \\ \left. + \left(\frac{H(\Omega')}{R}\right)^3\mathcal{J}_2(R+D,R,\psi)\right]\mathrm{d}\Omega'\,. \quad (4.81)$$

A connection between the radius of integration and the band limitation of the gravity disturbances and DTE, respectively, is described in Sec. 4.2. For the band-limited DTE in a series form we have (Novák et al. 2003a)

$$A_b(R+D,\Omega) \approx -2\pi\frac{G\rho}{R}\sum_{n=l}^{L}\frac{n(n+1)}{2n+1}\left(\frac{R}{R+D}\right)^{n+2}H_n^2(\Omega) - \\ -2\pi\frac{G\rho}{R^2}\sum_{n=l}^{L}\frac{n(n+1)(n+3)}{2n+1}\left(\frac{R}{R+D}\right)^{n+2}H_n^3(\Omega)\,. \quad (4.82)$$

The maximum degree L in the finite series in Eq. (4.82) depends on the width of the filter which was applied on measured aerial gravity data. For aerial gravity data of Taiwan, the degree $L = 3000$ was chosen, see Sec. 4.1. Unfortunately, the Laplace harmonics of the squared and cubed topographical height function H_n^2 and H_n^3, respectively, are available only to the degree $n = 2160$, which corresponds to the maximum degree and order of EGM08. Thus, the maximum degree is $L = 2160$. The minimum degree l corresponds to the maximum degree and order of GGM used for the evaluation of the low-frequency part of the gravity disturbances δg_{GGM}, see Sec. 4.2.

4.5.2 Indirect topographical effect on potential

The change in the disturbing gravity potential due to the Helmert reduction of the Earth's gravity field is the indirect topographical effect (ITE) on the potential called the Helmert residual potential δV. Using the Bruns formula, see Eq. (4.74), ITE on the geoid P can be derived. Since a truncated series was used in an evaluation of V^t and δV, respectively, the following formulas for ITE are approximate, similar to the case of DTE.

Analogous to DTE, ITE can be derived in the integral form (Novák et al. 2003a)

$$\begin{aligned} \delta V(R,\Omega) &\approx GR^2\rho \iint\limits_{\Omega_S} \left[\left(\frac{H(\Omega')}{R} \right)^2 \mathcal{M}_1(\psi) + \right. \\ &\quad \left. + \left(\frac{H(\Omega')}{R} \right)^3 \mathcal{M}_2(\psi) \right] \mathrm{d}\Omega' , \end{aligned} \tag{4.83}$$

or alternatively as the infinite series

$$\begin{aligned} \delta V(R,\Omega) &\approx -2\pi G\rho \sum_{n=0}^{\infty} \frac{n+1}{2n+1} H_n^2(\Omega) + \\ &\quad + \frac{2}{3}\pi \frac{G\rho}{R} \sum_{n=0}^{\infty} \frac{(n+1)(n-2)}{2n+1} H_n^3(\Omega) . \end{aligned} \tag{4.84}$$

The integration kernels $\mathcal{M}_1$ and $\mathcal{M}_2$ in Eq. (4.83) are defined as follows:

$$\mathcal{M}_1(\psi) = -\sum_{n=0}^{\infty} \frac{n+1}{2} P_n(\cos\psi) , \tag{4.85}$$

$$\mathcal{M}_2(\psi) = -\sum_{n=0}^{\infty} \frac{(n+1)(n-2)}{6} P_n(\cos\psi) . \tag{4.86}$$

Laplace harmonics of the squared topographical height function H_n^2 and of the cubed topographical height function H_n^3 are defined by Eqs. (4.79) and (4.80).

Since we have the band-limited aerial gravity disturbances and band-limited DTE, also ITE should correspond to the same frequency band. As in the case of A_b, the band limitation is approximately achieved by integrating only over the limited spherical cap Ω_0 when using Eq. (4.83), which yields

$$\begin{aligned} \delta V_b(R,\Omega) &\approx GR^2\rho \iint_{\Omega_0} \left[\left(\frac{H(\Omega')}{R}\right)^2 \mathcal{M}_1(\psi) + \right. \\ &\quad \left. + \left(\frac{H(\Omega')}{R}\right)^3 \mathcal{M}_2(\psi) \right] \mathrm{d}\Omega' \,. \end{aligned} \tag{4.87}$$

The band-limited ITE δV_b can also be evaluated using the finite series (Novák et al. 2003a):

$$\begin{aligned} \delta V_b(R,\Omega) &\approx -2\pi G\rho \sum_{n=l}^{L} \frac{n+1}{2n+1} H_n^2(\Omega) + \\ &\quad + \frac{2}{3}\pi \frac{G\rho}{R} \sum_{n=l}^{L} \frac{(n+1)(n-2)}{2n+1} H_n^3(\Omega) \,, \end{aligned} \tag{4.88}$$

where the maximum degree $L = 2160$ and the minimum degree l corresponds to the maximum degree and order of the used GGM, see Sec. 4.2. In order to get ITE corresponding to the geoidal height, Eqs. (4.87) and (4.88) have to be divided by normal gravity γ at the reference ellipsoid, which yields the integral form (Novák et al. 2003a)

$$\begin{aligned} P_b(\Omega) &\approx \frac{GR^2\rho}{\gamma} \iint_{\Omega_0} \left[\left(\frac{H(\Omega')}{R}\right)^2 \mathcal{M}_1(\psi) + \right. \\ &\quad \left. + \left(\frac{H(\Omega')}{R}\right)^3 \mathcal{M}_2(\psi) \right] \mathrm{d}\Omega' \,, \end{aligned} \tag{4.89}$$

and for the computation by the finite series

$$\begin{aligned} P_b(\Omega) &\approx -2\pi \frac{G\rho}{\gamma} \sum_{n=l}^{L} \frac{n+1}{2n+1} H_n^2(\Omega) + \\ &\quad + \frac{2}{3}\pi \frac{G\rho}{R} \sum_{n=l}^{L} \frac{(n+1)(n-2)}{2n+1} H_n^3(\Omega) \,. \end{aligned} \tag{4.90}$$

Chapter 5

Testing numerical methods using synthetic gravity data

There are three different numerical methods used in the thesis: Newton-Cotes formulas for numerical integration (NC), wavelet transform (WT) and the Taylor series (Linear – LTS and Quadratic – QTS).

The analytic continuation by LTS is tested on the set of $49,327$ synthetic gravity disturbances computed from EGM08 to the degree and order $n = m = 2160$ within the area limited by the parallels of 23° and 24° northern latitude, and by the meridians of 120° and 122° eastern longitude. In every point, two gravity disturbances are computed from EGM08 in two different heights (corresponding to radius r and $R + D$ of the reference sphere, see Eq. (4.68)), with the height difference reaching 150 m in maximum. The gravity disturbances corresponding to radius r are subsequently continued to radius $R + D$. We compare differences between the continued values and the synthetic gravity disturbances from EGM08 corresponding to radius $R+D$. The error is below 0.002 mGal in the standard deviation and below 0.014 mGal in the maximum value. When using the gravity data corrupted by the random noise $\epsilon = 3$ mGal, the error increases to the level of the noise, i.e., the standard deviation of the differences is 3 mGal.

Using QTS, see Eq. (4.69), the analytic continuation from the altitude $D = 5156$ m down to the reference sphere (i.e., $D = 0$ m) is tested on the set of $1,788$ synthetic gravity disturbances computed from EGM08 to the degree and order $n = m = 2160$ within the

area limited by the parallels of 24° and 24.25° northern latitude, and by the meridians of 121.25° and 121.5° eastern longitude, which includes the mountainous part of Taiwan. The error is below 0.1 mGal in the standard deviation. When using the gravity data corrupted by the random noise $\epsilon = 3$ mGal, the error increases significantly to 9 mGal in the standard deviation.

In order to test an accuracy and an efficiency of NC and WT in the "one-step approach", the EGM08 was used for computation of the band-limited gravity disturbances δg_b^H at the constant flight level D (Heiskanen and Moritz 1967, p. 88)

$$\delta g_{EGM08}(R+D,\Omega) = \frac{GM}{R^2}\sum_{n=l}^{L}(n+1)\left(\frac{R}{R+D}\right)^{n+2} T_n(\Omega)\,. \tag{5.1}$$

The test area is limited by two parallels of 22° and 25° northern latitude, and by two meridians of 119° and 123° eastern longitude. This area corresponds to $6,912$ data points spaced by $2.5'$ in latitude and longitude. The flight altitude $D = 5$ km is used. Since the minimum degree in Eq. (4.4) is $l = 181$, the corresponding integration radius used in the integration, see Eq. (4.5), is $\psi = 1^\circ$. Thus, the computation area is bounded by latitude of 23° and 24° and by longitude of 120° and 122° in order to avoid any edge effects in the results. This corresponds to $1,152$ computation points spaced by $2.5'$ in latitude and longitude. Since in the case of real aerial gravity data in Taiwan scattered GNSS/levelling points are used for comparison of the computed geoid rather than an equiangular grid, an interpolation step is added to the test. In the area bounded by latitude of 23° and 24° and by longitude of 120° and 122°, 737 points are chosen.

Two numerical tests are performed: without any noise ϵ, i.e., $\epsilon(R+D) = 0$ mGal; with the random noise $\epsilon(R+D) = 3$ mGal, see the scheme shown in Fig. 5.1. The random noise $\epsilon(R+D)$ added to the values of gravity disturbances δg_{EGM08} at the flight level is shown in Fig. 5.2. By comparing the results with the reference band-limited disturbing gravity potential T_{EGM08} at the mean sea level generated directly from EGM08

$$T_{EGM08}(R,\Omega) = \frac{GM}{R}\sum_{n=l}^{L} T_n(\Omega)\,, \tag{5.2}$$

we obtain the noise $\epsilon^T(R,\Omega)$ propagated via the integral formula in Eq. (4.3)

$$\epsilon^T(R,\Omega) = T_{EGM08}(R,\Omega) - T^\epsilon(R,\Omega)\,. \tag{5.3}$$

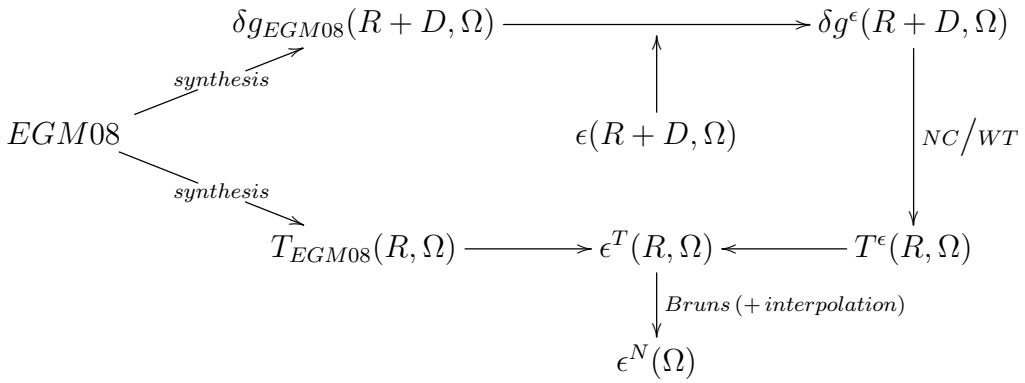

Figure 5.1: Scheme of testing using synthetic gravity

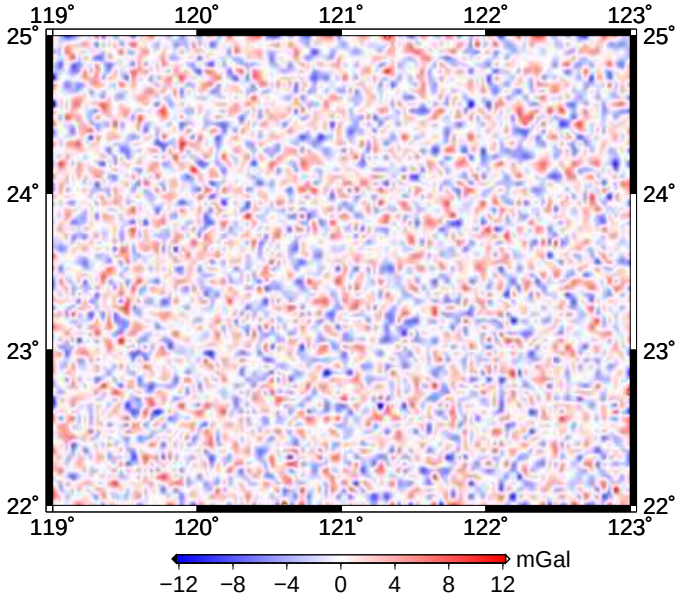

Figure 5.2: Random noise ϵ of 3 mGal added to the synthetic aerial gravity data (mGal)

The differences are converted into the effect on the geoid using the Bruns formula in the spherical approximation (Bruns 1878; Heiskanen and Moritz 1967, p. 85)

$$\epsilon^{N}(\Omega) = \frac{\epsilon^{T}(R,\Omega)}{\gamma(\theta)}\,, \tag{5.4}$$

where γ is normal gravity at the reference ellipsoid. Values of the disturbing gravity potential T obtained using NC are computed at scattered points directly. In the case of WT, values of T can be computed only in a form of an equiangular grid; they are

interpolated into scattered points if needed. For the interpolation, the Generic Mapping Tools[1] (GMT) are used. Tables 5.2 and 5.3 show results for NC and WT, respectively. Corresponding histograms are shown in Figs. D.1 to D.4, see Appendix D. Values of the synthetic disturbing gravity potential T are described in Tab. 5.1.

Although WT is in general an efficient tool for problems related to the signal processing, for the computation of an integral without any singularity it seems to lose the efficiency. Comparing with the numerical integration by NC, WT gives less accurate results. Standard deviations of the geoid noise ϵ^N are at the same level (for high degrees l) or worse (for low degrees l) than in the case of NC. Moreover, WT is a more time consuming method because for evaluation of a value at one point every points in the input grid are needed. Almost all computing time, more than 98%, is needed for the evaluation of the integral kernel. Thus, for WT, a computation takes approximately seventeen times more time than for NC.

	Mean	StDev	Min	Max	Range
$l = 181, L = 2160$	-0.440	$\pm$ 1.280	-1.947	3.108	5.054
$l = 361, L = 2160$	-0.081	$\pm$ 0.350	-1.018	0.922	1.940
$l = 721, L = 2160$	-0.002	$\pm$ 0.080	-0.253	0.190	0.444
$l = 1081, L = 2160$	0.009	$\pm$ 0.038	-0.112	0.162	0.274
$l = 1441, L = 2160$	0.003	$\pm$ 0.024	-0.082	0.095	0.178
$l = 1801, L = 2160$	0.002	$\pm$ 0.014	-0.042	0.044	0.087

Table 5.1: Synthetic geoidal heights N from EGM08 (m)

[1]Generic Mapping Tools (GMT) - an open source collection of tools for manipulating geographic and Cartesian data sets (including filtering, trend fitting, gridding, projecting, etc). It is released under the GNU Lesser General Public License. Source: http://gmt.soest.hawaii.edu/.

	Mean	StDev	Min	Max	Range
Error of integration ($\epsilon = 0$ mGal)					
$l = 181, L = 2160$	-0.001	$\pm$ 0.003	-0.012	0.011	0.024
$l = 361, L = 2160$	0.000	$\pm$ 0.004	-0.019	0.014	0.033
$l = 721, L = 2160$	0.000	$\pm$ 0.001	-0.003	0.002	0.005
$l = 1081, L = 2160$	0.000	$\pm$ 0.002	-0.007	0.014	0.021
$l = 1441, L = 2160$	0.000	$\pm$ 0.002	-0.010	0.018	0.028
$l = 1801, L = 2160$	0.000	$\pm$ 0.001	-0.003	0.002	0.005
Error of integration and noise propagation ($\epsilon = 3$ mGal)					
$l = 181, L = 2160$	-0.001	$\pm$ 0.020	-0.067	0.064	0.130
$l = 361, L = 2160$	0.001	$\pm$ 0.020	-0.060	0.057	0.117
$l = 721, L = 2160$	0.001	$\pm$ 0.017	-0.041	0.045	0.085
$l = 1081, L = 2160$	0.002	$\pm$ 0.015	-0.037	0.046	0.083
$l = 1441, L = 2160$	0.001	$\pm$ 0.011	-0.026	0.038	0.064
$l = 1801, L = 2160$	0.000	$\pm$ 0.005	-0.014	0.019	0.033

Table 5.2: Geoid noise ϵ^N for NC (m)

	Mean	StDev	Min	Max	Range
Error of WT ($\epsilon = 0$ mGal)					
$l = 181, L = 2160$	0.039	$\pm$ 0.094	-0.162	0.197	0.359
$l = 361, L = 2160$	-0.009	$\pm$ 0.028	-0.069	0.055	0.124
$l = 721, L = 2160$	-0.001	$\pm$ 0.006	-0.020	0.013	0.033
$l = 1081, L = 2160$	0.000	$\pm$ 0.003	-0.009	0.008	0.017
$l = 1441, L = 2160$	0.000	$\pm$ 0.002	-0.005	0.007	0.012
$l = 1801, L = 2160$	0.000	$\pm$ 0.001	-0.004	0.004	0.008
Error of WT and noise propagation ($\epsilon = 3$ mGal)					
$l = 181, L = 2160$	0.041	$\pm$ 0.098	-0.196	0.237	0.433
$l = 361, L = 2160$	-0.009	$\pm$ 0.032	-0.093	0.076	0.169
$l = 721, L = 2160$	0.001	$\pm$ 0.017	-0.044	0.051	0.095
$l = 1081, L = 2160$	0.001	$\pm$ 0.016	-0.041	0.046	0.088
$l = 1441, L = 2160$	0.001	$\pm$ 0.015	-0.038	0.049	0.087
$l = 1801, L = 2160$	0.001	$\pm$ 0.012	-0.036	0.039	0.075

Table 5.3: Geoid noise ϵ^N for WT (m)

Chapter 6

Application to aerial data of Taiwan – numerical results

In this chapter, numerical results of each computation step discussed in Sec. 2 are presented. The processed data originate from the aerial gravity surveys performed over the period of May 2004 to May 2005 (central area, flight altitude $H_1 = 5156$ m), of March 2006 to August 2008 (eastern area, flight altitude $H_2 = 1620$ m) and from 2008 to 2009 (western area, flight altitude $H_2 = 1620$ m), see Sec. 3. The position of the provided aerial gravity data was determined by the geodetic latitude φ and longitude λ, see Appendix B.3, and the orthometric height H. Since the geodetic coordinates are required for gravity disturbances, the orthometric height H was transformed into the geodetic height h first:

$$h(\varphi, \lambda) = H(\varphi, \lambda) + N(\varphi, \lambda)\,. \tag{6.1}$$

Geoidal height N was provided with the aerial gravity data at each point of the central area. For the western and eastern area, the values of N were computed by using EGM08. As a next step, the geodetic coordinates were transformed into the spherical coordinates (r, θ, λ), see Appendices B.2 and B.3. Since there is an assumption of the constant flight level for the input aerial gravity data, see Sec. 4.1, that is not satisfied in the spherical coordinates any more, the continuation of the aerial gravity disturbances $\delta g(r, \theta, \lambda) = (r, \Omega)$ to the mean observation height D in the spherical coordinates, i.e., to the geocentric sphere of radius $R + D =$ const., has to be done. The constant geocentric radius $R + D$

is determined as the average geocentric radius of all points, i.e., $R + D = \sum_{i=1}^{M} r_i/M$, where M is the number of all points in the data set. The differences in altitude reach 150 m in maximum. Thus, the transformation of the gravity disturbances $\delta g(r, \Omega)$ at different heights above the geocentric sphere R to the gravity disturbances $\delta g(R + D, \Omega)$ at the constant height D is done using LTS.

The gravity data are then processed by "remove-compute-restore" procedure (e.g., Rapp and Rummel 1975; Schwarz, Sideris and Forsberg 1990) shown in Fig. 6.1 and described in the following sections.

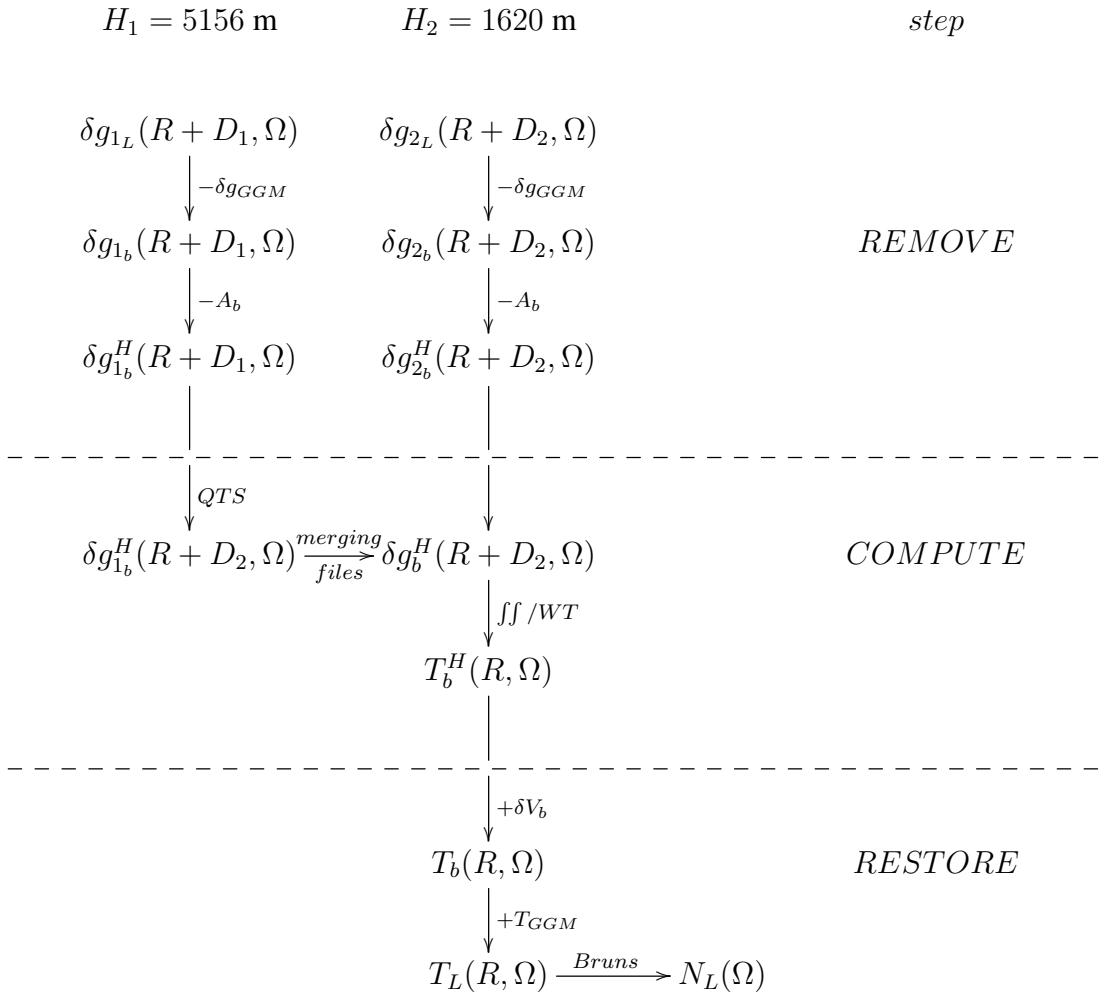

Figure 6.1: Diagram of the evaluation of geoidal heights from aerial gravity disturbances

6.1 Remove step

Since input aerial gravity data have to be band-limited and harmonic outside the geoid represented by the geocentric sphere of radius R, see the assumptions of the Neumann BVP of Eqs. (4.2), the following procedures must be performed:

- subtraction of the low-frequency part of the gravity disturbances δg_{GGM} ,
- subtraction of the band-limited DTE A_b .

Because of the time consuming numerical methods, only a small part of central Taiwan was chosen as a test area first, see Fig. 6.2. After that, all available aerial gravity disturbances were processed, see Figs. 3.1 and 3.2.

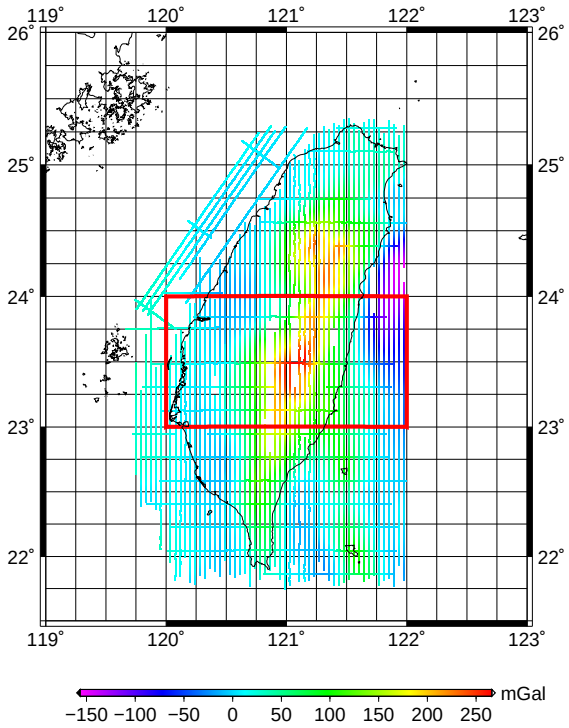

Figure 6.2: Aerial gravity data, $H_1 = 5156$ m (192,336 points) – test area (49,327 points)

For the subtraction of the low-frequency part of the gravity disturbances δg_{GGM}, two GGMs available to different degrees and orders are used, see Sec. 1.4.2: the global grav-

itational model 2008 (EGM08, Pavlis et al. 2008) and the combined satellite-only model GOCO03s (Mayer-Gürr et al. 2012). EGM08 was chosen as GGM with the highest maximum degree and order (up to $n = m = 2160$), GOCO03s was chosen as a representant of the latest satellite-only GGMs based on data of gravity-dedicated satellite missions. Four different maximum orders and degrees of these GGMs are chosen: $n = m = 200$ represents approximately a satellite-only low-frequency part, $n = m = 2160$ is the maximum available degree and order of GGM, $n = m = 360$ and $n = m = 1080$ represent degrees and orders between 200 and 2160.

The low-frequency gravity disturbances δg_{GGM} to the degree and order $n = m = 200$ (GOCO03s, EGM08), $n = m = 360$ (EGM08), $n = m = 1080$ (EGM08), $n = m = 2160$ (EGM08) and corresponding band-limited gravity disturbances δg_b are shown in Appendix E.1 on Figs. E.1 to E.5 (test area) and in Appendix E.2 on Figs. E.6 to E.15 (all available aerial gravity data). For every degree and order of EGM08/GOCO03s, the band-limited DTE A_b and corresponding Helmert's residual gravity disturbances δg_b^H are also shown there. The statistics of the remove step for the test area and all available gravity data are described in Tabs. 6.1 and 6.2. In Tabs. E.1, E.2 and E.3, see Appendix E.2, are the statistics for the central, western and eastern areas.

The band-limited DTE is evaluated using Eqs. (4.81) and (4.82) for the aerial gravity data within the test area, see Tab. 6.1. The frequency band of DTE depends on the radius of integration (I) when using Eq. (4.81), see Sec. 4.2, and on the minimum and maximum degree l and L, respectively, for the finite series (FS) in Eq. (4.82). The minimum degree l corresponds to the maximum degree and order of GGM used for the evaluation of the low-frequency part of the gravity disturbances δg_{GGM}.

The resolution of the digital elevation model (DEM) in case of our aerial gravity data has almost no influence on numerical values of DTE. Three DEMs with the different equiangular resolutions $(10'', 30''$ and $60'')$ derived from the local DEM of Taiwan of the resolution $3''$ were used for comparison. The difference in the standard deviation was on the level of the hundredths of mGal.

For all available aerial gravity data, see Tab. 6.2, the evaluation of DTE by the integration is used. Comparing with FS, the using of the integration leads to a bit smoother Helmert's residual gravity disturbances δg_b^H. The computation by FS takes the same time

	Mean	StDev	Min	Max	Range
aerial gravity disturbances	53.7	± *86.9*	-138.5	266.6	405.1
GOCO03s to $n = m = 200$:					
δg_{GGM}	58.4	± 36.4	-34.5	107.8	142.2
δg_b	-4.7	± 60.2	-129.1	161.9	291.1
A_b (I)	-0.6	± 5.7	-35.6	7.2	42.8
A_b (FS)	0.4	± 6.3	-33.5	13.0	46.5
δg_b^H (I)	-5.2	± 56.5	-128.2	144.2	272.4
δg_b^H (FS)	-4.3	± 56.7	-127.8	138.3	266.1
EGM08 to $n = m = 200$:					
δg_{GGM}	56.3	± 35.9	-35.3	105.8	141.0
δg_b	-2.6	± 60.0	-127.6	164.4	292.0
A_b (I)	-0.6	± 5.7	-35.6	7.2	42.8
A_b (FS)	0.4	± 6.3	-33.5	13.0	46.5
δg_b^H (I)	-3.2	± 56.3	-126.7	146.6	273.3
δg_b^H (FS)	-2.3	± 56.5	-126.3	140.7	267.0
EGM08 to $n = m = 360$:					
δg_{GGM}	51.8	± 75.1	-130.4	183.6	314.0
δg_b	1.9	± 27.9	-67.3	97.9	165.2
A_b (I)	-1.3	± 5.7	-36.1	6.6	42.7
A_b (FS)	0.0	± 5.8	-30.3	15.9	46.2
δg_b^H (I)	0.6	± 23.9	-64.0	78.7	142.8
δg_b^H (FS)	1.9	± 24.3	-60.0	80.8	140.8
EGM08 to $n = m = 1080$:					
δg_{GGM}	50.4	± 82.2	-137.3	243.6	380.9
δg_b	3.2	± 9.5	-28.6	53.9	82.5
A_b (I)	-3.1	± 6.9	-41.0	2.0	43.0
A_b (FS)	0.0	± 3.4	-18.4	20.5	38.8
δg_b^H (I)	0.2	± 7.2	-31.7	35.6	67.3
δg_b^H (FS)	3.2	± 8.0	-13.9	49.9	63.7

	Mean	StDev	Min	Max	Range
EGM08 to $n = m = 2160$:					
δg_{GGM}	50.4	$\pm$ 82.5	-135.1	252.5	387.7
δg_b	3.3	$\pm$ *6.9*	-13.9	43.0	56.9
A_b (I)	-4.7	$\pm$ 9.1	-48.5	0.5	49.0
A_b (FS)	–	–	–	–	–
δg_b^H (I)	-1.4	$\pm$ 7.3	-43.9	18.4	62.3
δg_b^H (FS)	–	–	–	–	–

Table 6.1: Statistics of aerial gravity data in the "remove" step – test area (mGal)

for all values of l which is comparable with the time needed for the computation by the integration for $\psi_{max} = 30'$ (time requirements were tested for DEM of the equiangular resolution $60''$). For the larger (smaller) radius of integration $\psi_{max} > 30'$ ($\psi_{max} < 30'$) the time needed for the computation increases (decreases) exponentially.

Tables 6.1 and 6.2 show a high accuracy of EGM08 in the area of Taiwan. Removing the low-frequency part δg_{GGM} from the aerial gravity disturbances δg_L yields much smoother band-limited gravity disturbances δg_b. For the maximum degree and order of EGM08 $n = m = 2160$, the standard deviations of δg_b are 6.9 and 5.4 mGal within the test area and for all available data, respectively, while the standard deviations of δg_L are 86.9 and 66.4 mGal, respectively. The Helmert residual gravity disturbances δg_b^H, obtained by removing the corresponding band-limited DTE, were expected to be even smoother than δg_b. Although this expectation was proved for all degrees and orders of GGMs except for $n = m = 2160$, differences between the standard deviations of δg_b and δg_b^H are on the level of only few mGal. These conclusions are valid for both I and FS.

6.2 Computation step

After the "remove step" we have two sets of gravity data, gravity disturbances δg_b^H at the constant heights D_1 (central area) and D_2 (western and eastern areas), respectively, above the reference sphere R. Since all aerial gravity data are required to be at the same level (choice is the lower height D_2 in order not to lose high frequencies by upward

	Mean	StDev	Min	Max	Range
aerial gravity disturbances	33.8	± *66.4*	-207.1	266.2	473.3
GOCO03s to $n = m = 200$:					
δg_{GGM}	35.3	± 35.4	-131.0	107.8	238.8
δg_b	-1.5	± 48.2	-185.8	173.5	359.3
A_b	-0.2	± 4.1	-33.4	8.8	42.3
δg_b^H	-2.2	± 46.5	-185.2	148.8	334.0
EGM08 to $n = m = 200$:					
δg_{GGM}	34.5	± 34.9	-129.2	105.8	234.9
δg_b	-0.7	± 48.0	-184.8	174.2	359.0
A_b	-0.2	± 4.1	-33.4	8.8	42.3
δg_b^H	-1.5	± 46.3	-184.2	150.8	335.0
EGM08 to $n = m = 360$:					
δg_{GGM}	31.3	± 56.0	-168.4	183.5	351.9
δg_b	2.4	± 26.3	-110.8	139.5	250.4
A_b	-0.7	± 3.9	-33.9	8.3	42.2
δg_b^H	1.7	± 24.4	-111.9	139.0	250.9
EGM08 to $n = m = 1080$:					
δg_{GGM}	31.2	± 63.7	-209.0	243.0	452.0
δg_b	2.5	± 7.0	-32.0	65.1	97.1
A_b	-1.6	± 4.9	-39.6	3.2	42.8
δg_b^H	1.0	± 6.2	-32.0	64.7	96.7
EGM08 to $n = m = 2160$:					
δg_{GGM}	31.3	± 64.0	-203.8	251.9	455.7
δg_b	2.5	± *5.4*	-27.2	55.2	82.4
A_b	-2.4	± 6.5	-46.2	0.7	46.9
δg_b^H	0.1	± 6.8	-45.4	54.7	100.1

Table 6.2: Statistics of aerial gravity data in the "remove" step – all available gravity data (mGal)

continuation of the gravity data), gravity disturbances within the central area have to be continued to this flight level. For a downward continuation, the QTS is used.

After the downward continuation of the band-limited Helmert gravity disturbances δg_b^H within the central area to the sphere of radius $R + D_2$ all gravity data are interpolated by GMT into the equiangular spherical coordinate grid. Two different angular resolutions of the grid are tested within the test area, $\Delta\theta = \Delta\lambda = 1'$ and $\Delta\theta = \Delta\lambda = 2.5'$. Since both grids yield comparable results, the coarser one is used because of faster integration. The error caused by the interpolation is below 0.01 mGal in the standard deviation, tested for the synthetic gravity disturbances computed from EGM08 to the degree and order $n = m = 2160$ within the area limited by the parallels of 22° and 25° northern latitude, and by the meridians of 119° and 123° eastern longitude. The test gravity disturbances were interpolated from the equiangular grid with the angular resolution $\Delta\theta = \Delta\lambda = 1'$ to the resolution of $2.5'$.

In the "one-step approach" (see Novák and Heck 2002) integral transformation of the gravity disturbances δg_b^H at the constant height D above the geocentric sphere of radius R to the disturbing gravity potential δT_b^H is performed by the integral in Eq. (4.5). This integral is computed using two methods, the Newton-Cotes formulas for numerical integration (see Sec. 4.2) and the wavelet transform (see Sec. 4.3). Since the integral in Eq. (4.5) is derived as the solution of the Neumann BVP, results related to the "one-step approach" are denoted in the following text as N-NC for the Newton-Cotes formulas and N-WT for the wavelet transform.

In the two-step approach the gravity disturbances at the constant height D_2 above the reference sphere of radius R are extended using QTS down to this sphere, i.e., to the constant height $D = 0$ m. For transformation of the gravity disturbances δg_b^H to the disturbing gravity potential δT_b^H, both on the geocentric sphere of radius R, the Hotine formula (Hotine 1969; Hofmann-Wellenhof and Moritz 2005, p. 115) evaluated by NC is used. Since the two-step approach consists of the analytic continuation (first step) and an evaluation of the Hotine formula (second step), results related to this approach are denoted as AC+H.

6.3 Restore step

As the last step of the evaluation scheme, the low-frequency disturbing gravity potential T_{GGM} and the corresponding ITE δV_b were added to the band-limited Helmert disturbing gravity potential T_b^H. Applying spherical Bruns's formula in Eq. (1.46) yields the final geoid

$$\begin{aligned} N(\Omega) &= \frac{T_b^H(R,\Omega)}{\gamma(\theta)} + \frac{T_{GGM}(R,\Omega)}{\gamma(\theta)} + \frac{\delta V_b(R,\Omega)}{\gamma(\theta)} = \\ &= N_b^H(\Omega) + N_{GGM}(\Omega) + P_b(\Omega)\,. \end{aligned} \tag{6.2}$$

Figures E.16 to E.29 in Appendix E.3 show Helmert's residual geoid N_b^H, its corresponding low-frequency part N_{GGM}, band-limited ITE P_b and the final geoid N for the test area, corresponding statistics are described in Tabs. E.4 (N-NC) and E.5 (N-WT, AC+H). Figures E.30 to E.39 in Appendix E.4 show the same for all available gravity data, corresponding statistics are in Tab. E.6. The GNSS/levelling points are shown as red dots.

6.4 Comparison with GNSS/levelling points

In order to verify the external accuracy of the geoidal heights obtained through the process described above, we used a set of GNSS/levelling points as a reference. At these points, ellipsoidal heights h with the centimetre-level accuracy were determined by GNSS with 24-hour observations and orthometric heights H_O at the millimetre-level accuracy (Hwang et al. 2007) were obtained by precise levelling requiring the double-run closure of $2.5\sqrt{k}$ [mm] (k is the distance in km between two adjacent points). Subtracting these two heights gives the reference geoidal height at the corresponding point

$$N_{GNSS/lev}(\Omega) = h(\Omega) - H_O(\Omega)\,. \tag{6.3}$$

In the area of interest 737 GNSS/levelling points are available, see Fig. 6.3. These points are located mostly along routes within coastal lowlands. Since GNSS/levelling points are taken as the reference geoidal heights, it decreases our ability to determine the precision of the geoid within the area of high mountains. First, the geoidal heights at the

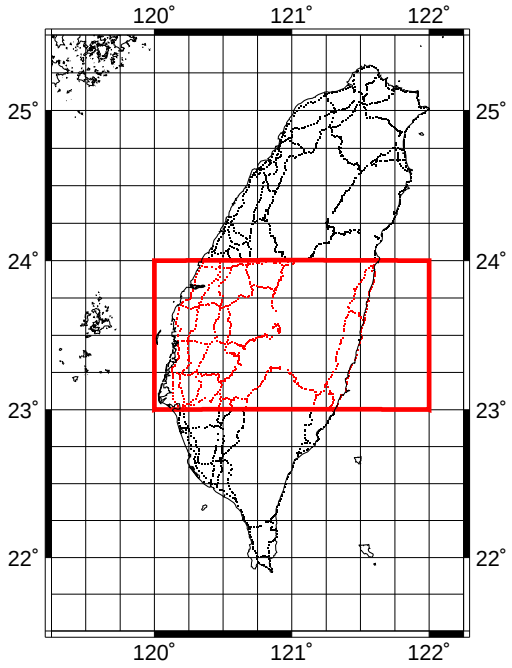

Figure 6.3: Distribution of GNSS/levelling points in Taiwan

GNSS/levelling points were evaluated just using EGM08/GOCO03s to the degrees and orders $n = m = 200$, $n = m = 360$, $n = m = 1080$ and $n = m = 2160$. As a next step, the geoidal heights at the GNSS/levelling points were determined using EGM08/GOCO03s for the low-frequency part and aerial gravity data for the high-frequency part. Tables 6.3 (test area) and 6.4 (all available gravity data) show differences between the computed geoidal heights and the reference geoid $N_{GNSS/lev}$. Corresponding histograms of the differences are in Figs. E.40 to E.49 in Appendices E.5, E.6.

In Tab. 6.3, each combination of EGM08/GOCO03s and the aerial gravity data corresponds to five rows. The first three rows refer to the models created by N-NC. The first row refers to the model where ITE is not taken into account because of its small contribution to the geoid. The second and third rows correspond to the models with the topographical effects determined by the integration and by the finite series, respectively. Since the integration turned out to be less time consuming computation with the same or higher accuracy than the accuracy of the finite series, we use only the integration for the model computed using N-WT (fourth row) and AC+H (fifth row).

In Tab. 6.4, the first row refers to the models created by N-NC, the second row by N-WT and the third row by AC+H. In all cases, the topographical effects are determined by the integration.

In Tab. 6.5, the differences between the GNSS/levelling and the geoidal heights evaluated just using GGMs are shown. Their corresponding histograms are in Fig. E.50 in Appendix E.7. For the evaluation of the geoidal heights from GGMs the harmonic synthesis, see Eq. (1.62), is used in the first five rows. The last row corresponds the geoidal heights from EGM08 to $n = m = 2160$ computed by a software distributed with EGM08 ("hsynth_WGS84.exe"[1]).

6.5 Accuracy of numerical results

The accuracy of the gravity field represented by EGM08 is high in the area of Taiwan, see Tab. 6.5. We assume it is because the available gravity data of Taiwan are included in EGM08. The precision of the local geoid model evaluated just using EGM08 to the degree and order $n = m = 2160$ is comparable with the most models obtained by combination of GGM and the local aerial gravity data, see Tabs. 6.3, 6.4 and 6.5. Only a few combined local geoid models of Taiwan show the higher accuracy. Moreover, the improvement is only at the level of millimetres, 13 mm at maximum for all available aerial gravity data.

For the aerial gravity data within the test area processed by N-NC, see Tab. 6.3, different approaches of computing the topographical effects (DTE and ITE) were used: ITE was not taken into account, DTE and ITE were determined by the integration and by the finite series. As we can see from Tab. 6.3, ITE cannot be neglected, although it is relatively small, at the level of centimetres. A comparison of the models with the topographical effects evaluated by the integration and by the finite series shows the higher accuracy for the integration in all cases, except for the minimum degree and order of GGMs $n = m = 200$. When using all aerial gravity data of Taiwan, the integration is used for the computation of DTE and ITE.

[1] Windows XP executable version of EGM2008 Harmonic Synthesis Program, hsynth_WGS84.exe, is the FORTRAN program for generation WGS 84 geoid undulations by spherical harmonic synthesis of EGM2008. Source: http://earth-info.nga.mil/GandG/wgs84/gravitymod/egm2008/egm08_wgs84.html.

Aerial gravity data were processed by the two approaches with the use of different numerical methods: “one-step approach” with both NC (N-NC) and WT (N-WT) and two-step approach (AC+H). A comparison of all methods from Tabs. 6.3 and 6.4 yields quite different conclusions. Whereas the differences from the test area, see Tab. 6.3, indicate AC+H as the most precise method, Tab. 6.4 describing the differences for all aerial gravity data shows N-NC as the best method. Since for the evaluation of the local geoid models in Tab. 6.4 all available aerial gravity data were used, i.e., approximately four times more aerial gravity disturbances than in the test area, we can assume that Tab. 6.4 is more consistent with the actual state. In both tables, the least accurate method is N-WT. This may be due to the fact that the contribution of the distant zone was not taken into account in the case of N-WT.

		Mean	StDev	Min	Max	Range
GGM + aerial data						
	1)	0.022	± 0.135	-0.379	0.492	0.871
GOCO03s to $n = m = 200$	2)	0.042	± 0.126	-0.295	0.509	0.805
	3)	-0.020	± 0.123	-0.401	0.431	0.833
	4)	0.120	± 0.129	-0.190	0.546	0.736
	5)	0.049	± 0.105	-0.186	0.368	0.554
	1)	0.137	± 0.116	-0.266	0.543	0.810
EGM08 to $n = m = 200$	2)	0.158	± 0.107	-0.124	0.561	0.685
	3)	0.096	± 0.101	-0.230	0.483	0.713
	4)	0.260	± 0.131	-0.052	0.626	0.678
	5)	0.190	± 0.082	-0.021	0.469	0.490
	1)	0.212	± 0.109	-0.284	0.494	0.778
EGM08 to $n = m = 360$	2)	0.240	± 0.095	-0.042	0.559	0.600
	3)	0.184	± 0.114	-0.218	0.477	0.696
	4)	0.219	± 0.088	-0.009	0.566	0.575
	5)	0.223	± 0.096	-0.069	0.504	0.573
	1)	0.247	± 0.126	-0.455	0.593	1.049
EGM08 to $n = m = 1080$	2)	0.270	± 0.103	-0.169	0.601	0.770
	3)	0.244	± 0.133	-0.464	0.604	1.068
	4)	0.258	± 0.104	-0.113	0.606	0.719
	5)	0.255	± 0.098	-0.094	0.557	0.652
	1)	0.236	± 0.118	-0.389	0.566	0.955
EGM08 to $n = m = 2160$	2)	0.255	± 0.093	-0.099	0.568	0.666
	3)	–	–	–	–	–
	4)	0.259	± 0.094	-0.100	0.566	0.666
	5)	0.256	± 0.093	-0.095	0.571	0.666

1) N-NC without ITE 2) N-NC with the topographical effects – I 3) N-NC with the topographical effects – FS
4) WT with the topographical effects – I 5) AC+H with the topographical effects – I

Table 6.3: Differences between the GNSS/levelling and the computed geoidal heights – test area (m)

		Mean	StDev	Min	Max	Range
GGM + aerial data						
GOCO03s to $n = m = 200$	1)	0.075	$\pm$ 0.109	-0.281	0.447	0.728
	2)	0.098	$\pm$ 0.138	-0.152	0.521	0.673
	3)	0.050	$\pm$ 0.121	-0.280	0.432	0.712
EGM08 to $n = m = 200$	1)	0.222	$\pm$ *0.083*	-0.063	0.530	0.594
	2)	0.248	$\pm$ 0.132	-0.036	0.615	0.651
	3)	0.198	$\pm$ 0.092	-0.073	0.524	0.597
EGM08 to $n = m = 360$	1)	0.239	$\pm$ 0.090	-0.059	0.527	0.586
	2)	0.217	$\pm$ 0.086	-0.019	0.466	0.485
	3)	0.225	$\pm$ 0.100	-0.081	0.479	0.559
EGM08 to $n = m = 1080$	1)	0.264	$\pm$ 0.095	-0.056	0.585	0.641
	2)	0.250	$\pm$ 0.105	-0.097	0.558	0.655
	3)	0.255	$\pm$ 0.101	-0.118	0.558	0.677
EGM08 to $n = m = 2160$	1)	0.256	$\pm$ 0.093	-0.096	0.571	0.667
	2)	0.256	$\pm$ 0.094	-0.092	0.577	0.669
	3)	0.256	$\pm$ 0.093	-0.096	0.571	0.667

1) N-NC 2) WT 3) AC+H

Table 6.4: Differences between the GNSS/levelling and the computed geoidal heights – all available gravity data (m)

	Mean	StDev	Min	Max	Range
GGM only					
GOCO03s to $n = m = 200$	-0.509	$\pm$1.183	-2.466	2.613	5.079
EGM08 to $n = m = 200$	-0.351	$\pm$1.149	-2.221	2.734	4.954
EGM08 to $n = m = 360$	0.032	$\pm$0.372	-1.115	0.794	1.908
EGM08 to $n = m = 1080$	0.223	$\pm$0.151	-0.325	0.590	0.915
EGM08 to $n = m = 2160$	0.237	$\pm$0.119	-0.396	0.570	0.966
EGM08 to $n = m = 2160$ (“hsynth_WGS84.exe”)	0.705	*$\pm$0.096*	0.466	1.035	0.569

Table 6.5: Differences between the GNSS/levelling and the computed geoidal heights – GGMs only (m)

Chapter 7

Conclusions and recommendations

The determination of the local geoid model from aerial gravity data in the area of Taiwan was discussed in the thesis. The process of the computation of the geoid model and the numerical results are summarized in Sec. 7.1. The last section 7.2 obtains the recommendations for the further research.

7.1 Conclusions

Taiwan is a small island (around 36 thousands km^2) located approximately within the area limited by the parallels of 22° and 25.25° northern latitude, and by the meridians of 120° and 122° eastern longitude. The determination of the local geoid model from aerial gravity data in Taiwan was the main goal of the thesis. The aerial gravity data available at two constant altitudes, $H_1 = 5156$ m and $H_2 = 1620$ m, were processed by the "remove-compute-restore" procedure. In the thesis, the spherical approximation of the geoid by the geocentric sphere of radius R was used. It was assumed that flight trajectories can be approximated by the geocentric sphere of radius $R + D$, i.e., in the geocentric spherical coordinates (r, θ, λ), the flight heights D_1 and D_2 above the sphere of radius R were constant.

The "remove" part included removing the low-frequency part of the gravity disturbances computed using GGMs, in particularly EGM08 and GOCO03s, and removing the corresponding gravitational effects of topography on the gravity disturbances (DTE). Dif-

ferent maximum degrees and orders of GGMs were used: $n = m = 200$, $n = m = 360$, $n = m = 1080$ and $n = m = 2160$.

The "compute" part consisted of the two steps: continuation of all gravity data down to the same flight height above the reference sphere and transformation of the band-limited gravity disturbances at the constant flight level to the band-limited disturbing gravity potential at the geoid (geocentric sphere). After the "remove" part, aerial gravity disturbances at the two constant heights D_1 (Taiwan Island Survey – "central area") and D_2 (Kuroshio Current Survey – "eastern area" and Taiwan Strait Survey – "western area") above the reference sphere R were available. Since all gravity data were required to be at the same level (choice was the lower height D_2 in order not to lose high frequencies by upward continuation of the gravity data), gravity disturbances within the central area were downward continued to this flight level using the quadratic part of the Taylor series.

The transformation of the band-limited gravity disturbances to the band-limited disturbing gravity potential was performed by the "one-step approach" (Novák and Heck 2002) and by the two-step approach. In the "one-step approach" the integral of the transformation was determined as a solution of the Neumann BVP. For the evaluation of the integral two numerical methods were used, Newton-Cotes formulas for numerical integration and a 4D wavelet transform (Keller and Hájková 2011). In the two-step approach, the gravity disturbances at the constant height D_2 above the reference sphere of radius R were downward continued using the quadratic part of the Taylor series down to this sphere, i.e., to the constant height $D = 0$ m. The transformation to the band-limited disturbing gravity potential on the geocentric sphere of radius R was performed using the Hotine formula (evaluated by Newton-Cotes formulas for a numerical integration).

In the "restore" step, the low-frequency part of the disturbing gravity potential and the corresponding ITE on the potential were restored to the band-limited disturbing gravity potential. The Bruns formula was applied on the resultant potential in order to get the geoidal heights. The accuracy of the computed local geoid models of Taiwan was verified using a set of GNSS/levelling points with the centimetre-level accuracy for ellipsoidal heights and the millimetre-level accuracy for orthometric heights.

The band-limited DTE and ITE were evaluated using the second Helmert method of gravity reduction. Two approaches were used for the evaluation of the topographical

effects: the integration and the finite series (Novák et al. 2003a).

7.1.1 Summary of results

The main goals of the thesis were as follows:

- to use different tools (numerical integration by Newton–Cotes formulas and wavelet transform for evaluation of the "one-step approach" and two-step approach) for estimation of the local geoid model of Taiwan from available aerial gravity data; numerical integration by Newton–Cotes formulas represents the standard numerical method, whereas *4D wavelet transform is the new method developed in Keller and Hájková (2011)*;
- to use different GGMs (EGM08 and GOCO03s) for evaluation of the low-frequency part of geoid;
- to validate or disprove the ability of the aerial gravity data to improve the local geoid model based on EGM08 in the area of Taiwan;
- to compare our conclusions with those based on results from other areas and with the previous local geoid model of Taiwan.

The comparison of the estimated local geoid models should focus on the following questions:

- accuracy estimation of the local geoid model by its comparing with GNSS/levelling points;
- time requirements of different numerical methods;
- hardware requirements (mostly the computer memory) of different numerical methods.

Except the main goals, three approaches for the computation of the band-limited topographical effects were tested for the aerial gravity data from the limited test area: the integration, the finite series and neglecting the ITE. A comparison of the results based on the evaluations in the thesis yields:

- the band-limited ITE cannot be neglected if the second Helmert method of gravity reduction is used;
- the time needed for computation by integration corresponds to the time of the finite series approximately for the radius of integration $\psi_{max} = 30'$ and for a greater (smaller) radius increases (decreases) exponentially; time requirements were tested for DEM of the equiangular resolution $60''$;
- except the minimum degree and order $n = m = 200$ of GGMs, the geoid models with the topographical effects computed by integration show the same or higher accuracy than in the case of the topographical effects computed by the finite series;
- both methods do not have any special hardware demands.

Considering both the precision of results and time requirements, the evaluation of the band-limited topographical effects by the integration seems to be better method for harmonization of aerial gravity data when the low-frequency part of aerial gravity data are computed from GGM to the degrees and orders higher than approximately $n = m = 360$. For lower degrees and orders of used GGM, the evaluation of the band-limited topographical effects by the finite series is more convenient.

Concerning the main goals, the local geoid models computed by the three methods (N-NC, N-WT, AC+H) were compared. First, the low-frequency part from GGMs was combined with the high-frequency part from the aerial gravity data only from the test area, then all available aerial gravity data were used. The results are as follows:

- accuracy of the local geoid model in comparing with GNSS/levelling points:
  - when using the aerial gravity data only from the test area, the most accurate method is AC+H; for all available gravity data, which should be more consistent with the actual state, N-NC is the most accurate method;
  - the less accurate results are obtained using N-WT;
- time demands of the numerical methods:
  - NC requires times at the level of seconds to minutes, depending on the radius of integration (from 1 sec for $\psi_{max} = 5'$ to almost 5 min for $\psi_{max} = 54'$);

  - WT is approximately seventeen times more time consuming method, more than 98% time is needed for the evaluation of the integration kernel; time consumption depends on a number of points in the input grid;
  - QTS is the most time consuming method; since the analytic continuation by the quadratic part of the Taylor series was performed at every point ($217,786$ points), for a computation of the first and second derivatives of the gravity disturbance nearly four weeks were needed;

- hardware demands of the numerical methods:
  - NC and the harmonic synthesis of the first and second derivatives of the gravity disturbance have no special hardware demands;
  - in the case of WT, memory demands depend on the number of points 2^N in the input grid; for the computation performed in the thesis ($2^N = 128$ was used for the degree and order $n = m = 200$ and $2^N = 64$ for all the other degrees and orders), at least 4 GB RAM (Random-Access Memory) were needed for $2^N = 64$ and 8 GB RAM for $2^N = 128$.

Based on the results described above, *the "one-step approach" computed using NC with the topographical effects evaluated by the integration* (for all available aerial gravity data) *is the optimal method providing the most accurate local geoid model of Taiwan*. The comparison of all computed geoid models at the GNSS/levelling points shows a very high accuracy of EGM08 in the area of Taiwan. Using the methods for the local geoid modelling from aerial gravity data in Taiwan, that are described in the thesis, yields the improvement of EGM08 just at the level of millimetres. For all available aerial gravity data *the best improvement is* 13 *mm for the combination of EGM08 to the degree and order* $n = m = 200$ *and the residual aerial gravity data*. Since the GNSS/levelling points are located mostly along routes within coastal lowlands, the very high accuracy of EGM08 relates rather to the lowlands than to the entire island. In the mountainous areas of Taiwan, the improvement of EGM08 could be more significant because the lack of available terrestrial gravity data in these areas.

The comparison of the local geoid models with the low-frequency part from EGM08 and GOCO03s to the degree and order $n = m = 200$ shows that for the chosen maxi-

mum degree and order EGM08 determines the global gravity field in the area of Taiwan better than GOCO03s. The low-frequency part of EGM08 is based on satellite-only ITG-GRACE03s (Mayer-Gürr 2007) complete to the degree and order $n = m = 180$ (Pavlis et al. 2012). Since we used the maximum degree and order $n = m = 200$, additional gravity data are contained in the corresponding part of EGM08, whereas GOCO03s is the satellite-only model[1]. It could caused the higher accuracy of EGM08.

In the thesis, the standard deviation of the optimal method ranges from 8.3 to 9.5 cm for different maximum degrees and orders of GGMs. Since aerial gravimetry is a standard method used in the local gravity field modelling, there are local geoid models from the other areas. Nevertheless, these models differ, e.g., in processing methods, an accuracy and amount of the available aerial gravity data or in the used GGM:

- the local geoid model of Taiwan determined in (Hwang et al. 2007) using aerial and terrestrial gravity data; a comparison with GNSS/levelling points along four first-order levelling routes gives the standard deviation ranging from 0.2 to 19.0 cm for different levelling routes;
- the local gravimetric geoid of South Korea determined in (Bae et al. 2012) using terrestrial, aerial, shipborne and altimetry-derived data; a comparison with GNSS/levelling points gives the standard deviation of 5.5 cm over the whole country;
- the hybrid local geoid model of Malaysia MyGEOID (Nordin et al. 2005) consists of two basic models, WMGEOID04 in Peninsular Malaysia and EMGEOID05 in Sabah and Sarawak; the geoid model is hybrid of gravimetric geoids computed using terrestrial and aerial data with GNSS ellipsoidal heights on levelled bench marks; accuracy of fitted geoid models of WMGeoid04 and EMGeoid05 is 3.3 and 4.2 cm, respectively;
- etc.

The local geoid models computed in the thesis show the lower accuracy than the other geoid models. Nevertheless, only aerial gravity data were used for the computation and

[1] In GOCO02s, GRACE contribution is dominant up to the degree and order $n = m = 120$, GOCE is dominant from $n = m = 140$ to 220 (Goiginger et al. 2011). It can be assumed that the contributions of these two gravity-dedicated satellite missions are similar for GOCO03s.

no fitting on GNSS/levelling heights was performed. It can be assumed that the use of the other local gravity data (terrestrial, marine, ...) and creating a hybrid geoid model could improve the accuracy.

7.2 Recommendations

Based on the results described above, a few recommendations can be formulated for further research. Recommended possibilities of improving the results were not included in the thesis mostly because of assumed significant extension of the thesis.

The one of the main goals of the thesis was to verify the suitability of the 4D wavelet transform for the computation of the non-inverse and non-singular integral. The wavelet transform was used without compression of the integral kernel and only one decomposition step was performed. Nevertheless, in our case, the number of decomposition steps does not influences the efficiency of the method. The greatest problem was related to the number of points in the input grid. The grid has to be a square with the number N of points in latitude/longitude corresponding to the power of 2, i.e., $N \in \{2, 4, 8, 16, 32, 64, \ldots\}$. Since in the case of aerial gravity data of Taiwan $N = 64$ and $N = 128$ were used, the integral kernel was computed for every pair of points in the grid with 64×64 and 128×128 points. Thus, the evaluation of the integral kernel took the 98% of the computing time. The evaluations were performed using the FORTRAN and Java codes. It could be interesting and helpful to adjust these codes in order to reduce the computing time.

As it has been already mentioned above, the improvement of the local geoid model could be achievement using the other local gravity data (terrestrial, marine, ...). A processing of the different type of gravity data and their combination is another suggestion for further research.

In the thesis, the second Helmert method of gravity reduction was used because of the small effect on the disturbing gravity potential on the geoid. Nevertheless, the direct topographical effect is small to be able to smooth enough the aerial gravity data before an interpolation. The using different methods of compensation could be more suitable, especially when terrestrial gravity data are used.

The last recommendation concerns used GGMs. For the evaluation of the low-fre-

quency part of the gravity data, two GGMs to the degree and order $n = m = 200$ were used, EGM08 and GOCO03s. The maximum order and degree was chosen in order to compare the low-frequency part computed before GOCE (EGM08 with GRACE satellite gravity data) with the low-frequency part computed using the GOCE satellite gravity data (GOCO03s). Despite the expectations, there was no improvement when using GOCO03s instead of EGM08. On the contrary, using of EGM08 provided more accurate results. It is possible that the choice of the lower maximum degree and order, e.g., $n = m = 180$, would lead to the better results for GOCO03s in comparison to EGM08.

Bibliography

ABRAMOWITZ, M.; STEGUN, I.A. (1972) *Handbook of mathematical functions with formulas, graphs and mathematical tables*. United States Department of Commerce, National Bureau of Standards, Applied Mathematics Series - 55.

ALBERTS, B.A. (2009) *Regional gravity field modelling from airborne gravimetry data*. Publications on Geodesy 70, Netherlands Geodetic Commission, Delft. 179 pp.

ANDERSEN, O.B.; KNUDSEN, P.; KENYON, S.; TRIMMER, R. (1999) Recent improvement in the KMS global marine gravity field. *Bollettino di Geofisica Teorica e Applicata*, 40(3-4): 369–377.

ANTONI, M.; KELLER, W.; WEIGELT, M. (2009) Representation of regional gravity fields by radial base functions. *Observation our Changing Earth. IAG Symposia*, 133: 293-299.

BAE, T.-S.; LEE, J.; KWON, J. H.; HONG, C.-K. (2012) Update of the precision geoid determination in Korea. *Geophysical Prospecting*, 60(3): 555–571.

BELL, R.E.; COAKLEY, B.J.; BLANKENSHIP, D.D,; HODGE, S.M.; BROZENA, J.M. (1992) Airborne gravimetry from a light aircraft. *From Mars to Greenland: Charting Gravity With Space and Airborne Instruments. IAG Symposia*, 110: 225-234.

BELL, R.E.; CHILDERS, V.A.; ARKO, R.A.; BLANKENSHIP, D.D,; BROZENA, J.M. (1999) Airborne gravity and precise positioning for geologic applications. *Journal of Geophysical Research*, 104(B7): 15281–15292.

BEYLKIN, A.; COIFMAN, R.; ROHLIN, V. (1991) Fast wavelet transforms and numerical algorithms I. *Communications on Pure and Applied Mathematics*, 44(2): 141–183.

BEYLKIN, A.; COIFMAN, R.; ROHLIN, V. (1992) *Wavelets in numerical analysis*. Wavelets and their applications. Jones and Bartlett, Boston, pp. 181–210.

BJERHAMMAR, A. (1963) A new theory of gravimetric geodesy. Report of the Royal Institute of Technology, Geodesy Division, Stockholm.

BROZENA, J.M. (1992). The Greenland Aerogeophysics Project – Airborne gravity, topographic and magnetic mapping of an entire continent. *From Mars to Greenland: Charting gravity with space and airborne instruments – Fields, tides, methods, results*: 203–214.

BROZENA, J.M.; MADER, G.L.; PETERS, M.F. (1989) Interferometric Global Positioning System: three-dimensional positioning source for airborne gravimetry. *Journal of Geophysical Research*, 94(B9): 12153-12162.

BROZENA, J.M.; PETERS, M.F. (1988) An airborne gravity study of eastern North Carolina. *Geophysics*, 53(2): 245-253.

BROZENA, J.M.; PETERS, M.F. (1994) Airborne gravity measurement at NRL. *Proceedings of the International Symposium on Kinematic Systems in Geodesy, Geomatics and Navigation (KIS94)*: 495–506. Banff, Canada.

BROZENA, J.M.; PETERS, M.F.; SALMAN, R. (1997) Arctic airborne gravity measurement program. *Gravity, Geoid and Marine Geodesy. IAG Symposia*, 117: 131-138. Springer-Verlag, Berlin, Heidelberg.

BRUNS, H. (1878) *Die Figur der Erde*. Stankiewicz, Berlin.

BRUTON, A.M. (2000) Improving the accuracy and resolution of SINS/DGPS airborne gravimetry. UCGE Report No. 20145, Department of Geomatics Engineering, The University of Calgary, Calgary, Canada.

CHANG, R.-G.; CHANG, C.-C.; LEE, J.-T. (1990) A gravimetric geoid in Taiwan area. *Sea Surface Topography and the Geoid. IAG Symposia*, 104: 61-72.

CHILDERS, V.A.; MCADOO, A.D.C.; BROZENA, J.M.; LAXON, S.W. (2001) New gravity data in the Arctic Ocean: Comparison of airborne and ERS gravity. *Journal of Geophysical Research: Solid Earth (1978–2012)*, 106(B5): 8871–8886.

CZOMPO, J. (1994) Airborne scalar gravimetry system errors in the spectral domain. UCGE Reports, 20067, 141 pp. Department of Geomatics Engineering, The University of Calgary, Calgary, Alberta, Canada.

DAUBECHIES, I. (1992) *Ten lectures on wavelets*. Philadelphia, Pennsylvania : Society for Industrial and Applied Mathematics (SIAM), volume 61 of CBMS-NSF Regional Conference Series in Applied Mathematics.

DRINKWATER, M.R.; FLOBERGHAGEN, R.; HAAGMANS, R.; MUZI, D.; POPESCU, A. (2003) GOCE: ESA's first Earth Explorer Core mission. *Earth Gravity Field from Space – from Sensors to Earth Sciences*. In the Space Sciences Series of ISSI, 18: 419-432.

EL-HABIBY, M. (2007) Wavelet representation of geodetic operators. UCGE Report No. 20250, Department of Geomatics Engineering, The University of Calgary, Calgary, Alberta, Canada.

ESA (1999) Gravity Field and Steady-State Ocean Circulation Mission. Reports for Mission Selection, SP-1233(1), ESA Publication Division, ESTEC, Noordwijk, The Netherlands.

FEI, Z.L.; SIDERIS, M.G. (2000) A new method for computing the ellipsoidal correction for Stokes's formula. *Journal of Geodesy*, 74: 223–231.

FEYNMAN, R.P. (1963) *The Feynman Lectures on Physics*. Massachusetts: Addison–Wesley, fifth printing, 1970.

FORSBERG, R. (1993) Impact of airborne gravimetry on geoid determination – the Greenland example. *International Geoid Service Bulletin*, 2: 32-43. Milano, Italy.

FORSBERG, R. (2002) Downward continuation of airborne gravity data. *Proceedings of the 3rd meeting of the International Gravity and Geoid Commission "Gravity and Geoid 2002"*, Thessaloniki, Greece.

FORSBERG, R.; HEHL, K.; BASTOS, L.; GIDSKEHAUG, A.; MEYER, U. (1997) Development of an airborne geoid mapping system for coastal oceanography (AGMASCO). *Gravity, Geoid and Marine Geodesy. IAG Symposia*, 117: 163–170.

FORSBERG, R.;, KELLER, K.; HVIDEGAARD, S.M.; OLESEN, A. (2003) ESAG-2002: European airborne gravity and lidar survey in the Arctic Ocean. Technical Report No. 21, National Survey and Cadastre (KMS), Denmark.

FORSBERG, R.; KENYON, S. (1994) Evaluation and downward continuation of airborne gravity data – the Greenland example. *Proceedings of the International Symposium on Kinematic Systems in Geodesy, Geomatics and Navigation (KIS94)*: 531-538. Banff, Canada.

FORSBERG, R.; OLESEN, A.V.; KELLER, K. (1999) Airborne gravity survey of the North Greenland continental shelf 1998. Technical Report No. 10, National Survey and Cadastre (KMS), Copenhagen, Denmark.

FORSBERG, R.; RUBEK, F. (1998) Gravity and GPS measurements in Greenland 1997. Survey and data processing report, Office of Geodynamics, National Survey and Cadastre (KMS), Denmark.

FORSBERG, R.; SOLHEIM D. (2000) Geoid of the Nordic/Baltic region from surface/airborne gravimetry and GPS drapping. *IAG International Symposium on Gravity, Geoid, and Geodynamics*. Banff, Canada.

FREEDEN, W. (1999) *Multiscale modellling of spaceborne geodata*. BSG Teubner, Stuttgart.

FREEDEN, W.; WINDHEUSER, U. (1997) Combined spherical harmonic and wavelet expansion — A future concept in Earth's gravitational determination. *Applied and Computational Harmonic Analysis*, 4(1): 1-37.

FREEDEN, W.; SCHNEIDER, F. (1998) An integrated wavelet concept of physical geodesy. *Journal of Geodesy*, 72(5): 259-281.

GAUSS, C.F. (1828) *Bestimmung des Breitenunterschiedes zwischen den Sternwarten von Göttingen und Altona durch Beobachtungen am Ramsdenschen Zenithsector*. Göttingen : Vanderschoeck und Ruprecht.

GIBERT, D.; HOHLSCHNEIDER, M.; LE MOUËL, J.L. (1998) Wavelet analysis of the Chandler wobble. *Journal of Geophysical Research: Solid Earth (1978–2012)*, 103(B11): 27069–27089.

GILBERT, A.; KELLER, W. (2000) Deconvolution with wavelets and vaguelettes. *Journal of Geodesy*, 74: 306-320.

GOIGINGER, H.; REISER, D.; MAYER-GÜRR, T.; PAIL, R.; SCHUH, W.-D.; JÄGGI, A.; MAIER, A.; GOCO Consortium (2011) The combined satellite-only global gravity field model GOCO02S. *EGU General Assembly 2011*, Wien. Presentation.

GRAFAREND, E.W. (1978) The definition of the telluroid. *Bulletin Géodésique*, 52(1): 25-37.

GREEN, G. (1828) *An essay on the application of mathematical analysis to the theories of electricity and magnetism*. Nottingham.

GUMERT, W.R.; COBB, G.E. (1970) Helicopter gravity measuring system. *Proceedings of the symposium on dynamic gravimetry "Advances in dynamic gravimetry"*, pp. 79-85, Fort Worth, Texas, USA.

GUMERT, W.R. (1998) An historical review of airborne gravity. *The Leading Edge*, 17(1): 113-116.

HAAGMANS, R.; DE MIN, E.; VAN GELDEREN, M. (1993) Fast evaluation of convolution integrals on the sphere using 1D FFT and a comparison with existing methods for Stokes' integral. *Manuscripta Geodaetica*, 18: 227–241.

HADAMARD, J. (1902) Sur les problèmes aux dérivés partielles et leur signification physique. *Princeton University Bulletin*, 13: 49-52.

HAMMER, S. (1950) Recent development in gravity prospecting. *Colorado School of Mines Quart.*, 45(4A): 87-103.

HAMMER, S. (1983) Airborne gravity is here! *Geophysics*, 48(2): 213-223.

HECK, B. (1986) A numerical comparison of some telluroid mappings. *Proceedings of the I. Hotine–Marussi Symposium on Mathematical Geodesy*, pp. 19–38, Milano.

HECK, B. (2003) On Helmert's methods of condensation. *Journal of Geodesy*, 77(3-4): 155-170.

HEHL, K.; BASTOS, L.; CUNHA, S.; FORSBERG, R.; OLESEN, A.V.; GIDSKEHAUG, A.; MEYER, U.; BOEBEL, T.; TIMMEN, L.; XU, G.; NESEMANN, M. (1997) Concepts and first results of the AGMASCO project. *Proceedings of the International Symposium on Kinematic Systems in Geodesy, Geomatics and Navigation (KIS97)*, pp. 557–563, Banff, Canada.

HEISKANEN, W.A.; MORITZ, H. (1967) *Physical Geodesy*. W.H. Freeman & Co., San Francisco.

HIRVONEN, R. (1960) New theory of gravimetric geodesy. *Annales Academiae Scientarium Fennicae A III* (56). Helsinki.

HOFMANN-WELLENHOF, B.; MORITZ, H. (2005) *Physical Geodesy*. Springer-Verlag, Wien-New York.

HOLOTA, P. (1995) Two branches of the Newton potential and geoid. *Gravity and Geoid. IAG Symposia*, 113: 205-214. Springer-Verlag, Berlin etc.

HOLOTA, P. (1997) Variational methods for geodetic boundary value problems. *Geodetic Boundary Value Problems in View of the One Centimeter Geoid, Lecture Notes in Earth Sciences*, 65: 468-481.

HOLOTA, P.; NESVADBA, O. (2008) Model refinements and numerical solutions of weakly formulated boundary-value problems in physical geodesy. *VI Hotine-Marussi Symposium on Theoretical and Computational Geodesy. IAG Symposia*, 132: 320-326.

HOTINE, M. (1969) *Mathematical Geodesy*. ESSA (Environmental Science Services Administration) Monograph 2, US Department of Commerce, Washington.

HUANG, C.-H.; HWANG, C.;HSIAO, Y.-S.;WANG, Y.M.; ROMAN, D.R. (2013) Analysis of Alabama Airborne Gravity at three altitudes: Expected accuracy and spatial resolution from a future Tibetan Airborne Gravity Survey. *Terrestrial, Atmospheric and Oceanic Sciences*, 24(4): 551-563.

HUYGENS, C. (1703) *De vi centrifuga*. Oeuvres complètes, XVI: 255-301.

HWANG, C. (1996) A study of the Kuroshio's seasonal variabilities using an altimetric-gravimetric geoid and TOPEX/POSEIDON altimeter data. *Journal of Geophysical Research: Oceans (1978–2012)*, 101(C3): 6313–6335.

HWANG, C. (1997a) Analysis of some systematic errors affecting altimeter-derived sea surface gradient with application to geoid determination over Taiwan. *Journal of Geodesy*, 71: 113-130.

HWANG, C. (1997b) The height system of Taiwan from satellite and terrestrial data. *Journal of Surveying Engineering, ASCE*, 123(4): 126-180.

HWANG, C.; HSIAO, Y.-S.; SHIH, H.-C.; YANG, M.; CHEN, K.-H.; FORSBERG, R.; OLESEN, A.V. (2007) Geodetic and geophysical results from a Taiwan airborne gravity survey: Data reduction and accuracy assessment. *Journal of Geophysical Research: Solid Earth*, 112(B04407).

HWANG, C.; HWANG, L-S. (2002) Use of geoid for assessing trigonometric height accuracy and detecting vertical land motion. *Journal of Surveying Engineering*, 128(1): 1–20.

HWANG, C.; SHIH, H.-C.; HSIAO, Y.-S.; HUANG, C.-H. (2012) Airborne gravity surveys over Taiwan Island and Strait, Kuroshio Current and South China Sea: comparison of GPS and gravity accuracies at different flight altitudes. *Marine Geodesy*, 35(3): 287–305.

HWANG, C.; HSU, H.-J.; CHANG, E.T.Y.; FEATHERSTONE, W.E.; TENZER, R.; LIEN, T.; HSIAO, Y.-S.; SHIH, H.-C.; JAI, P.-H. (2014) New free-air and Bouguer gravity fields of Taiwan from multiple platforms and sensors. *Tectonophysics*, 611: 83–93.

JEKELI, C.; KWON, J.H. (1999) Results of airborne vector (3-D) gravimetry. *Geophysical Research Letters*, 26(23): 3533–3536.

KELLER, W. (2004) *Wavelets in Geodesy and Geodynamics*. Walter de Gruyter, Berlin.

KELLER, W.; HÁJKOVÁ, J. (2011) Representation of planar integral-transformations by 4-D wavelet decomposition. *Journal of Geodesy*, 85(6): 341-356.

KELLOGG, O.D. (1929) *Foundations of potential theory*. Springer, Berlin.

KLEES, R.; TENZER, R.; PRUTKIN, I.; WITTWER, T. (2008) A data-driven approach to local gravity field modelling using spherical radial basis functions. *Journal of Geodesy*, 82: 457-471.

KLEUSBERG, A.; PEYTON, D.; WELLS, D. (1990) Airborne gravimetry and the Global Positioning System. *Proceedings of IEEE Plans '90. The 1990's – a decade of excelence in the navigation sciences*, pp. 273-278.

KLINGELÉ, E.; HALLIDAY, M.; COCARD, M.; KAHLE, H.G. (1995) Airborne gravimetric survey of Switzerland. *Vermessung, Photogrammetrie, Kulturtechnik*, 4: 248–253.

KNICKMEYER, I.T. (1990) Vector gravimetry by a combination of inertial and GPS satellite measurements. UCGE Reports, 20335. Department of Surveying Engineering, The University of Calgary, Calgary, Alberta, Canada.

KOORNWINDER, T.H. (1993) *Fast wavelet transform and Calderon-Zygmund operatots*. Wavelets: an elementary treatment of theory and applications. World Scientific Publishing, pp. 161–182, Singapore.

KOORNWINDER, T.H. (1995) *Wavelets: an elementary treatment of theory and applications*. World Scientific Publishing, 225 pp. London. Series in approximations and decompositions, 1.

KRARUP, T. (1969) A contribution to the mathematical foundations of physical geodesy. Report 44, Danish Geodetic Institute, Copenhagen, Denmark.

KRARUP, T. (1973) Letters on Molodensky's Problem I-IV. Communication to the members of Special Study Group 4.31 of IAG.

KUROISHI, Y.; KELLER, W. (2005) Wavelet approach to improvement of gravity field – geoid modeling for Japan. *Journal of Geophysical Research: Solid Earth (1978–2012)*, 110(B03402).

L&R Air-sea Gravity System II (2003) *Model "S" air-sea dynamic gravity meter system*, LaCoste & Romberg Instruction Manual, LaCoste & Romberg LLC, Austin, Texas.

LAPLACE, P.-S. (1784) *Théorie du mouvement et de la figure elliptique des planètes, Part II*. Reprinted in the third volume of the *Mécanique Céleste* in 1802.

LEBEDEV, L.P.; VOROVICH, I.I. (2003) *Functional analysis in mechanics*. New York, Springer.

LEMOINE, F.G.; KENYON, S.C.; FACTOR, J.K.; TRIMMER, R.G.; PAVLIS, N.K.; CHINN, D.S.; COX, C.M.; KLOSKO, S.M.; LUTHCKE, S.B.; TORRENCE, M.H.; WANG, Y.M.; WILLIAMSON, R.G.; PAVLIS, E.C.; RAPP, R.H.; OLSON, T.R. (1998) The development of the joint NASA GSFC and NIMA Geopotential Model EGM96. NASA/TP-1998-206861.

LI Y. (2000) *Airborne gravimetry for geoid determination*. Department of Geomatics Engineering, The University of Calgary, Calgary, Alberta, Canada.

LISTING, J.B. (1873) *Über unsere jetzige Kenntnis der Gestalt und Grösse der Erde*. Göttingen : Nachrichten der Königlichen Gesellschaft der Wissenschaft und der Georg-August-Universität: 33-98.

LIU, Q.; SIDERIS, M.G. (2003) Wavelet evaluation of Stokes' and Venning-Meinesz integrals. *Journal of Geodesy*, 77: 345–356.

LIU, Q.; SIDERIS, M.G. (2005) Wavelet evaluation of some singular geodetic integrals. *A Window on the Future of Geodesy. IAG Symposia*, 128: 392-397.

LOUIS, A.K.; MAASS, P.; RIEDER, A. (1998) *Wavelets: Theorie und Anwendungen*. B.G. Teubner, Stuttgart.

LUNDBERG, H. (1957) Airborne gravity surveys. *Canadian Mining and Metallurgical Bulletin*: 465-473.

LUNDQUIST, C.A.; VEIS, G. (1966) Geodetic parameters for a 1966 Smithonian Institution Standard Earth. Special Report No. 200, Smithonian Astrophysical Observatory. Cambridge, Massachusetts.

MARCHENKO, A.N,; BARTHELMES, F.; MEYER, U.; SCHWINTZER, P. (2001) Regional geoid determination: An application to airborne gravity data in the Skagerrak. Scientific Technical Report STR01/07, GeoForschungsZentrum Potsdam.

MARTINEC, Z. (1993) Effect of lateral density variations of topographical masses in view of improving geoid model accuracy over Canada. Contract report for Geodetic Survey of Canada, Ottawa.

MARTINEC, Z. (1998) *Boundary-value problems for gravimetric determination of a precise geoid*. Lecture Notes in Earth Sciences 73, Springer-Verlag, Heidelberg.

MARTINEC, Z.; GRAFAREND, E.W. (1997) Solution to the Stokes boundary-value problem on an ellipsoid of revolution. *Studia Geophysica et Geodaetica*, 41(2): 103-129.

MARUSSI, A. (1985) *Intrinsic geodesy*. Springer-Verlag, Berlin.

MAYER-GÜRR, T. (2007) ITG-Grace03s: The latest GRACE gravity field solution computed in Bonn. *Joint International GSTM and DFG SPP Symposium*, Potsdam, Germany. Presentation.

MAYER-GÜRR, T.; RIESER, D.; HOECK, E.; BROCKMANN, J.M.; SCHUH, W.-D.; KRASBUTTER, I.; KUSCHE, J.; MAIER, A.; KRAUSS, S.; HAUSLEITNER, W.; BAUR, O.; JAEGGI, A.; MEYER, U.; PRANGE, L.; PAIL, R.; FECHER, T.; GRUBER, T. (2012) The new combined satellite only model GOCO03s. *International Symposium on Gravity, Geoid and Height Systems GGHS 2012*. Venice, Italy. Poster.

McCARTHY, D.D.; PETIT, G. (2003) IERS Conventions. IERS Technical Note, No. 32. Verlag des Bundesamts für Kartographie und Geodäsie, Frankfurt am Main, Germany.

MOLODENSKY, M.S. (1945) *Basic problems of geodetic gravimetry*. Trudy TsNIIGAiK 42, Geogezizdat, Moskva.

MOLODENSKY, M.S.; EREMEEV V.F.; YURKINA M.I. (1960) *Methods for study of the external gravitational field and figure of the Earth*. Translated from Russian by the Israel program for scientific translations, Office of Technical Services, Department of Commerce, 1962, Washington.

MORITZ, H. (1977) Recent developments in the geodetic boundary-value problem. Department of Geodetic Science, Report No. 266. The Ohio State University, Columbus, Ohio.

MORITZ, H. (1980) *Advanced Physical Geodesy*. Herbert Wichmann Verlag, Karlsruhe, Abacus Press, Tunbridge Wells, Kent.

MORITZ, H. (1984) Geodetic Reference System 1980. *Bulletin Géodésique*, 58: 388-398.

NETTLETON, L.L.; LACOSTE, L.; HARRISON, J.C. (1960) Tests of an airborne gravity meter. *Geophysics*, 25(1), 181–202.

NEWTON, I. (1686) *Philosophiae naturalis principia mathematica*. Londini : Jussu Societatis Regiae ac Typis Josephi Streater. Prostat apud plures bibliopolas. (in Latin)

NOVÁK, P.; HECK, B. (2002) Downward continuation and geoid determination based on band-limited airborne gravity data. *Journal of Geodesy*, 76: 269-278.

NOVÁK, P.; KERN, M.; SCHWARZ, K.-P.; HECK, B. (2003a) Evaluation of band-limited topographical effects in airborne gravimetry. *Journal of Geodesy*, 76: 597-604.

NOVÁK, P.; KERN, M.; SCHWARZ, K.-P.; SIDERIS, M.G.; HECK, B.; FERGUSON, S.; HAMMADA, Y.; WEI, M. (2003b) On geoid determination from airborne gravity. *Journal of Geodesy*, 76: 510-522.

NOVÁK, P.; KOSTELECKÝ, J.; KLOKOČNÍK, J. (2009) EGM08: nový globální model zemského gravitačního pole. *Geodetický a kartografický obzor*, 55(3): 44-53.

NORDIN, A. F.; ABU, S. H.; HUA, C. L.; NORDIN, S. (2005) Malaysia precise geoid (MyGEOID). *Coordinates*, 09: 1–40.

OLESEN, A.V,; FORSBERG, R. (2007) Regional airborne scalar gravimetry for geoid determination. *XXIV IUGG General Assembly 2007*, Perugia, Italy. Presentation.

OLESEN, A.V,; FORSBERG, R.; KELLER, K.; GIDSKEHAUG, A. (2000) Airborne gravity survey of Lincoln Sea and Wandel Sea, North Greenland. *Physics and Chemistry of the Earth, Part A: Solid Earth and Geodesy*, 25(1): 25-29.

PAIL, R.; GOIGINGER, H.; SCHUH, W.-D.; HÖCK, E.; BROCKMANN, J.M.; FECHER, T.; GRUBER, T.; MAYER-GÜRR, T.; KUSCHE, J.; JÄGGI, A.; RIESER, D. (2010) Combined satellite gravity field model GOCO01S derived from GOCE and GRACE. *Geophysical Research Letters*, 37(20).

PAUL, M.K. (1973) A method of evaluation the truncation error coefficients for geoidal height. *Bulletin Géodésique*, 110: 413-425.

PAVLIS, N.K.; FACTOR, J.K.; HOLMES, S.A. (2007) Terrain-related gravimetric quantities computed for the next EGM. *Proceedings of the 1st International Symposium of the International Gravity Field Service*, 18: 318-323. Harita Dergisi, Istanbul, Turkey.

PAVLIS, N.K.; HOLMES, S.A.; KENYON, S.C.; FACTOR, J.K. (2012) The development and evaluation of the Earth Gravitational Model 2008 (EGM2008). *Journal of Geophysical Research: Solid Earth (1978-2012)*, 117(B4406).

PICK, M.; PÍCHA, J.; VYSKOČIL, V. (1973) *Theory of the earth's gravity field*. 1^{st} ed. Academia, Prague.

PIZZETTI, P. (1911) Sopra in calcolo teorico delle deviazioni del geoide dall'ellissoide. *Atti Reale Accademia delle Scienze*, 46: 331-350. Torino.

RAPP, R.H.; RUMMEL, R. (1975) Methods for the computation of detailed geoids and their accuracy. OSU Report 233, Department of Geodetic Science and Surveying, Ohio State University, Columbus.

RAPP, R.H.; WANG, Y.M.; PAVLIS, N.K. (1991) The Ohio State 1991 geopotential model and sea surface topography harmonic coefficient model. Report No. 410, Department of Geodetic Science and Surveying, The Ohio State University, Columbus.

REIGBER, C.; LÜHR, H.; SCHWINTZER, P. (2002) CHAMP mission status. *Advances in Space Research*, 30(2): 129–134.

REKTORYS, K.; DRÁBEK, K.; FIEDLER, M.; FISCHER, O.; FUKA, J.; HÁJEK, J.; KEJLA, F.; KEPR, B.; KORVASOVÁ, K.; NEČAS, J.; NOŽIČKA, F.; PLESKOT, V.; POKORNÁ, O.; PRÁGER, M.; VEJVODA, O.; VILHELM, V.; VITÁSEK, E.; ZELENKA, M. (1963) *Survey of applicable mathematics*. SNTL, Prague.

ROLAND, M.; DENKER, H. (2005) Stokes integration versus wavelet techniques for regional geoid modelling. *A Window on the Future of Geodesy. IAG Symposia*, 128: 368-373. Springer, Berlin.

SALOMONOVICZ, R.H. (2000) A wavelet based gravity model with an application to the evaluation of Stokes' integral. *Gravity, geodesy and geodynamics 2000. IAG Symposia*, 123: 85–90. Springer, Berlin.

SALYCHEV, O.S.; BYKOVSKY, A.V.; VORONOV, V.V.; SCHWARZ, K.P.; LIU, Z.; WEI, M.; PANENKA, J. (1994) Determination of gravity and deflections of the vertical for geophysical applications using the ITC-2 Platform. *Proceedings of the International Symposium on Kinematic Systems in Geodesy, Geomatics and Navigation (KIS 94)*, Banff, Canada, pp. 521–529.

SCHMIDT, M.; FENGLER, M.; MAYER-GÜRR, T.; EICKER, A.; KUSCHE, J.; SANCHEZ, L.; HAN, S.C. (2007) Regional gravity modeling in terms of spherical base functions. *Journal of Geodesy*, 81(1): 17-38.

SCHUH, H.; NAGEL, S.; SEITZ, T. (2001) Linear drift and periodic variations observed in long time series of polar motion. *Journal of Geodesy*, 74: 701–710.

SCHWARZ, K.P. (1980) Gravity field approximation using inertial survey systems. *The Canadian Surveyor*, 34(4): 383-395.

SCHWARZ, K.P.; CANNON, M.E.; WONG, R.V.C. (1989) A comparison of GPS kinematic models for the determination of position and velocity along a trajectory. *Manuscripta Geodaetica*, 14(2): 345-353.

SCHWARZ, K.P.; LI, Z. (1997) An introduction to airborne gravimetry and its boundary value problems. *Geodetic Boundary Value Problems in View of the One Centimeter Geoid. Lecture Notes in Earth Sciences*, 65: 312-358.

SCHWARZ, K.P.; SIDERIS, M.G.; FORSBERG, R. (1990) The use of FFT techniques in physical geodesy. *Geophysical Journal International*, 100(3): 485-514.

SCHWARZ, K.P.; WEI, M. (1993) Inertial Geodesy and INS/GPS Integration. Lecture notes, Department of Geomatics Engineering, The University of Calgary, Calgary, Alberta, Canada.

SIDERIS, M.G.; SCHWARZ, K.P. (1986) Solving Molodensky's series by fast Fourier transform techniques. *Bulletin Géodésique*, 60: 51–63.

SOMIGLIANA, C. (1929) *Teoria generale del campo gravitazionale dell'ellissoide di rotazione*. Memoire della Societa Astronomica Italiana IV. Milano.

STOKES, G.G. (1849) *On the variation of gravity on the surface of the Earth*. Transactions of the Cambridge Philosophical Society 8: 672-695.

STRANG VAN HEES, G. (1990) Stokes formula using fast Fourier transform techniques. *Manuscripta Geodaetica*, 15: 235–239.

TAPLEY, B.D.; BETTADPUR, S.; WATKINS, M.; REIGBER, C. (2004) The gravity recovery and climate experiment: Mission overview and early results. *Geophysical Research Letters*, 31(9).

THOMPSON, L.G.D.; LACOSTE, L.J.B. (1960) Aerial gravity measurements. *Journal of Geophysical Research*, 65(1): 305–322.

TORGE, W. (1980) *Geodesy*. Walter de Gruyter, third edition, 2001, Berlin.

TSUEI, G.-C.; ARABELOS, D.; FORSBERG, R.; SIDERIS, M.G.; TZIAVOS, I.N. (1995) Geoid computations in Taiwan. *Gravity and Geoid. IAG Symposia*, 113: 446-458.

VANÍČEK, P.; CHRISTOU, N. (1994) *Geoid and its geophysical interpretations*. CRC Press, Boca Raton, Florida, USA.

VANÍČEK, P.; NAJAFI, M.; MARTINEC, Z.; HARRIE, L.; SJÖBERG, L.E. (1995) Higher-degree reference field in the generalized Stokes-Helmert scheme for geoid computation. *Journal of Geodesy*, 70(3): 176-182.

VERDUN, J.; KLINGELÉ, E.E.; BAYER, R,; COCARD, M.; GEIGER, A.; KAHLE, H.G. (2003) The alpine Swiss-French airborne gravity survey. *Geophysical Journal International*, 152(1): 8-19.

WANG, Y.M.; PREAUX, S.; DIEHL, T.; CHILDERS, V.; ROMAN, D.; SMITH, D. (2013) Accuracy assessment of test flights using the Turnkey Airborne Gravity System over Alabama in 2008. *Journal of Geodetic Science*, 3(2): 136–142.

WEI, M. (1999) From airborne gravimetry to airborne geoid mapping – Report of SSG 3.164. Determination of the gravity field. Report of IAG section III: 25–32. Danish National Survey and Cadastre (KMS), Copenhagen.

WEI, M.; SCHWARZ, K.P. (1998) Flight test results from a strapdown airborne gravity system. *Journal of Geodesy*, 72: 323–332.

WEI, M.; FERGUSON, S.; SCHWARZ, K.P. (1992) Accuracy of GPS-derived acceleration from moving platform tests. *From Mars to Greenland: Charting Gravity With Space and Airborne Instruments. IAG Symposia*, 110: 235-249.

WINDHEUSER, U. (1995) *Sphärische Wavelets: Theorie und Anwendungen in der Physikalischen Geodäsie*. Dissertation Universität Kaiserslautern.

ZIENKIEWICZ, O.C.; TAYLOR, R.L.; ZHU, J.Z. (1967) *The finite element method: its basis and fundamentals*. Elsevier, sixth edition, 2005, Oxford.

List of Publications

HÁJKOVÁ, J. (2009) Local geoid determination based on airborne gravity data. *Proceedings of conference JUNIORSTAV 2009*. Brno.

HÁJKOVÁ, J. (2010) Local geoid determination based on airborne gravity data and a comparison with GPS/levelling points. *Proceedings of conference JUNIORSTAV 2010*. Brno.

HÁJKOVÁ, J.; MINTOURAKIS, I.; DELIKARAOGLOU, D. (2010) Spectral decomposition and signal processing techniques of airborne gravity data for earth gravity field modeling - A case study for Taiwan. *Proceedings of conference 4th IC-SCCE*. Athens, Greece.

HÁJKOVÁ, J. (2011) Local geoid determination based on airborne gravity data. *Studia Geophysica et Geodaetica*, 55(3): 515-528.

KELLER, W.; HÁJKOVÁ, J. (2011) Representation of planar integral-transformations by 4-D wavelet decomposition. *Journal of Geodesy*, 85(6): 341-356.

Appendix A

Geocentric coordinate system

A Terrestrial Reference System (TRS) is a geocentric orthogonal coordinate system (also called Earth-Centred, Earth-Fixed – ECEF) which rotates with the Earth. It is defined by the following parameters:

- three parameters to define the origin ,
- three parameters to define the orientations of its axes ,
- one parameter to define the scale (assume the orthogonal axes with the same scale) .

The origin of this system is located to the Earth's centre of gravity (geocentre). The z-axis coincides with the mean Earth's axis of rotation, the x-axis points through the intersection of Equator and Prime Meridian (Greenwich). The y-axis completes the right-handed system. The scale is close to an SI metre (McCarthy and Petit, 2003).

A realization of TRS is called a Terrestrial Reference Frame (TRF). TRF is a set of physical points with precisely determined coordinates in a specific coordinate system (Cartesian, . . .) attached to TRS (McCarthy and Petit, 2003).

Appendix B

Coordinates

In the coordinate system described in Appendix A, one can use Cartesian (rectangular) coordinates (x, y, z) or curvilinear coordinates. Since we usually use the geocentric sphere and the ellipsoid of revolution as reference surfaces, it is more convenient to use curvilinear coordinates: the spherical coordinates (r, θ, λ) and the Gauss-ellipsoidal (geodetic) coordinates (h, φ, λ).

B.1 Cartesian coordinates

Let every point on the reference surface is defined by its position vector $\mathbf{r}$. Denoting the unit vectors in the directions of axes x, y, z as $\mathbf{i}, \mathbf{j}, \mathbf{k}$ yields

$$\mathbf{r} = x\mathbf{i} + y\mathbf{j} + z\mathbf{k}\,, \tag{B.1}$$

where x, y, z are the Cartesian coordinates of the point of interest, see Fig. B.1.

B.2 Spherical coordinates

The position of the point of interest is also uniquely determined by the magnitude of the position vector from the Eq. (B.1) $r = |\mathbf{r}|$ and two angles θ and λ, see Fig. B.2. The co-latitude $\theta \in \langle 0; \pi \rangle$ is defined as the angle between the position vector $\mathbf{r}$ and the z-axis, the spherical longitude $\lambda \in \langle 0; 2\pi \rangle$ is the angle between the x-axis and the projection of $\mathbf{r}$

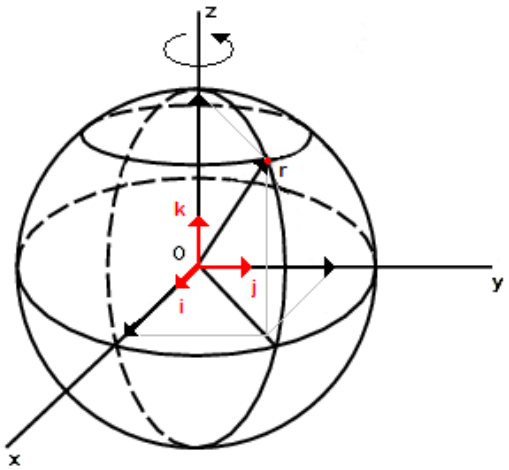

Figure B.1: Cartesian coordinates x, y and z (reference surface – sphere)

to the xy-plane (equator). The Cartesian coordinates and the spherical coordinates relate as follows (Heiskanen and Moritz 1967, p. 18):

- Cartesian coordinates $\rightarrow$ spherical coordinates:

$$\begin{aligned} r &= \sqrt{x^2 + y^2 + z^2}\,, \\ \lambda &= \arctan\frac{y}{x}\,, \\ \theta &= \arctan\frac{\sqrt{x^2 + y^2}}{z} = \arccos\frac{z}{r}\,; \end{aligned} \tag{B.2}$$

- spherical coordinates $\rightarrow$ Cartesian coordinates:

$$\begin{aligned} x &= r\sin\theta\cos\lambda\,, \\ y &= r\sin\theta\sin\lambda\,, \\ z &= r\cos\theta\,. \end{aligned} \tag{B.3}$$

B.3 Gauss ellipsoidal coordinates (geodetic coordinates)

The Gauss ellipsoidal coordinates (geodetic coordinates) refer to the ellipsoid of revolution. The position of the point of interest is uniquely determined by the ellipsoidal

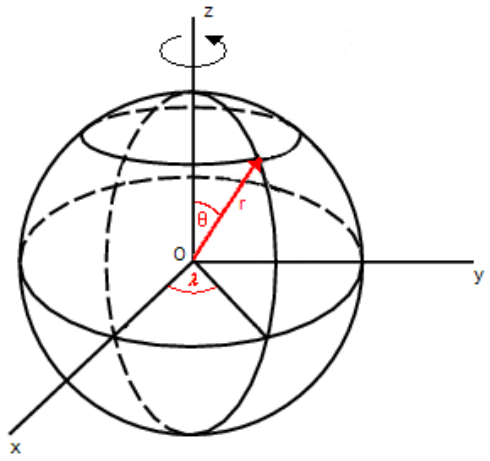

Figure B.2: Spherical coordinates r, θ and λ

height h (height above the ellipsoid) and two angles φ and λ. The geodetic latitude $\varphi \in \langle -\frac{\pi}{2}; \frac{\pi}{2} \rangle$ is the angle between the ellipsoidal normal and the xy-plane, the geodetic longitude $\lambda \in \langle 0; 2\pi)$ is the angle between the x-axis and the projection of the ellipsoidal normal to the xy-plane.

The Cartesian coordinates and the Gauss ellipsoidal coordinates relate as follows (Heiskanen and Moritz 1967, pp. 182-183):

- Cartesian coordinates $\rightarrow$ Gauss ellipsoidal coordinates (iterative procedure):

$$\begin{aligned} \lambda &= \arctan \frac{y}{x}\,, \\ h &= \frac{\sqrt{x^2+y^2}}{\cos\varphi} - N\,, \\ \varphi &= \arctan\left[\frac{z}{\sqrt{x^2+y^2}}\left(1 - e^2\frac{N}{N+h}\right)^{-1}\right]\,; \end{aligned} \tag{B.4}$$

- Gauss ellipsoidal coordinates $\rightarrow$ Cartesian coordinates:

$$\begin{aligned} x &= (N+h)\cos\varphi\cos\lambda\,, \\ y &= (N+h)\cos\varphi\sin\lambda\,, \\ z &= [N(1-e^2)+h]\sin\varphi\,. \end{aligned} \tag{B.5}$$

The parameter e stands for the first eccentricity, N is the transverse radius of curvature:

$$N(\varphi) = \frac{a}{\sqrt{1 - e^2 \sin^2 \varphi}}, \tag{B.6}$$

where a is the major semi-axis of the ellipsoid of revolution.

B.4 Astronomical (natural) coordinates

The astronomical coordinates (natural coordinates) refer to the geoid. The position of the point P of interest is uniquely determined by the orthometric height H (height above the mean sea-level) or the potential W of the point P, the astronomic latitude Φ and the astronomic longitude Λ. The astronomic latitude Φ of a point P is the angle between the vertical (direction of the plumb line) at P and the equatorial plane. Consider a straight line through P parallel to the Earth's axis. This parallel and the vertical at P define the meridian plane at P. The angle between this meridian plane and the meridian plane of Greenwich is the astronomical longitude Λ. The latitude Φ and the longitude Λ are also called the geographical coordinates (Heiskanen and Moritz 1967, p. 55).

Appendix C

Mathematical operators

In this section four mathematical operators are defined: gradient, curl, divergence and Laplacian (e.g., Rektorys et al. 1963, Sec. 7.2). Although all of them are independent of a coordinate system, they have different forms in different coordinates. In this appendix we introduce only the forms in the Cartesian coordinates, see Appendix B.1.

C.1 Gradient

Assume a scalar function f at the point $\mathbf{r}$. The gradient of the scalar function f is a vector operator denoted as ∇f or $\mathrm{grad} f$ which is given by

$$\nabla f(\mathbf{r}) = \frac{\partial f}{\partial x}|_{\mathbf{r}}\,\mathbf{i} + \frac{\partial f}{\partial y}|_{\mathbf{r}}\,\mathbf{j} + \frac{\partial f}{\partial z}|_{\mathbf{r}}\,\mathbf{k}\,, \tag{C.1}$$

where $\mathbf{i}, \mathbf{j}, \mathbf{k}$ are the unit vectors of the coordinate system and the coefficients x, y, z in the partial derivations are the Cartesian coordinates of the point of interest, see Eq. (B.1). The direction of ∇f is the orientation in which the directional derivative has the largest value and $|\nabla f|$ is the value of that directional derivative.

C.2 Curl

Let us denote $\mathbf{F}$ a vector field and p, q, s three scalar fields which are the components of this vector field $\mathbf{F}$:

$$\mathbf{F}(\mathbf{r}) = p(\mathbf{r})\mathbf{i} + q(\mathbf{r})\mathbf{j} + s(\mathbf{r})\mathbf{k}\,. \tag{C.2}$$

The curl of the vector field $\mathbf{F}$, denoted $\mathrm{curl}\,\mathbf{F}$ or $\nabla \times \mathbf{F}$, is a vector field defined as follows:

$$\mathrm{curl}\,\mathbf{F}(\mathbf{r}) = \left[\frac{\partial s}{\partial y}|_{\mathbf{r}} - \frac{\partial q}{\partial z}|_{\mathbf{r}}\right]\mathbf{i} + \left[\frac{\partial p}{\partial z}|_{\mathbf{r}} - \frac{\partial s}{\partial x}|_{\mathbf{r}}\right]\mathbf{j} + \left[\frac{\partial q}{\partial x}|_{\mathbf{r}} - \frac{\partial p}{\partial y}|_{\mathbf{r}}\right]\mathbf{k}\,. \tag{C.3}$$

If $\mathrm{curl}\,\mathbf{F}(\mathbf{r}) = 0$, then the field is said to be an irrotational field.

C.3 Divergence

Assume a vector field $\mathbf{F}$. The divergence of the vector field $\mathbf{F}$, denoted $\mathrm{div}\mathbf{F}$ or $\nabla \cdot \mathbf{F}$, is a scalar field defined by

$$\mathrm{div}\mathbf{F}(\mathbf{r}) = \frac{\partial p}{\partial x}|_{\mathbf{r}} + \frac{\partial q}{\partial y}|_{\mathbf{r}} + \frac{\partial s}{\partial z}|_{\mathbf{r}}\,, \tag{C.4}$$

where p, q, s are the components of the vector field $\mathbf{F}$, see Eq. (C.2).

C.4 Laplacian

A scalar differential operator defined by

$$\Delta f(\mathbf{r}) = \mathrm{div}\nabla f(\mathbf{r})\,, \tag{C.5}$$

is called the Laplace operator or Laplacian. Substituting Eqs. (C.1) and (C.4) to Eq. (C.5) gives in the Cartesian coordinates

$$\Delta f(\mathbf{r}) = \mathrm{div}\left[\frac{\partial f}{\partial x}|_{\mathbf{r}}\,\mathbf{i} + \frac{\partial f}{\partial y}|_{\mathbf{r}}\,\mathbf{j} + \frac{\partial f}{\partial z}|_{\mathbf{r}}\,\mathbf{k}\right] = \frac{\partial^2 f}{\partial x^2}|_{\mathbf{r}} + \frac{\partial^2 f}{\partial y^2}|_{\mathbf{r}} + \frac{\partial^2 f}{\partial z^2}|_{\mathbf{r}}\,. \tag{C.6}$$

If $\Delta f(\mathbf{r}) = 0$, then the scalar field f is said to be harmonic.

Appendix D

Numerical results – synthetic gravity data

In this section figures and histograms corresponding to the tests described in Sec. 5 are presented.

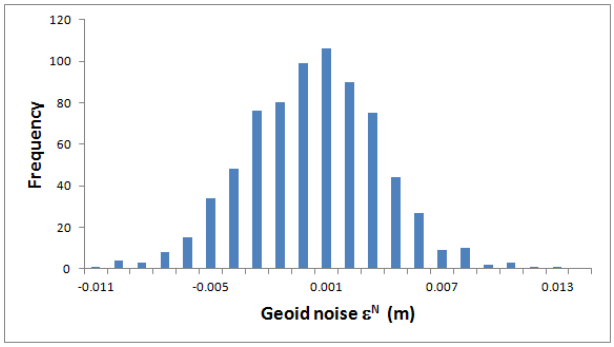

1)

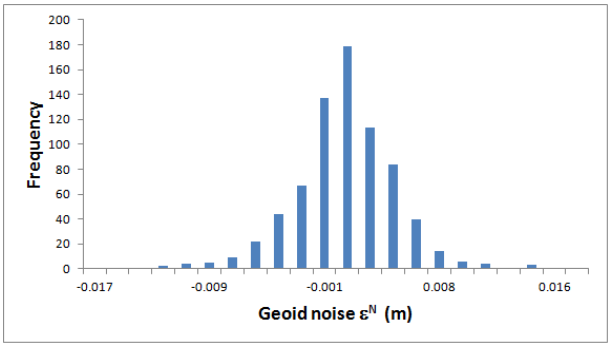

2)

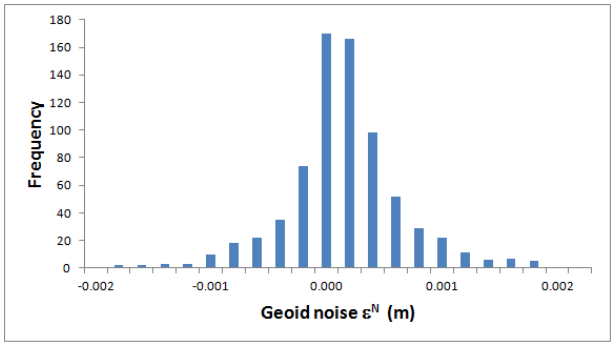

3)

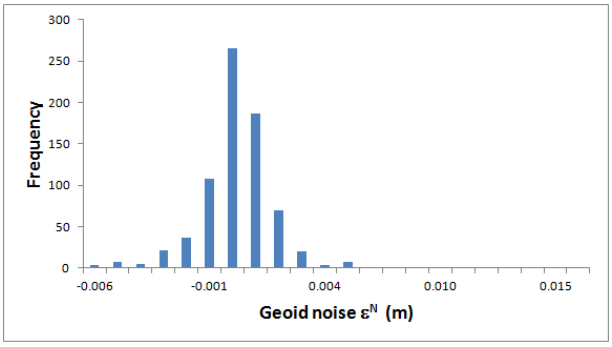

4)

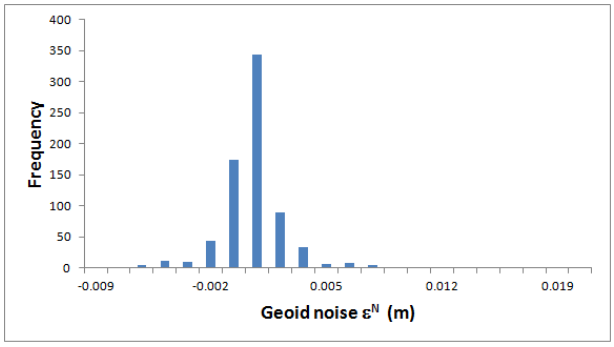

5)

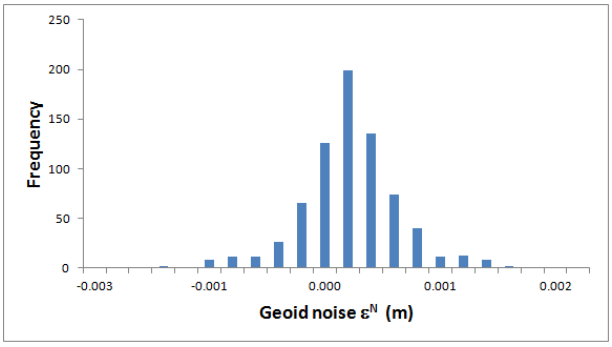

6)

Figure D.1: Histograms of the geoid noise ϵ^N for NC (m), $\epsilon = 0$ mGal: 1) $l = 181$, 2) $l = 361$, 3) $l = 721$, 4) $l = 1081$, 5) $l = 1441$ and 6) $l = 1801$

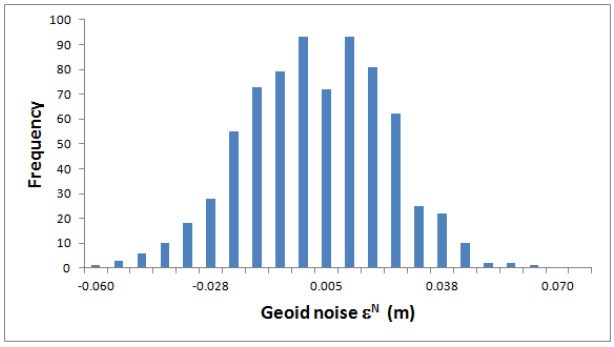

1)

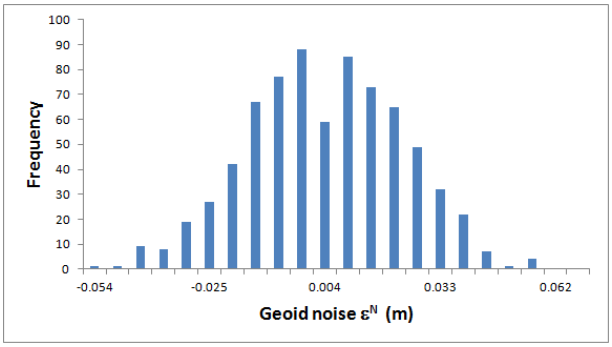

2)

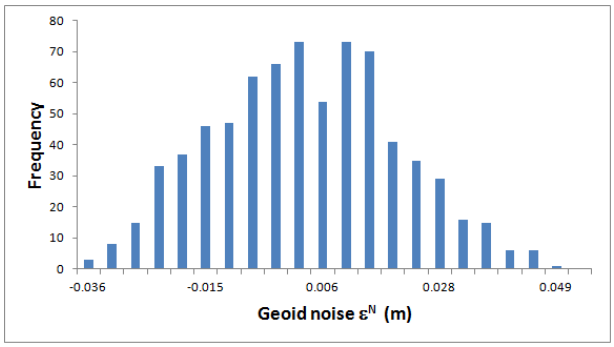

3)

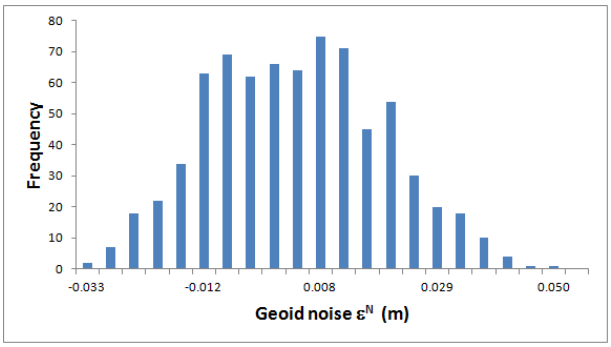

4)

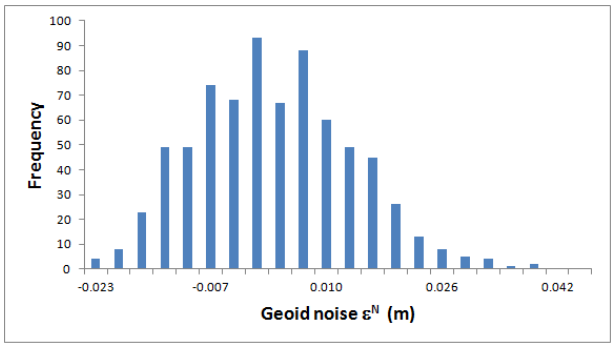

5)

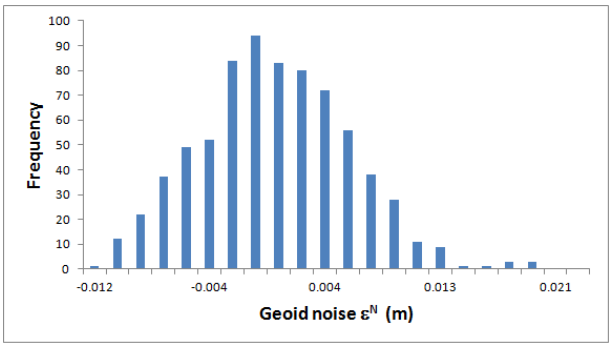

6)

Figure D.2: Histograms of the geoid noise ϵ^N for NC (m), $\epsilon = 3$ mGal: 1) $l = 181$, 2) $l = 361$, 3) $l = 721$, 4) $l = 1081$, 5) $l = 1441$ and 6) $l = 1801$

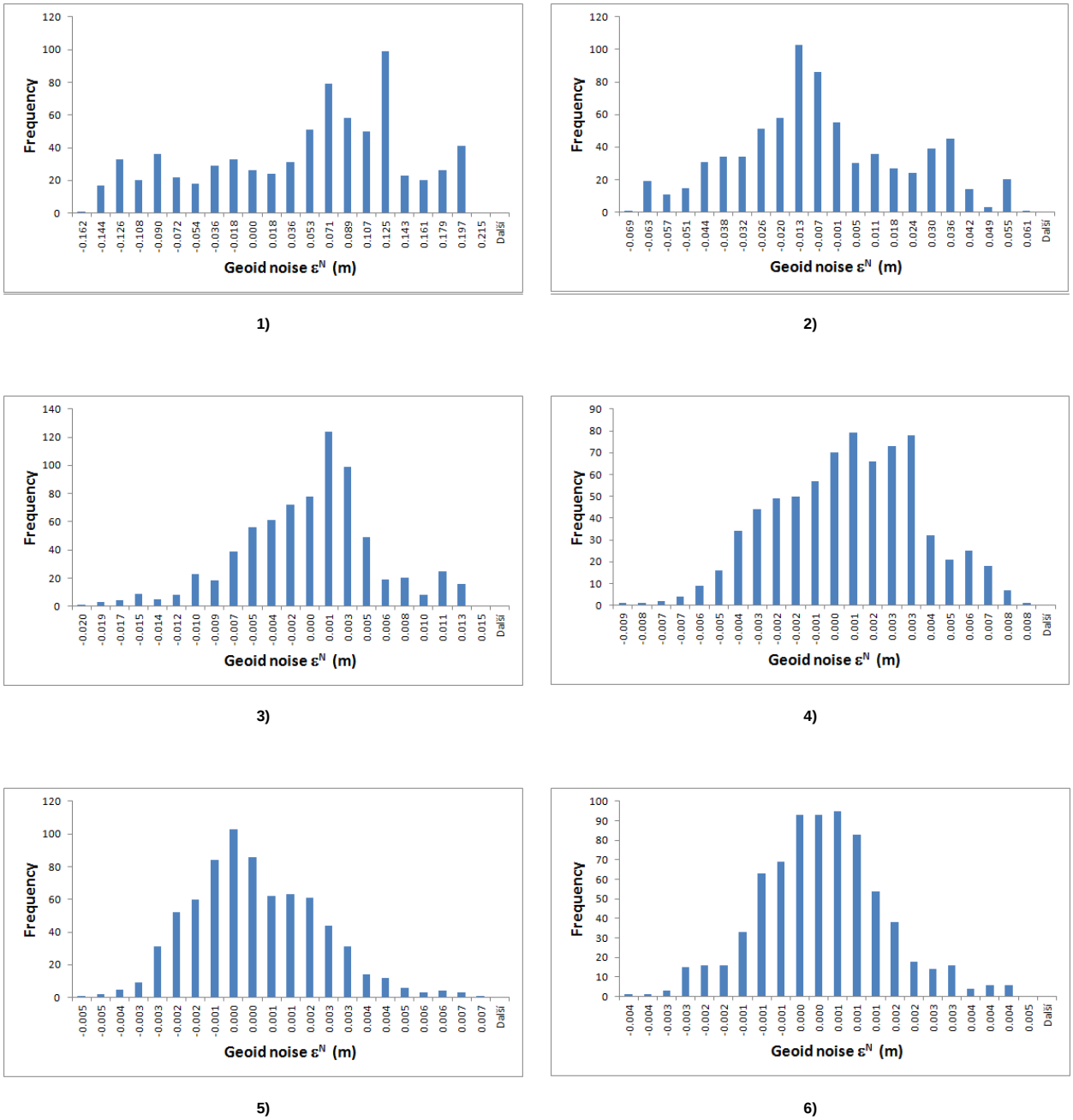

Figure D.3: Histograms of the geoid noise ϵ^N for WT (m), $\epsilon = 0$ mGal: 1) $l = 181$, 2) $l = 361$, 3) $l = 721$, 4) $l = 1081$, 5) $l = 1441$ and 6) $l = 1801$

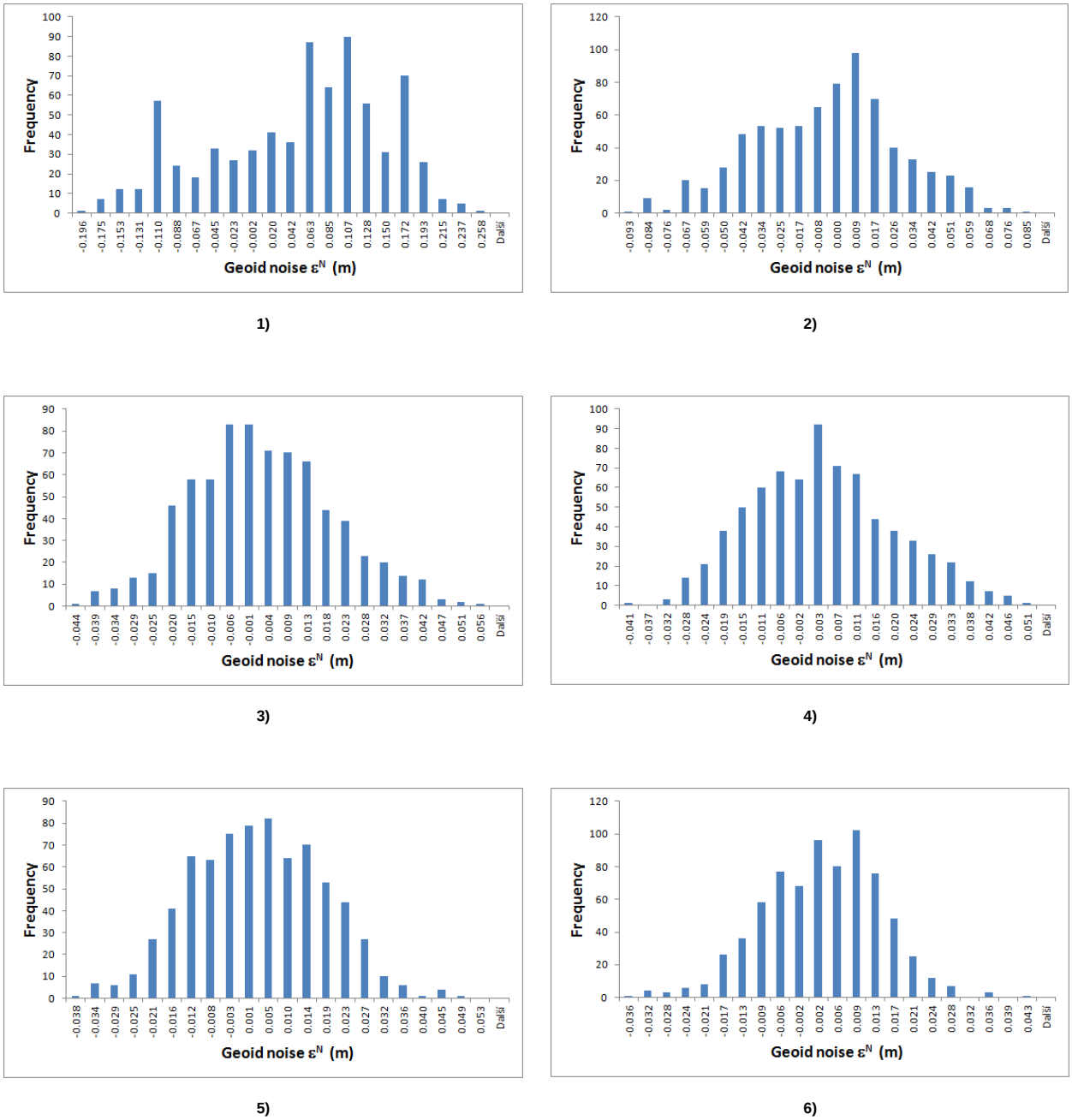

Figure D.4: Histograms of the geoid noise ϵ^N for WT (m), $\epsilon = 3$ mGal: 1) $l = 181$, 2) $l = 361$, 3) $l = 721$, 4) $l = 1081$, 5) $l = 1441$ and 6) $l = 1801$

Appendix E

Numerical results – aerial gravity data

In this section figures, tables and histograms corresponding to the steps of the 'remove-compute-restore' procedure are presented.

E.1 Remove step – test area

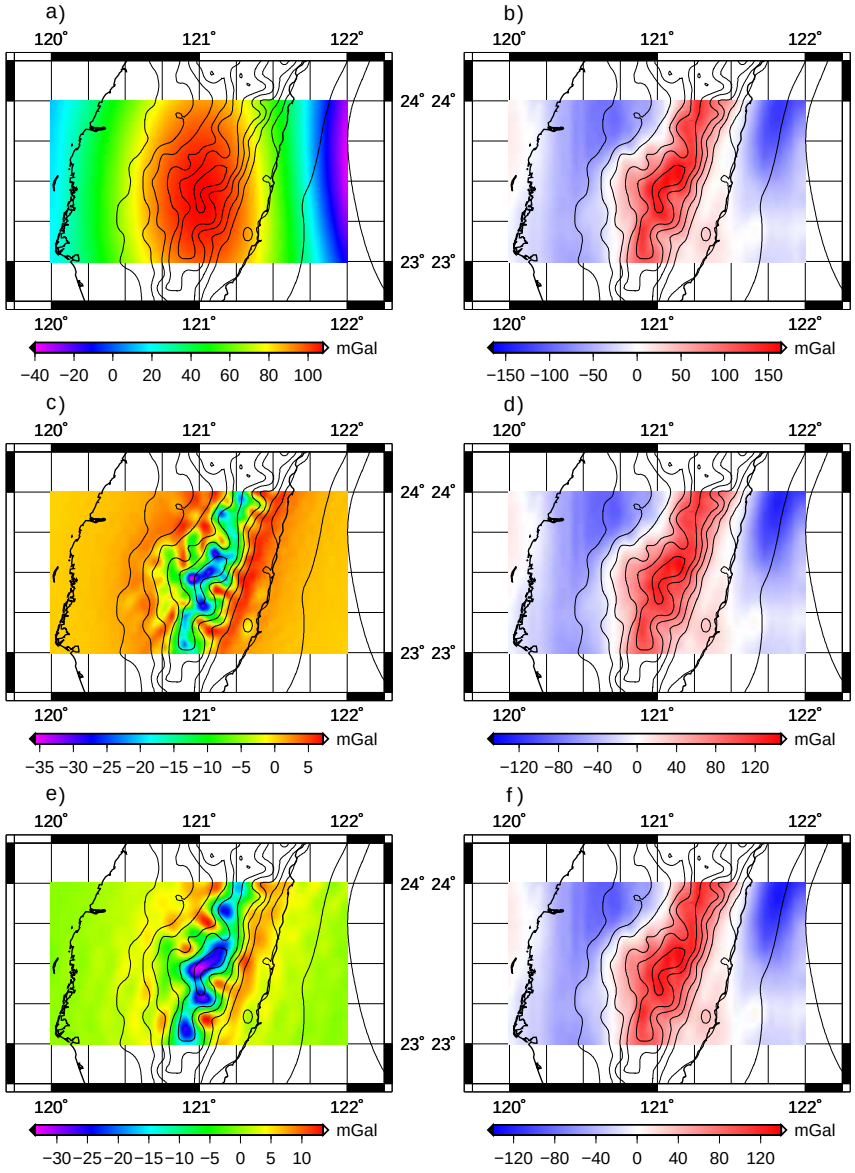

Figure E.1: Test area, $H_1 = 5156$ m: a) low-frequency gravity disturbances δg_{GGM} (GOCO03s to $n = m = 200$), b) band-limited gravity disturbances δg_b, c) band-limited DTE A_b (I), d) Helmert's residual gravity disturbances δg_b^H (I), e) band-limited DTE A_b (FS) and f) Helmert's residual gravity disturbances δg_b^H (FS)

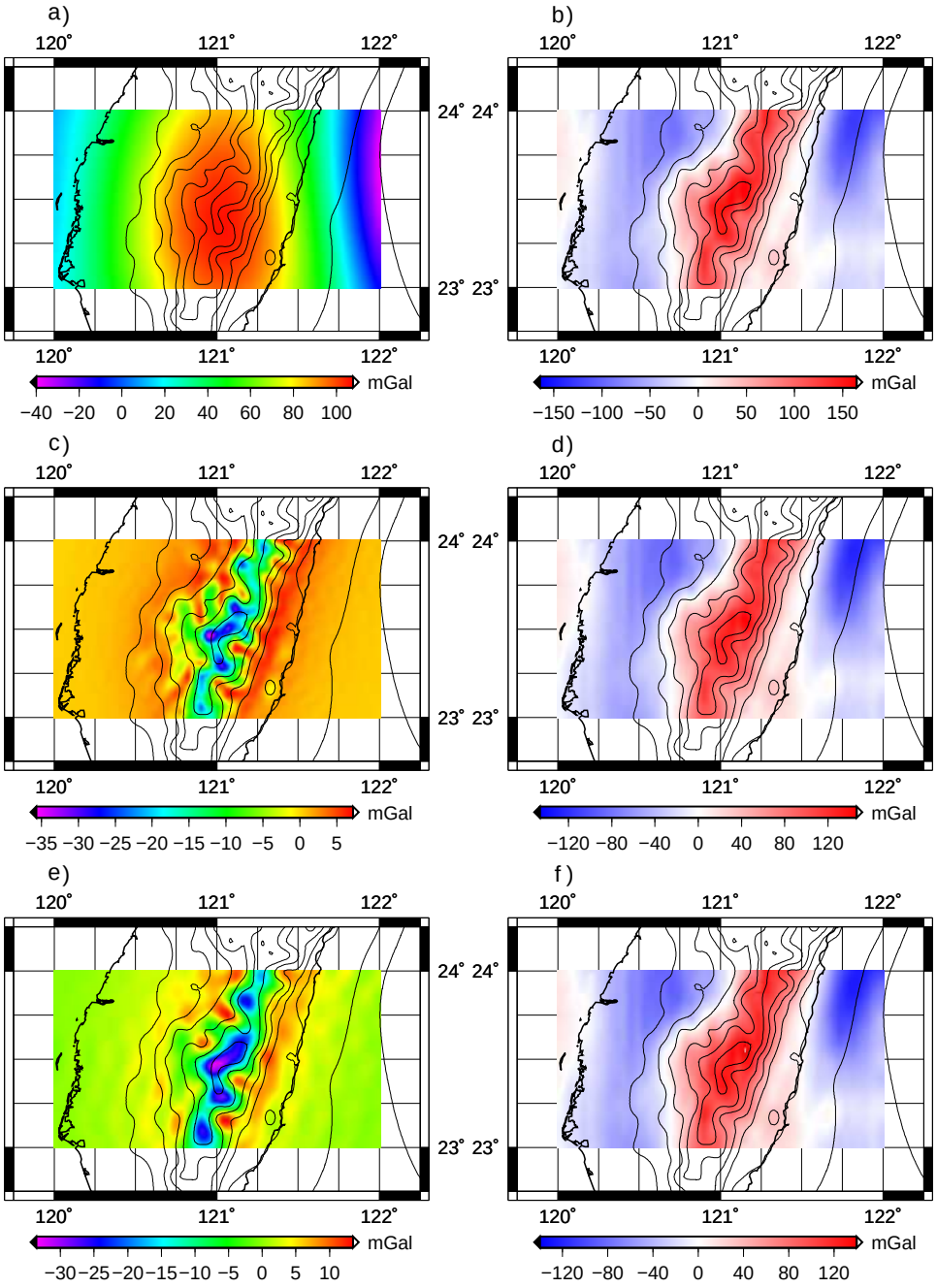

Figure E.2: Test area, $H_1 = 5156$ m: a) low-frequency gravity disturbances δg_{GGM} (EGM08 to $n = m = 200$), b) band-limited gravity disturbances δg_b, c) band-limited DTE A_b (I), d) Helmert's residual gravity disturbances δg_b^H (I), e) band-limited DTE A_b (FS) and f) Helmert's residual gravity disturbances δg_b^H (FS)

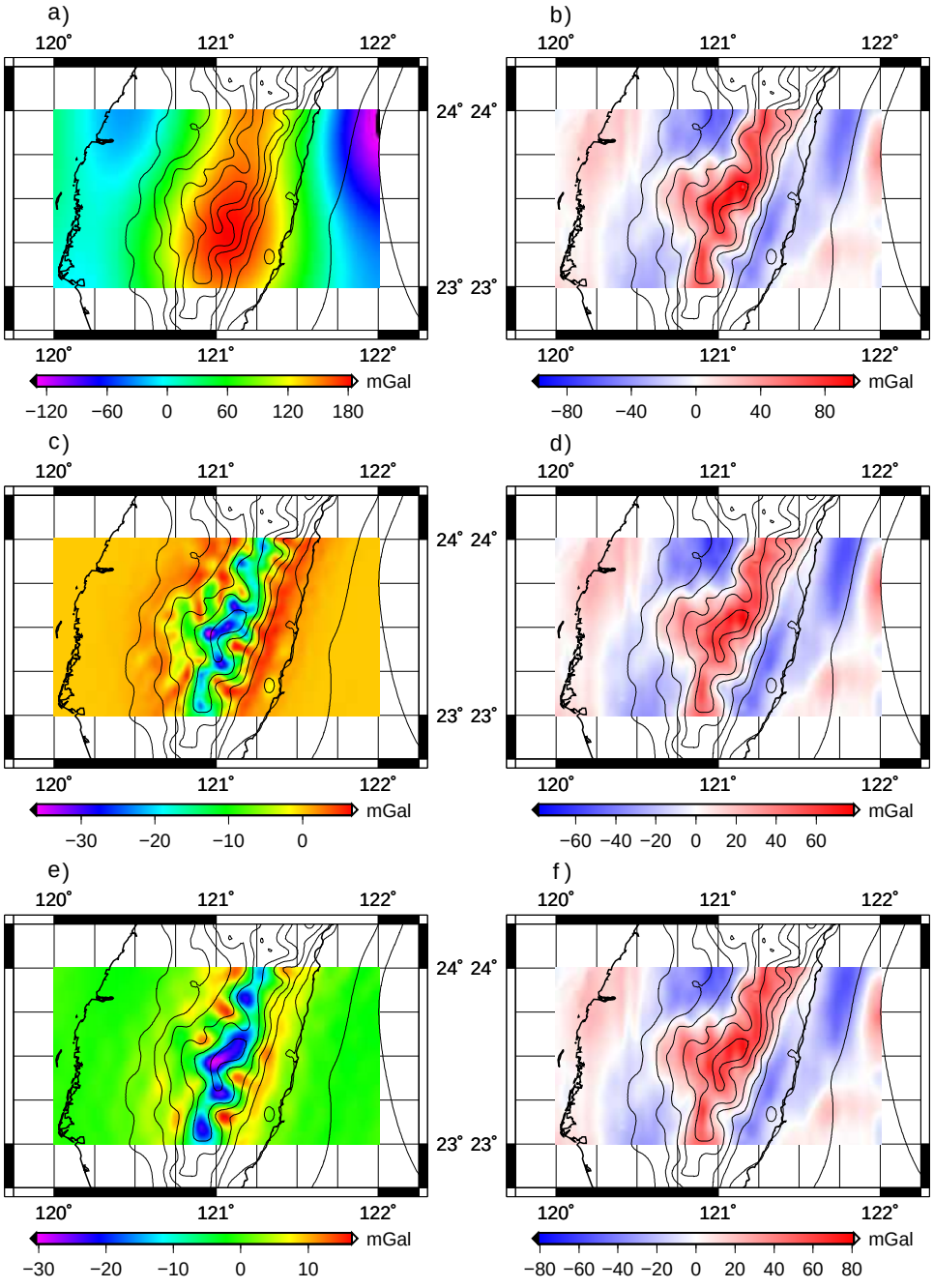

Figure E.3: Test area, $H_1 = 5156$ m: a) low-frequency gravity disturbances δg_{GGM} (EGM08 to $n = m = 360$), b) band-limited gravity disturbances δg_b, c) band-limited DTE A_b (I), d) Helmert's residual gravity disturbances δg_b^H (I), e) band-limited DTE A_b (FS) and f) Helmert's residual gravity disturbances δg_b^H (FS)

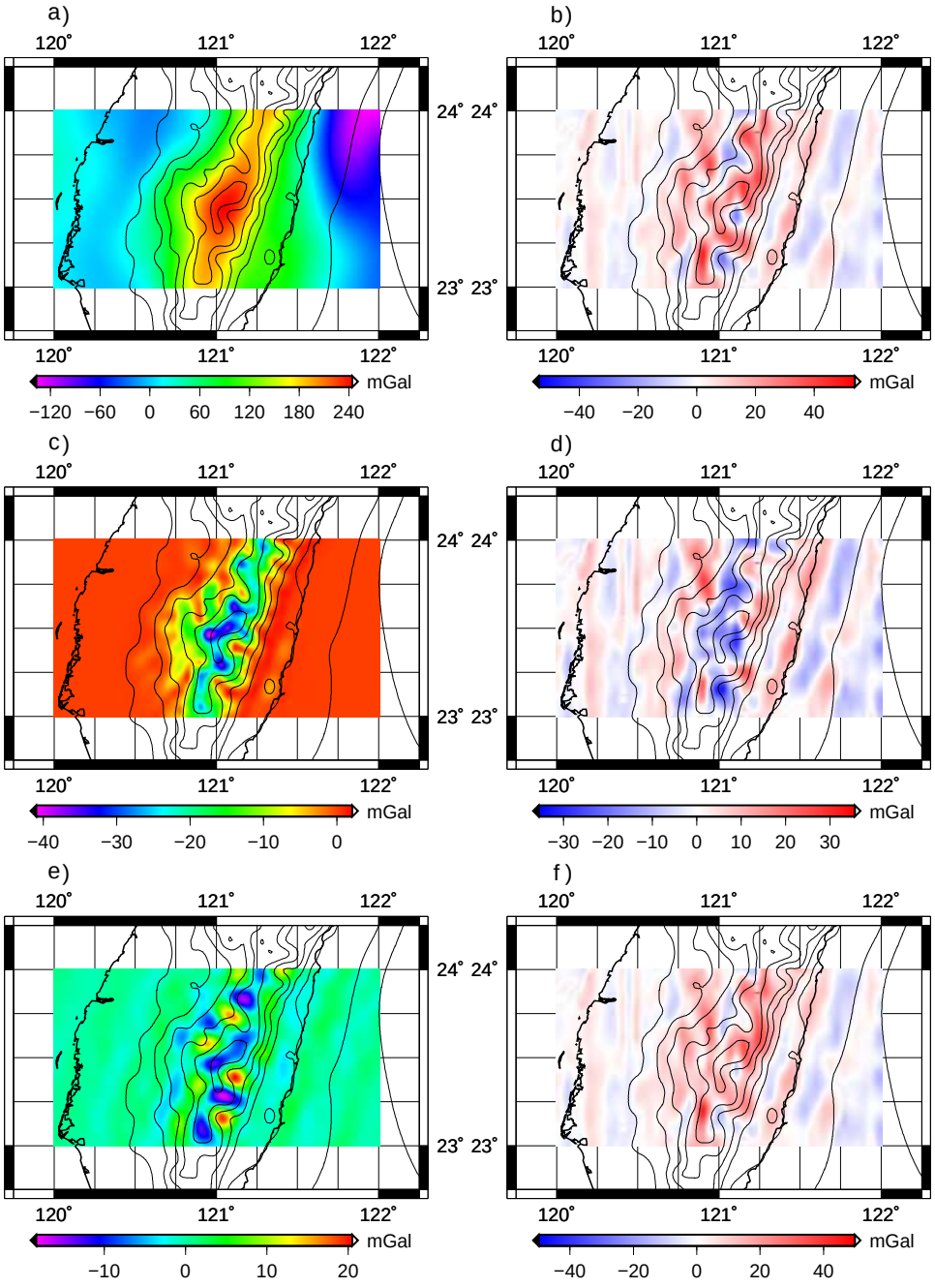

Figure E.4: Test area, $H_1 = 5156$ m: a) low-frequency gravity disturbances δg_{GGM} (EGM08 to $n = m = 1080$), b) band-limited gravity disturbances δg_b, c) band-limited DTE A_b (I), d) Helmert's residual gravity disturbances δg_b^H (I), e) band-limited DTE A_b (FS) and f) Helmert's residual gravity disturbances δg_b^H (FS)

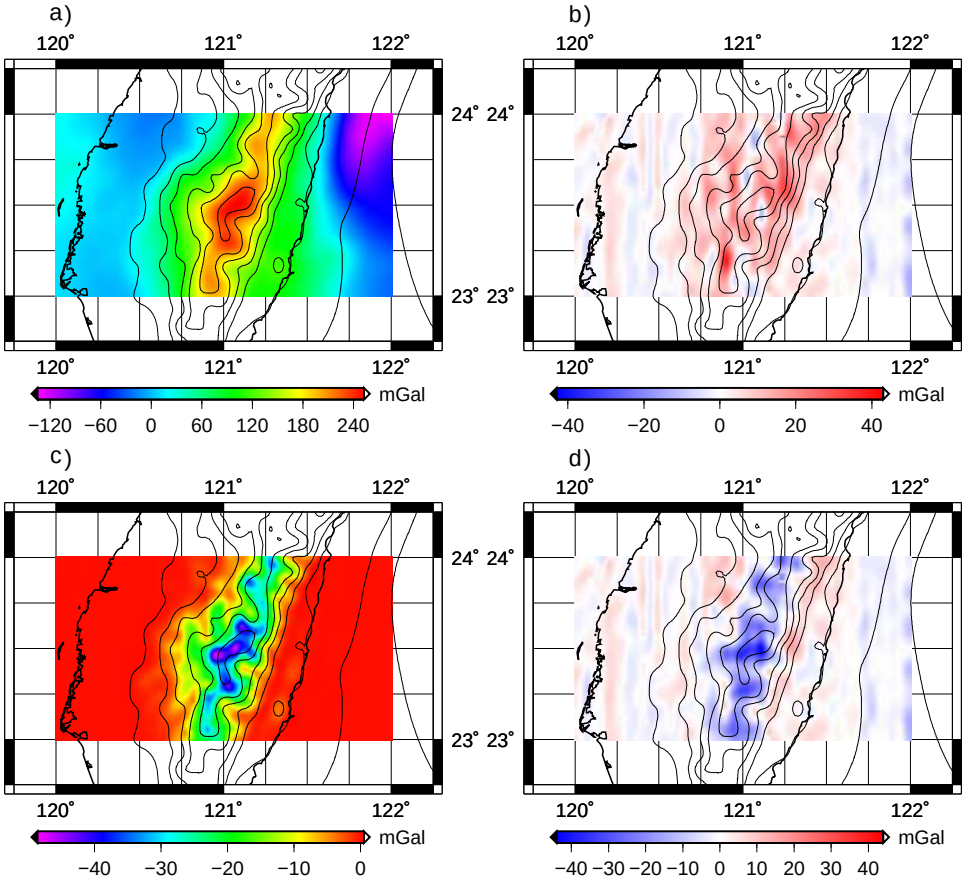

Figure E.5: Test area, $H_1 = 5156$ m: a) low-frequency gravity disturbances δg_{GGM} (EGM08 to $n = m = 2160$), b) band-limited gravity disturbances δg_b, c) band-limited DTE A_b (I) and d) Helmert's residual gravity disturbances δg_b^H (I)

E.2 Remove step – all available gravity data

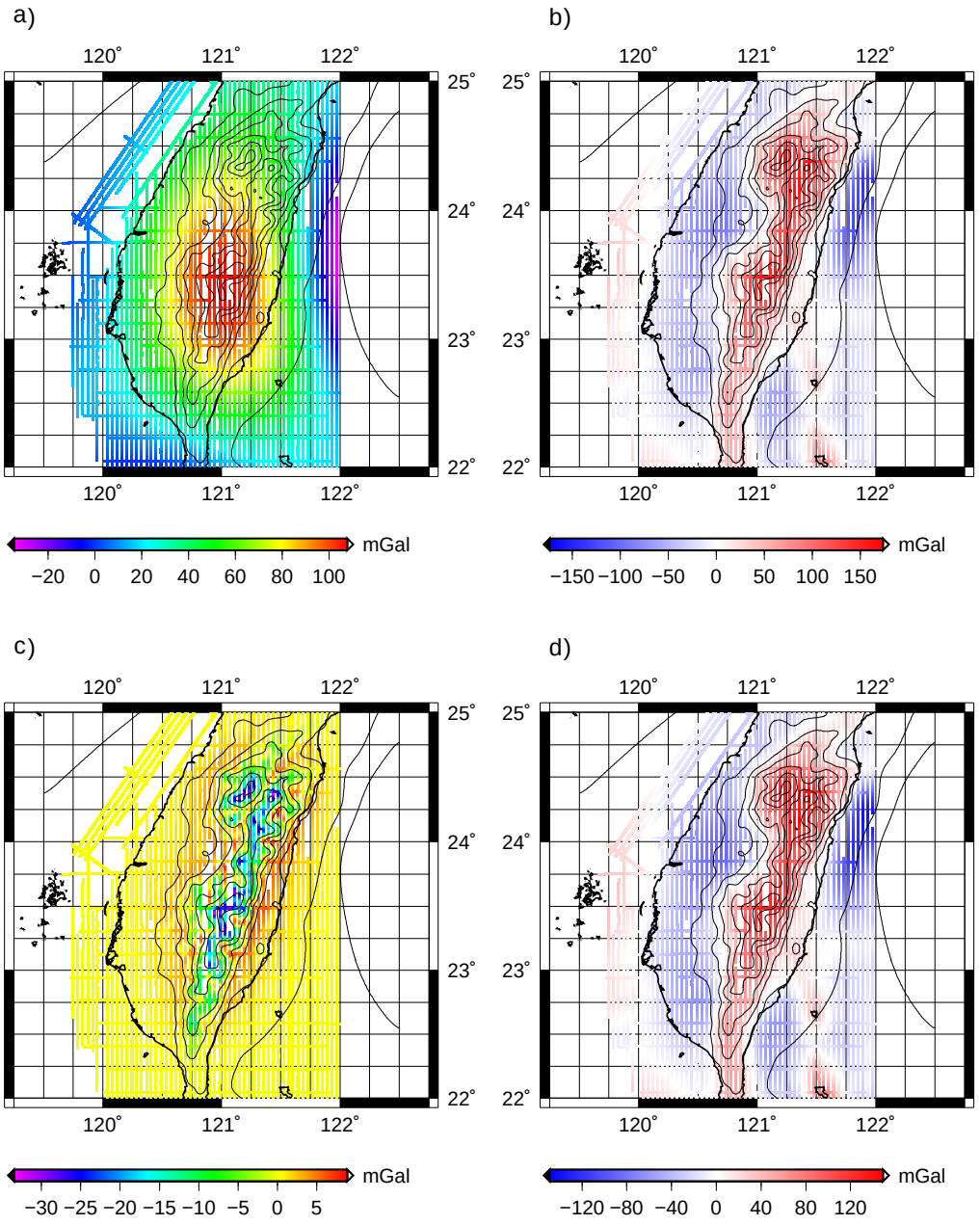

Figure E.6: Central area, $H_1 = 5156$ m: a) low-frequency gravity disturbances δg_{GGM} (GOCO03s to $n = m = 200$), b) band-limited gravity disturbances δg_b, c) band-limited DTE A_b and d) Helmert's residual gravity disturbances δg_b^H

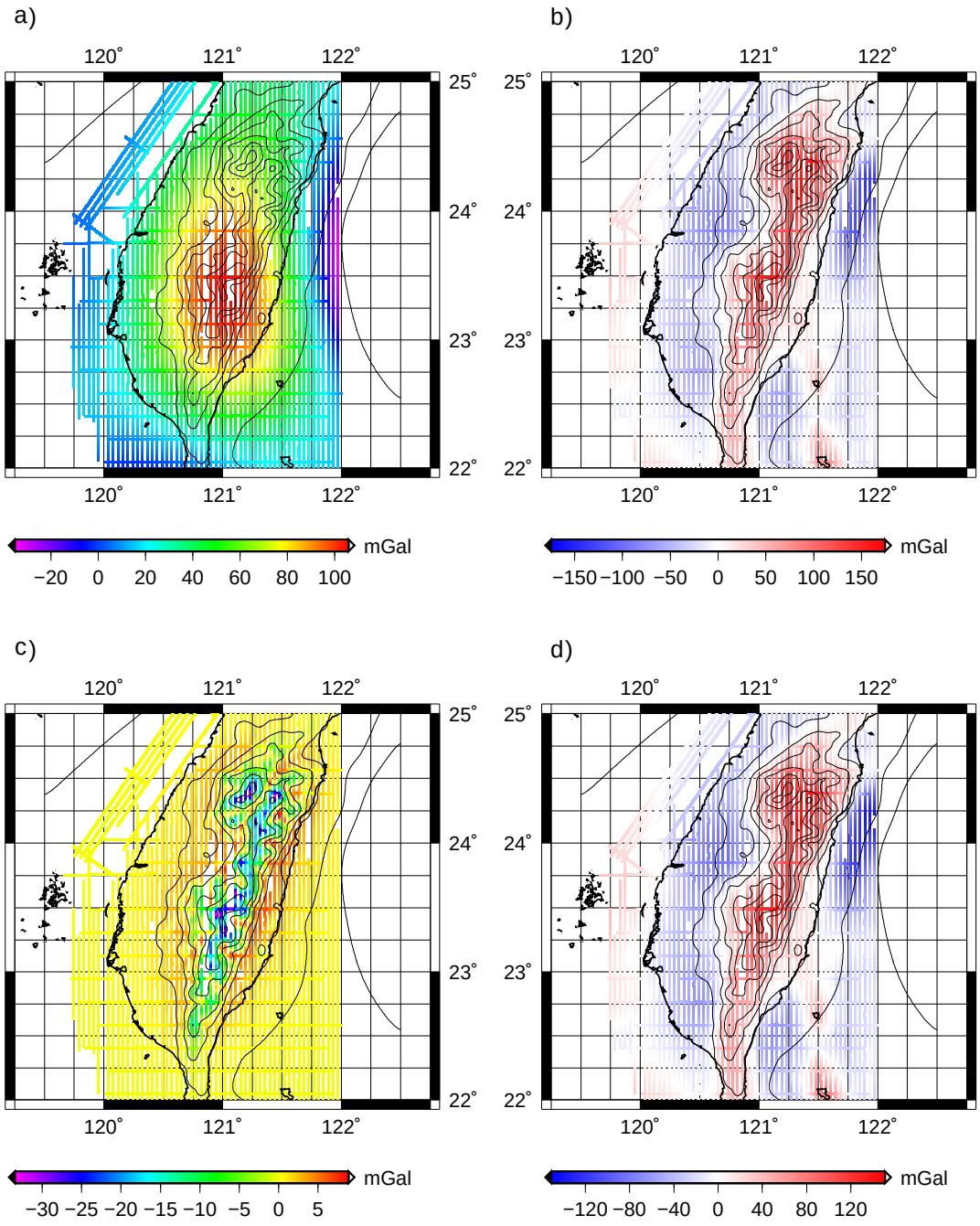

Figure E.7: Central area, $H_1 = 5156$ m: a) low-frequency gravity disturbances δg_{GGM} (EGM08 to $n = m = 200$), b) band-limited gravity disturbances δg_b, c) band-limited DTE A_b and d) Helmert's residual gravity disturbances δg_b^H

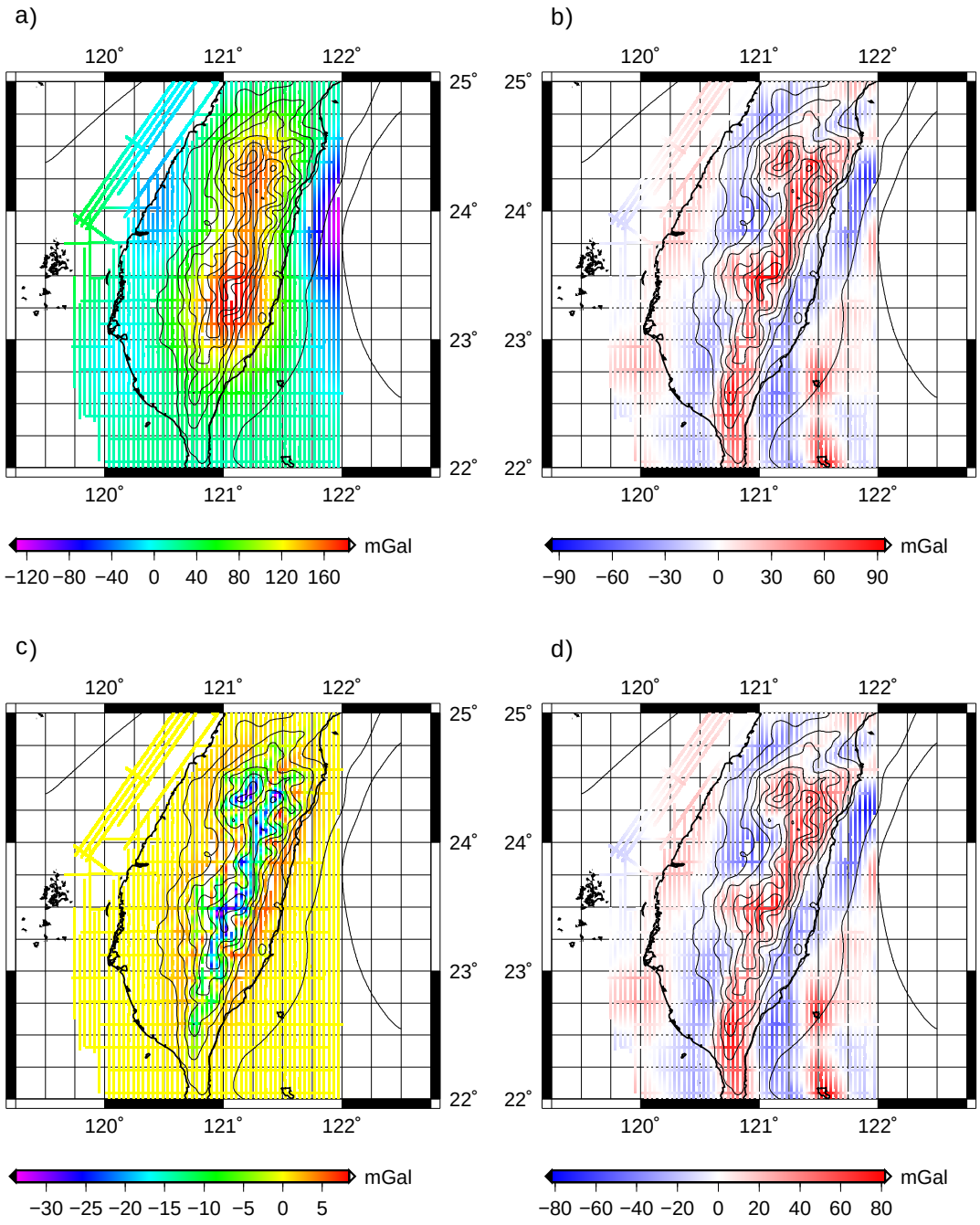

Figure E.8: Central area, $H_1 = 5156$ m: a) low-frequency gravity disturbances δg_{GGM} (EGM08 to $n = m = 360$), b) band-limited gravity disturbances δg_b, c) band-limited DTE A_b and d) Helmert's residual gravity disturbances δg_b^H

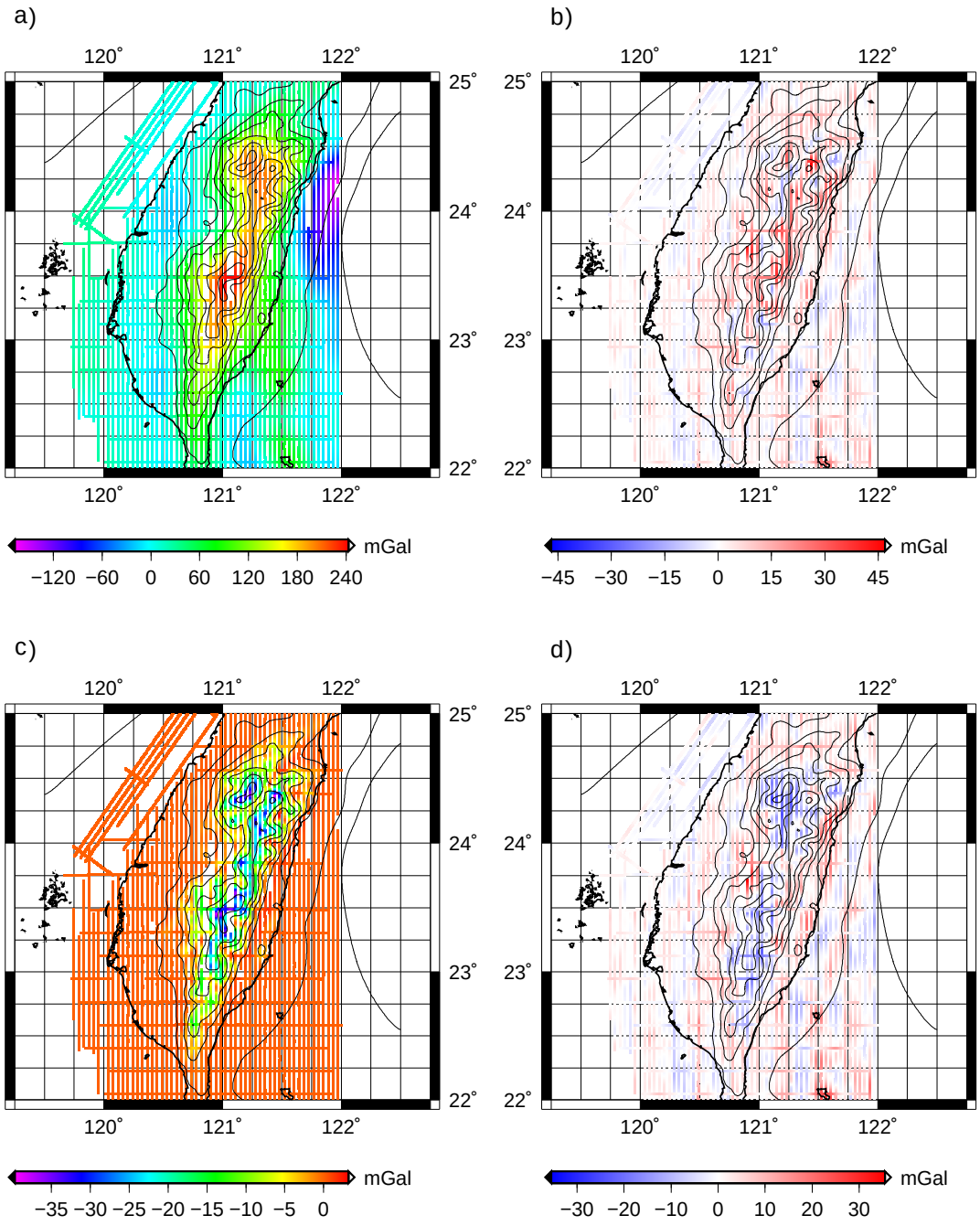

Figure E.9: Central area, $H_1 = 5156$ m: a) low-frequency gravity disturbances δg_{GGM} (EGM08 to $n = m = 1080$), b) band-limited gravity disturbances δg_b, c) band-limited DTE A_b and d) Helmert's residual gravity disturbances δg_b^H

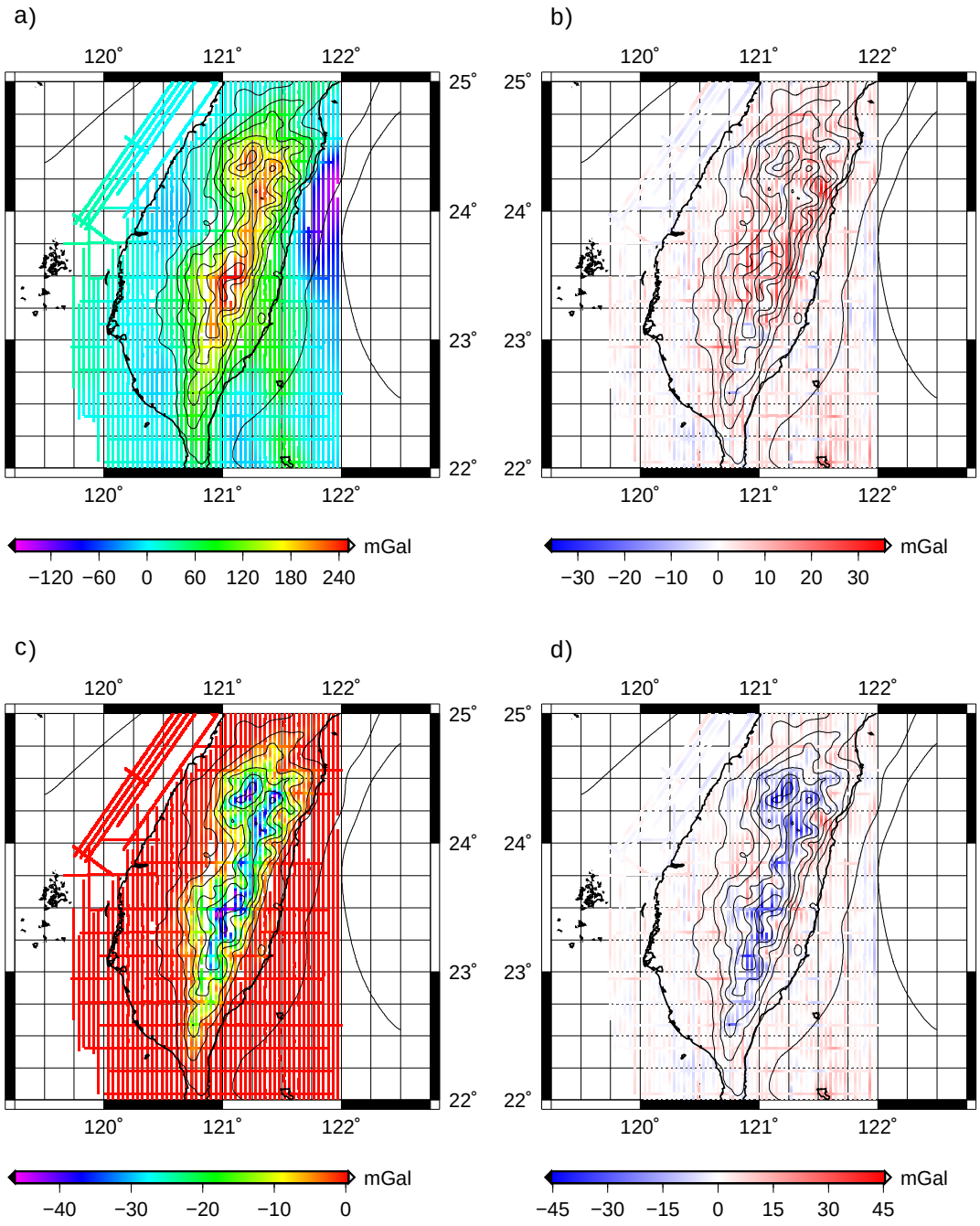

Figure E.10: Central area, $H_1 = 5156$ m: a) low-frequency gravity disturbances δg_{GGM} (EGM08 to $n = m = 2160$), b) band-limited gravity disturbances δg_b, c) band-limited DTE A_b and d) Helmert's residual gravity disturbances δg_b^H

	Mean	StDev	Min	Max	Range
aerial gravity disturbances	40.4	± 64.9	-156.6	266.2	422.8
GOCO03s to $n = m = 200$:					
δg_{GGM}	41.2	± 29.6	-34.5	107.8	142.2
δg_b	-0.8	± 48.9	-141.0	173.5	314.5
A_b	-0.3	± 4.3	-33.4	8.8	42.3
δg_b^H	-1.7	± 47.1	-140.1	148.8	289.0
EGM08 to $n = m = 200$:					
δg_{GGM}	40.4	± 29.1	-35.2	105.8	141.0
δg_b	0.0	± 48.8	-140.0	174.2	314.2
A_b	-0.3	± 4.3	-33.4	8.8	42.3
δg_b^H	-0.8	± 46.9	-139.2	150.8	290.0
EGM08 to $n = m = 360$:					
δg_{GGM}	37.6	± 53.8	-130.4	183.5	314.0
δg_b	2.8	± 25.9	-76.8	94.2	171.1
A_b	-0.8	± 4.2	-33.9	8.3	42.2
δg_b^H	2.1	± 23.8	-76.2	81.7	157.9
EGM08 to $n = m = 1080$:					
δg_{GGM}	37.4	± 62.2	-167.3	243.0	410.3
δg_b	3.0	± 6.9	-21.0	46.9	67.8
A_b	-1.8	± 5.2	-39.6	3.2	42.8
δg_b^H	1.2	± 6.1	-26.3	35.5	61.7
EGM08 to $n = m = 2160$:					
δg_{GGM}	37.4	± 62.6	-165.2	251.9	417.1
δg_b	3.0	± 5.4	-12.7	35.6	48.4
A_b	-2.7	± 6.9	-46.2	0.4	46.6
δg_b^H	0.3	± 7.0	-45.4	29.8	75.1

Table E.1: Statistics of aerial gravity data in the "remove" step – central area (mGal)

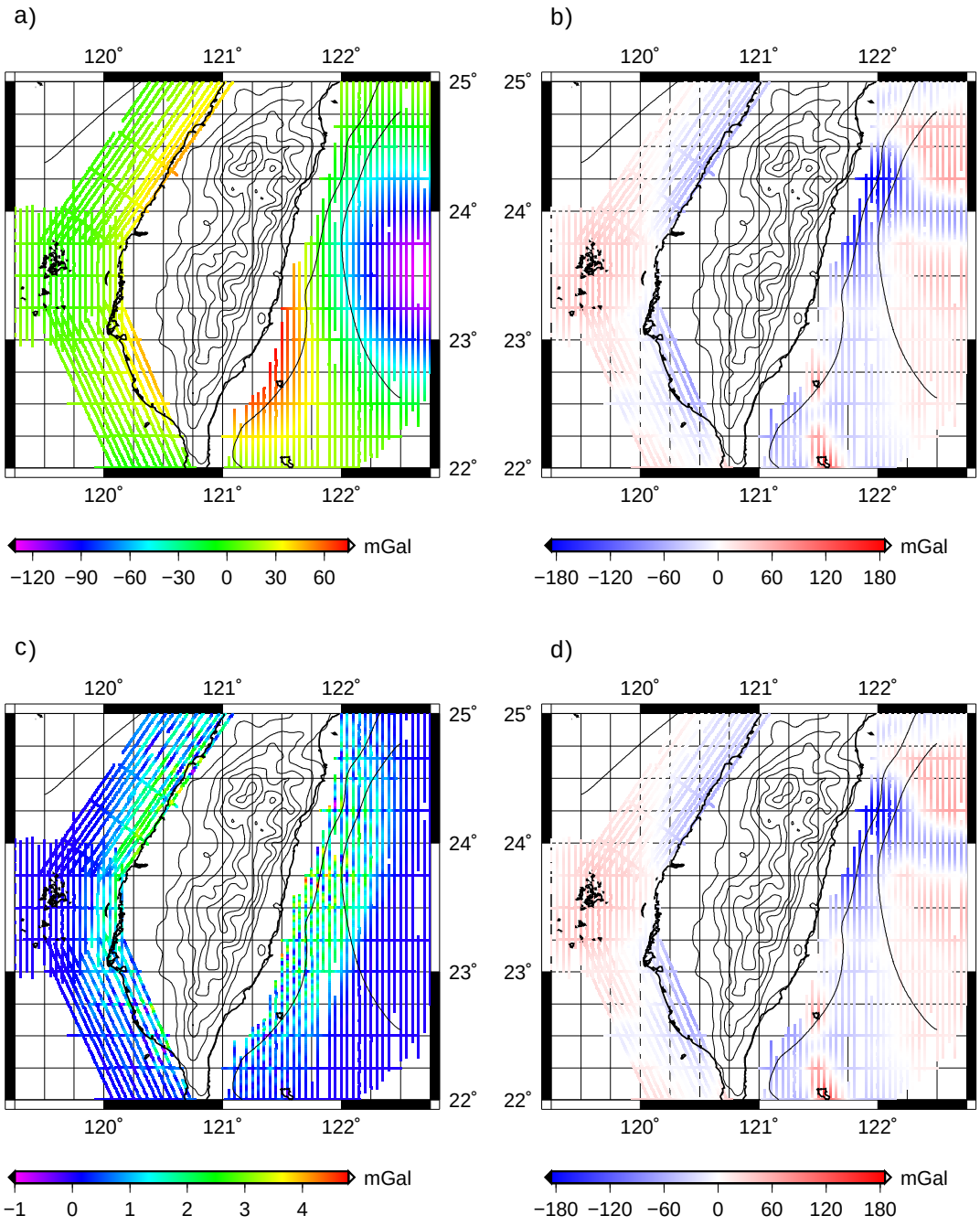

Figure E.11: Western and eastern area, $H_2 = 1620$ m: a) low-frequency gravity disturbances δg_{GGM} (GOCO03s to $n = m = 200$), b) band-limited gravity disturbances δg_b, c) band-limited DTE A_b and d) Helmert's residual gravity disturbances δg_b^H

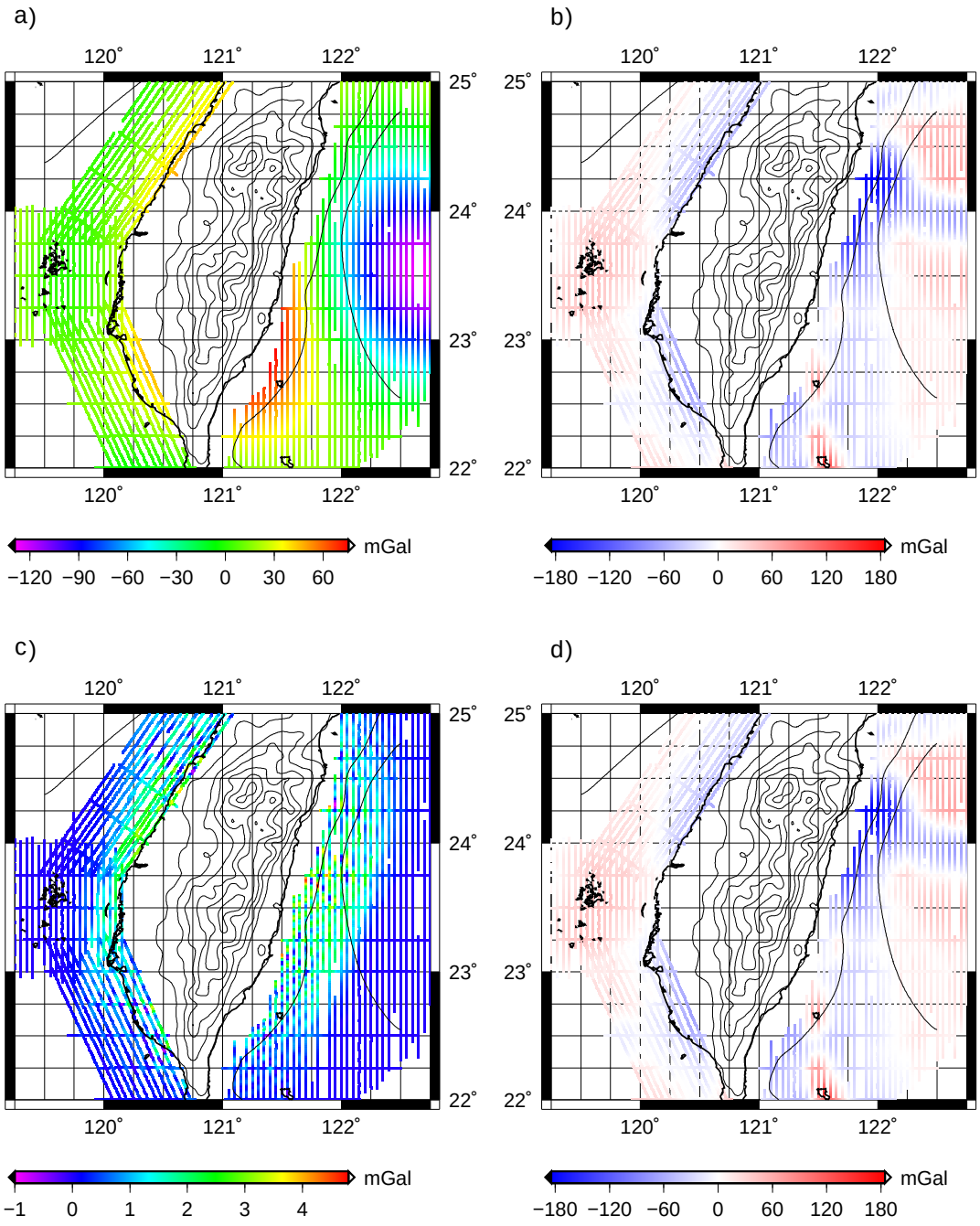

Figure E.12: Western and eastern area, $H_2 = 1620$ m: a) low-frequency gravity disturbances δg_{GGM} (EGM08 to $n = m = 200$), b) band-limited gravity disturbances δg_b, c) band-limited DTE A_b and d) Helmert's residual gravity disturbances δg_b^H

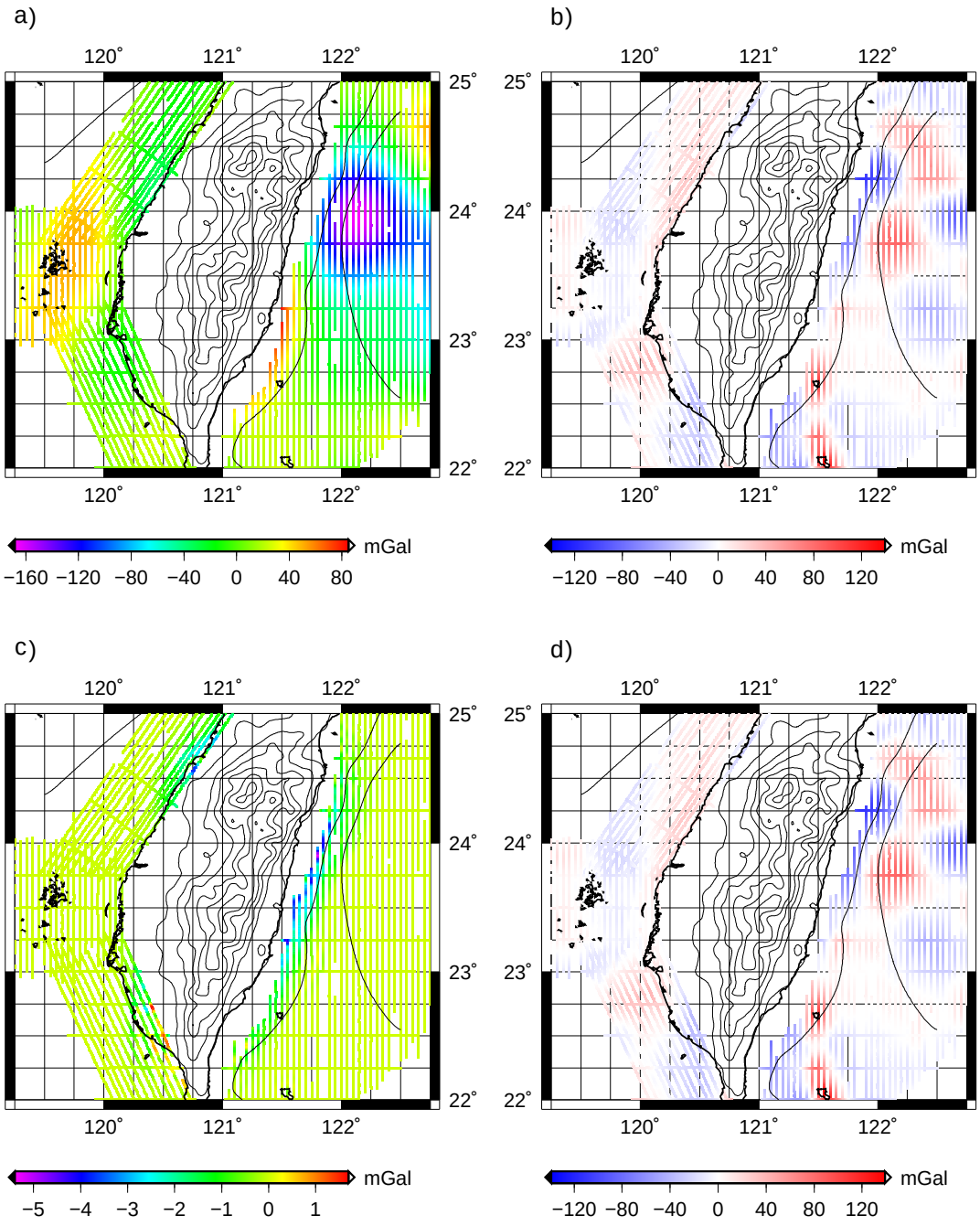

Figure E.13: Western and eastern area, $H_2 = 1620$ m: a) low-frequency gravity disturbances δg_{GGM} (EGM08 to $n = m = 360$), b) band-limited gravity disturbances δg_b, c) band-limited DTE A_b and d) Helmert's residual gravity disturbances δg_b^H

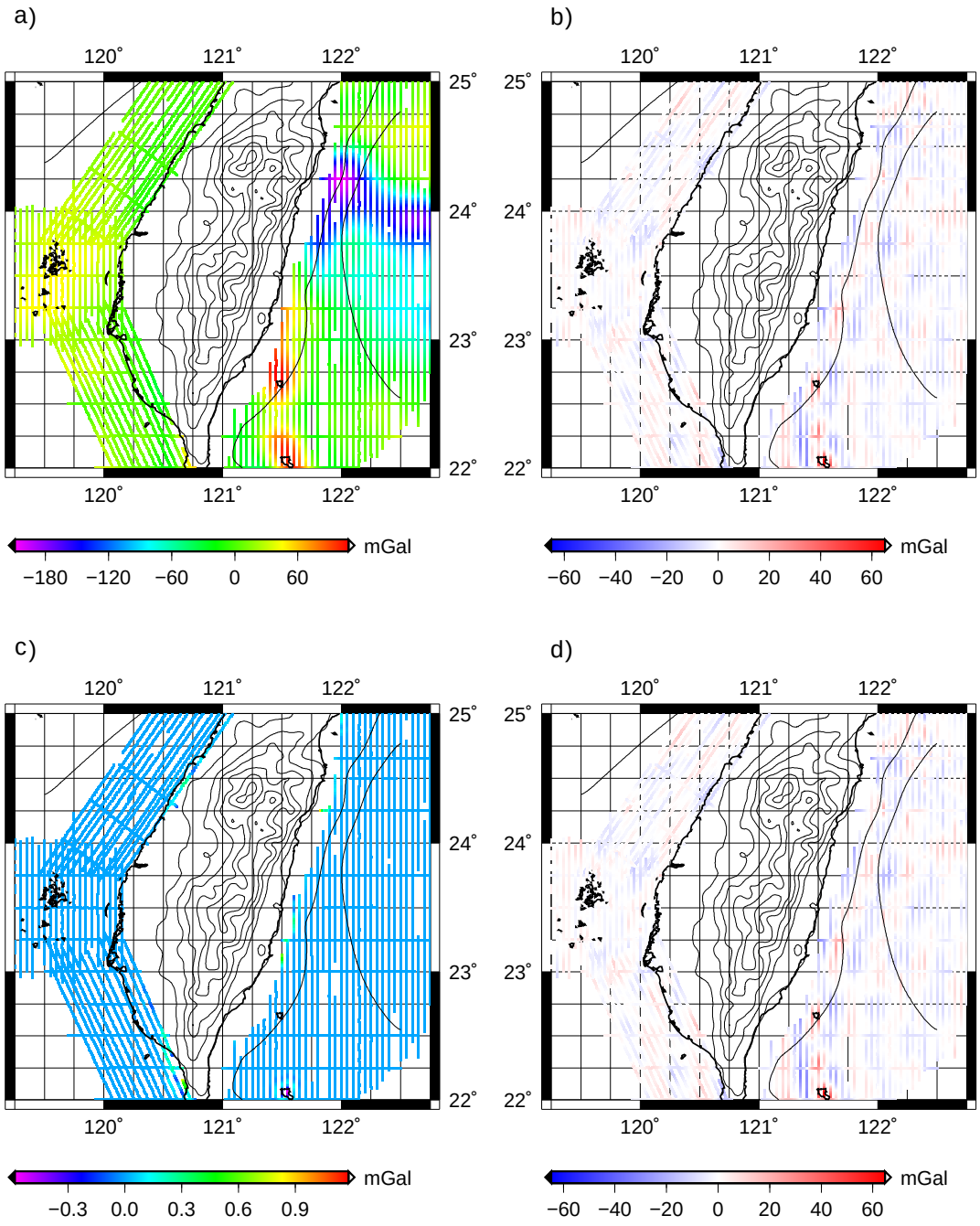

Figure E.14: Western and eastern area, $H_2 = 1620$ m: a) low-frequency gravity disturbances δg_{GGM} (EGM08 to $n = m = 1080$), b) band-limited gravity disturbances δg_b, c) band-limited DTE A_b and d) Helmert's residual gravity disturbances δg_b^H

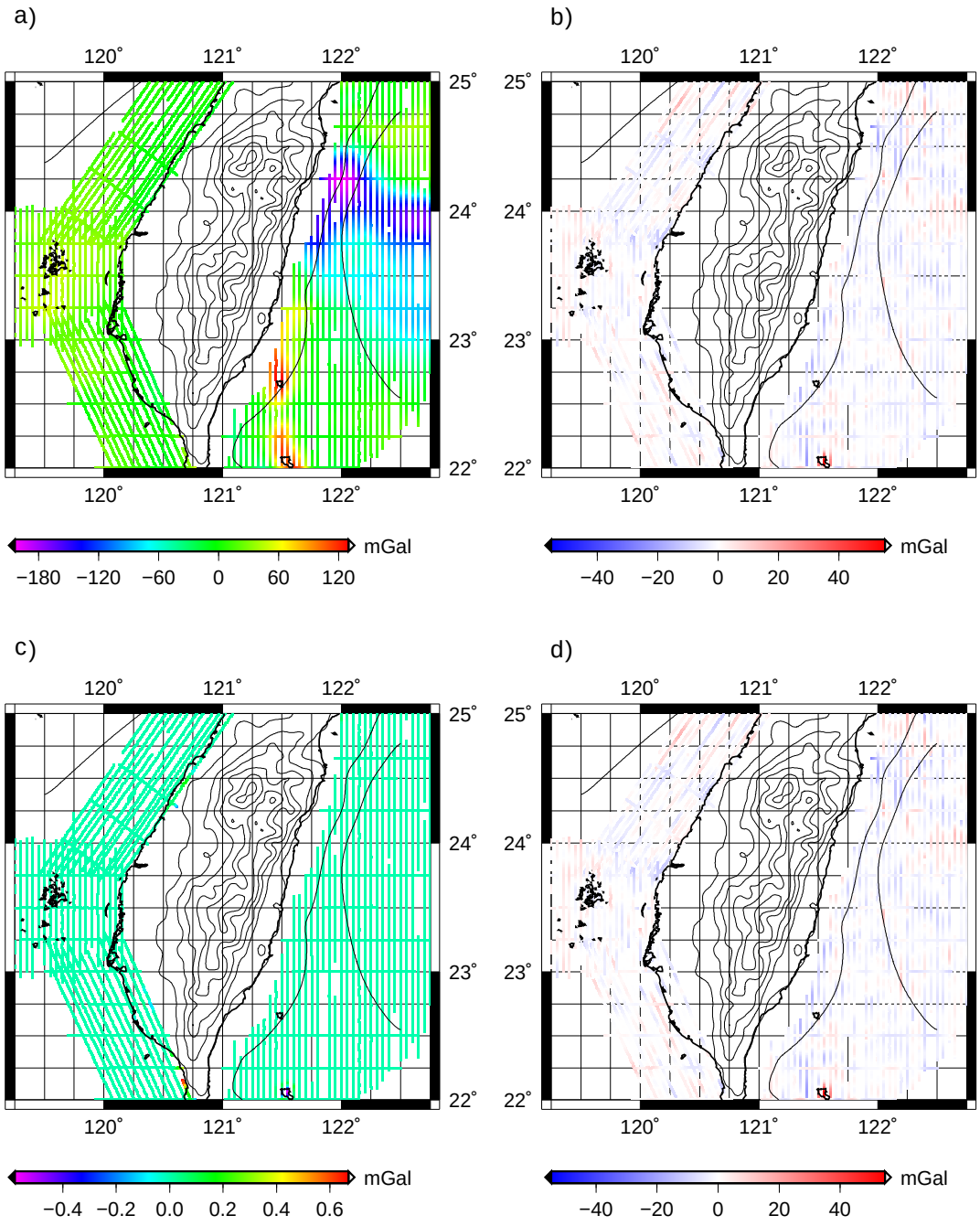

Figure E.15: Western and eastern area, $H_2 = 1620$ m: a) low-frequency gravity disturbances δg_{GGM} (EGM08 to $n = m = 2160$), b) band-limited gravity disturbances δg_b, c) band-limited DTE A_b and d) Helmert's residual gravity disturbances δg_b^H

	Mean	StDev	Min	Max	Range
aerial gravity disturbances	16.1	± 15.3	-24.6	52.3	76.9
GOCO03s to $n = m = 200$:					
δg_{GGM}	14.4	± 12.4	-20.6	53.3	73.9
δg_b	1.8	± 24.6	-69.0	48.9	117.9
A_b	0.64	± 0.70	-0.73	3.82	4.55
δg_b^H	1.8	± 24.4	-68.0	48.9	116.9
EGM08 to $n = m = 200$:					
δg_{GGM}	14.2	± 11.9	-22.1	49.4	71.5
δg_b	1.9	± 23.6	-68.4	47.2	115.7
A_b	0.64	± 0.70	-0.73	3.82	4.55
δg_b^H	1.9	± 23.4	-67.5	47.3	114.8
EGM08 to $n = m = 360$:					
δg_{GGM}	14.8	± 20.0	-39.3	51.7	91.0
δg_b	1.4	± 13.2	-36.7	38.7	75.5
A_b	-0.14	± 0.41	-3.76	1.64	5.40
δg_b^H	1.2	± 13.2	-37.1	38.7	75.9
EGM08 to $n = m = 1080$:					
δg_{GGM}	16.3	± 15.5	-34.7	57.2	91.9
δg_b	-0.2	± 4.4	-18.5	14.2	32.7
A_b	0.00	± 0.03	-0.14	0.80	0.94
δg_b^H	-0.2	± 4.4	-18.0	14.2	32.2
EGM08 to $n = m = 2160$:					
δg_{GGM}	16.3	± 15.4	-23.9	53.3	77.1
δg_b	-0.1	± 3.7	-14.2	15.9	30.1
A_b	0.00	± 0.02	-0.18	0.66	0.84
δg_b^H	-0.1	± 3.7	-14.2	15.9	30.1

Table E.2: Statistics of aerial gravity data in the “remove” step – western area (mGal)

	Mean	StDev	Min	Max	Range
aerial gravity disturbances	-29.4	± 63.1	-207.1	163.2	370.3
GOCO03s to $n = m = 200$:					
δg_{GGM}	-18.9	± 49.5	-131.0	75.0	206.0
δg_b	-10.5	± 48.7	-185.8	140.0	325.8
A_b	0.63	± 0.80	-0.98	4.72	5.70
δg_b^H	-10.0	± 48.4	-185.2	139.7	324.9
EGM08 to $n = m = 200$:					
δg_{GGM}	-19.0	± 48.8	-129.2	75.6	204.8
δg_b	-10.4	± 48.3	-184.8	142.1	326.9
A_b	0.63	± 0.80	-0.98	4.72	5.70
δg_b^H	-10.0	± 48.0	-184.2	141.8	326.0
EGM08 to $n = m = 360$:					
δg_{GGM}	-28.0	± 55.5	-168.4	85.0	253.4
δg_b	-1.4	± 33.7	-110.8	139.5	250.4
A_b	-0.24	± 0.63	-5.36	0.38	5.74
δg_b^H	-1.6	± 33.9	-111.9	139.0	250.9
EGM08 to $n = m = 1080$:					
δg_{GGM}	-28.1	± 62.8	-209.0	108.1	317.1
δg_b	-1.3	± 7.6	-32.0	65.1	97.1
A_b	0.00	± 0.04	-0.57	1.18	1.75
δg_b^H	-1.3	± 7.5	-32.0	64.7	96.7
EGM08 to $n = m = 2160$:					
δg_{GGM}	-28.1	± 63.0	-203.8	129.9	333.7
δg_b	-1.3	± 4.4	-27.2	55.2	82.4
A_b	0.00	± 0.01	-0.57	0.12	0.70
δg_b^H	-1.3	± 4.4	-27.2	54.7	81.8

Table E.3: Statistics of aerial gravity data in the "remove" step – eastern area (mGal)

E.3 Restore step – test area

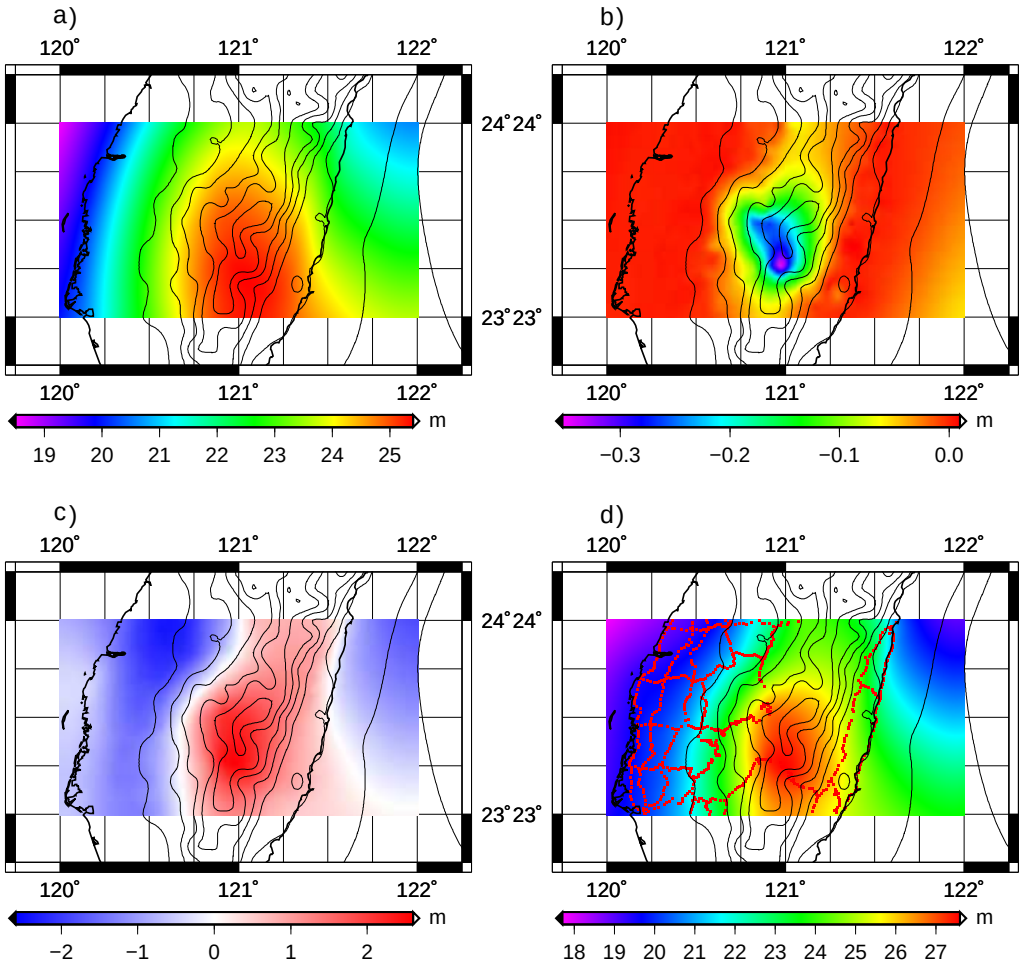

Figure E.16: Test area, N-NC: a) low-frequency geoid N_{GGM} (GOCO03s to $n = m = 200$), b) band-limited ITE P_b (I), c) Helmert's residual geoid N_b^H (I) and d) final geoid N (I)

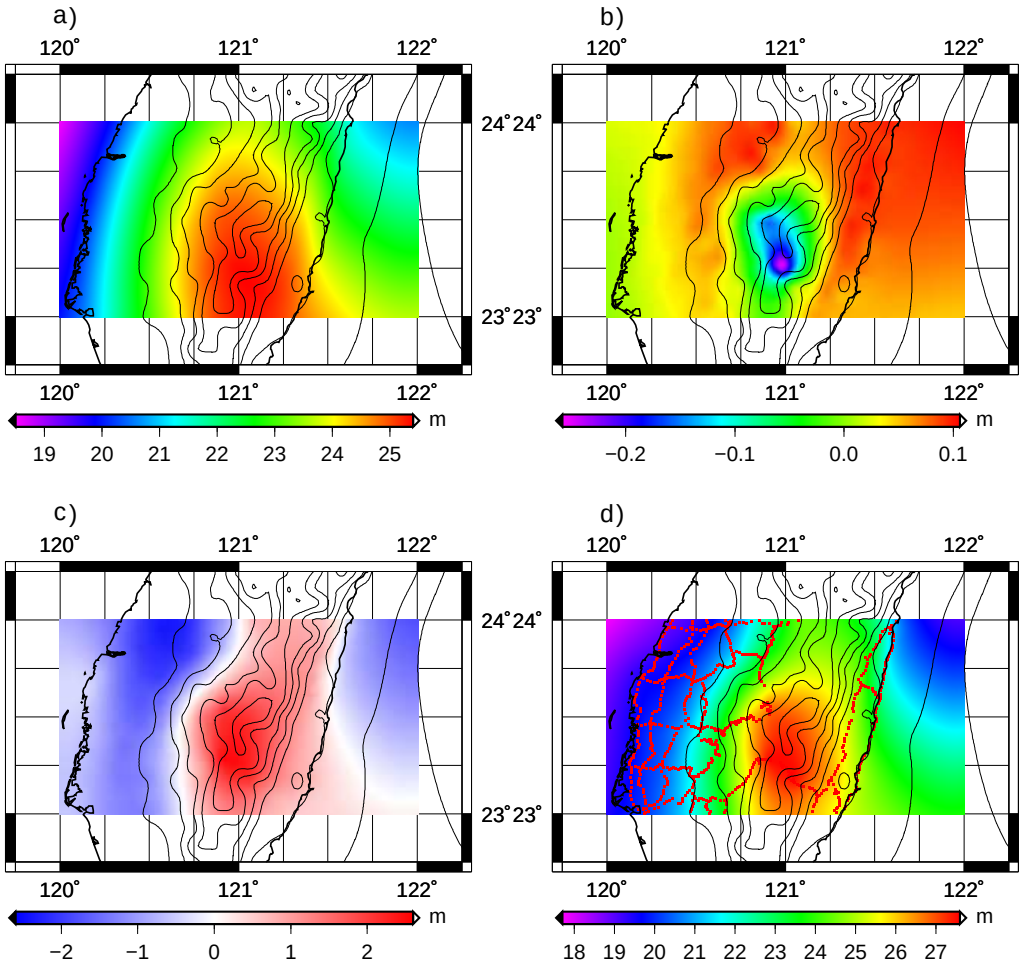

Figure E.17: Test area, N-NC: a) low-frequency geoid N_{GGM} (GOCO03s to $n = m = 200$), b) band-limited ITE P_b (FS), c) Helmert's residual geoid N_b^H (FS) and d) final geoid N (FS)

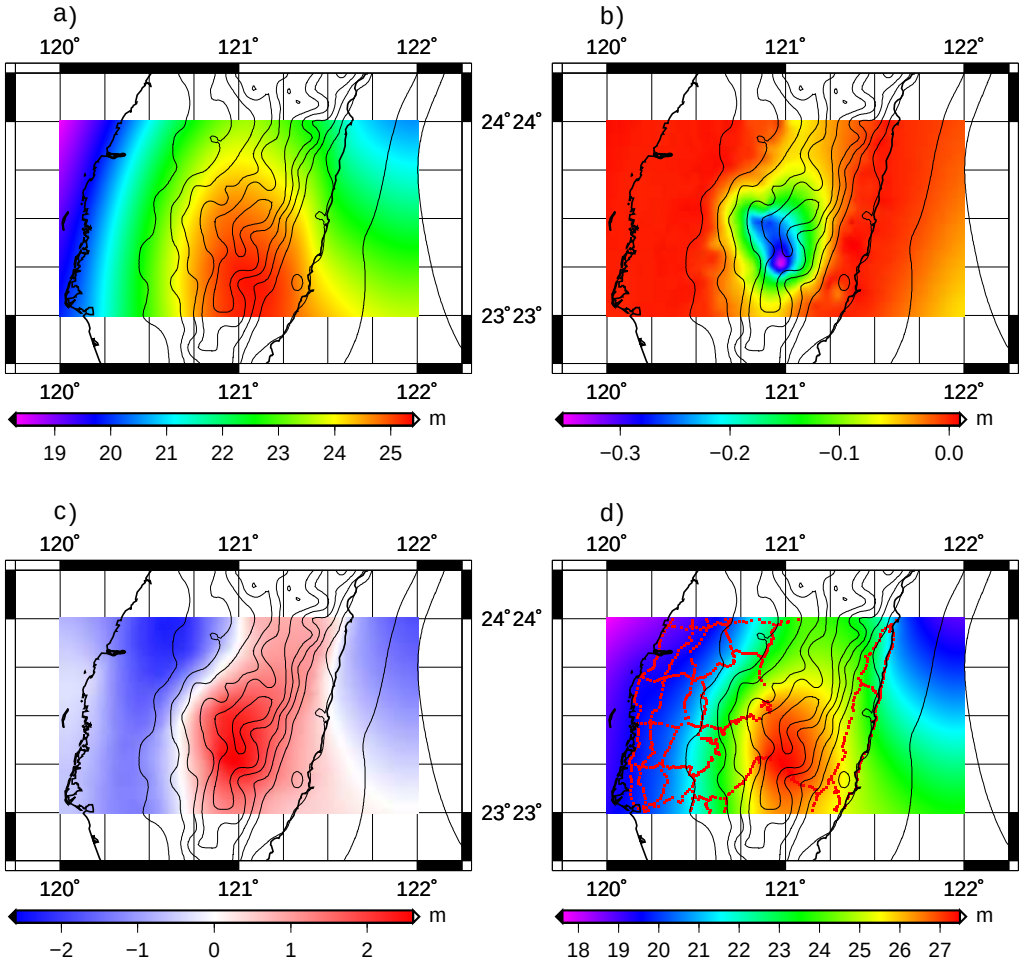

Figure E.18: Test area, N-NC: a) low-frequency geoid N_{GGM} (EGM08 to $n = m = 200$), b) band-limited ITE P_b (I), c) Helmert's residual geoid N_b^H (I) and d) final geoid N (I)

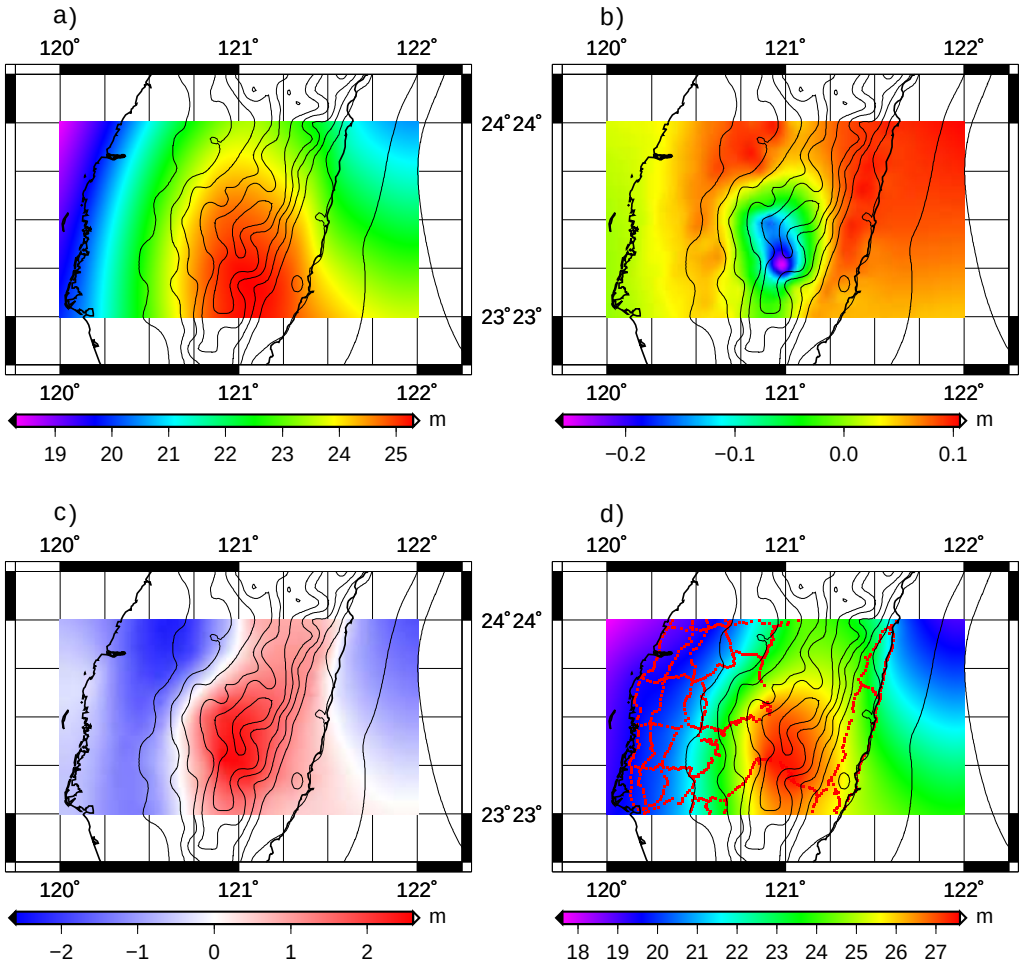

Figure E.19: Test area, N-NC: a) low-frequency geoid N_{GGM} (EGM08 to $n = m = 200$), b) band-limited ITE P_b (FS), c) Helmert's residual geoid N_b^H (FS) and d) final geoid N (FS)

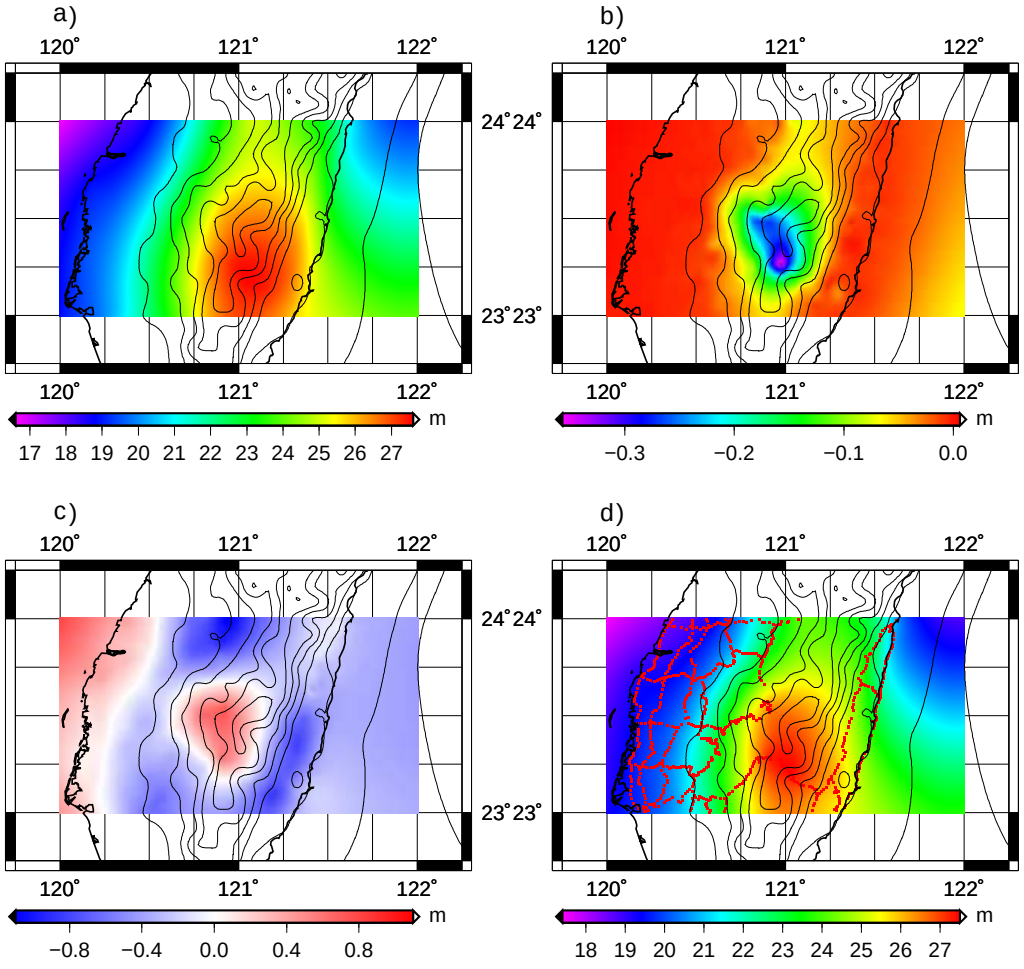

Figure E.20: Test area, N-NC: a) low-frequency geoid N_{GGM} (EGM08 to $n = m = 360$), b) band-limited ITE P_b (I), c) Helmert's residual geoid N_b^H (I) and d) final geoid N (I)

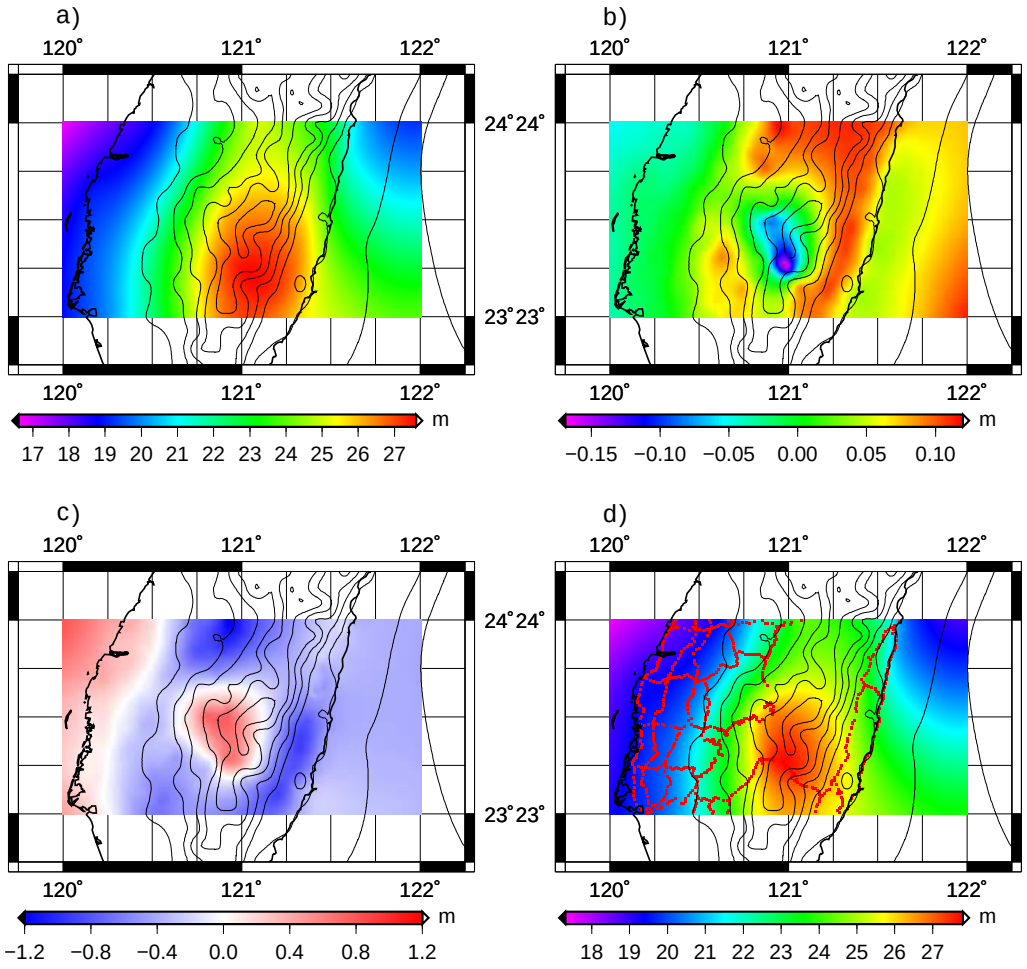

Figure E.21: Test area, N-NC: a) low-frequency geoid N_{GGM} (EGM08 to $n = m = 360$), b) band-limited ITE P_b (FS), c) Helmert's residual geoid N_b^H (FS) and d) final geoid N (FS)

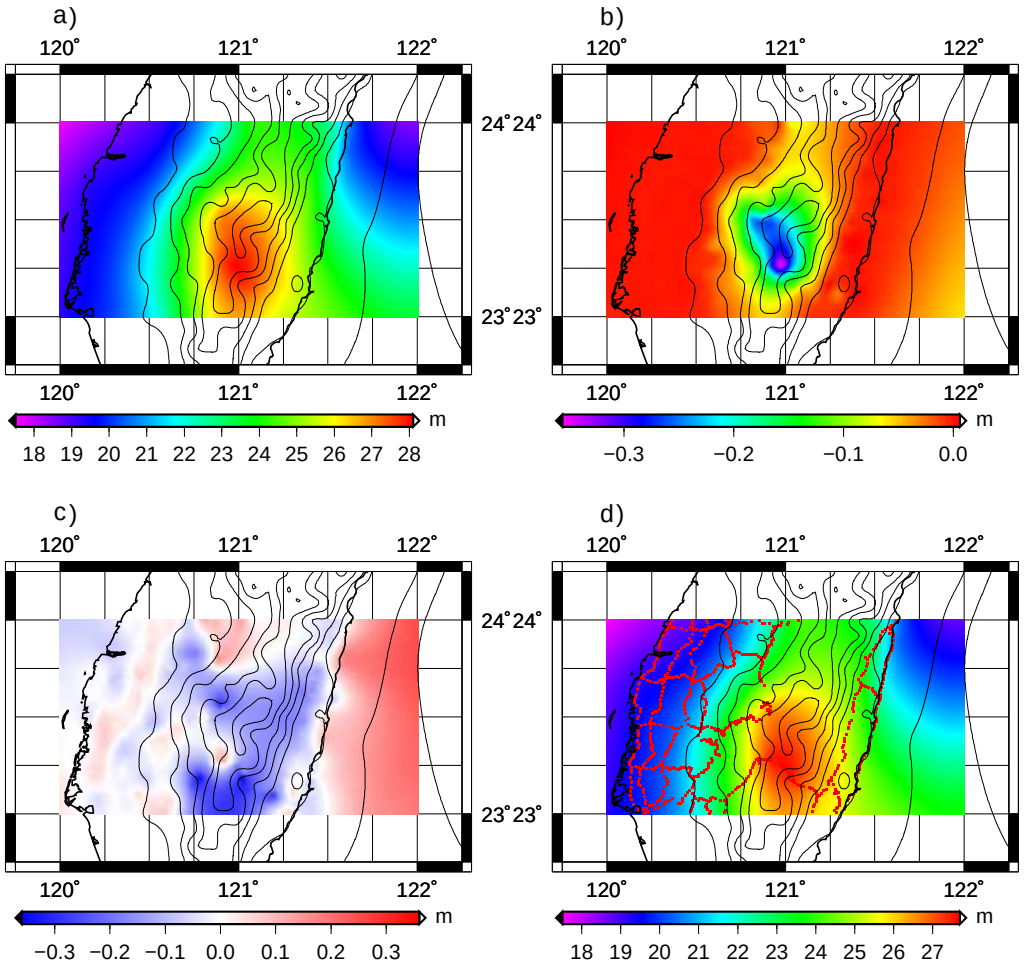

Figure E.22: Test area, N-NC: a) low-frequency geoid N_{GGM} (EGM08 to $n = m = 1080$), b) band-limited ITE P_b (I), c) Helmert's residual geoid N_b^H (I) and d) final geoid N (I)

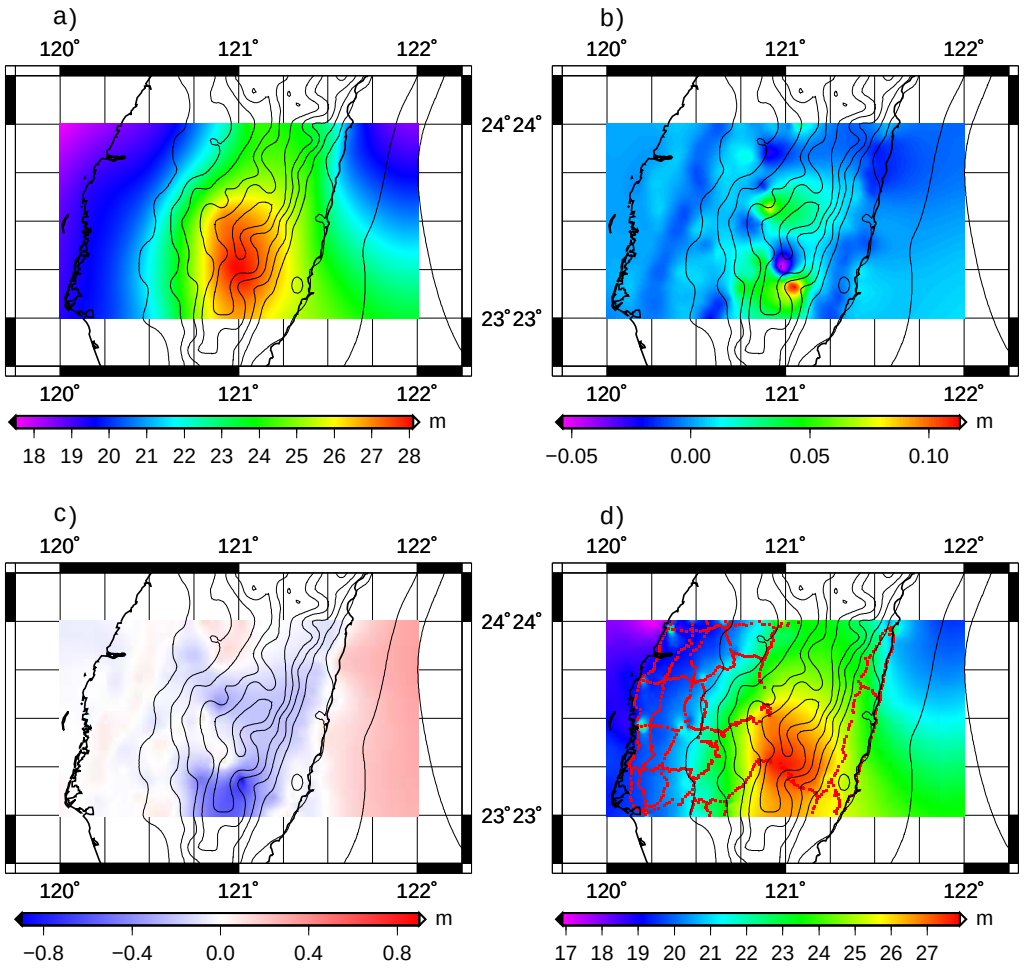

Figure E.23: Test area, N-NC: a) low-frequency geoid N_{GGM} (EGM08 to $n = m = 1080$), b) band-limited ITE P_b (FS), c) Helmert's residual geoid N_b^H (FS) and d) final geoid N (FS)

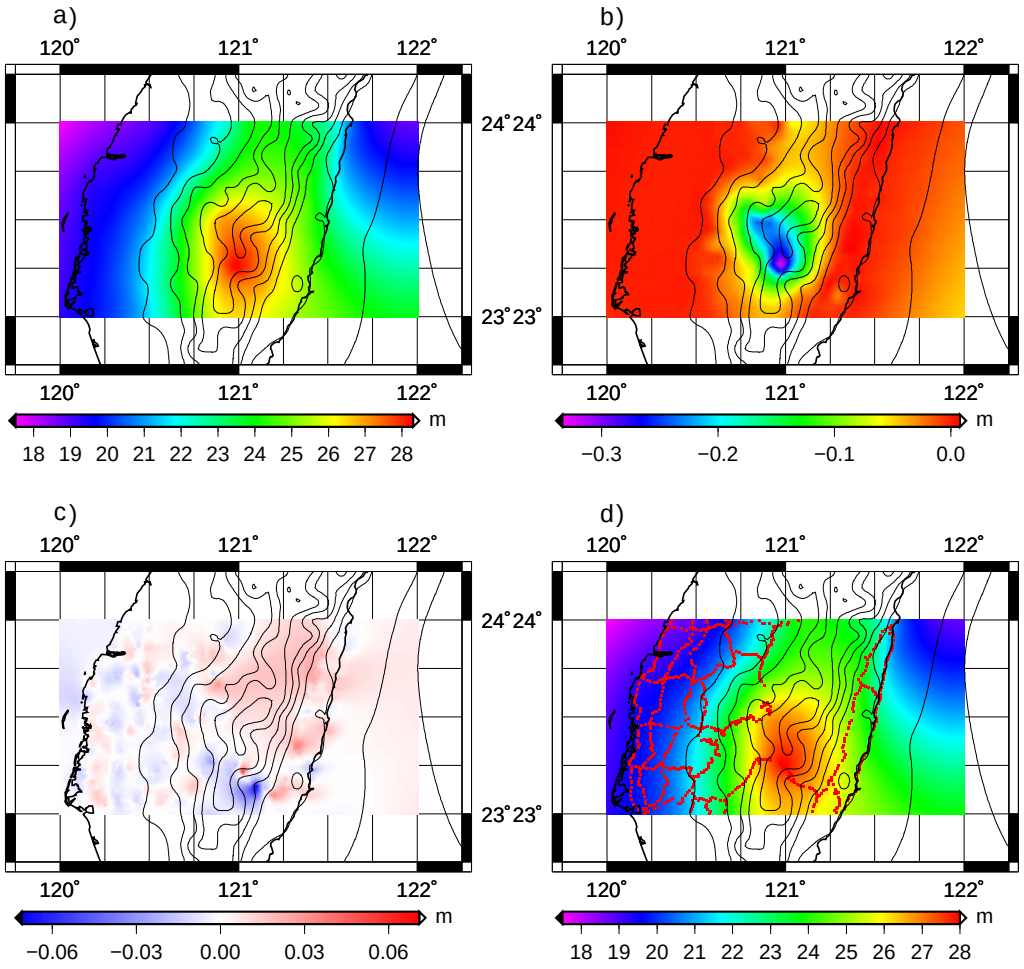

Figure E.24: Test area, N-NC: a) low-frequency geoid N_{GGM} (EGM08 to $n = m = 2160$), b) band-limited ITE P_b (I), c) Helmert's residual geoid N_b^H (I) and d) final geoid N (I)

	Mean	StDev	Min	Max	Range
$N_{GNSS/lev}$	22.317	$\pm$ 2.449	18.763	27.955	9.192
GOCO03s to $n = m = 200$:					
N_{GGM}	22.668	$\pm$ 1.510	19.821	25.295	5.473
P_b (I)	-0.020	$\pm$ 0.055	-0.357	0.009	0.366
P_b (FS)	0.041	$\pm$ 0.051	-0.260	0.101	0.361
N_b^H (I)	-0.531	$\pm$ 1.150	-2.405	2.582	4.987
N_b^H (FS)	-0.604	$\pm$ 1.184	-2.598	2.551	5.149
N (I)	22.275	$\pm$ 2.385	18.808	27.571	8.763
N (FS)	22.201	$\pm$ 2.389	18.791	27.579	8.789
EGM08 to $n = m = 200$:					
N_{GGM}	22.668	$\pm$ 1.510	19.821	25.295	5.473
P_b (I)	-0.020	$\pm$ 0.055	-0.357	0.009	0.366
P_b (FS)	0.041	$\pm$ 0.051	-0.260	0.101	0.361
N_b^H (I)	-0.488	$\pm$ 1.134	-2.319	2.604	4.923
N_b^H (FS)	-0.587	$\pm$ 1.165	-2.542	2.537	5.079
N (I)	22.160	$\pm$ 2.394	18.667	27.471	8.805
N (FS)	22.061	$\pm$ 2.395	18.624	27.454	8.831
EGM08 to $n = m = 360$:					
N_{GGM}	22.285	$\pm$ 2.589	18.151	27.559	9.408
P_b (I)	-0.028	$\pm$ 0.054	-0.362	0.000	0.361
P_b (FS)	0.028	$\pm$ 0.048	-0.171	0.119	0.290
N_b^H (I)	-0.180	$\pm$ 0.365	-1.089	0.742	1.831
N_b^H (FS)	-0.218	$\pm$ 0.390	-1.191	0.777	1.968
N (I)	22.077	$\pm$ 2.452	18.537	27.480	8.943
N (FS)	22.096	$\pm$ 2.482	18.504	27.773	9.268

	Mean	StDev	Min	Max	Range
EGM08 to $n = m = 1080$:					
N_{GGM}	22.094	± 2.500	18.578	28.060	9.482
P_b (I)	-0.023	± 0.055	-0.359	0.005	0.364
P_b (FS)	0.003	± 0.017	-0.055	0.113	0.167
N_b^H (I)	-0.024	± 0.086	-0.364	0.173	0.537
N_b^H (FS)	-0.042	± 0.126	-0.832	0.190	1.022
N (I)	22.047	± 2.427	18.574	27.632	9.058
N (FS)	22.055	± 2.439	18.580	27.883	9.302
EGM08 to $n = m = 2160$:					
N_{GGM}	22.080	± 2.472	18.551	28.265	9.714
P_b (I)	-0.019	± 0.049	-0.338	0.008	0.346
P_b (FS)	–	–	–	–	–
N_b^H (I)	0.001	± 0.010	-0.072	0.055	0.127
N_b^H (FS)	–	–	–	–	–
N (I)	22.062	± 2.443	18.551	27.919	9.368
N (FS)	–	–	–	–	–

Table E.4: Statistics of the parameters in the “restore” step (N-NC) – test area (m)

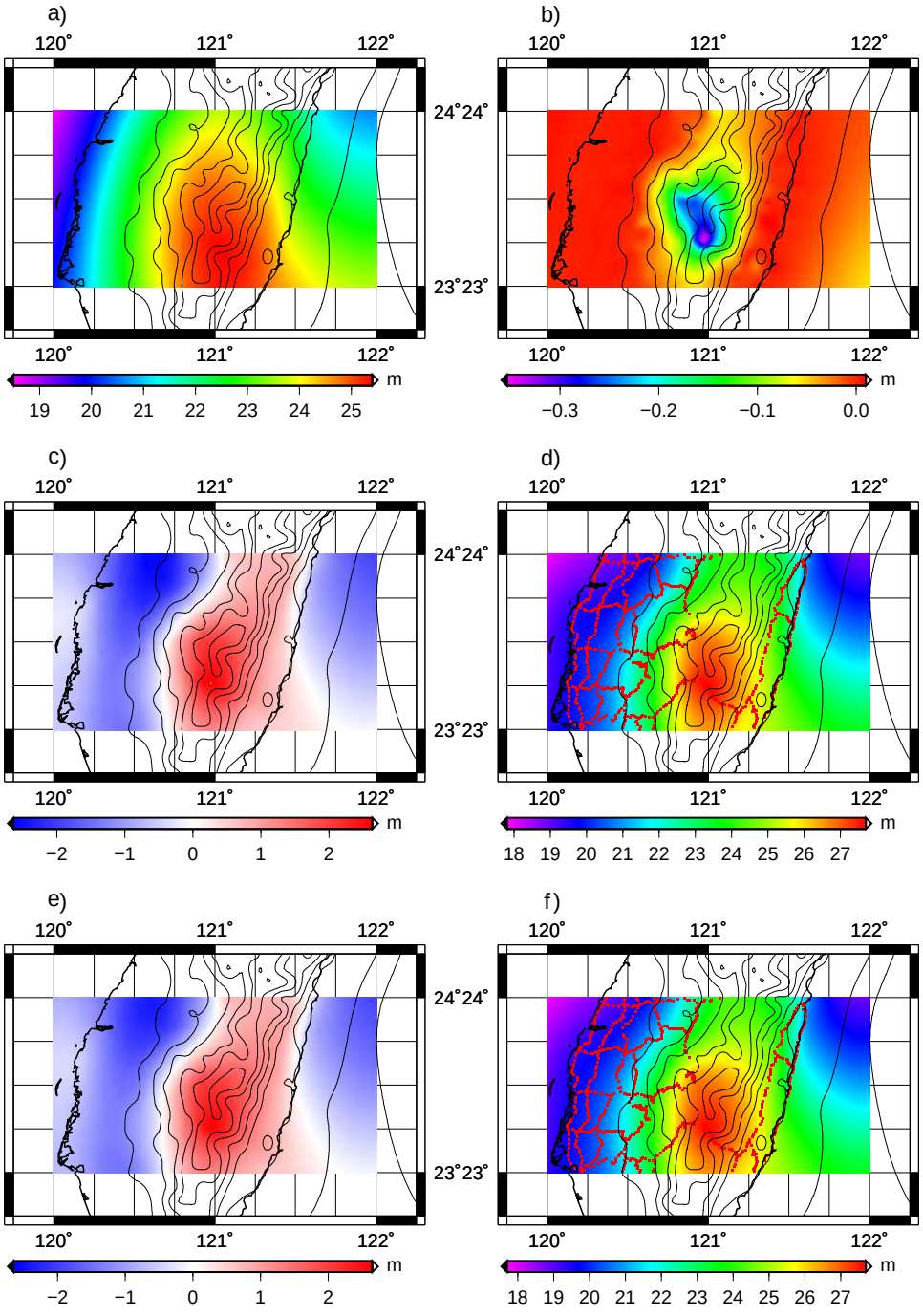

Figure E.25: Test area: a) low-frequency geoid N_{GGM} (GOCO03s to $n = m = 200$), b) band-limited ITE P_b, c) Helmert's residual geoid N_b^H (N-WT), d) final geoid N (N-WT), e) Helmert's residual geoid N_b^H (AC+H) and f) final geoid N (AC+H)

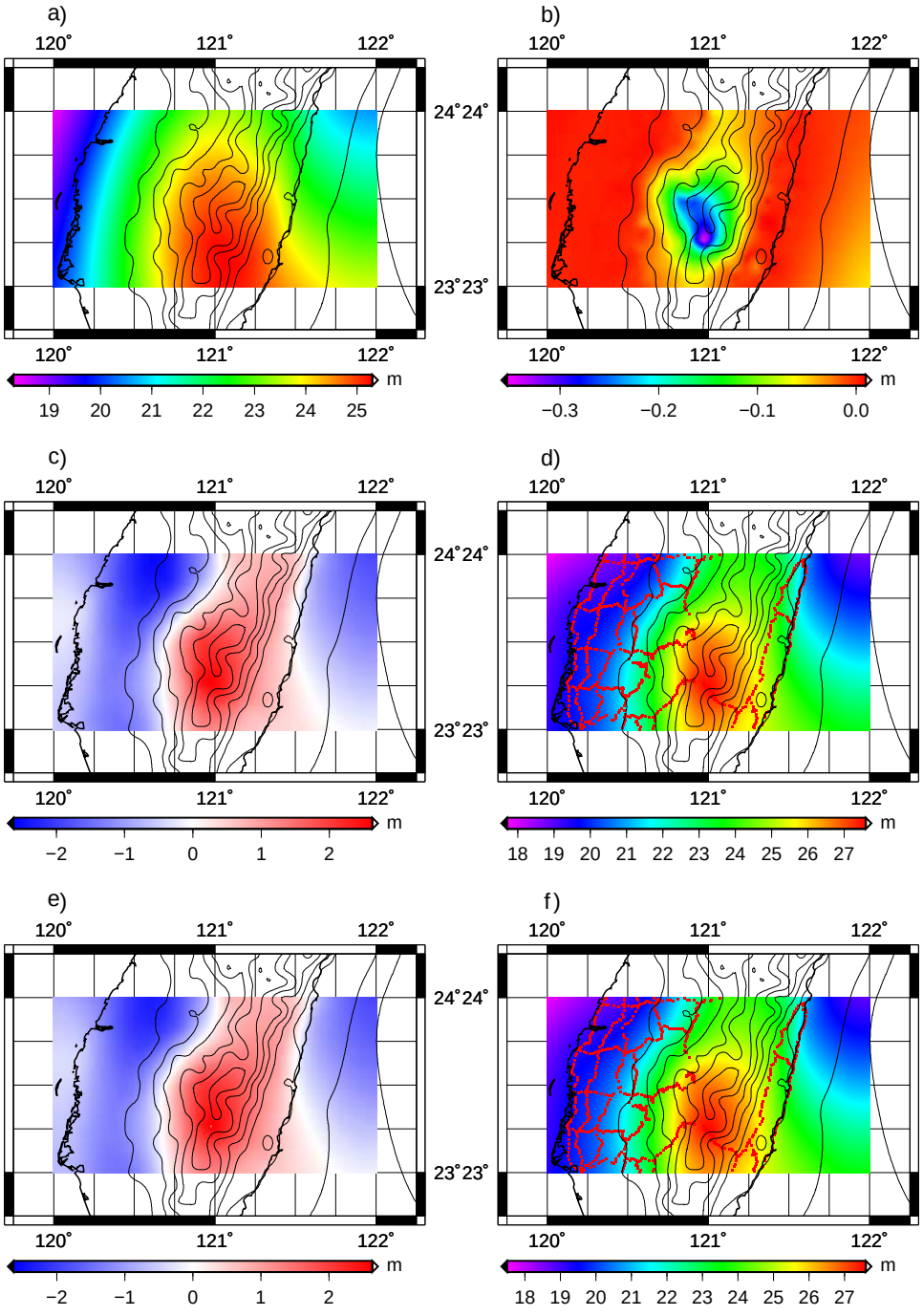

Figure E.26: Test area: a) low-frequency geoid N_{GGM} (EGM08 to $n = m = 200$), b) band-limited ITE P_b, c) Helmert's residual geoid N_b^H (N-WT), d) final geoid N (N-WT), e) Helmert's residual geoid N_b^H (AC+H) and f) final geoid N (AC+H)

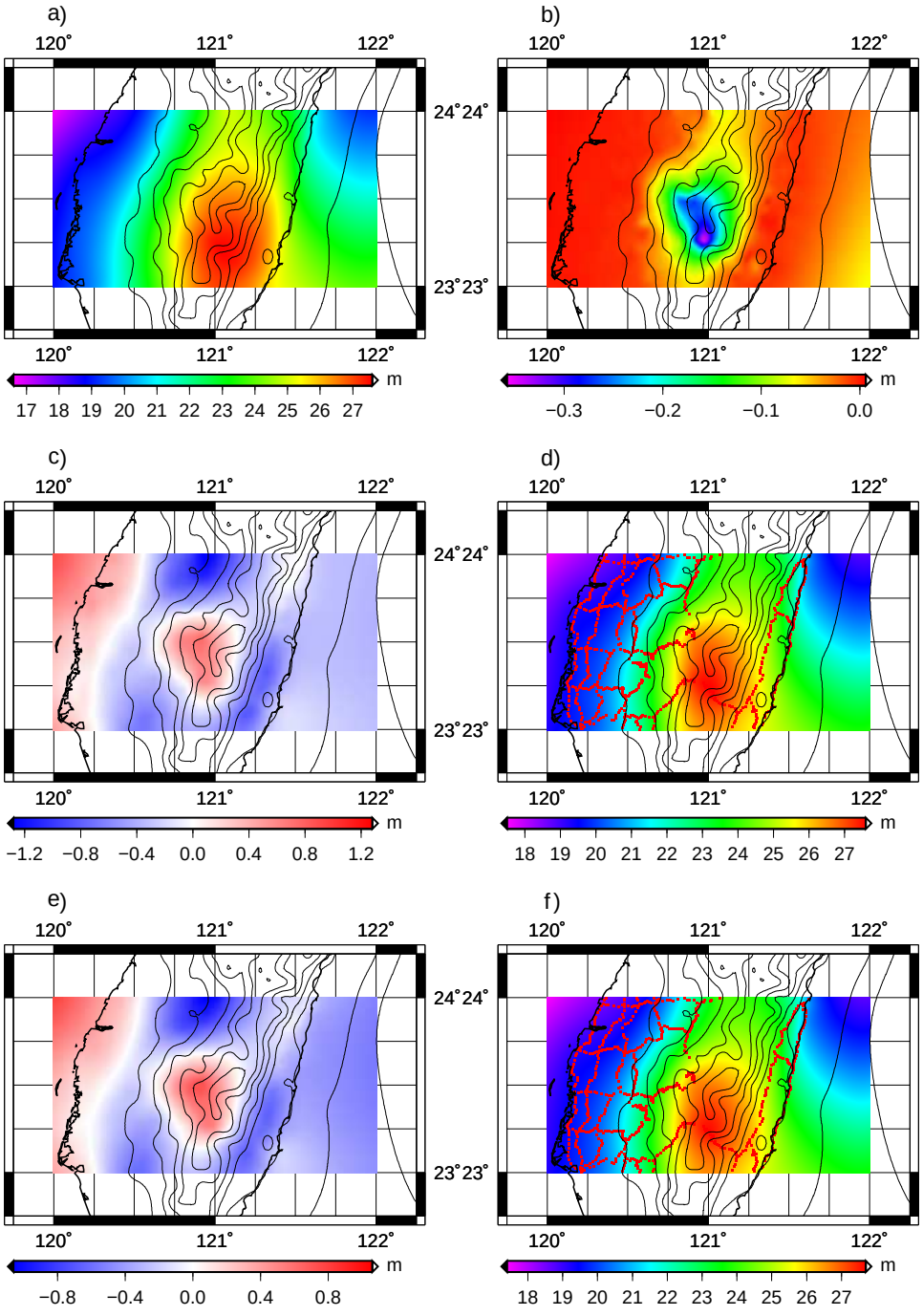

Figure E.27: Test area: a) low-frequency geoid N_{GGM} (EGM08 to $n = m = 360$), b) band-limited ITE P_b, c) Helmert's residual geoid N_b^H (N-WT), d) final geoid N (N-WT), e) Helmert's residual geoid N_b^H (AC+H) and f) final geoid N (AC+H)

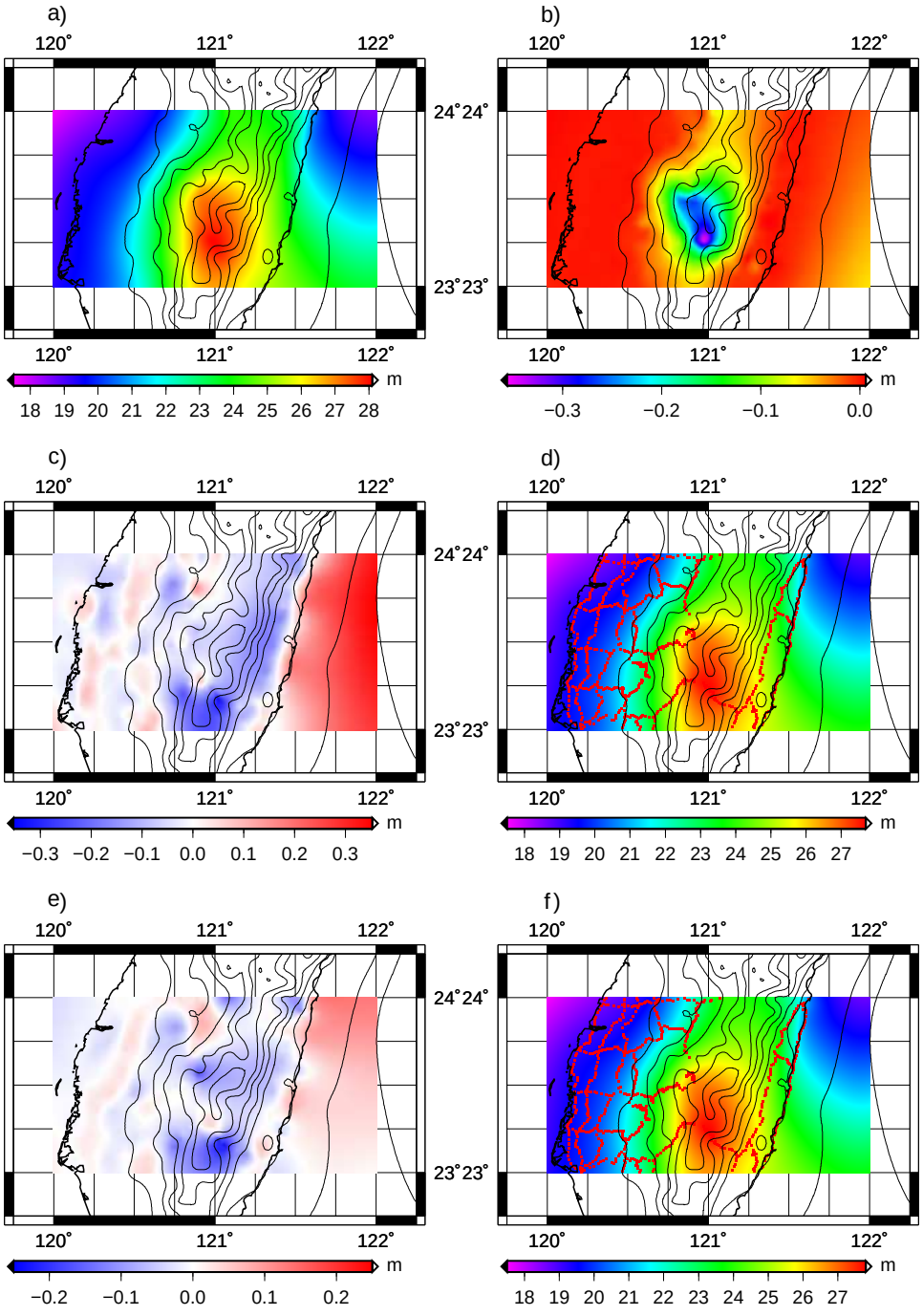

Figure E.28: Test area: a) low-frequency geoid N_{GGM} (EGM08 to $n = m = 1080$), b) band-limited ITE P_b, c) Helmert's residual geoid N_b^H (N-WT), d) final geoid N (N-WT), e) Helmert's residual geoid N_b^H (AC+H) and f) final geoid N (AC+H)

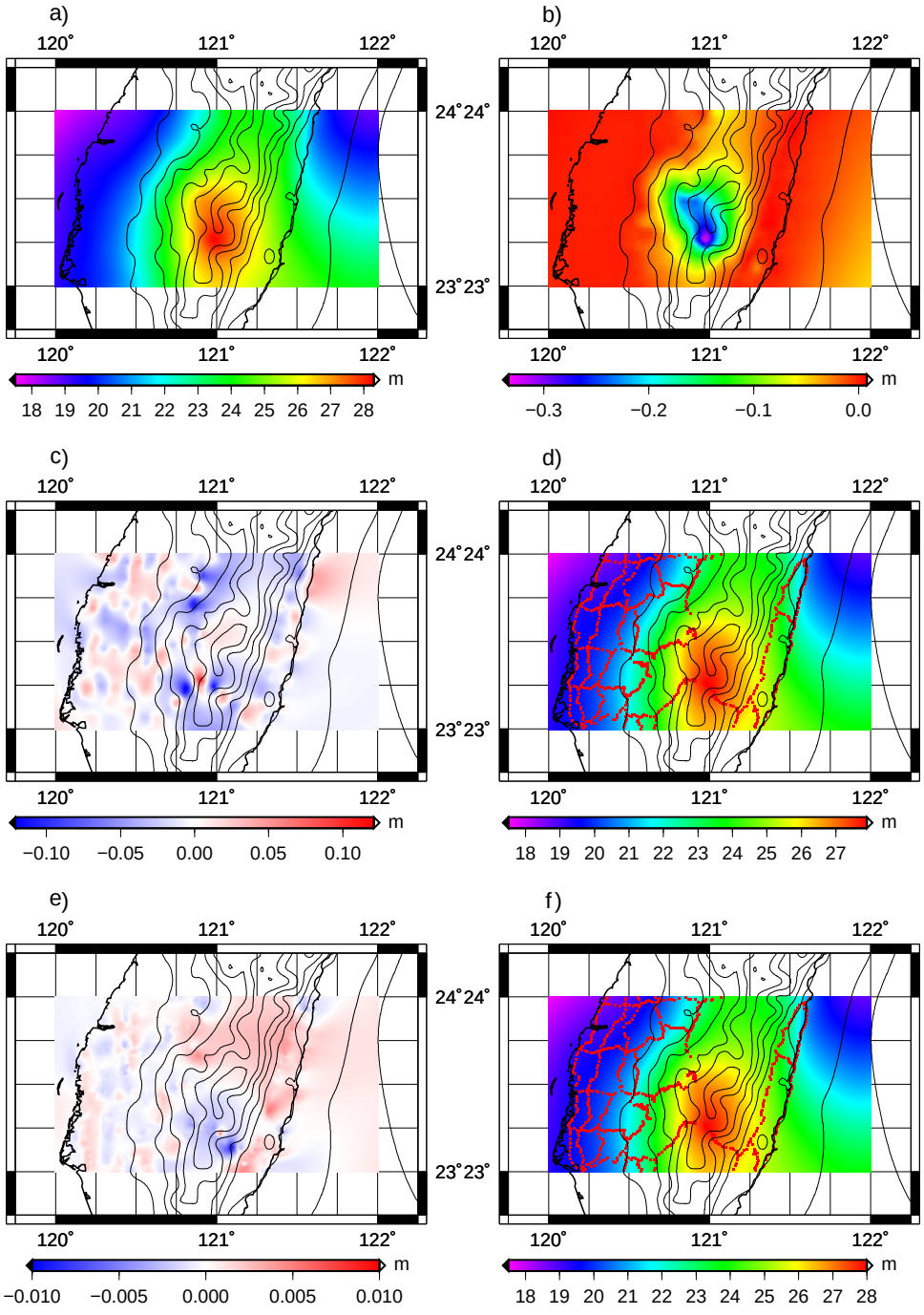

Figure E.29: Test area: a) low-frequency geoid N_{GGM} (EGM08 to $n = m = 2160$), b) band-limited ITE P_b, c) Helmert's residual geoid N_b^H (N-WT), d) final geoid N (N-WT), e) Helmert's residual geoid N_b^H (AC+H) and f) final geoid N (AC+H)

	Mean	StDev	Min	Max	Range
$N_{GNSS/lev}$	22.317	± 2.449	18.763	27.955	9.192
GOCO03s to $n = m = 200$:					
N_{GGM}	22.668	± 1.510	19.821	25.295	5.473
P_b	-0.020	± 0.055	-0.357	0.009	0.366
N_b^H (WT)	-0.608	± 1.178	-2.601	2.651	5.253
N_b^H (AC+H)	-0.537	± 1.154	-2.381	2.650	5.031
N (WT)	22.197	± 2.380	18.802	27.645	8.842
N (AC+H)	22.268	± 2.398	18.810	27.669	8.859
EGM08 to $n = m = 200$:					
N_{GGM}	22.668	± 1.510	19.821	25.295	5.473
P_b	-0.020	± 0.055	-0.357	0.009	0.366
N_b^H (WT)	-0.591	± 1.159	-2.544	2.637	5.181
N_b^H (AC+H)	-0.521	± 1.141	-2.345	2.641	4.986
N (WT)	22.057	± 2.387	18.635	27.512	8.877
N (AC+H)	22.127	± 2.408	18.625	27.539	8.915
EGM08 to $n = m = 360$:					
N_{GGM}	22.285	± 2.589	18.151	27.559	9.408
P_b	-0.028	± 0.054	-0.362	0.000	0.361
N_b^H (WT)	-0.172	± 0.407	-1.273	0.742	2.015
N_b^H (AC+H)	-0.163	± 0.345	-1.042	0.755	1.797
N (WT)	22.086	± 2.435	18.605	27.587	8.982
N (AC+H)	22.094	± 2.474	18.489	27.620	9.131

	Mean	StDev	Min	Max	Range
EGM08 to $n = m = 1080$:					
N_{GGM}	22.094	$\pm$ 2.500	18.578	28.060	9.482
P_b	-0.023	$\pm$ 0.055	-0.359	0.005	0.364
N_b^H (WT)	-0.012	$\pm$ 0.075	-0.334	0.183	0.517
N_b^H (AC+H)	-0.009	$\pm$ 0.046	-0.251	0.111	0.361
N (WT)	22.059	$\pm$ 2.439	18.575	27.653	9.078
N (AC+H)	22.062	$\pm$ 2.447	18.572	27.774	9.202
EGM08 to $n = m = 2160$:					
N_{GGM}	22.080	$\pm$ 2.472	18.551	28.265	9.714
P_b	-0.019	$\pm$ 0.049	-0.338	0.008	0.346
N_b^H (WT)	-0.003	$\pm$ 0.027	-0.127	0.103	0.230
N_b^H (AC+H)	0.000	$\pm$ 0.002	-0.009	0.006	0.015
N (WT)	22.062	$\pm$ 2.443	18.551	27.919	9.368
N (AC+H)	22.061	$\pm$ 2.442	18.551	27.924	9.373

Table E.5: Statistics of the parameters in the "restore" step (N-WT, AC+H) – test area (m)

E.4 Restore step – all available gravity data

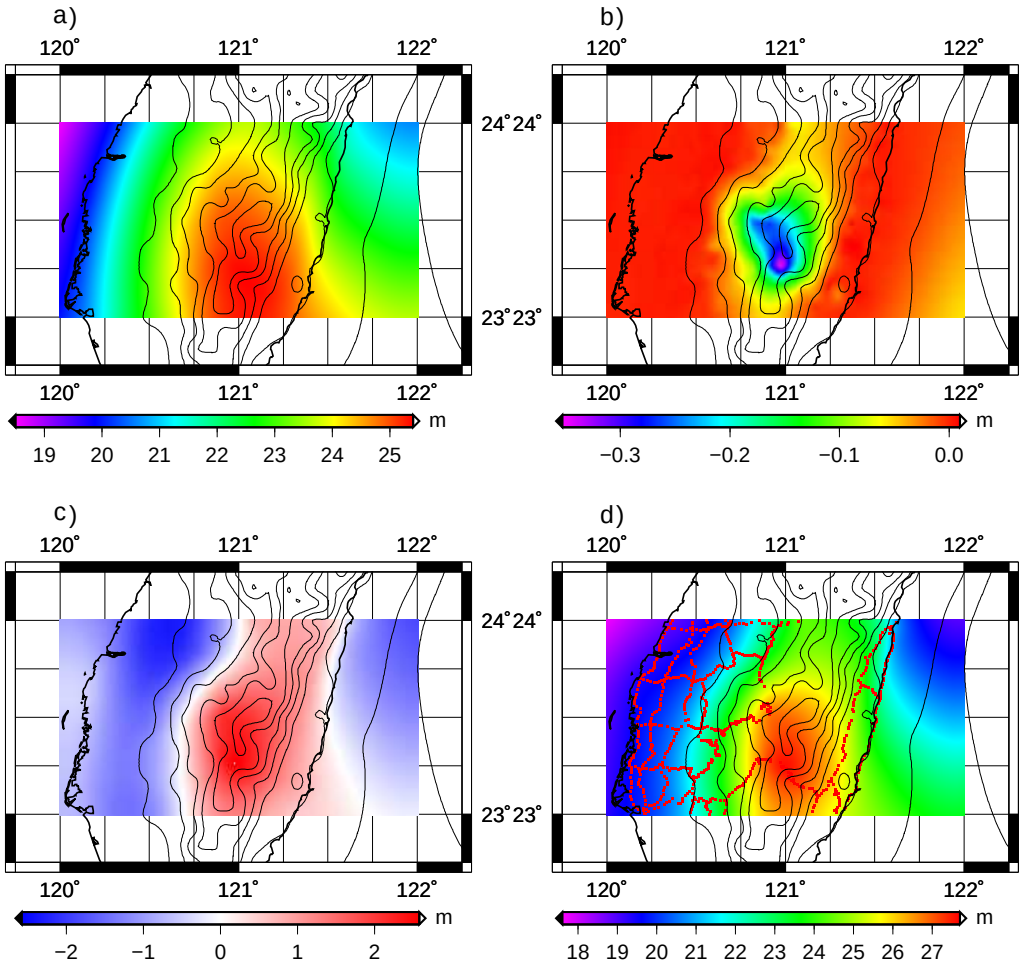

Figure E.30: All available data (GOCO03s to $n = m = 200$): a) low-frequency geoid N_{GGM}, b) band-limited ITE P_b, c) Helmert's residual geoid N_b^H (N-NC) and d) final geoid N (N-NC)

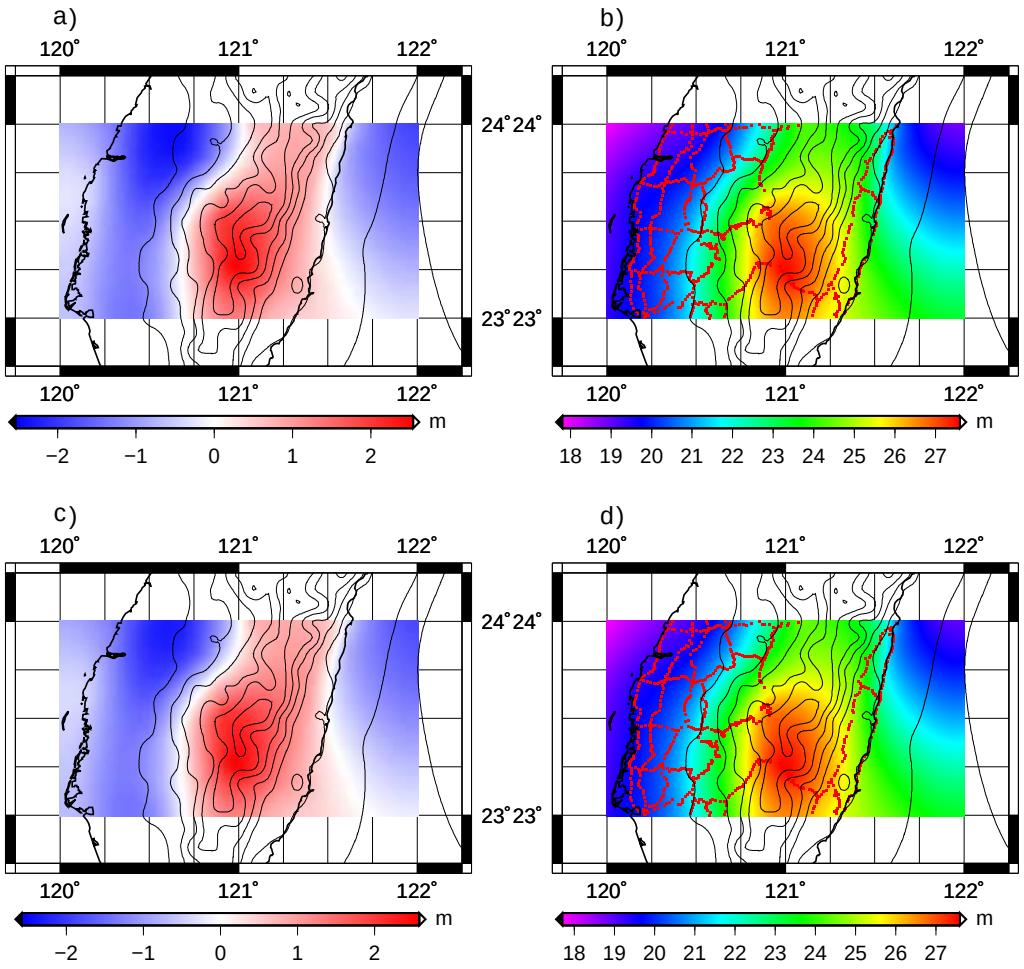

Figure E.31: All available data (GOCO03s to $n = m = 200$): a) Helmert's residual geoid N_b^H (N-WT), b) final geoid N (N-WT), c) Helmert's residual geoid N_b^H (AC+H) and d) final geoid N (AC+H)

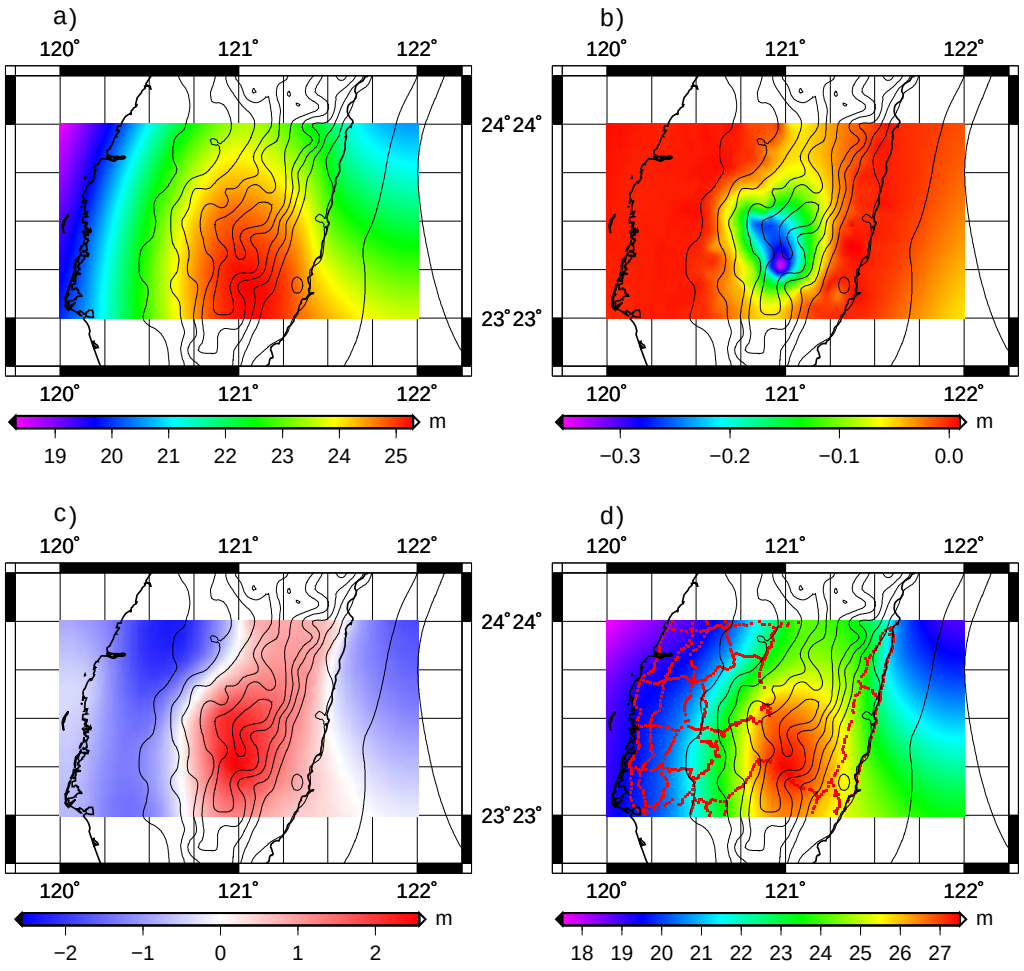

Figure E.32: All available data (EGM08 to $n = m = 200$): a) low-frequency geoid N_{GGM}, b) band-limited ITE P_b, c) Helmert's residual geoid N_b^H (N-NC) and d) final geoid N (N-NC)

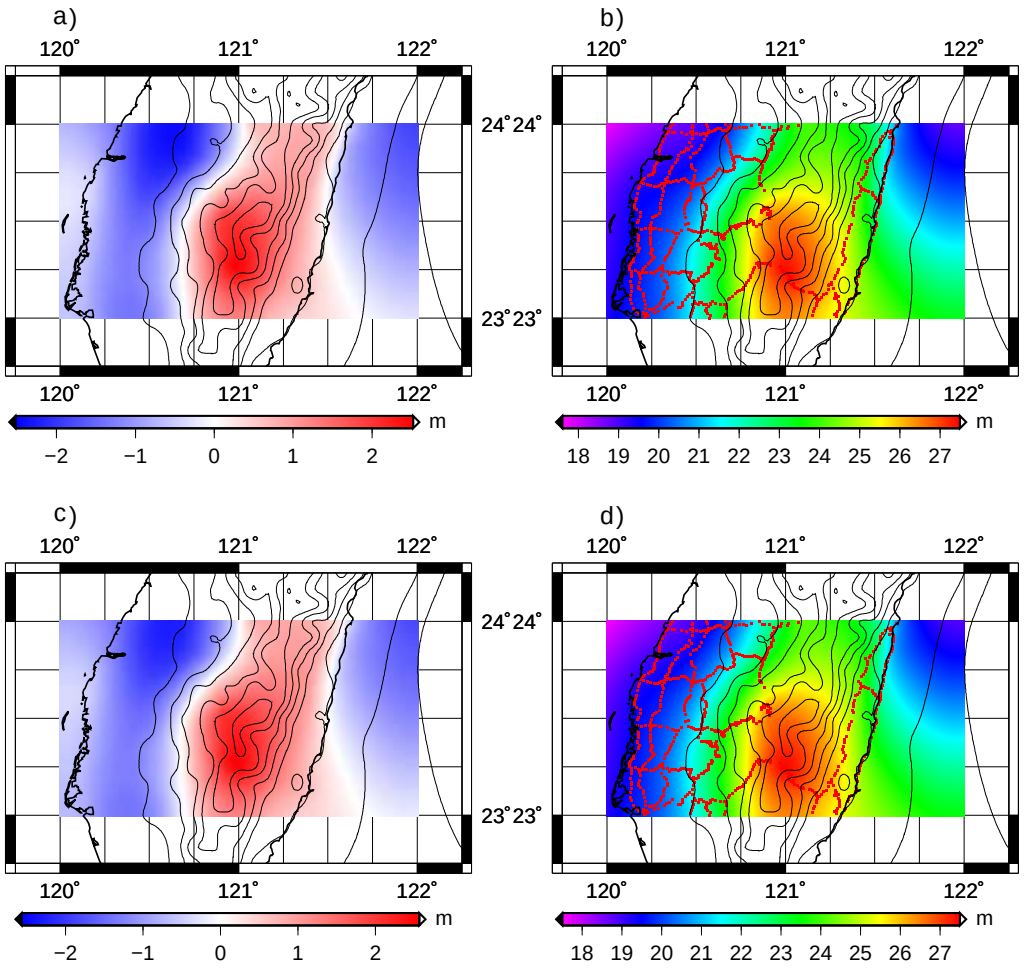

Figure E.33: All available data (EGM08 to $n = m = 200$): a) Helmert's residual geoid N_b^H (N-WT), b) final geoid N (N-WT), c) Helmert's residual geoid N_b^H (AC+H) and d) final geoid N (AC+H)

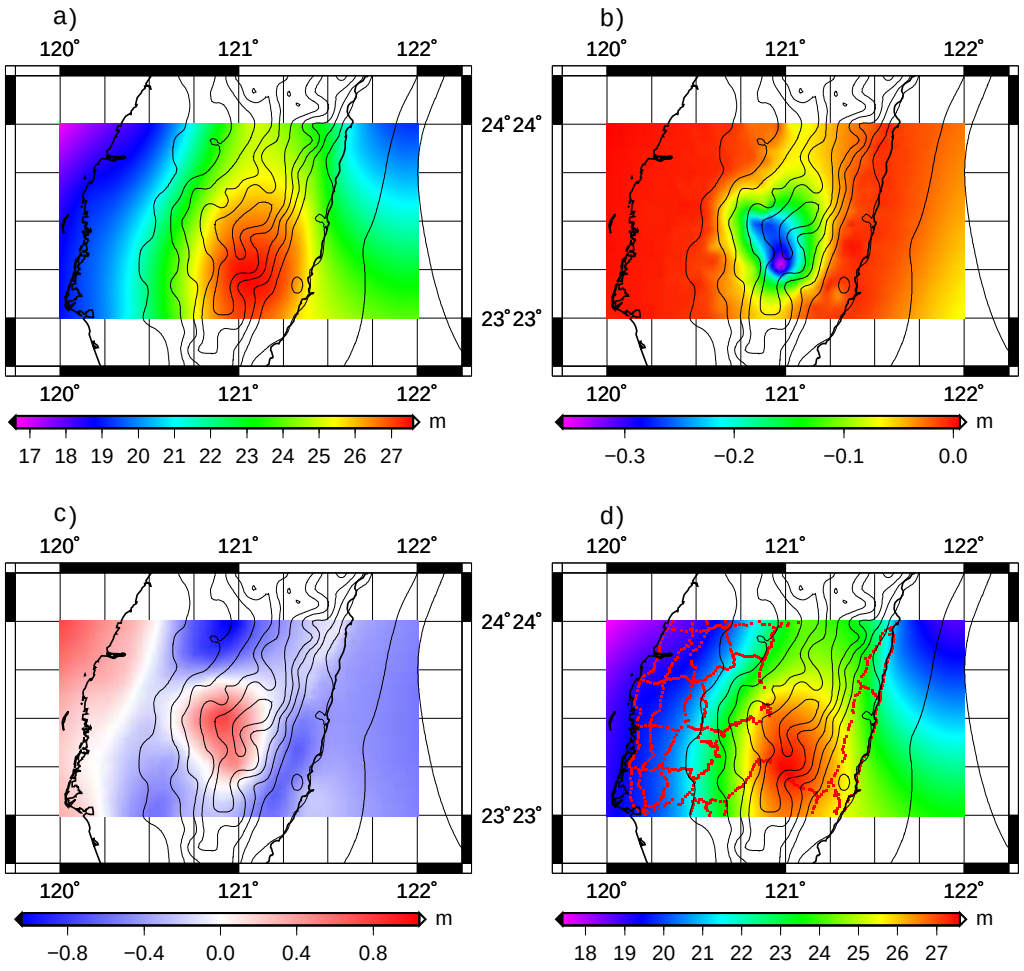

Figure E.34: All available data (EGM08 to $n = m = 360$): a) low-frequency geoid N_{GGM}, b) band-limited ITE P_b, c) Helmert's residual geoid N_b^H (N-NC) and d) final geoid N (N-NC)

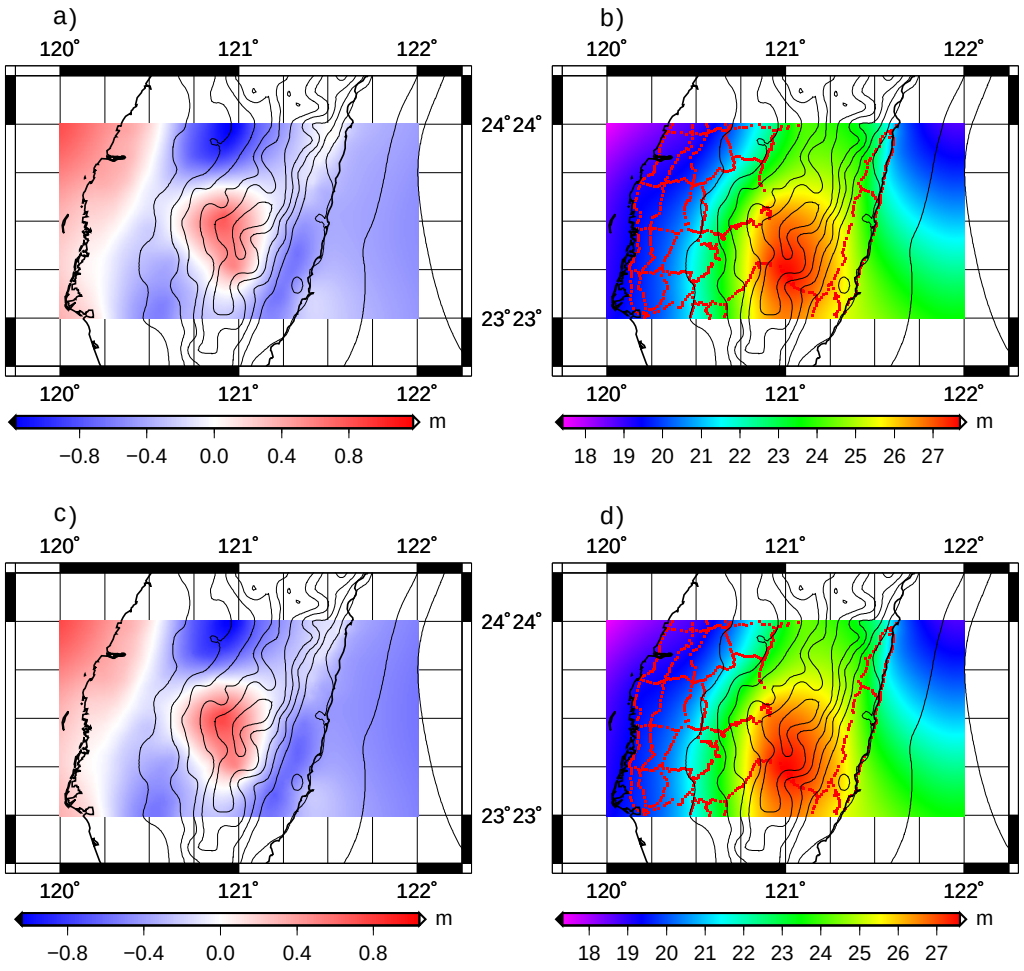

Figure E.35: All available data (EGM08 to $n = m = 360$): a) Helmert's residual geoid N_b^H (N-WT), b) final geoid N (N-WT), c) Helmert's residual geoid N_b^H (AC+H) and d) final geoid N (AC+H)

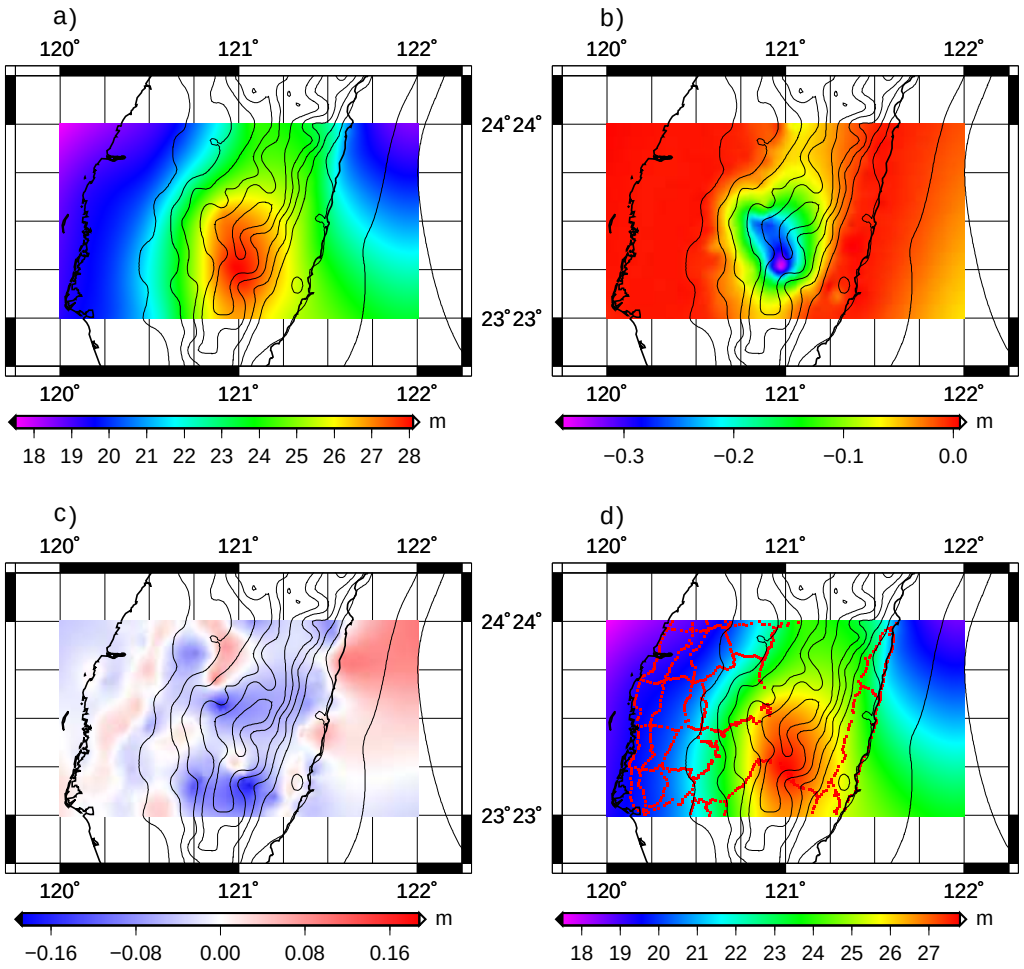

Figure E.36: All available data (EGM08 to $n = m = 1080$): a) low-frequency geoid N_{GGM}, b) band-limited ITE P_b, c) Helmert's residual geoid N_b^H (N-NC) and d) final geoid N (N-NC)

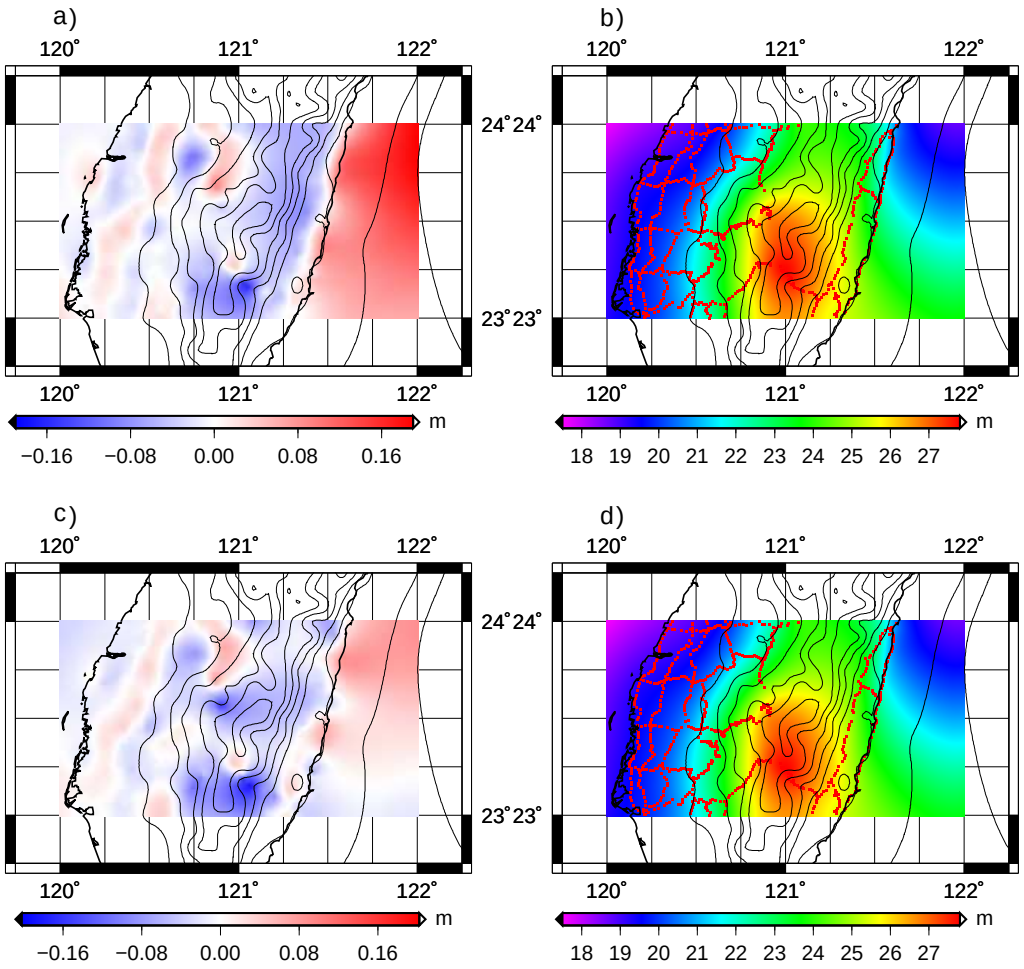

Figure E.37: All available data (EGM08 to $n = m = 1080$): a) Helmert's residual geoid N_b^H (N-WT), b) final geoid N (N-WT), c) Helmert's residual geoid N_b^H (AC+H) and d) final geoid N (AC+H)

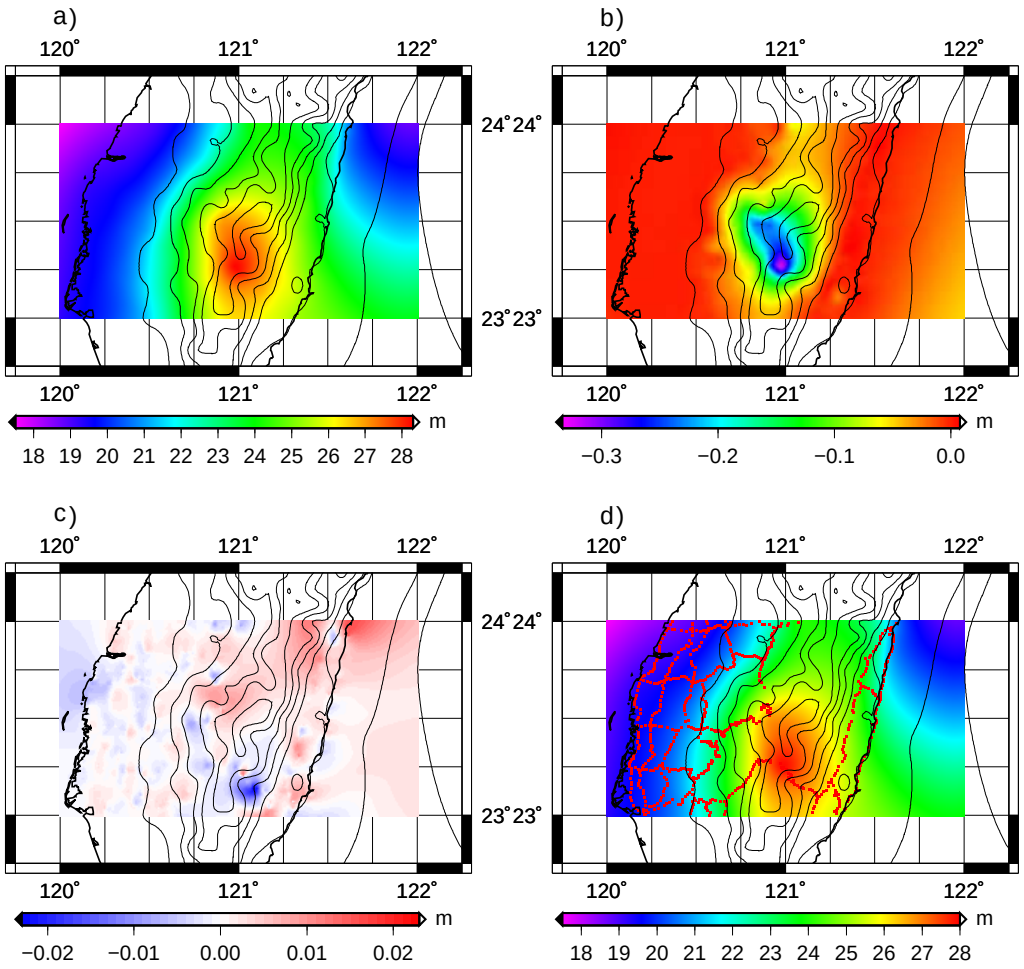

Figure E.38: All available data (EGM08 to $n = m = 2160$): a) low-frequency geoid N_{GGM}, b) band-limited ITE P_b, c) Helmert's residual geoid N_b^H (N-NC) and d) final geoid N (N-NC)

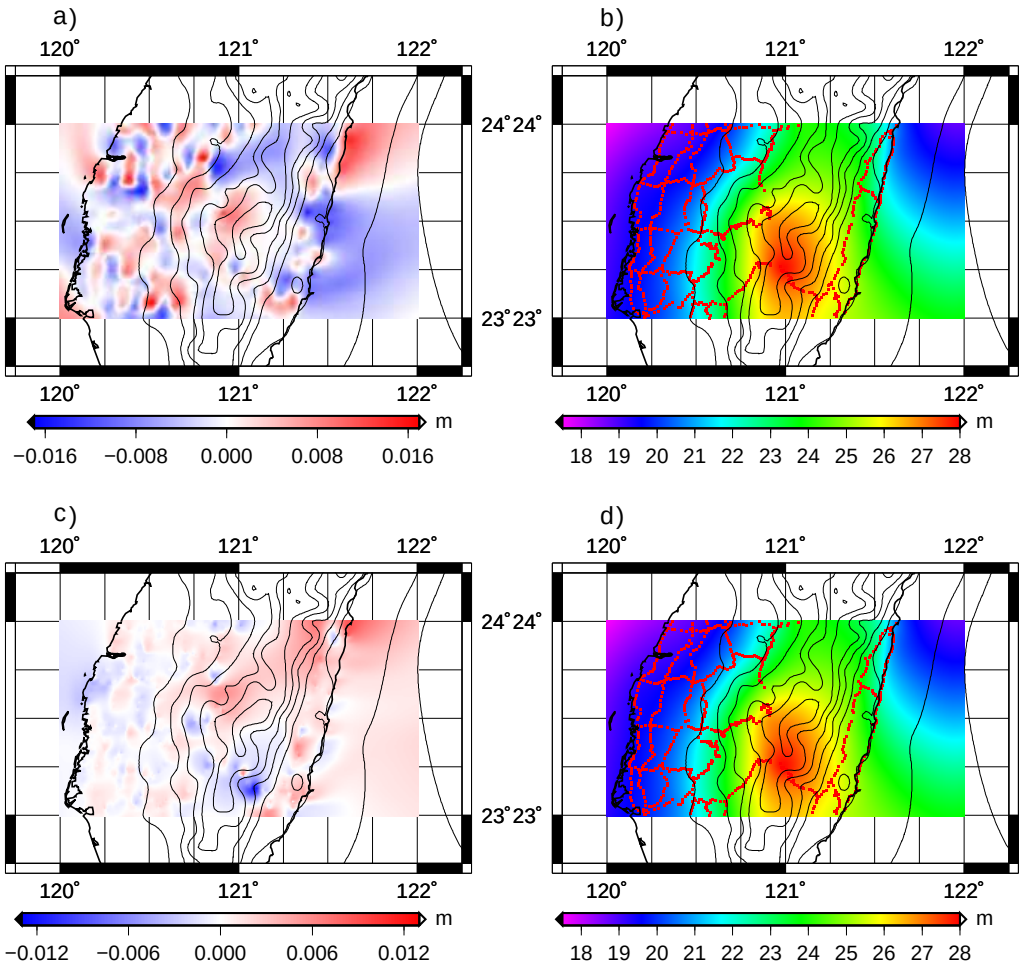

Figure E.39: All available data (EGM08 to $n = m = 2160$): a) Helmert's residual geoid N_b^H (N-WT), b) final geoid N (N-WT), c) Helmert's residual geoid N_b^H (AC+H) and d) final geoid N (AC+H)

	Mean	StDev	Min	Max	Range
$N_{GNSS/lev}$	22.317	± 2.449	18.763	27.955	9.192
GOCO03s to $n = m = 200$:					
N_{GGM}	22.668	± 1.510	19.821	25.295	5.473
P_b	-0.020	± 0.055	-0.357	0.009	0.366
N_b^H (NC)	-0.541	± 1.149	-2.339	2.581	4.920
N_b^H (WT)	-0.585	± 1.129	-2.442	2.540	4.982
N_b^H (AC+H)	-0.536	± 1.138	-2.326	2.571	4.896
N (NC)	22.262	± 2.398	18.813	27.603	8.790
N (WT)	22.219	± 2.350	18.855	27.552	8.696
N (AC+H)	22.267	± 2.385	18.849	27.593	8.744
EGM08 to $n = m = 200$:					
N_{GGM}	22.668	± 1.510	19.821	25.295	5.473
P_b	-0.020	± 0.055	-0.357	0.009	0.366
N_b^H (NC)	-0.531	± 1.138	-2.313	2.569	4.882
N_b^H (WT)	-0.576	± 1.116	-2.420	2.519	4.939
N_b^H (AC+H)	-0.527	± 1.127	-2.291	2.564	4.855
N (NC)	22.115	± 2.408	18.627	27.474	8.847
N (WT)	22.069	± 2.360	18.665	27.415	8.750
N (AC+H)	22.119	± 2.401	18.632	27.469	8.838
EGM08 to $n = m = 360$:					
N_{GGM}	22.285	± 2.589	18.151	27.559	9.408
P_b	-0.028	± 0.054	-0.362	0.000	0.361
N_b^H (NC)	-0.168	± 0.342	-1.029	0.797	1.827
N_b^H (WT)	-0.157	± 0.370	-1.174	0.789	1.963
N_b^H (AC+H)	-0.165	± 0.338	-1.014	0.783	1.797
N (NC)	22.090	± 2.476	18.497	27.583	9.086
N (WT)	22.100	± 2.463	18.567	27.650	9.083
N (AC+H)	22.092	± 2.477	18.493	27.602	9.109

	Mean	StDev	Min	Max	Range
EGM08 to $n = m = 1080$:					
N_{GGM}	22.094	$\pm$ 2.500	18.578	28.060	9.482
P_b	-0.023	$\pm$ 0.055	-0.359	0.005	0.364
N_b^H (NC)	-0.011	$\pm$ 0.041	-0.189	0.099	0.288
N_b^H (WT)	-0.005	$\pm$ 0.037	-0.160	0.105	0.265
N_b^H (AC+H)	-0.009	$\pm$ 0.039	-0.202	0.090	0.292
N (NC)	22.060	$\pm$ 2.449	18.557	27.774	9.218
N (WT)	22.067	$\pm$ 2.455	18.563	27.776	9.214
N (AC+H)	22.062	$\pm$ 2.450	18.559	27.792	9.233
EGM08 to $n = m = 2160$:					
N_{GGM}	22.080	$\pm$ 2.472	18.551	28.265	9.714
P_b	-0.019	$\pm$ 0.049	-0.338	0.008	0.346
N_b^H (NC)	0.000	$\pm$ 0.004	-0.024	0.021	0.044
N_b^H (WT)	0.000	$\pm$ 0.006	-0.015	0.016	0.032
N_b^H (AC+H)	0.000	$\pm$ 0.002	-0.013	0.011	0.024
N (NC)	22.061	$\pm$ 2.442	18.553	27.923	9.370
N (WT)	22.061	$\pm$ 2.442	18.550	27.921	9.371
N (AC+H)	22.061	$\pm$ 2.442	18.552	27.924	9.372

Table E.6: Statistics of the parameters in the "restore" step (N-NC, N-WT, AC+H) – all available gravity data (m)

E.5 Comparison with GNSS/levelling points – test area

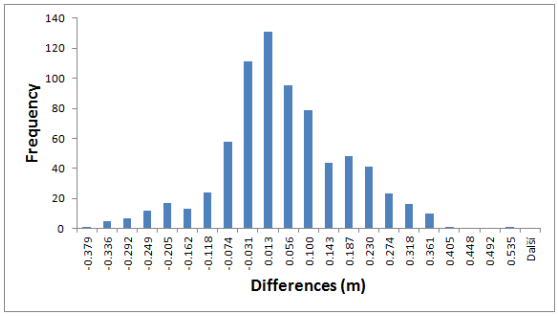

1)

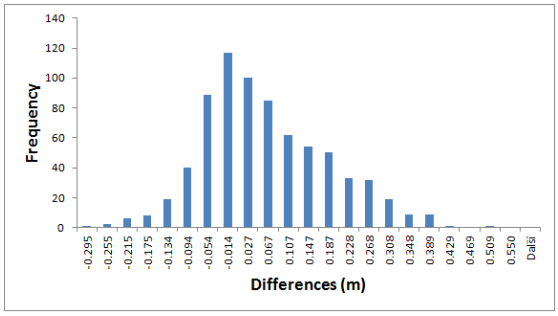

2)

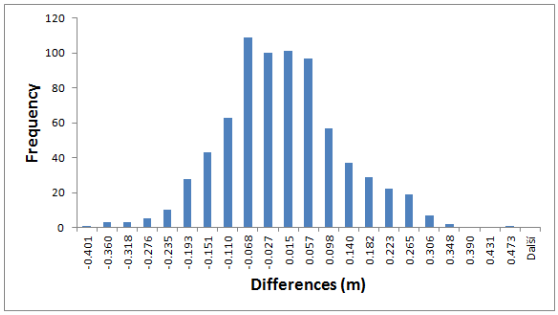

3)

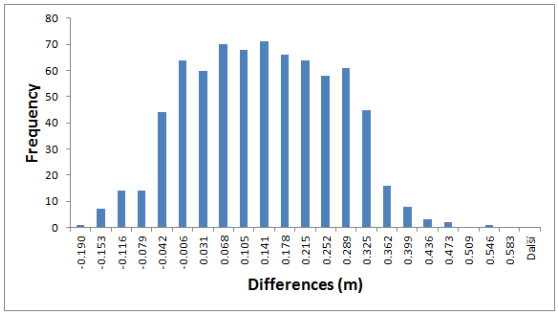

4)

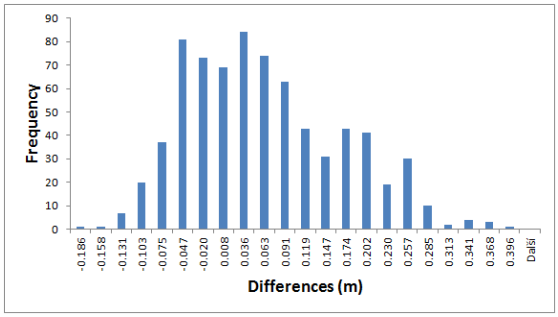

5)

Figure E.40: Histograms of the differences between the GNSS/levelling and the computed geoidal heights – test area (m) (GOCO03s to $n = m = 200$): $1)$ without the topographical effect, $2)$ the topographical effect – integration, $3)$ the topographical effect – spherical series, $4)$ wavelet transform with the topographical effect – integration and $5)$ analytic continuation and Hotine's formula

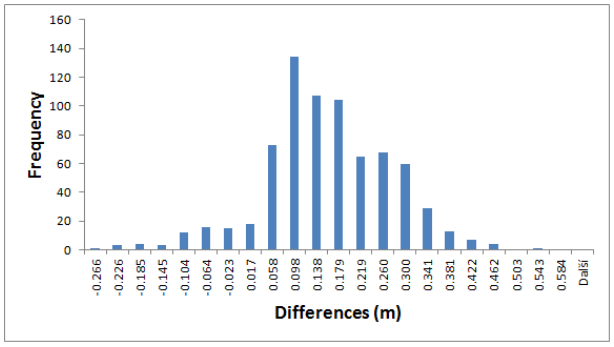

1)

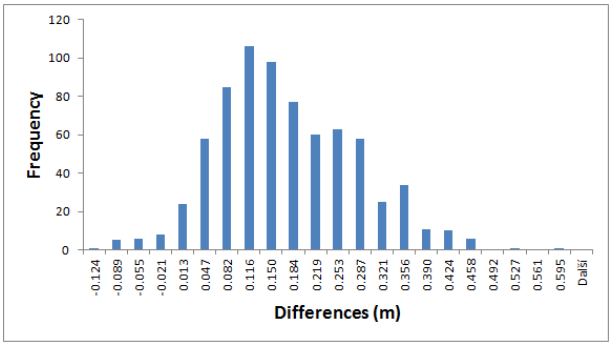

2)

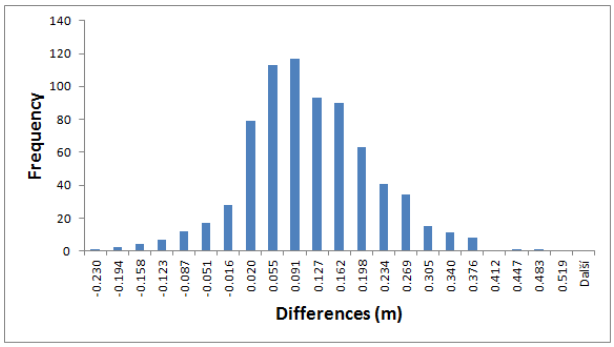

3)

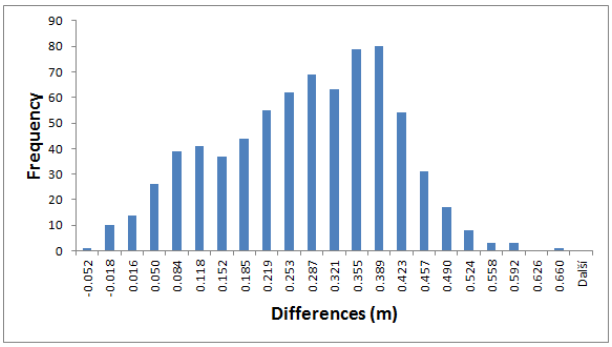

4)

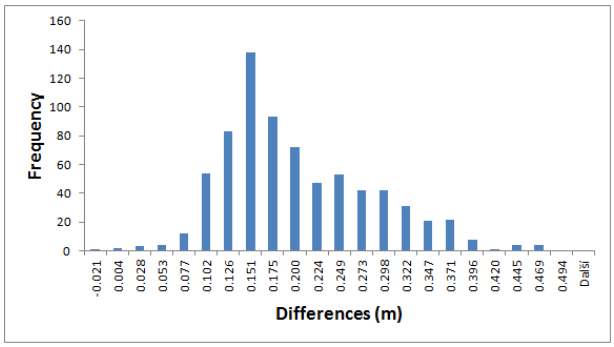

5)

Figure E.41: Histograms of the differences between the GNSS/levelling and the computed geoidal heights – test area (m) (EGM08 to $n = m = 200$): $1)$ without the topographical effect, $2)$ the topographical effect – integration, $3)$ the topographical effect – spherical series, $4)$ wavelet transform with the topographical effect – integration and $5)$ analytic continuation and Hotine's formula

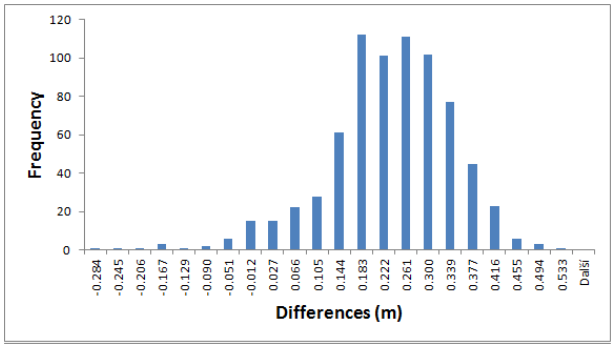

1)

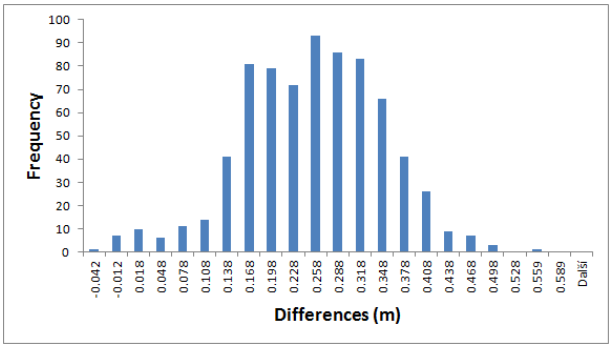

2)

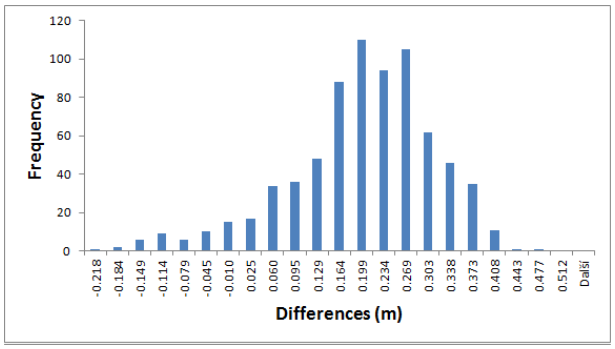

3)

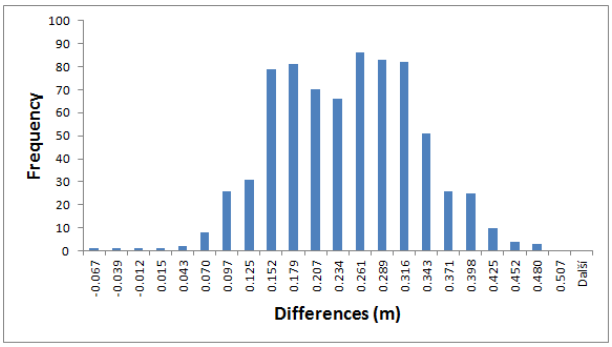

4)

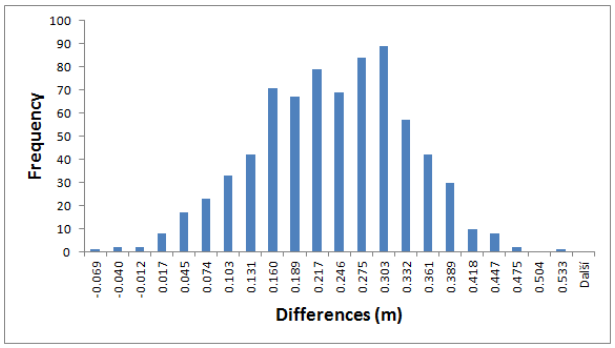

5)

Figure E.42: Histograms of the differences between the GNSS/levelling and the computed geoidal heights – test area (m) (EGM08 to $n = m = 360$): $1)$ without the topographical effect, $2)$ the topographical effect – integration, $3)$ the topographical effect – spherical series, $4)$ wavelet transform with the topographical effect – integration and $5)$ analytic continuation and Hotine's formula

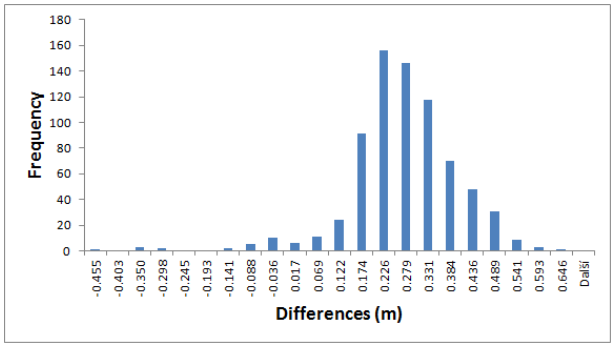

1)

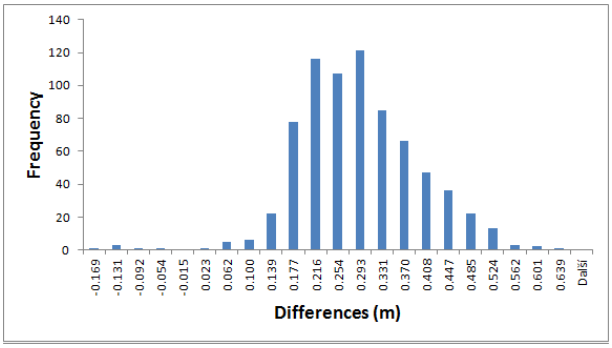

2)

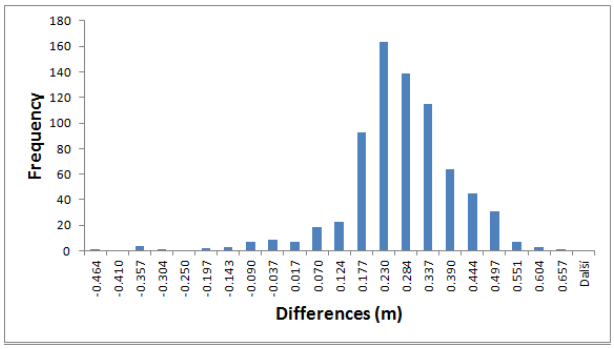

3)

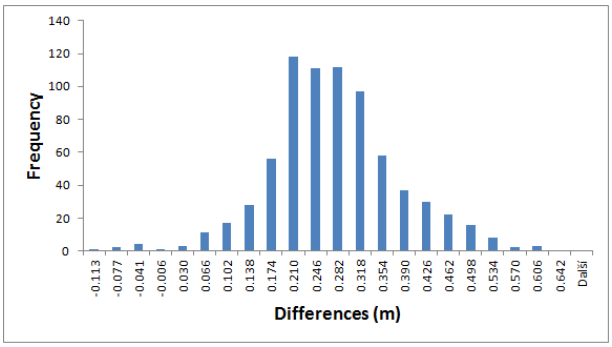

4)

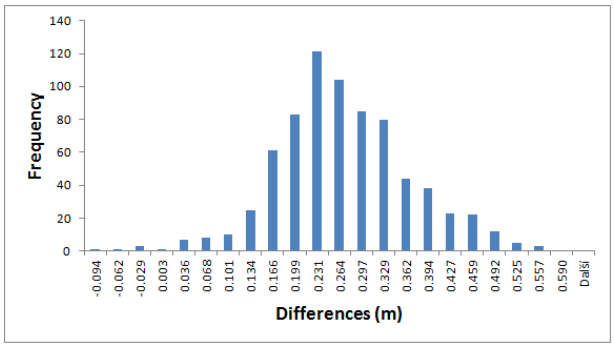

5)

Figure E.43: Histograms of the differences between the GNSS/levelling and the computed geoidal heights – test area (m) (EGM08 to $n = m = 1080$): 1) without the topographical effect, 2) the topographical effect – integration, 3) the topographical effect – spherical series, 4) wavelet transform with the topographical effect – integration and 5) analytic continuation and Hotine's formula

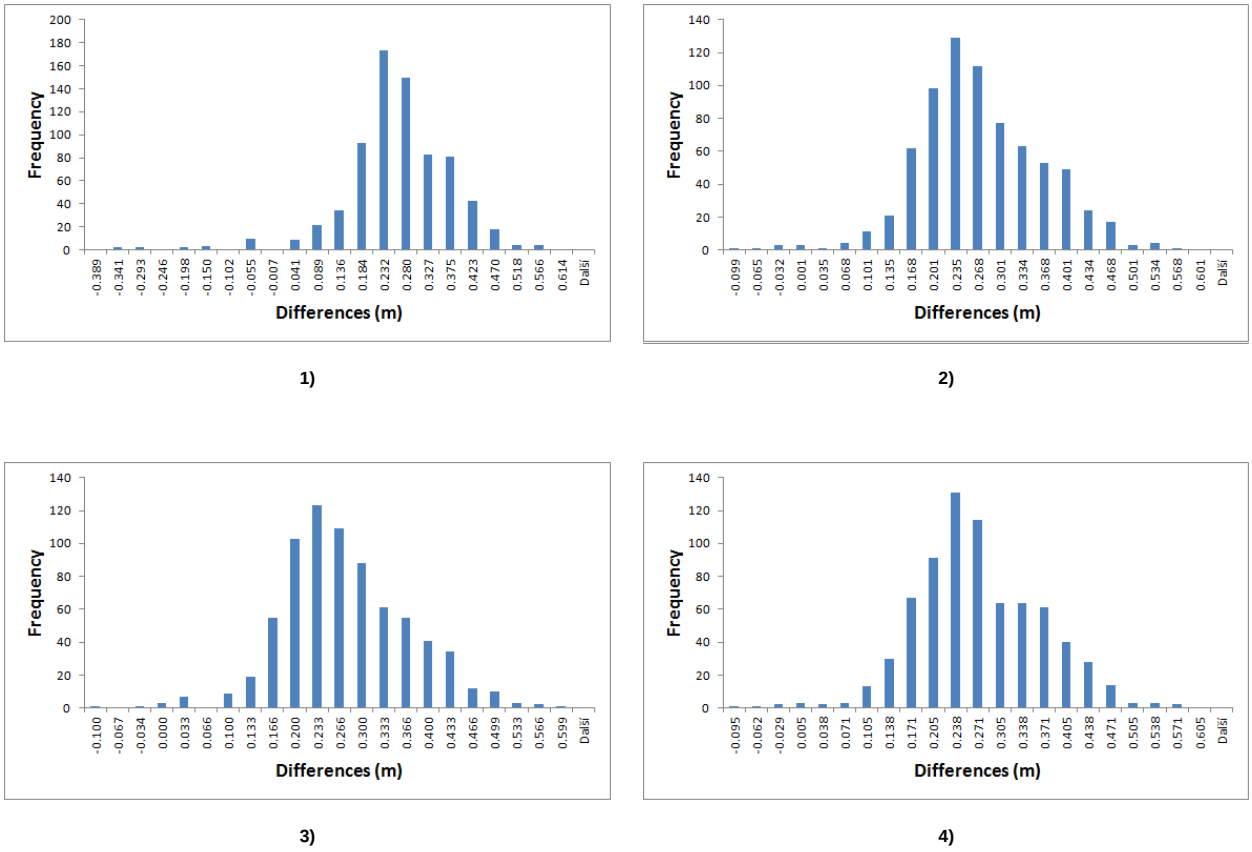

Figure E.44: Histograms of the differences between the GNSS/levelling and the computed geoidal heights – test area (m) (EGM08 to $n = m = 2160$): $1)$ without the topographical effect, $2)$ the topographical effect – integration, $3)$ wavelet transform with the topographical effect – integration and $4)$ analytic continuation and Hotine's formula

E.6 Comparison with GNSS/levelling points – all available gravity data

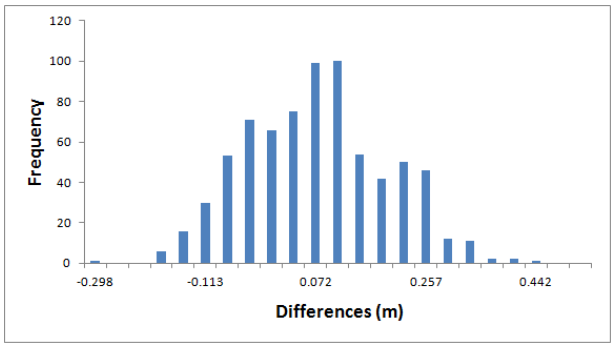

1)

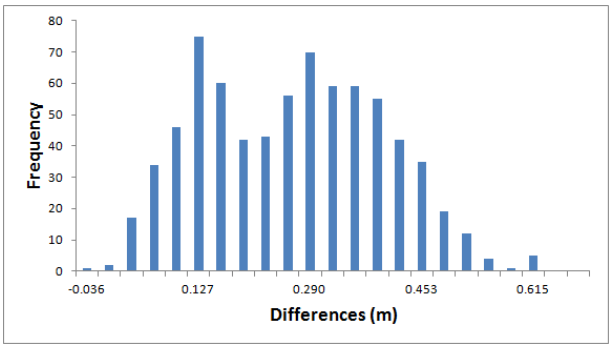

2)

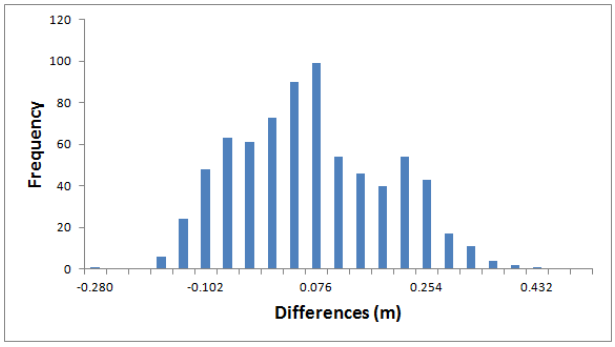

3)

Figure E.45: Histograms of the differences between the GNSS/levelling and the computed geoidal heights – all available gravity data (m) (GOCO03s to $n = m = 200$): $1)$ numerical integration, $2)$ wavelet transform and $3)$ analytic continuation and Hotine's formula

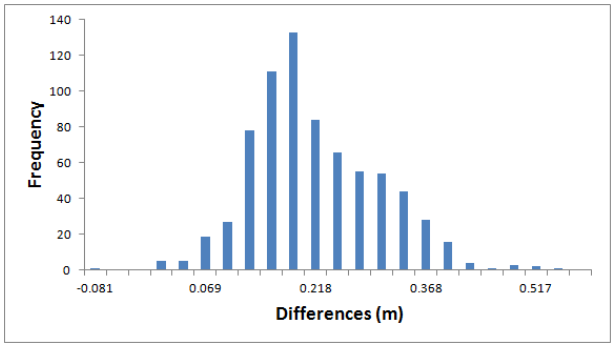

1)

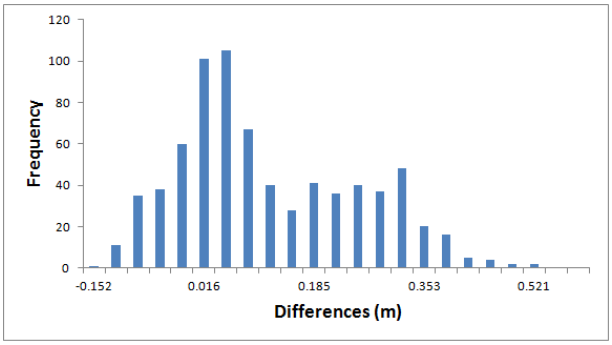

2)

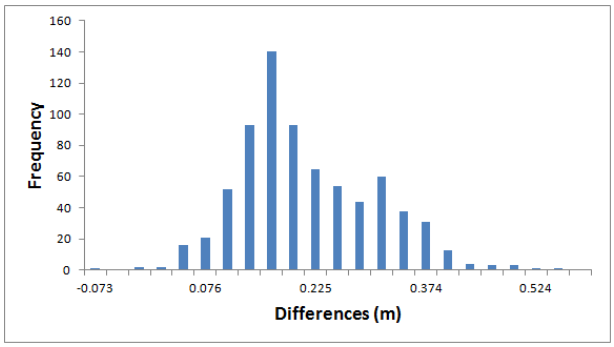

3)

Figure E.46: Histograms of the differences between the GNSS/levelling and the computed geoidal heights – all available gravity data (m) (EGM08 to $n = m = 200$): $1)$ numerical integration, $2)$ wavelet transform and $3)$ analytic continuation and Hotine's formula

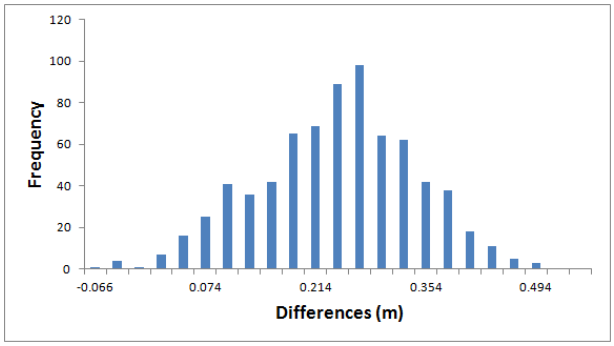

1)

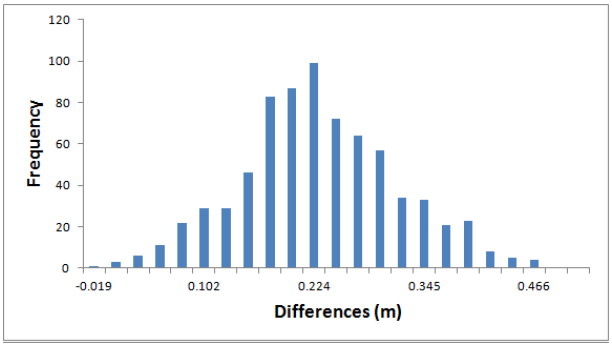

2)

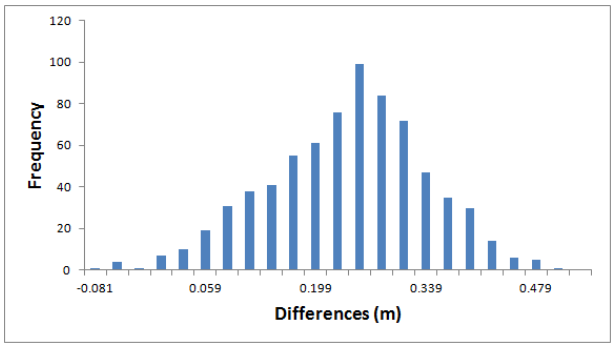

3)

Figure E.47: Histograms of the differences between the GNSS/levelling and the computed geoidal heights – all available gravity data (m) (EGM08 to $n = m = 360$): $1)$ numerical integration, $2)$ wavelet transform and $3)$ analytic continuation and Hotine's formula

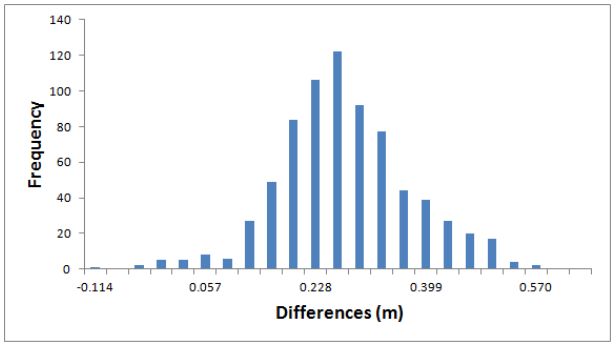

1)

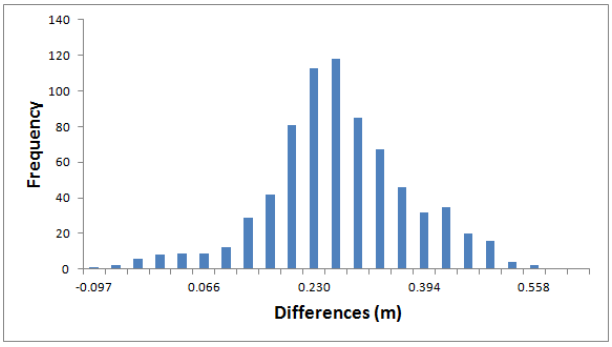

2)

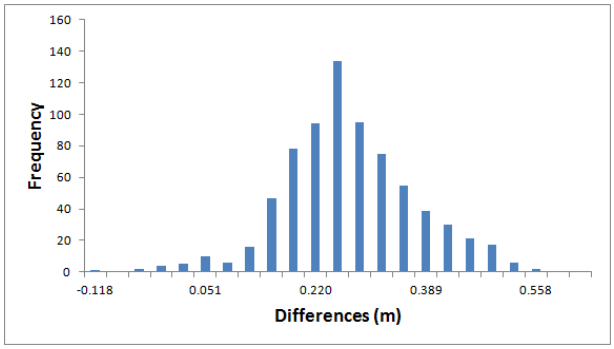

3)

Figure E.48: Histograms of the differences between the GNSS/levelling and the computed geoidal heights – all available gravity data (m) (EGM08 to $n = m = 1080$): $1)$ numerical integration, $2)$ wavelet transform and $3)$ analytic continuation and Hotine's formula

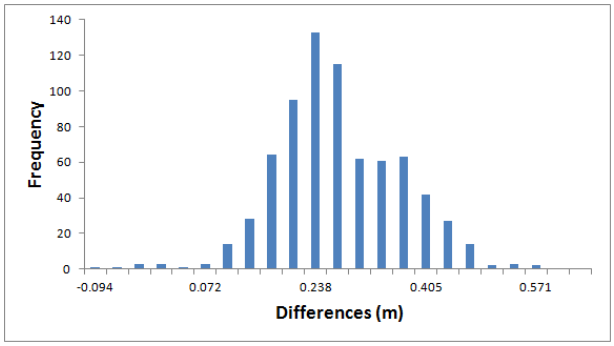

1)

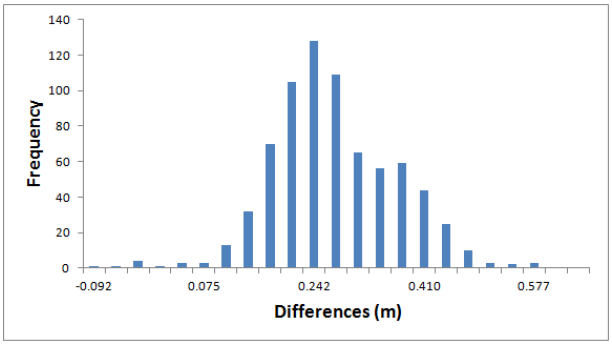

2)

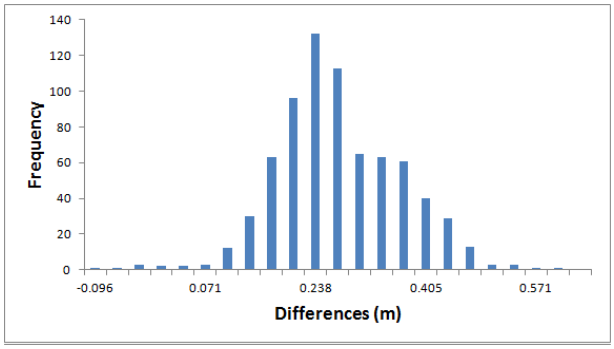

3)

Figure E.49: Histograms of the differences between the GNSS/levelling and the computed geoidal heights – all available gravity data (m) (EGM08 to $n = m = 2160$): $1)$ numerical integration, $2)$ wavelet transform and $3)$ analytic continuation and Hotine's formula

E.7 Comparison with GNSS/levelling points – GGMs only

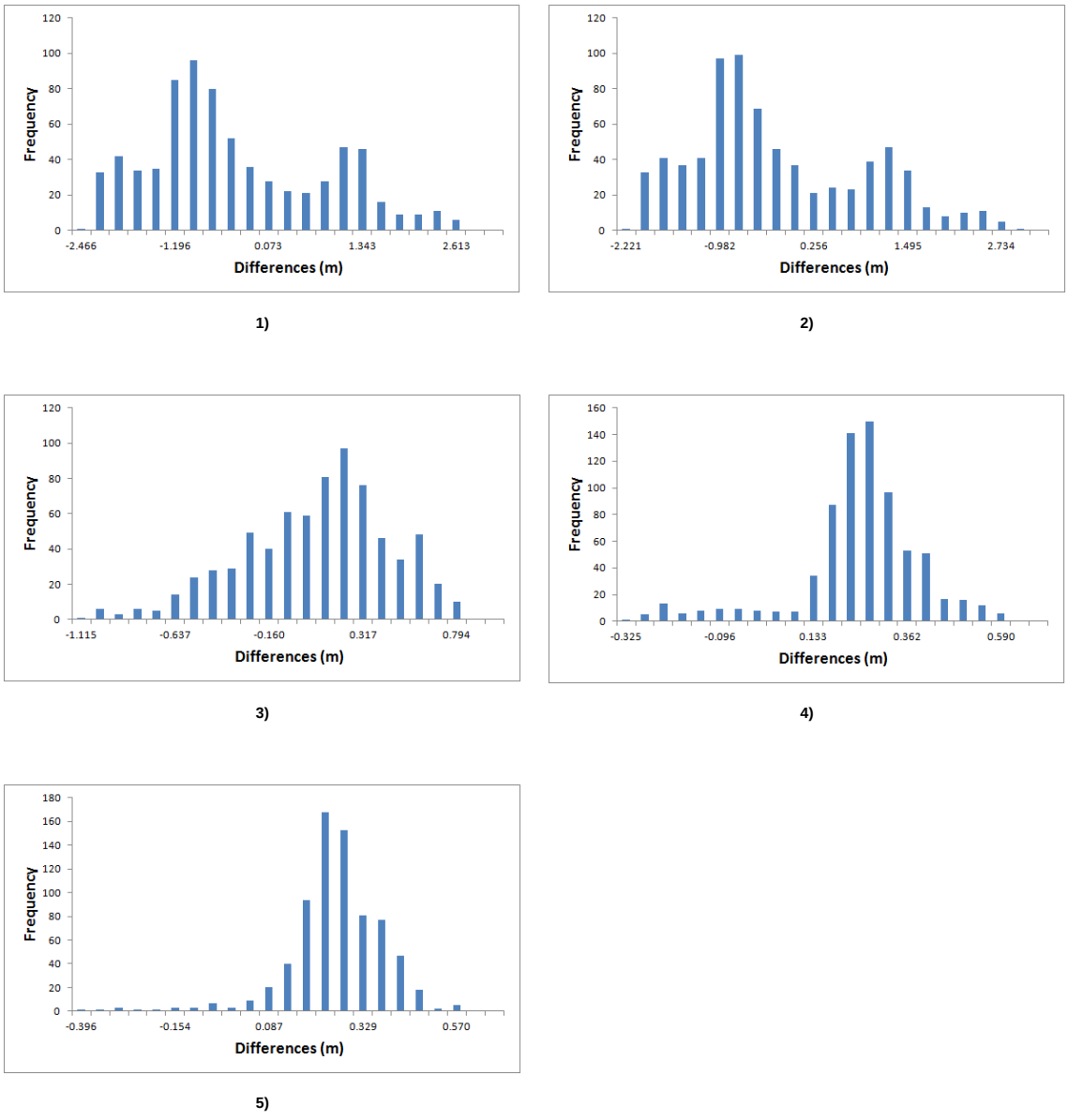

Figure E.50: Histograms of the differences between the GNSS/levelling and the computed geoidal heights – GGMs only (m): 1) GOCO03s to $n = m = 200$, 2) EGM08 to $n = m = 200$, 3) EGM08 to $n = m = 360$, 4) EGM08 to $n = m = 1080$ and 5) EGM08 to $n = m = 2160$